THE UNIVERSITY *of* EDINBURGH

Controls on fluvial networks in upland landscapes: from hillslopes to floodplains

Fiona J. Clubb

THE UNIVERSITY
of EDINBURGH

Thesis submitted in fulfillment of
the requirements for the degree of
Doctor of Philosophy
to the
University of Edinburgh — 2017

Declaration

I declare that this thesis has been composed solely by myself and that it has not been submitted, either in whole or in part, in any previous application for a degree. Except where otherwise acknowledged, the work presented is entirely my own.

Fiona J. Clubb

July 2017

Abstract

Mountainous regions are ubiquitously dissected by river networks. These networks are the main drivers by which climate and tectonic signals are transmitted to the rest of the landscape, and control the response timescale of the landscape to these external forcings. Furthermore, river systems set the downslope boundary conditions for hillslope sediment transport, which controls landscape denudation. Therefore, understanding the controls on the organisation and structure of river networks in upland landscapes is an important goal in Earth surface processes research. The recent introduction of high-resolution topographic data, such as airborne lidar data, has revolutionised our ability to extract information from the topography, providing new opportunities for linking geomorphic process with landscape form.

This thesis is focused on developing techniques for analysing high-resolution topographic data to quantify and understand controls on the structure of fluvial systems in upland landscapes. Firstly, I develop and test new algorithms for objective feature extraction from lidar-derived digital elevation models (DEMs). I present a new method for identifying the upstream extent of channel processes by identifying scaling breaks in river long profiles. I then compare this new method to three existing methods of channel extraction, using field-mapped channel heads from four field sites in the US. I find that the new method presented here, along

with another method of identifying channels based on valley geometry, most accurately reproduces the measured channel heads in all four field sites.

I then present a new method for identifying floodplains and fluvial terraces from DEMs based on two thresholds: local gradient, and elevation compared to the nearest channel. These thresholds are calculated statistically from the DEM using quantile-quantile plots and do not need to be set manually for each landscape in question. I test this new method against field-mapped floodplain initiation points, published flood hazard maps, and digitised terrace surfaces from eight field sites in both the US and the UK. This method provides a new tool for rapidly and objectively identifying floodplain and terrace features on a landscape scale, with applications including flood risk mapping, landscape evolution modelling, and quantification of sediment storage and routing.

Finally, I apply these new algorithms to examine the density of channel networks across a range of mountainous landscapes, and explore implications for fluvial incision models. I compare the relationship between drainage density (D_d) and erosion rate (E) using both analytical solutions and numerical modelling, and find that varying the channel slope exponent (n) in detachment-limited fluvial incision models controls the relationship between D_d and E. Following on from this, I quantify D_d for five field sites throughout the US. For two of these field sites I compare D_d to cosmogenic radionuclide (CRN)-derived erosion rates, and for each site I use mean hilltop curvature as a proxy for erosion rate where CRN-derived erosion rates are not available. I find that there is a significant positive relationship between D_d, E, and hilltop curvature across four out of the five field sites. In contrast to assumptions made in many studies of fluvial incision, this positive relationship suggests that the channel slope exponent n is greater than unity for each of these landscapes, with fundamental implications for both landscape evolution and sediment transport.

Lay Summary

Mountainous regions are dissected and shaped by river channels, their valleys, and their surrounding hillslopes. Understanding how external factors, such as climate or tectonics, controls the structure and organisation of these channel networks is essential for applications such as flood forecasting, understanding patterns of erosion and deposition, and the transfer of sediment and nutrients through river catchments. In the past 30 years, the availability and resolution of topographic data, such as airborne lidar data, has increased exponentially. These data have revolutionised our ability to extract information from the topography and quantify the shape of river networks and their valleys.

This thesis is focused on developing new techniques to analyse these high-resolution topographic data to understand controls on the structure of river networks in mountainous regions. Firstly, I develop new algorithms for identifying channel networks from topographic data. I compare this new method to three existing methods of channel extraction, using field-mapped channel networks as a benchmark. I find that the new method presented here, along with one of the existing methods, most accurately identifies the field-mapped channel network. This new method of identifying channel networks provides new opportunities for more accurately modelling how water and sediment move through river networks.

Following on from this work, I then present a new method for identifying

floodplains and river terraces from topographic data. This method identifies these features as continuous, flat areas near to the height of the modern channel. I identify parameters in this method using statistically-defined thresholds, so that the method can be run rapidly across many landscapes without needing to be compared to field-mapped data. I test this new method against published flood maps and field-mapped terraces from eight field sites in both the US and the UK. This method provides a new tool for rapidly identifying floodplains and terraces on a large scale, with applications including flood risk mapping, and helping us to understand how rivers erode the landscape over time.

Finally, I apply these new algorithms to examine controls on the structure and organisation of channel networks across a range of mountainous landscapes. I analyse the density of channel networks in each river basin across five landscapes in the US, and compare this to measurements of landscape erosion rate. I find a positive relationship between the density of channel networks and erosion rate across four of the five field sites, suggesting that in faster-eroding landscapes, the channel network expands, and therefore water and sediment move more quickly through these basins. This has important implications for hydrology, flow routing, and long-term landscape evolution.

Acknowledgements

During my PhD at Edinburgh I've had the support and help of far too many people to mention them all properly.

First and foremost, I would like to thank Simon Mudd for his advice, mentorship, and guidance throughout both my undergraduate and PhD degrees. When I first went to Simon and asked about doing my undergraduate dissertation in hillslope geomorphology, little did I know what I was getting myself in for: I never thought that five years later I would be coding on Saturday mornings for fun! Simon's knowledge, ideas and genuine passion for research have inspired me to pursue an academic career, and I'd like to thank him for all the time and effort he's put into helping me, and for being so approachable.

I would also like to particularly thank Mikaël Attal and Hugh Sinclair, whose mentorship and help over my time at Edinburgh have been invaluable. Thank you both for many fond memories of field trips, discussion meetings, lectures, conferences, and drinks together!

I couldn't have done any of the work in this thesis without the help of the LSDTopoHackers: doing research and developing software in such a collaborative environment has been an amazing experience, and has really shaped my approach to science. I'd like to particularly thank David Milodowski and Stuart Grieve for their ideas, creativity, and patience in helping me fix endless segmentation faults,

as well as their insight and contributions on the papers that they've helped me to produce. I'd also like to thank Boris Gailleton for all the coding, beer, and coffee breaks (even if he doesn't take milk) - I hope that I can continue to work with you all for years to come.

I'd like to particularly thank Martin Hurst and Louise Slater for their useful advice and contributions to the papers that I've published from my PhD, which I'm very grateful for. I went into the field with TC Hales and Rob Parker: thank you both for having me along on the trip and teaching me a lot about field geomorphology, as well as good techniques for digging soil pits!

The past four years in Edinburgh wouldn't have been the same without the help and support of my fellow office mates in Lower and Upper Lewis: in particular I'd like to mention Lizzie Dingle for being an amazing field assistant, Luca Foresta for nerding out with me about code and Linux, and Lauren Shotter for all the swimming and climbing, and for letting me tag along on her fieldwork to Iceland. I'd also like to thank Marie-Alice Harel and Shasta Marrero for the numerous tea breaks and advice.

I would like to thank Penny How for her friendship and support. Thank you for all the food and tea while I was writing up my thesis, and for being there to lean on for the past four years. I'd also like to especially mention Louis Kinnear: we met in our first practical class in Edinburgh in 2009, and eight years and two degrees later, he still hasn't managed to get rid of me. I don't know what I will do without you!

Finally, I'd like to thank my family for their love and support, especially my parents, Robert and Lesley. Your guidance and understanding has made me who I am today, and I couldn't have done this without you all.

Fiona Clubb, July 2017

Contents

List of Figures

List of Tables

Notation

General notation

z	Elevation $[L]$
t	Time $[T]$
A	Upstream contributing area $[L^2]$
S	Topographic gradient
U	Rock uplift rate $[L/T]$
E	Channel incision rate $[L/T]$
∇z	Differential of elevation $(= S)$
$\nabla^2 z$	Laplacian of elevation, or local curvature $[L^{-1}]$
k_t	Tangential or planform curvature $[L^{-1}]$
C	Total curvature $[L^{-1}]$
C_{HT}	Mean hilltop curvature $[L^{-1}]$
R_G	Grid resolution $[L]$

Structure of fluvial networks

ω	Horton-Strahler stream order
ω_b	Maximum basin order
$N(\omega)$	Number of streams of a given order
$L(\omega)$	Length of streams of a given order $[L]$
$A(\omega)$	Drainage area of streams of a given order $[L^2]$
R_B	Bifurcation ratio
R_L	Length ratio
R_A	Area ratio
ℓ	Directed distance from the divide $[L]$
L_T	Length of trunk stream $[L]$
h	Hack's exponent
D_d	Basin drainage density $[L^2/L]$
L	Total length of channels in a basin $[L]$
L_h	Hillslope length $[L]$
α	Junction angle

Fluvial incision into bedrock

Ω	Unit stream power $[M/T^3]$
K_p	Coefficient relating erosion rate with stream power
W	Bankfull flow width $[L]$
ρ	Density of water $[M/L^3]$
g	Acceleration due to gravity $[L/T/T]$
Q	Bankfull discharge $[L^3/T]$
K_a	Coefficient relating discharge and drainage area
a	Exponent relating discharge and drainage area
K_w	Coefficient relating width and discharge
b	Exponent relating width and discharge
K_y	Consolidation of coefficients $= (\rho g {K_p} {K_a}^{1-b})/K_w$
τ_b	Bed shear stress
K_z	Consolidation of coefficients $= K_t \rho g ({N_m} {K_a}^{1-b}/K_w K_p K_n)^{0.6}$
K_r	Rock erodibility
N_m	Manning's roughness coefficient
K_n	Coefficient representing shape of channel cross section
K	Combined erodibility coefficient
m	Exponent on drainage area in stream power incision model
n	Exponent on slope in stream power incision model
x_d	Distance downstream $[L]$
k_{sn}	Channel steepness index, $= (E/K)^{\frac{1}{n}}$
θ	Concavity index, $= -m/n$
x	Location of current point on river channel $[L]$
x_b	Location of baselevel $[L]$
A_0	Reference drainage area $[L^2]$
χ	Transformed longitudinal coordinate for integral analysis $[L]$
M_χ	Gradient of transformed river profiles

Hillslope-valley transitions

q_s	Sediment flux $[L^3/L/T]$
D	Hillslope diffusivity $[L^2/T]$
S_c	Critical gradient for non-linear hillslope sediment flux
x_c	Critical hillslope length for channel initiation $[L]$
c	Threshold for channel initiation $[L^2]$
μ	Exponent on area for channel initiation
β	Exponent on slope for channel initiation
Pe	Péclet number
L_c	Characteristic basin length scale for non-dimensionalisation $[L]$
ζ	Characteristic basin relief for non-dimensionalisation $[L]$

Transport-limited models

q_c	Volumetric sediment transport capacity $[ML^{-1}T^{-1}]$
K_t	Coefficient in transport-limited stream power law
m_t	Exponent on area in transport-limited stream power law
n_t	Exponent on slope in transport-limited stream power law
λ_p	Porosity of sediment
B	Fraction of the total sediment load made up of bedload
θ_t	Concavity index for transport-limited conditions $= (m_t - 1)/n_t$
A_{cr}	Critical drainage area for bedrock-alluvial transition

Channel extraction

$p(\nabla z)$	Edge stopping function for Perona-Malik filter
$\|H(v)^2\|$	Power-law spectrum characterising valley morphology
$\|N(v)^2\|$	Flat power spectrum characterising white noise
η	Test value for DrEICH algorithm
R_c^2	R^2 value of channel segment in DrEICH algorithm
d_h	Durbin-Watson statistic of hillslope segment in DrEICH algorithm
r	Reliability, used for quality analysis
s	Sensitivity, used for quality analysis
Q_t	Overall quality, used for quality analysis
k_{th}	Tangential curvature threshold for channel extraction $[L^{-1}]$

Floodplain and terrace identification

R_c	Channel relief, used for floodplain and terrace identification $[L]$
w_v	Valley width $[L]$

Drainage density

S_{CH}	Equilibrium channel gradient for channel initiation
S_H	Equilibrium hillslope gradient for channel initiation
w	Width of flow strip for channel initiation $[L]$
k_f	Combined erodibility coefficient for channel initiation model $= Kw^m$ $[[T^{-1}L^{1-3m}]]$
ψ	Exponent on erosion rate in prediction of drainage density $= (1 - n)/(m + n)$

Landscape evolution model

k_b	Specific bedrock erodibility coefficient $[LT^{-1}]$

pb	Dimensionless shear stress exponent
k_g	Coefficient relating shear stress and discharge
mb	Exponent relating Q/W and shear stress
nb	Exponent relating slope and shear stress
k_w	Hydraulic scaling coefficient [$L^{-1/2}$ $T^{1/2}$]
P	Precipitation rate [L T^{-1}]

Chapter 1

Introduction

1.1 Overview

Mountainous regions are ubiquitously dissected by fluvial channels. These channels control spacing between ridges and valleys, as well as the distribution of relief [e.g. Perron *et al.*, 2008a, 2009]. Channel networks act as the mechanism by which climatic or tectonic signals are transmitted to the rest of the landscape, and therefore control the response time of a catchment to these external forcings [Tucker and Slingerland, 1997; Whipple, 2001; Mudd, 2016]. Furthermore, fluvial channels set the downslope boundary conditions for hillslope sediment transport processes, which are fundamental in controlling landscape denudation rates [Whipple and Tucker, 1999; Whipple *et al.*, 2000]. Therefore, determining controls on the structure and scale of fluvial networks is a key goal in geomorphic research.

A fundamental parameter in the fluvial network is the channel head, the transition point between diffusive hillslope processes which act to smooth the landscape and advective processes which incise the landscape [Tarboton *et al.*, 1992; Tucker

and Bras, 1998; Perron *et al.*, 2008a, 2012]. The transition between hillslopes and valleys controls the drainage density of the landscape, a basic length scale that reflects the total length of channels normalised for the drainage area of the basin [Horton, 1945; Tarboton *et al.*, 1992; Tucker and Bras, 1998]. The drainage density controls how fluxes of water and sediment are delivered to the river system [Montgomery and Dietrich, 1989], and is therefore important on a range of timescales, from short-term flood forecasting to long-term landscape evolution.

A second key transition within upland fluvial systems occurs at the onset of alluviation within channels. This alluviation is characterised by a fundamental change in geomorphic process, with supply-limited conditions occurring above the transition and transport-limited conditions occurring below [Montgomery and Buffington, 1997; Wohl and Merritt, 2001]. At this transition point, the onset of sediment deposition can result in the initiation of floodplains, or if these are abandoned as the channel incises, fluvial terraces. Understanding the controls on floodplain initiation in upland landscapes is essential on human timescales for flood forecasting and planning. On geological timescales, the morphology and location of fluvial terraces can provide insight into channel response to climate, tectonics, and base-level [Bull, 1991; Merritts *et al.*, 1994; Pazzaglia *et al.*, 1998]; sediment storage and dynamics [Pazzaglia, 2013; Gran *et al.*, 2013]; and the relative importance of vertical and lateral fluvial incision [Finnegan and Dietrich, 2011].

Identifying the location of these transition points within fluvial networks has long been a key goal within geomorphology. Traditionally, channel heads have been identified using basic topographic information, such as contributing area thresholds [O'Callaghan and Mark, 1984; Band, 1986; Tarboton *et al.*, 1991] or slope-area scaling relationships [Montgomery and Dietrich, 1988; Dietrich *et al.*, 1992, 1993]. However, coarse-resolution digital elevation models (DEMs) made

the accurate extraction of channel networks problematic, as channel initiation processes occur on a metre to sub-metre scale. Floodplain identification was typically performed using detailed hydraulic modelling studies [e.g Noman *et al.*, 2001; Grimaldi *et al.*, 2013], whereas the delineation of fluvial terraces typically required extensive field mapping, combined with aerial imagery and analysis of topographic maps [Stout and Belmont, 2014]. These techniques are computationally and financially expensive, as well as being extremely time consuming, and are difficult to reproduce since different workers will produce different field maps.

The recent introduction of high-resolution topographic data, such as airborne lidar data, has revolutionised our ability to extract information about geomorphic process and form across landscapes. Lidar-derived DEMs, typically with a grid resolution of <2 m, have been used in many fields in geomorphology, for example in the identification of channel networks [Lashermes *et al.*, 2007; Tarolli and Dalla Fontana, 2009; Passalacqua *et al.*, 2010b, 2012; Thommeret *et al.*, 2010; Sofia *et al.*, 2011; Pelletier, 2013]; landslides [Booth *et al.*, 2009]; hillslope flow paths [Grieve *et al.*, 2016c]; fluvial terraces [Stout and Belmont, 2014]; bedrock outcrops [Milodowski *et al.*, 2015b]; and anthropogenic features [Sofia *et al.*, 2014a,b].

This thesis builds on past research by using high-resolution topographic data to identify and explore controls on fluvial drainage networks in upland landscapes. It is split into two main components: i) the development and testing of new algorithms for automatic feature extraction from lidar-derived DEMs, including the detection of hillslope-valley transitions, floodplains, and fluvial terraces; and ii) the application of these algorithms to understanding controls on the density of fluvial networks across a range of mountainous landscapes. Chapter 2 introduces digital terrain analysis and the use of lidar for topographic analysis, as well as developing a framework for algorithms necessary for reproducible topographic analysis. This is followed by Chapters 3 to 5, which have all been published in

scientific journals, and can be read individually as stand-alone research chapters. Chapter 3 introduces a new method for identifying hillslope-valley transitions, and tests it against three other existing methods of channel extraction. This chapter has been published in *Water Resources Research*. Chapter 4 presents a new method of delineating floodplains and fluvial terraces from DEMs using thresholds of elevation compared to the nearest channel and local gradient, validated against field data, published flood maps, and digitised fluvial terraces. This chapter has been published in *Earth Surface Dynamics*. In Chapter 5, I apply these new algorithms for channel extraction to examine the density of channel networks across a range of mountainous landscapes, to examine how drainage density varies with erosion rate and hilltop curvature, and explore implications of this for fluvial incision models. This chapter has been published in the *Journal of Geophysical Research: Earth Surface*. These chapters are followed by an extended discussion and conclusion (Chapter 6) which synthesises the results from each of the research chapters, and speculates on potential future directions of the research.

The remainder of this chapter presents a detailed background and literature review for the project, aiming to situate this research within the broader geomorphic context. It provides a review of the relevant literature on fluvial geomorphology, including the historical development of the field; common models of fluvial incision; and process domain transitions within fluvial systems.

1.2 Theoretical background

1.2.1 Geometry of fluvial networks

The structure and organisation of channel networks can provide insight into both geomorphic processes and the impact of allogenic forcings on landscape form.

Many different approaches have been proposed for quantifying the planform structure and scale of fluvial networks [e.g. Horton, 1932, 1945; Hack, 1957; Strahler, 1957; Shreve, 1966, 1967; Tarboton *et al.*, 1992; Rodriguez-Iturbe *et al.*, 1992; Rigon *et al.*, 1993; Tarboton, 1996; Dodds and Rothman, 1999; Tarolli and Dalla Fontana, 2009; Gangodagamage *et al.*, 2011]. The organisation of channel networks controls drainage basin hydrology [e.g. Kirkby, 1976], and the speed at which water, sediment, and pollutants travel through the catchment [Montgomery and Dietrich, 1989; Novotny, 2002]. The patterns of fluvial networks have been suggested to represent the influence of tectonics [e.g. Cox, 1989; Burbank, 1992], climate [e.g. Tucker *et al.*, 2001b; Sangireddy *et al.*, 2016a; Seybold *et al.*, 2017], geomorphic process regimes [e.g Dunne, 1980; Hooshyar *et al.*, 2017], and lithology [e.g. Abrahams and Flint, 1983; Moglen *et al.*, 1998].

Scientists have been investigating controls on the patterns of channel networks in upland landscapes for several centuries. One of the first attempts at qualitatively describing the relationship between valleys and the rivers that form them was set out elegantly by Playfair [1802], in his *Illustrations of the Huttonian Theory of the Earth*:

> 'Every river appears to consist of a main trunk, fed from a variety of branches, each running in a valley proportioned to its size, and all of them together forming a system of valleys, communicating with one another, and having such a nice adjustment of their declivities, that none of them join the principal valley, either on too high or too low a level; a circumstance which would be infinitely improbably, if each of these valleys were not the work of the stream that flows in it.' (pp. 102)

Nearly a century after Playfair's work, in his seminal study of the geology of the Henry Mountains, Utah, Gilbert [1877] speculated that the morphology of

drainage networks and ridges separating them was a result of geomorphic processes which led to erosion and transportation of sediment. Gilbert's observations of the spectacular badlands in the Henry Mountains were some of the first to examine the density of channel networks, where he theorised that the concentration of flow into rills caused erosion of badland drainage divides (Figure 1.1).

Figure 1.1: Photograph looking south towards Mount Ellen, the northernmost of the Henry Mountains. The badlands in the foreground, in the Mancos shale, were the focus of Gilbert's early studies of drainage network formation. Credit: U.S. Geological Survey, Department of the Interior, 1935.

Gilbert [1909] later developed a more detailed qualitative analysis of drainage network patterns and the relationship between process and topographic form. He hypothesised that the transition between convex or planar hillslopes and concave valleys represented a change in process domain, from hillslope creep to valley wash. He suggested that an increase in velocity could lead to an expansion of the domain of overland flow and a reduction in the domain of hillslope diffusion.

These early studies in the nineteenth and earliest twentieth centuries were focused on describing river network morphology in a qualitative sense. However, in a

series of seminal papers, Horton [1932, 1945] developed the first quantitative treatment of the subject, by outlining a series of 'laws of drainage network composition' which describe the basic planform geometric properties of drainage networks. Horton defined the river network as a series of links, consisting of upstream sources, tributary junctions, and downstream outlets. Each link in the channel network was assigned an index, or stream order, based on the number of tributaries flowing into that link. This stream ordering system was revisited by Strahler [1952, 1957], creating the widely used Horton-Strahler stream ordering scheme. In Horton's original scheme, the main trunk was assigned the highest order in a basin, and tributaries were progressively reduced in stream order by one (Figure 1.2a). This was modified by Strahler, so that a channel with no tributaries is referred to as first order, and this is increased by one when it reaches another channel of the same order. If a channel joins another of a higher order, the higher stream order is assigned to the downstream link (Figure 1.2b). An additional ordering system was proposed by Shreve [1966, 1967], where first order channels are defined in the same way as that of the Horton-Strahler scheme, but at tributary junctions, the order of the downstream channel is assigned as the sum of the upstream tributaries. This ordering system provides additional topological information over the Horton-Strahler scheme as it encodes the number of tributaries contributing to each link in the network.

Using stream order as a scaling parameter, Horton [1945] proposed a series of laws, expanded upon by Schumm [1956], which define the number, length, and upstream contributing area of channels of a given order (ω), where ω is equal or less than the maximum basin order (ω_b):

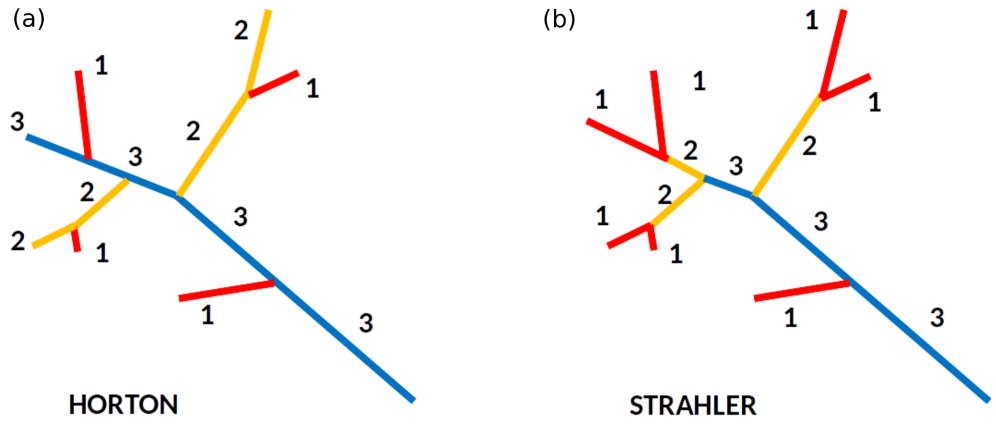

Figure 1.2: Schematic diagram showing (a) Horton stream ordering; and (b) Strahler stream ordering.

$$N(\omega) \propto {R_B}^{\omega_b - \omega} \qquad R_B = \frac{N(\omega)}{N(\omega+1)}, \tag{1.1a}$$

$$L(\omega) \propto {R_L}^{\omega-1} \qquad R_L = \frac{l_s(\omega)}{l_s(\omega-1)}, \tag{1.1b}$$

$$A(\omega) \propto {R_A}^{\omega-1} \qquad R_A = \frac{A(\omega)}{A(\omega-1)}, \tag{1.1c}$$

where $N(\omega)$ is the number, $L(\omega)$ is the length, and $A(\omega)$ is the drainage area of streams of order ω. R_B, R_L, and R_A are the corresponding bifurcation, length, and area ratios respectively, which are independent of scale and are referred to as Horton's ratios. In studies of landscapes without a significant structural control, these ratios have been shown to fall within a relatively narrow range of values: R_B generally varies between 3 and 5; R_L between 1.5 and 3; and R_A between 3 and 6 [Chorley, 1957; Smart, 1978; Abrahams, 1984].

Many authors have used Horton's laws to test geomorphic theories such as the development of drainage networks [Roth *et al.*, 1989; Rodriguez-Iturbe *et al.*, 1992], or to suggest that fluvial networks must be topologically random [Shreve,

1966, 1967, 1969]. However, Kirchner [1993] analysed the Horton ratios (R_B, R_L, and R_A) from a series of numerically generated networks with varying structures, and found that these ratios were insensitive to the structure of the network, and could not distinguish between random and non-random networks. Kirchner [1993] therefore suggested that these laws were simply an artefact of stream ordering, and the value of these ratios does not reflect any underlying structural controls on the channel network. More recent work by Gangodagamage *et al.* [2011] suggested using 'directed distance from the divide', or ℓ, as the scaling parameter rather than stream order, defined as the distance from each pixel in the landscape to the drainage divide along the longest flow path. Computing ℓ for a landscape does not require *a priori* knowledge of channel head locations, and can be applied across both fluvial and hillslope regimes [Gangodagamage *et al.*, 2011].

Another widely-used scaling law within fluvial geomorphology is 'Hack's Law', which empirically relates the length of the main trunk channel to the basin drainage area:

$$L_T \sim A^h, \tag{1.2}$$

where L_T is the length of the trunk stream, and h is generally referred to as Hack's exponent. Hack [1957] suggested that h typically has a value of 0.6, and a number of studies analysing a range of basin sizes suggest $0.57 < h < 0.6$ [Gray, 1961; Maritan *et al.*, 1996; Dodds and Rothman, 1999]. Hack's Law has been used to investigate changes in basin shape as size increases, as Hack [1957] suggested that if $h > 0.5$ then drainage basins should become more elongate with increasing contributing area. However, other authors have shown from field data that variations in channel sinuosity may offset the change in trunk stream length, such that basin shape is independent of contributing area [e.g. Willemin, 2000].

In his seminal paper, Horton [1945] also defined the fundamental network property of drainage density, which quantifies landscape dissection (Figure 1.3). Drainage density (D_d) describes the total length of channels in a basin (L) normalised for the basin drainage area (A):

$$D_d = L/A, \tag{1.3}$$

The drainage density of the basin is also related to the average length of overland flow from the drainage divide to the start of the channel network, or the hillslope length (L_h):

$$L_h = \frac{1}{2D_d}. \tag{1.4}$$

The drainage density of the landscape is defined by the extent of the fluvial network, and is important for understanding the routing of discharge, sediment, and other particles through catchments, as transport processes will generally be more efficient in channels compared to hillslopes. Many authors have attempted to investigate potential controls on drainage density [e.g. Kirkby, 1980; Montgomery and Dietrich, 1989; Willgoose *et al.*, 1991; Kirkby, 1993; Howard, 1994; Oguchi, 1997; Tucker and Bras, 1998; Talling and Sowter, 1999; DiBiase *et al.*, 2012; Sweeney *et al.*, 2015; Sangireddy *et al.*, 2016a]. Drainage density has been suggested to be controlled by erosion thresholds, such as for runoff generation [e.g. Kirkby, 1980; Dietrich *et al.*, 1993] or landsliding [Montgomery and Dietrich, 1989; Howard, 1994]. Alternatively, authors have hypothesised that D_d is set by the relative efficiency of diffusive processes occurring on hillslopes (such as gravity-driven creep and bioturbation) and advective processes in channels [Tarboton *et al.*, 1992; Tucker and Bras, 1998; Perron *et al.*, 2012]. The impact of the competition between these processes on valley spacing, and hence drainage

density, has been demonstrated recently through both numerical modelling [Perron *et al.*, 2008a] and experimental studies [Sweeney *et al.*, 2015].

The effect of these sediment transport processes on D_d has also been examined by investigating the relationship between D_d and topographic form, including relief and local gradient. For example, slope models developed by Kirkby [1980, 1993] predicted a negative relationship between drainage density and relief in humid climates, but no relationship in semi-arid environments. Tucker and Bras [1998] used a combination of analytical and numerical modelling to predict a positive relationship between D_d and relief in semi-arid, low relief landscapes, and a negative relationship in humid landscapes. In the mountainous regions of Japan, where landsliding is a dominant process of sediment transport, Oguchi [1997] found an inverse correlation between D_d and relief.

Local climate, by controlling the delivery of surface runoff to the channel system, may also be an important factor determining the drainage density of a landscape. Melton [1957] studied the variation in drainage density with the Thornthwaite precipitation-evaporation (P-E) index [Thornthwaite, 1931] across over 80 basins in the U.S. southwest, with climatic conditions ranging from arid to humid, and found an inverse relationship between precipitation and drainage density. Further analysis by Abrahams [1984] showed a variable distribution, where D_d decreased with increasing P-E index in semi-arid environments, and vice versa in humid environments. He suggested that this reversal in trend was due to the increasing impact of vegetation on runoff and infiltration capacity. Links between drainage network organisation and vegetation were investigated numerically by Istanbulluoglu and Bras [2005], showing that increasing vegetation cover produced less-dissected numerical landscapes. Further modelling by Collins and Bras [2010] showed an initial increase in D_d with precipitation in arid environments, then a decrease in semi-arid environments as vegetation cover begins to reduce sediment transport, and finally an increase in D_d with precipitation in humid environments

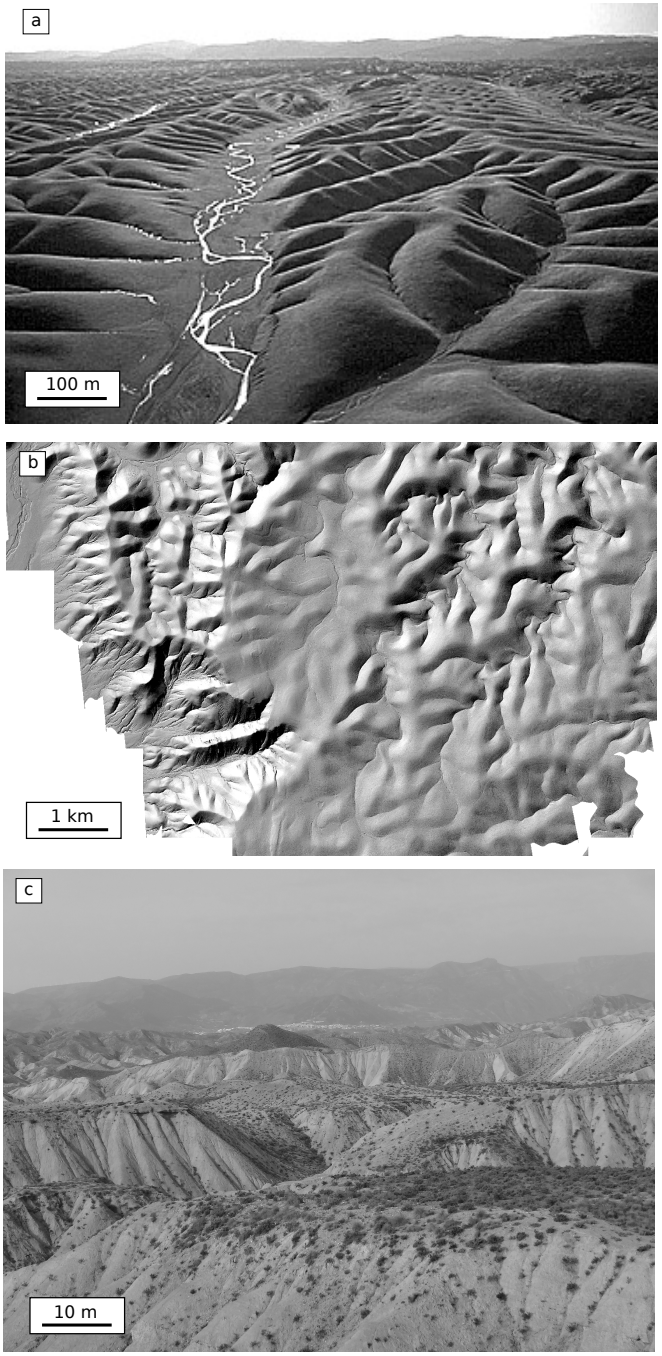

Figure 1.3: Drainage density and valley spacing across different landscapes. (a) Aerial photograph of Orland, California, showing regular valley spacing of around 100 m, modified from Perron *et al.* [2008a]. (b) Shaded relief map of Guadalupe Mountains, NM, showing variation in drainage density from W to E. (c) Highly dissected landscape in Tabernas, Spain, showing channels initiating up to the ridgetops.

with the stabilisation of vegetation cover. A similar relationship between D_d and mean annual precipitation (MAP) was shown from high-resolution topographic data by Sangireddy *et al.* [2016a].

Along with climate, lithology may also exert a control on the degree of landscape dissection by channels [Melton, 1957; Carlston, 1963; Oguchi, 1997; Talling and Sowter, 1999]. The analysis of Melton [1957] showed that the mean D_d for basins primarily composed of shales and schists exceeded the mean for all the basins analysed, whereas the mean for basins with limestone or volcanic bedrock was lower than the total. Furthermore, Oguchi [1997] found that in the Japanese mountains, D_d was systematically greater for basins draining granitic lithologies. However, previous studies of drainage density based on coarse-resolution topographic data have struggled to accurately delineate the upstream extent of the channel network, which can lead to large differences when compared to field-mapped data [e.g. Morisawa, 1957].

Another fundamental property used to analyse fluvial networks in plan view is the angle between tributaries, also referred to as the junction angle [Horton, 1932, 1945; Lubowe, 1964; Howard, 1971a,b, 1990; Roy, 1983; Seybold *et al.*, 2017; Hooshyar *et al.*, 2017]. The concept of the junction angle was first introduced by Horton [1932] to quantify the angle between overland flow on hillslopes and the channel to which it contributes. Horton [1945] then used the same concept to examine the angle between a tributary and the higher order stream which it joins, defined as:

$$cos(\alpha) = \frac{tan(S_1)}{tan(S_2)}, \tag{1.5}$$

where α is the angle between the two channels, S_1 is the gradient of the higher order stream, and S_2 is the gradient of the tributary (Figure 1.4). This theory

provided a useful starting point for the analysis of stream junction angles, but is somewhat flawed: if the gradient of the two channels is zero, then it predicts that the angle between them should also be zero. Therefore, Howard [1971a,b] expanded upon this model to hypothesise that the junction angle was related to channel discharge as well as gradient. This dependency of junction angle on discharge and slope suggests that climate may be an important influence. Seybold *et al.* [2017] examined the relationship between climatic variables and junction angles of channels throughout the contiguous US, consisting of a dataset of nearly one million junctions. They found that the average junction angle in arid landscapes dominated by surface runoff was $\sim 45°$, whereas the mean angle in humid landscapes was $\sim 72°$ (Figure 1.4), suggesting channel initiation through groundwater seepage [e.g. Devauchelle *et al.*, 2012]. Junction angle has also been shown to be sensitive to geomorphic process. Hooshyar *et al.* [2017] analysed the stream angles of 120 catchments across the US, and again found two distinct populations of junction angles at $\sim 49.5°$ and $\sim 75°$. They linked these different branching angles to the relative importance of colluvial and fluvial processes, as the junction angles systematically increased in the network from upper colluvial reaches to downstream fluvial reaches.

The properties of fluvial networks reviewed here compose a set of diagnostic tools for examining fluvial response to external forcing, such as climate, tectonics, or base-level change, as well as the influence of internal processes such as lithological variations or geomorphic processes. These geometric properties are straightforward to extract from topographic data, providing a means of easily comparing the topological organisation of drainage networks across different basins and landscapes. However, crucially, the extraction of these parameters on the landscape relies on the accurate delineation of the channel network. Correctly determining the transition between hillslopes and valleys is notoriously difficult [Montgomery and Foufoula-Georgiou, 1993; Zhang and Montgomery, 1994; Tarolli

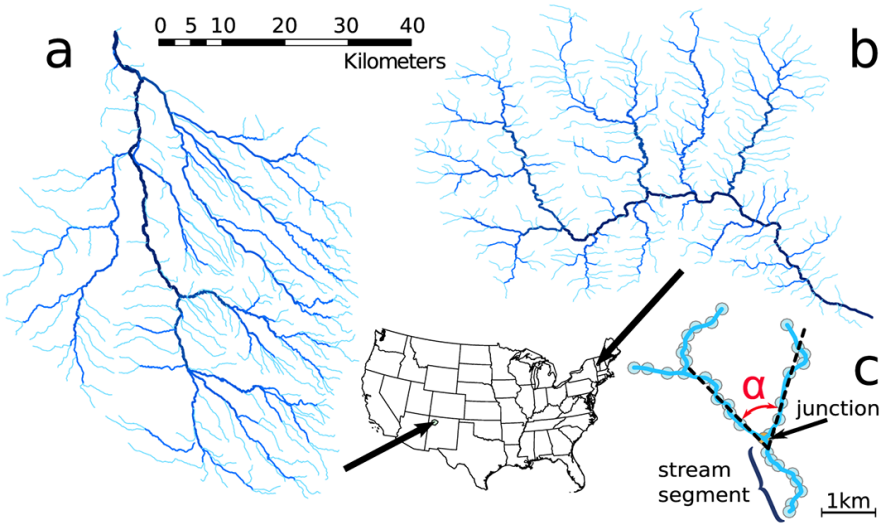

Figure 1.4: Channel networks from two sites in the US showing variation in junction angles. (a) Drainage network structure in the arid Colorado Plateau, northwest Arizona, with a mean junction angle of 47°; (b) drainage network structure in central Vermont, a humid region, with a mean junction angle of 74°. (c) Schematic diagram showing the calculation of the junction angle, α. Reproduced from Seybold *et al.* [2017].

and Dalla Fontana, 2009; Orlandini *et al.*, 2011], especially from coarse-resolution topographic data used in many of these earlier studies.

1.2.2 Fluvial incision into bedrock

Understanding controls on fluvial networks involves analysis of channel profile form as well as the planform network geometry. Incision of channels into bedrock in upland landscapes controls the relief structure of the landscape, or the difference in elevation between ridges and valleys [Whipple and Tucker, 1999], the response time of channels to climatic or tectonic perturbations [Tucker and Slingerland, 1997; Whipple, 2001], and sets the boundary conditions for the rest of the landscape [Whipple and Tucker, 1999; Whipple *et al.*, 2000]. Therefore, many authors have developed mathematical models to describe and understand the mechanisms by which rivers incise into their bedrock. One commonly used model for river incision proposes that erosion rate (E) is proportional to the stream power (Ω), or rate of energy expenditure of the flow, exerted per unit area of the bed [Seidl and Dietrich, 1992; Howard, 1994]:

$$E = \frac{K_p \Omega}{W} = \frac{K_p \rho g Q S}{W}, \tag{1.6}$$

where K_p is a dimensional constant depending on the efficiency of the incision process, ρ is the density of water, g is acceleration due to gravity, Q is the bankfull discharge, S is the channel gradient, and W is the bankfull flow width. Discharge is assumed to be proportional to drainage area:

$$Q = K_a A^a, \tag{1.7}$$

and width is assumed to be proportional to discharge:

$$W = K_w Q^b = K_w {K_a}^b A^{ab}. \tag{1.8}$$

Hydraulic scaling relationships demonstrated for alluvial channels have shown that width generally scales with the square root of drainage area, such that $ab = 0.5$ [Leopold and Maddock, 1953]. Combining equations 1.6 - 1.8 allows erosion rate to be expressed in terms of drainage area and slope:

$$E = K_y A^{a(1-b)} S, \tag{1.9}$$

where $K_y = (\rho g K_p K_a^{1-b})/K_w$ [Sklar and Dietrich, 1998]. An alternative formulation proposes that fluvial incision as proportional to bed shear stress (τ_b) rather than unit stream power, and can be expressed in a similar form to equation 1.9 [Howard and Kerby, 1983; Howard, 1994]:

$$E = K_z A^{0.6a(1-b)} S^{0.7}, \tag{1.10}$$

where $K_z = K_r \rho g ({N_m {K_a}^{1-b}}/{K_w K_p K_n})^{0.6}$. K_r represents rock erodibility, N_m is Manning's roughness coefficient, and K_n is a coefficient representing the shape of the channel cross section.

These formulations can be generalised into the stream power incision model:

$$E = K A^m S^n, \tag{1.11}$$

where E is the long-term fluvial incision rate, A is the upstream drainage area, S is the channel gradient, K is the erodibility coefficient, which is a measure of the efficiency of the incision process, and m and n are constant exponents. In order to model landscape evolution, equation 1.11 is often combined with detachment-limited model of channel evolution, where the change in channel elevation is the difference between rock uplift and the ability of the river to detach or remove rock from its bed:

$$\frac{\partial z}{\partial t} = U - E = U - KA^m\Big(\frac{\partial z}{\partial x_d}\Big)^n, \tag{1.12}$$

where z is the elevation of the channel bed, t is time, x_d is the distance downstream, and U is the rock uplift rate, equivalent to the rate of baselevel lowering if the baselevel elevation is fixed [Howard and Kerby, 1983; Howard, 1994; Whipple and Tucker, 1999].

In order to examine fluvial response to climatic and tectonic forcing, equation 1.11 is often rearranged for channel slope, assuming uniform incision rate [Hack, 1973; Flint, 1974; Sklar and Dietrich, 1998; Whipple and Tucker, 1999; Wobus *et al.*, 2006]:

$$S = k_{sn}A^{-\theta}, \tag{1.13}$$

where $\theta = m/n$, and represents the concavity of the channel profile, and $k_{sn} = (E/K)^{\frac{1}{n}}$, and represents the steepness of the profile. θ and k_{sn} are referred to as the concavity and steepness indices respectively. Equation 1.13 therefore predicts a power-law relationship between slope and drainage area, which is often represented on a logarithmic scale (Figure 1.5). The concavity and steepness indices can be extracted from plots of slope against drainage area along a channel,

where θ is the gradient of a best-fit line through the data, and k_{sn} is the y-intercept. These slope-area plots have been used by many studies to examine fluvial response to climate, lithology and tectonics [e.g. Flint, 1974; Tarboton *et al.*, 1989; Kirby and Whipple, 2001; Wobus *et al.*, 2006].

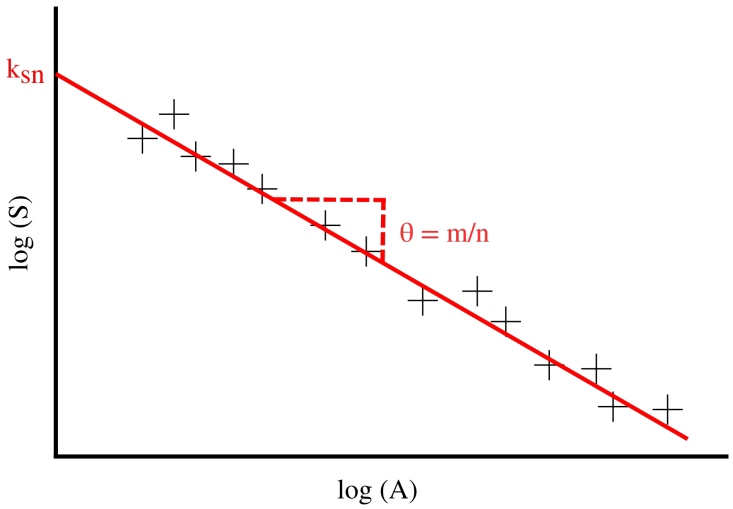

Figure 1.5: Schematic diagram showing logarithmic plot of channel slope, S, against drainage area, A. Equation 1.13 predicts a negative relationship for a channel in slope-area space, where k_{sn} is the y-intercept and θ is the gradient of a best-fit linear regression (red line) through the data in log-log space.

However, there are limitations with using these plots of slope against drainage area in order to analyse channel profiles. Topographic data is inherently noisy, either as a result of fine-scale sediment transport processes, bed roughness, or from processing of the data in the creation of DEMs. Furthermore, this noise is amplified by the derivation of the topographic surface in order to extract values for channel gradient [Perron and Royden, 2013]. This noise leads to significant scatter within the profile trends, potentially obscuring any deviations from the power law signal which may represent changes in process, lithology, climate, or uplift. In order to circumvent these problems, more recent studies have turned to the 'integral method' of slope-area analysis, which normalises river profiles for

their drainage area, allowing comparison of the steepness of channels across basins of different size [Royden *et al.*, 2000; Harkins *et al.*, 2007; Perron and Royden, 2013; Mudd *et al.*, 2014]. The integral method only requires the extraction of elevation and drainage area along the channel, and is therefore less subject to topographic noise than slope-area analysis. The technique involves integrating equation 1.13, assuming spatially constant incision equal to uplift (steady-state) and erodibility:

$$z(x) = z(x_b) + \left(\frac{E}{K}\right)^{\frac{1}{n}} \int_{x_b}^{x} \frac{dx}{A(x)^{\frac{m}{n}}}, \tag{1.14}$$

where the integration is performed upstream from baselevel (x_b) to a chosen point on the river channel, x. The profile is then normalised to a reference drainage area (A_0) to ensure the integrand is dimensionless:

$$z(x) = z(x_b) + \left(\frac{E}{K {A_0}^m}\right)^{\frac{1}{n}} \chi, \tag{1.15}$$

where the longitudinal coordinate χ is equal to:

$$\chi = \int_{x_b}^{x} \left(\frac{A_0}{A(x)}\right)^{m/n} dx. \tag{1.16}$$

The longitudinal coordinate χ has dimensions of length, and is linearly related to the elevation $z(x)$. Therefore, if a channel incises based on the stream power incision model, then its profile should be linear on a plot of elevation against χ according to equation 1.15. As well as providing a method to test whether channel profiles obey common incision models, χ-plots also provide means of

testing the appropriate θ, or m/n, for a channel [Perron and Royden, 2013; Mudd *et al.*, 2014]. If the integral analysis is performed for all channels within a basin, the correct value of θ can be determined by identifying at which value all of the channels are both linear in χ-elevation space, and collinear, where main channel and tributaries all collapse onto a single profile (Figure 1.6).

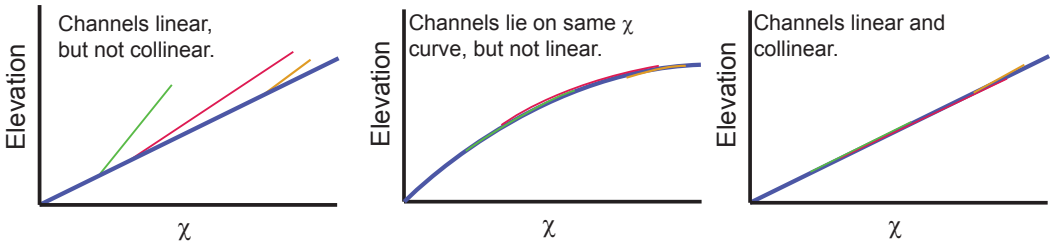

Figure 1.6: Schematic plots of channel elevation against χ. In a steady state landscape with uniform uplift and lithology, channel profiles should be both linear and collinear in χ - elevation space. Reproduced from Mudd *et al.* [2014].

Perron and Royden [2013] suggested a technique to find the best fit θ which involves iterating through a series of θ values and selecting the value of θ with the maximum R^2. However, in landscapes undergoing transient uplift, or with variations in lithology, the χ profile for a channel may not be perfectly linear, as shown by panels 1 and 2 in Figure 1.6. Mudd *et al.* [2014] therefore developed a statistical technique for fitting segments to the χ profiles to identify the best-fit θ in non-linear channels.

The techniques outlined here provide a mechanism for determining the value of θ (or m/n), which has been reported for many landscapes [Stock and Montgomery, 1999; Whipple and Tucker, 1999; Anthony and Granger, 2007; Perron and Royden, 2013; Mudd *et al.*, 2014]. However, the individual values of the coefficient K and the exponents m and n are major unknowns within the stream power incision model, which are difficult to determine as they are directly related to incision mechanisms, unlike the m/n ratio [Whipple and Tucker, 1999]. Many landscape

evolution models, where incision is proportional to stream power (equation 1.6), set values of $m = 0.5$ and $n = 1$ based on equation 1.8 [e.g. Rodriguez-Iturbe and Rinaldo, 1997; Sklar and Dietrich, 1998]. If incision is proportional to shear stress (equation 1.10), then it is assumed that $m = 0.3$ and $n = 0.7$ [Howard and Kerby, 1983; Sklar and Dietrich, 1998]. Both of these incision models therefore predict $m/n = 0.5$. Howard and Kerby [1983] analysed channel profiles in badlands in Virginia with a gradient in incision rates, and found $m = 0.45$ and $n = 0.7$, corresponding with erosion proportional to bed shear stress. Whipple *et al.* [2000] suggested that the n exponent commonly varies between $\sim 2/3$ and $5/3$, depending on the dominant incision process. Analysis of channel profiles from a range of different landscapes show broad variability in the reported m and n exponents, with data from the Siwaliks in the Himalaya [Lavé and Avouac, 2001], Eastern Tibet [Ouimet *et al.*, 2009], and the Mendocino triple junction along the coast of California [Snyder *et al.*, 2000], suggesting $m = 0.55, 0.85$, and 2, and $n = 1.1, 1.7$ and 4 respectively. Lague [2014] reanalysed data from a range of studies, suggesting that in the majority of cases $m \approx 1$ and $n \approx 2$, although with some exceptions. Recent studies using the integral profile analysis set out in equations 1.14 - 1.16 found values of n ranging from 0.5 to 0.82 [Perron and Royden, 2013; Mudd *et al.*, 2014], whereas a global compilation of stream power law parameters using the same methodology found that in most landscapes $n > 1$ [Harel *et al.*, 2016].

The coefficient K represents the efficiency of the erosion process, incorporating the effects of lithology, channel geometry, hydraulic roughness, precipitation, and sediment supply [e.g. Sklar and Dietrich, 1998; Whipple and Tucker, 1999]. K is generally unconstrained in most studies, with values ranging over several orders of magnitude depending on the landscape in question. Furthermore, the value of K co-varies with the m exponent, as the dimensions of K depend on m [Sklar and Dietrich, 1998; Stock and Montgomery, 1999]. Stock and

Montgomery [1999] analysed dated palaeo-river profiles from Australia, Kauai, California, and Japan, fixing $m = 0.4$. They found a large variation in K with lithology, where $K = 10^{-7} - 10^{-6}$ $m^{0.2}$ yr^{-1} for granitic and metamorphic rocks; $K = 10^{-5} - 10^{-4}$ $m^{0.2}$ yr^{-1} for volcaniclastic rocks; and $K = 10^{-4} - 20^{-2}$ $m^{0.2}$ yr^{-1} for mudstones. Harel *et al.* [2016] used integral profile analysis to perform the first global quantification of K, normalising it to a reference θ of 0.5, and found a median normalised $K = 2.9 \times 10^{-10} \pm 1.0 \times 10^{-9}$ $[T^{-1}L^{1-2m}]$.

Although the stream power incision model is by far the most commonly used model for understanding fluvial erosion, it has many limitations which should be carefully considered when applying it. The simplicity of the model means that important parameters influencing rates of incision are neglected [Lague, 2014]. For example, the model assumes that channel width does not vary temporally, although many studies have shown that channels may adjust their width in response to changing incision rates [e.g. Lavé and Avouac, 2001; Finnegan *et al.*, 2005; Whittaker *et al.*, 2007]. Furthermore, the model does not take into account the impact of sediment supply on enhancing or retarding incision rates [e.g. Sklar and Dietrich, 2001; Finnegan *et al.*, 2007; Turowski *et al.*, 2008; Cook *et al.*, 2013], or the effect of thresholds for erosion and stochastic discharge [e.g. Snyder *et al.*, 2003; Tucker, 2004; Lague *et al.*, 2005]. Alternative model formulations have been suggested which take into account the effects of sediment flux and erosion thresholds, which can also be formulated according to equation 1.11 [Gasparini and Brandon, 2011]. Detailed reviews of the evidence for, and limitations of, the stream power incision model are presented by Turowski [2012], Whipple *et al.* [2013], and Lague [2014].

1.2.3 Hillslope-valley transitions and the channel head

Valley networks determine the drainage density of the landscape, and control the routing of water and sediment through the catchment. Therefore, understanding and delineating the extent of the valley network, and the fluvial processes that occur within them, is a fundamental problem in geomorphology that has been investigated for many decades [e.g. O'Callaghan and Mark, 1984; Band, 1986; Montgomery and Dietrich, 1988, 1989; Tarboton *et al.*, 1992; Dietrich and Dunne, 1993; Montgomery and Foufoula-Georgiou, 1993; Molloy and Stepinski, 2007; Tarolli and Dalla Fontana, 2009; Passalacqua *et al.*, 2010a; Thommeret *et al.*, 2010; Sofia *et al.*, 2011; Henkle *et al.*, 2011; Orlandini *et al.*, 2011; Pelletier, 2013]. Within the valley network, a key morphological feature is the 'channel head', which represents the upstream extent of sediment transport by overland flow, and can often occur tens to hundreds of metres downstream of the valley head [Dietrich and Dunne, 1993]. Dietrich and Dunne [1993] define a channel head in the field as 'the upstream boundary of concentrated water flow and sediment transport between definable banks' (pp. 178). These banks must be able to be recognised morphologically without the presence of flow within the channel, and may be represented by a zone steeper than that of the channel bed or the surrounding hillslopes, or as a bedrock step. This definition separates the channel network from other areas of topographic concavity, such as colluvial hollows, swales, or debris flow chutes [e.g. Benda and Dunne, 1987; Stock and Dietrich, 2003].

The importance of understanding the location of channel heads was first emphasised by Horton [1945]. He argued that landscapes were progressively dissected by a growing channel network, until hillslope lengths became shorter than a critical value (x_c), where overland flow could no longer result in incision and hence, channelisation. Horton [1945] also suggested that groundwater seepage played an

important role in channel initiation, and that contributing flow from groundwater could reduce the hillslope length below x_c. A variety of processes have since been suggested to contribute to channel initiation, including saturation overland flow [Kirkby and Chorley, 1967], groundwater seepage [Dunne, 1980], and shallow landsliding [Dietrich *et al.*, 1986]. Montgomery and Dietrich [1989] suggest that saturation overland flow should be the dominant mechanism for channel initiation on shallow slopes, with seepage erosion and landsliding becoming dominant in higher-relief landscapes. Therefore, several authors have suggested that channels initiate at a point beyond a critical threshold drainage area for runoff erosion [O'Callaghan and Mark, 1984; Tarboton *et al.*, 1991]. Montgomery and Dietrich [1988] mapped channel heads in the field from three areas in Oregon and California, and found an inverse relationship between channel source area and local gradient (Figure 1.7).

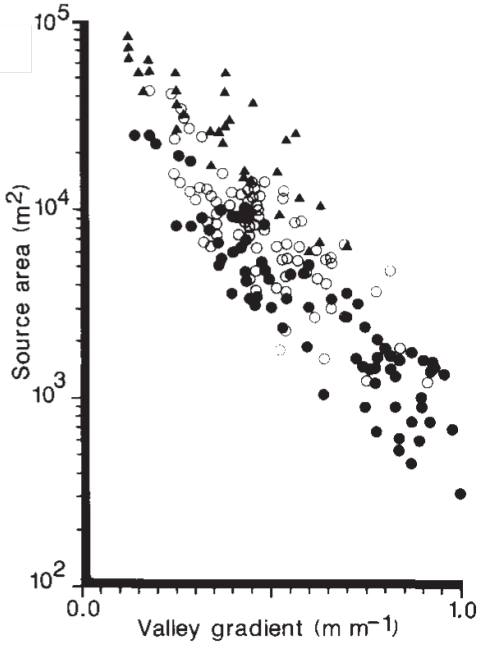

Figure 1.7: Contributing area against local gradient for field-mapped channel heads from Coos Bay, OR (solid circles); Sierra Nevada, CA (triangles); and Marin County, CA (open circles). Reproduced from Montgomery and Dietrich [1988].

Based on these data, several authors have proposed a threshold for channel initiation (c) based on both contributing area and local slope:

$$c = A^{\mu} S^{\beta}, \tag{1.17}$$

where β depends on factors such as climate, lithology, vegetation, and land use, and can be estimated from scatter plots of gradient against contributing area at mapped channel heads [Montgomery and Dietrich, 1988; Ijjasz-Vasquez and Bras, 1995; Desmet *et al.*, 1999; Orlandini *et al.*, 2011; Jefferson and McGee, 2013]. Based on field data, many studies assume that $\beta = 2$, which allows channel heads to be predicted without *a priori* knowledge of their locations [Orlandini *et al.*, 2011]. The area exponent μ is often assumed to be 1 [Jefferson and McGee, 2013].

An alternative view of channel initiation suggests that the location of the channel head is controlled by the competing processes of diffusional hillslope processes, and advective fluvial processes. Sediment flux (q_s) on hillslopes is often modelled using a linear diffusion equation [e.g. Culling, 1960, 1963]:

$$q_s = DS, \tag{1.18}$$

where D is hillslope diffusivity, with dimensions of L^2/T. In steep landscapes, where hillslopes approach the angle of repose, sediment transport has suggested to become non-linear, increasing rapidly as the gradient approaches a critical value (S_c) [Andrews and Bucknam, 1987; Densmore *et al.*, 1998; Roering *et al.*, 1999, 2001]:

$$q_s = \frac{DS}{1 - (S/S_c)^2}. \tag{1.19}$$

These diffusional processes transport colluvium into hollows, resulting in the infilling of depressions in the landscape [Dietrich and Dunne, 1978], whereas advective fluvial processes excavate sediment from depressions, enhancing them. Therefore, the relative efficiency of these processes has been suggested to determine the upstream extent of the fluvial network, influencing the drainage density and controlling the spacing between ridges and valleys [e.g. Gilbert, 1877, 1909; Davis, 1892; Willgoose *et al.*, 1991; Tarboton *et al.*, 1992; Howard, 1994, 1997; Tucker and Bras, 1998; Moglen *et al.*, 1998; Perron *et al.*, 2008a, 2009; Sweeney *et al.*, 2015].

Perron *et al.* [2008a, 2009] present a numerical model of topographic evolution based on combining equations 1.18 with 1.12:

$$\frac{\partial z}{\partial t} = D\nabla^2 z - KA^m \nabla z + U, \tag{1.20}$$

where ∇^2 is the Laplacian of elevation (the local curvature), and ∇z is the differential of elevation (the local gradient, $= S$). Equation 1.20 assumes that sediment transport on hillslopes follows a linear diffusion model, and that fluvial incision obeys the stream power incision model. This formulation can be non-dimensionalised using a characteristic horizontal (L_c) and vertical (ζ) length scale, to obtain a landscape Péclet number (Pe), which is a ratio of the timescales of advective fluvial processes and diffusive hillslope processes:

$$Pe = \frac{K {L_c}^{2m+1}}{D\zeta}. \tag{1.21}$$

Channel initiation should occur where the timescales of the two processes are equal ($Pe = 1$), and therefore we can rearrange equation 1.21 to solve for the

characteristic length scale at which channel initiation occurs, equivalent to the hillslope length:

$$L_c = \left(\frac{D\zeta}{K} \right)^{\frac{1}{2m+1}}. \tag{1.22}$$

This competition between hillslope and fluvial processes has often been investigated in the field using slope-area plots, similar to the approach for estimating k_{sn} and θ outlined in Section 1.2.2. Where hillslope processes are dominant, local gradient is expected to increase with drainage area, whereas where fluvial processes are dominant, there should be a negative correlation between drainage area and gradient. This leads to a characteristic 'boomerang shape' in slope-area space if the data for an entire basin are plotted [e.g. Tucker and Bras, 1998; Roering *et al.*, 2007]. Identifying the inflexion point in these slope-area plots can be used to estimate the characteristic hillslope length of the landscape, and thus identify a characteristic contributing area and slope at which channels should initiate (Figure 1.8). However, in steep landscapes, debris flows-dominated reaches commonly occur in the concave valleys above the channel head, and have been shown to have a constant slope with drainage area [Montgomery and Foufoula-Georgiou, 1993; Stock and Dietrich, 2003, 2006]. This may lead to difficulties in extracting a characteristic hillslope length using this method in landscapes with higher relief.

1.2.4 Channel alluviation, floodplains, and fluvial terraces

Fluvial channels in mountainous regions can be classified depending on either bed morphology or their dynamics. Classification of channels based on their bed morphology is typically based on whether the bed and banks are made of bedrock, alluvium, or consist of bedrock with a thin cover of sediment,

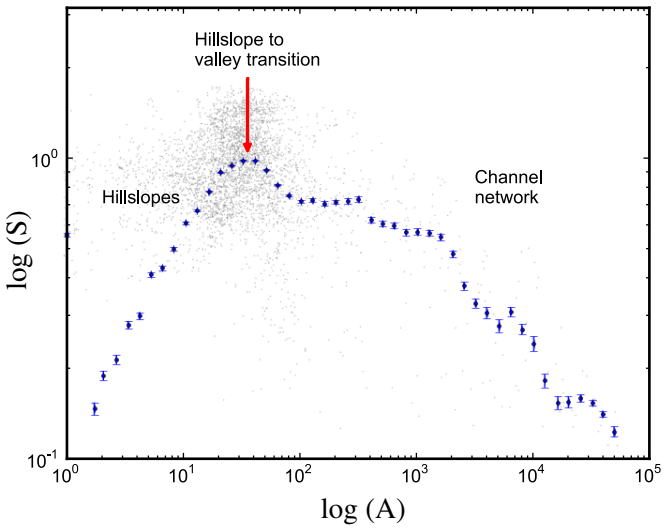

Figure 1.8: Schematic logarithmic plot of local slope against contributing area, showing the characteristic 'boomerang' shape. In the hillslope regime, S increases with A and vice versa in the fluvial regime. The inflexion point is used to identify the hillslope-valley transition (red arrow). If the analysis is performed on every pixel in the basin then the raw data (grey points) need to be smoothed and binned (blue points).

referred to as mixed bedrock-alluvial channels [Howard, 1980, 1987; Howard *et al.*, 1994; Montgomery and Buffington, 1997; Howard, 1998]. An alternative method of channel classification depends on the key controls on fluvial incision. 'Detachment-limited' systems can transport all of the sediment that is supplied from the surrounding hillslopes, and incision is thus limited by the rate of channel erosion into bedrock, primarily through abrasion and plucking [Hancock *et al.*, 1998; Whipple *et al.*, 2000; Whipple and Tucker, 2002]. 'Transport-limited' systems, in contrast, are defined by reaches where the river cannot transport all of the sediment that is supplied from upstream. Therefore, incision in these systems is limited by the transport capacity, such that erosion will only occur if the upstream supply of sediment is less than the transport capacity [Howard, 1980; Howard and Kerby, 1983; Whipple and Tucker, 2002]. Generally, bedrock-dominated channels are assumed to be detachment-limited, and alluvial channels to be transport-limited, although bedrock systems may be transport-limited if the divergence of transport capacity is the primary factor controlling incision rate [Howard, 1980; Howard and Kerby, 1983].

The transition from bedrock-dominated channels in the steep, upper reaches of catchments to alluvial-dominated channels downstream therefore represents a fundamental change in the dominant erosional processes. Howard [1980, 1987] suggested that this transition should occur where the transport capacity (q_c) is less than the sediment supply (q_s) across the range of grain sizes supplied to the channel, leading to the start of sediment deposition. Understanding where deposition occurs in fluvial systems is essential for predicting patterns of bed incision and aggradation, modelling both short term flood risk and long term landscape evolution, and assessing stream habitat characteristics [Montgomery *et al.*, 1996]. Many authors have therefore attempted to predict the transition between detachment and transport-limited regimes, either analytically [Howard, 1980, 1987; Sklar and Dietrich, 1998; Whipple and Tucker, 2002], or based

on empirical data [Howard and Kerby, 1983; Montgomery *et al.*, 1996]. This transition has been suggested to occur at a critical gradient, where channel banks primarily consist of bedrock above the critical gradient, and primarily consist of alluvium below [Howard and Kerby, 1983; Montgomery *et al.*, 1996].

The models of fluvial incision reviewed so far in this chapter, such as the stream power incision model (equation 1.11), generally assume detachment-limited conditions. Whipple and Tucker [2002] developed a similar analytical model for transport-limited conditions, where volumetric transport capacity (q_c) is dependent on stream power:

$$q_c = K_t A^{m_t} S^{n_t}, \tag{1.23}$$

where m_t and n_t are positive exponents, and K_t is a dimensional transport coefficient incorporating the effects of climate, the efficiency of sediment transport, and channel width. Equation 1.23 can be used to derive the following equation for the evolution of a river profile, analogous to equation 1.12 for detachment-limited conditions:

$$\frac{\partial z}{\partial t} = U - \frac{1}{1-\lambda_p}\frac{1}{W}(K_t A^{m_t} S^{n_t}), \tag{1.24}$$

where λ_p is the porosity of the sediment [Whipple and Tucker, 2002]. At steady state conditions, the transport capacity at every point in the basin should equal the sediment flux from upstream plus the sediment supplied from local erosion of the channel bed [Willgoose *et al.*, 1991; Tucker and Bras, 1998]. Assuming that most of the incision of the channel will occur through the impact of the bedload, the steady state sediment flux can be expressed as:

$$q_s = BAE, \tag{1.25}$$

where B is the fraction of the total load that is made up of bedload. At steady state, where $q_c = q_s$, we can combine equations 1.23 and 1.25 to derive the following equation for channel slope:

$$S = \left(\frac{BE}{K_t}\right)^{\frac{1}{n_t}} A^{-\theta_t}, \tag{1.26}$$

where $\theta_t = (m_t - 1)/n_t$, analogous to equation 1.13 for detachment-limited conditions. Therefore, we can predict the critical drainage area (A_{cr}) at which the transition from detachment to transport-limited conditions should occur, by equating channel gradient from equations 1.13 and 1.26:

$$A_{cr} = \left(K^{\frac{1}{n}} \frac{B}{K_t}^{\frac{1}{n_t}}\right)^{1/(\theta_t - \theta)} E^{(1/n_t - 1/n)/(\theta_t - \theta)}. \tag{1.27}$$

The transition from detachment to transport-limited conditions should therefore depend on the erosion rate, the erodibility coefficient (K), the transport coefficient (K_t), the bed load fraction (B) and the concavity indices for both the detachment and transport-limited reaches of the channel (θ and θ_t). Equation 1.27 therefore predicts that a more easily erodible substrate (higher value of K) or a larger proportion of bedload (higher value of B) should result in expansion of the transport-limited reach, and vice-versa for detachment-limited. Importantly, equation 1.27 also suggests that, in order for the detachment-limited portion of the channel to increase with incision rates (and uplift rates if steady state conditions are assumed), then $n < n_t$ [Whipple and Tucker, 2002].

The initiation of floodplains in upland regions is closely associated to that of the onset of alluviation within channels. Floodplains represent a key transition in many river systems, and floodplain evolution and development has long been studied in geomorphology [Mackin, 1937; Wolman and Leopold, 1957]. Floodplains initiate where sediment begins to be stored outside of the banks of the active channel, with this transition referred to as the floodplain initiation point (FIP) [Jain *et al.*, 2008]. Downstream of the FIP, floodplain morphology varies with the relative valley width, and constraint of the surrounding hillslopes [Brierley and Fryirs, 2013]. Close to the FIP, where valleys are narrow and confined, small discontinuous pockets of floodplain commonly form, which become laterally continuous at a certain distance downstream of the FIP (Figure 1.9).

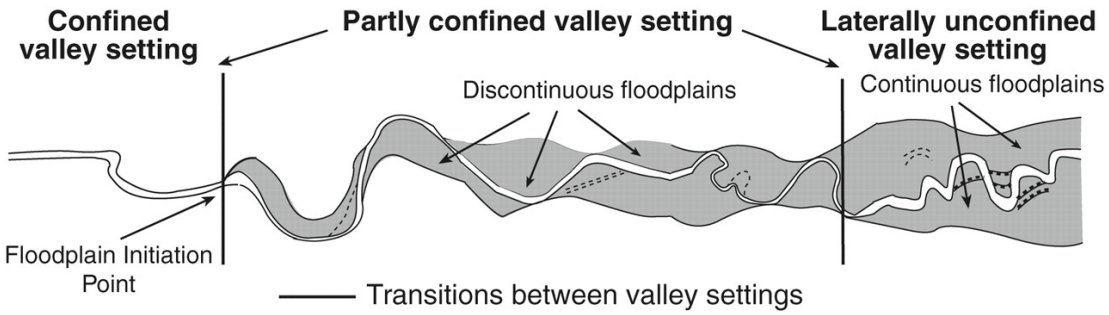

Figure 1.9: Diagram showing onset of floodplain initiation and the change in floodplain morphology as valleys transition from confined, to partly confined, to laterally unconfined. Reproduced from Jain *et al.* [2008].

The detection and identification of floodplains is an important problem in both hydrology and geomorphology. From a hydrological viewpoint, the initiation and spatial continuity of floodplains is essential for flood forecasting and hydrological modelling in order to predict the extent and depth of flood inundation [e.g. Beven and Kirkby, 1979; Beven, 1993, 1997]. This is of increasing societal relevance, as one of the major unknown impacts of climate change is the frequency and magnitude of future precipitation events [Schreider *et al.*, 2000; Booij, 2005; Hartmann

et al., 2013]. From a geomorphological perspective, floodplains, formed by previous channel overbank deposits, may provide insight into prior fluvial conditions at a given location. Furthermore, floodplain sediments provide indications of fluvial sediment dynamics, potentially allowing quantification of storage rates and sediment recycling histories over millennial timescales [Nardi *et al.*, 2006; Belmont, 2011]. Floodplain dynamics are also important for understanding hydrologic flow paths [Townsend, 2001; Jung *et al.*, 2004; Katsuyama *et al.*, 2005; Vivoni *et al.*, 2006], biogeochemical cycling [Pionke *et al.*, 1988], and aquatic ecosystems [Morrison *et al.*, 1994; Williams *et al.*, 2000]. At present, there is no overarching theory for predicting the relationship between floodplain morphology and controlling factors, such as sediment flux, bankfull discharge, or drainage area. This is due to two major unknowns: the relative importance of these processes; and the response time of floodplain morphology to these forcings [Belmont, 2011].

Fluvial terraces are closely related landforms to that of modern floodplains, and are distinguished by their position in the fluvial system, above the depth of modern flood inundation [Pazzaglia, 2013]. The preservation of terraces is thought to represent fundamental unsteadiness within the fluvial system, and can provide important information about the geomorphic and climatic processes operating within the catchment over geological timescales. Terraces are commonly used to understand channel response to variations in climate or tectonics [Bull, 1991; Merritts *et al.*, 1994; Pazzaglia *et al.*, 1998]; to examine both lateral and vertical channel mobility [Finnegan and Dietrich, 2011], and to investigate sediment storage and dynamics [Pazzaglia, 2013; Gran *et al.*, 2013]. Fluvial terraces are generally classified as either strath or fill terraces, depending on their sedimentology. Fill terraces are composed entirely of alluvial material transported and deposited by the channel (Figure 1.10a). They represent the filling in of the original fluvial valley by alluvium, and are therefore commonly thought to represent sudden environmental variations within a catchment [Bull, 1991]. Strath

terraces, on the other hand, are composed primarily of bedrock with a thin drape of alluvial material, and are thus created by fluvial incision (Figure 1.10b). The thickness of the drape of alluvial material may vary, but is generally thin compared to the depth of the modern channel [Pazzaglia, 2013].

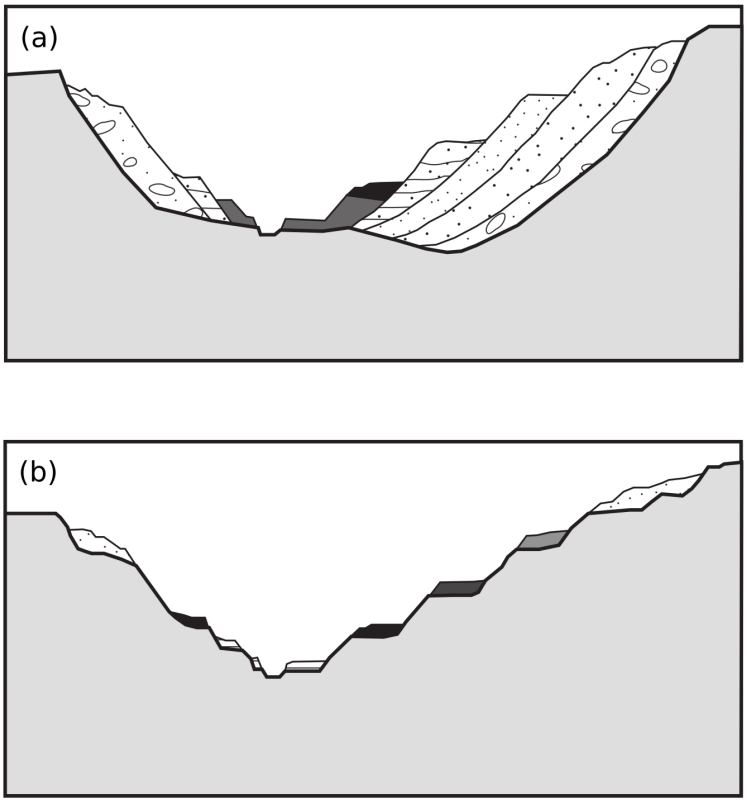

Figure 1.10: Schematic diagram showing (a) fill terraces, where the entire terrace is made up of channel deposits, and (b) strath terraces, where the terrace is composed of bedrock with a thin layer of alluvium. Modified from Pazzaglia [2013].

Field campaigns to map terrace features have been conducted by many authors to investigate the impact of climate, tectonics, and base level fall on fluvial systems [e.g. Merritts and Bull, 1989; Bull, 1991; Merritts *et al.*, 1994; Lavé and Avouac, 2000, 2001; Wegmann and Pazzaglia, 2002; Gran *et al.*, 2009]. For example, Lavé and Avouac [2000] conducted field surveys of terraces from the the Siwalik Foothills of central Nepal, based on their morphology and sedimentological characteristics, and found that the terrace morphologies record evidence of

active deformation due to folding from recent convergence. Wegmann and Pazzaglia [2002] undertook detailed field mapping of Holocene terraces sequences in the Clearwater River, Washington, and suggested that the formation of these terraces was due to punctuated fluvial incision caused by climatically-controlled alluviation. These field-mapping campaigns are clearly valuable exercises, providing fundamental insights into external controls on fluvial systems. However, field mapping of terrace features is expensive and time consuming. Developing new methods of objectively extracting terraces from digital elevation models would allow the rapid analysis of terraces on a landscape-scale, facilitating understanding of channel response to fluctuations in climate, tectonic perturbations, or lateral channel mobility.

1.3 Thesis outline

This thesis aims to build upon this body of research and improve our understanding on the structure and organisation of fluvial networks in upland landscapes. In order to achieve this, it is split into two main components: i) the development and testing of new algorithms for automatic feature extraction from lidar-derived DEMs, including the detection of hillslope-valley transitions, floodplains, and fluvial terraces; and ii) the application of these algorithms to understanding controls on the density of fluvial networks across a range of mountainous landscapes. Therefore, the structure of this thesis is as follows:

- In Chapter 2, I review methods for analysing and extracting geomorphic process domains from high-resolution topographic data. I also set out a framework for algorithm development in order to ensure this topographic analysis is objective and reproducible.
- In Chapter 3, I develop a new method for identifying the upstream extent

of fluvial processes from high resolution digital elevation models. I compare this new method to field-mapped channel heads, along with other published channel extraction techniques, to provide a reference for the most suitable methods of accurate channel network delineation in different landscapes.

- Following on from this work, in Chapter 4 I present a new method of identifying both floodplains and fluvial terraces from digital elevation models, using the distribution of local gradient and elevation across the landscape.

- Chapter 5 applies these new techniques for objective feature extraction from digital elevation models to explore the density of channel networks across a range of mountainous landscapes. I compare the density of channel networks to erosion rates derived from cosmogenic radionuclide analysis, as well as using hilltop curvature as a proxy for erosion rate on a landscape scale. This topographic analysis is combined with both analytical and numerical modelling to explore the implications of these relationship for common models of fluvial incision, sediment transport, and long-term landscape evolution.

- In Chapter 6 I present a synthesis of the main results of the thesis, along with an extended discussion and ideas for future research directions.

Chapter 2

Digital terrain analysis

As reviewed in Chapter 1, there is a rich body of theoretical predictions about the structure and organisation of fluvial systems, which link the geometry and statistical properties of fluvial networks to external forcings, such as climate or tectonics. These predictions are falsifiable: we can compare predicted landscapes with measured landscapes. But how do we quantify landscape form? This was a major challenge for early workers such as Gilbert, Powell and Davis, as validation of their theories required significant improvements in topographic surveying.

Today, geomorphologists have no shortage of excellent topographic data against which theoretical predictions can be tested. Digital topography is available over much of the Earth's surface, and in recent years many authors have developed techniques for analysing digital elevation models and extracting the signature of geomorphic processes [e.g. Stock and Dietrich, 2003; Lashermes *et al.*, 2007; Roering *et al.*, 2007; Booth *et al.*, 2009; Tarolli and Dalla Fontana, 2009; DiBiase *et al.*, 2010, 2012; Passalacqua *et al.*, 2010a; Thommeret *et al.*, 2010; Orlandini *et al.*, 2011; Sofia *et al.*, 2011; Milodowski *et al.*, 2015b; Grieve *et al.*, 2016a,b].

In this chapter I review the evolution of both topographic data and techniques used for analysing these data.

2.1 Topographic analysis before lidar

Early studies which used topographic data to investigate geomorphic processes typically quantified landscape form using contour map analysis. For example, early workers used these maps to extract the topology of fluvial networks [e.g. Horton, 1945; Strahler, 1957; Shreve, 1967], or to calculate slope and drainage area, and quantify relationships between them [e.g. Leopold and Maddock, 1953; Leopold and Miller, 1956; Flint, 1974]. Others used contour maps to examine relationships between denudation, uplift, and relief [e.g. Hack, 1960; Ahnert, 1970], and to investigate controls on hillslope-valley transitions [e.g. Montgomery and Dietrich, 1989]. As one might imagine, however, extracting such landscape metrics from contour maps was hugely time consuming. Early studies were not only hindered by the amount of time required to analyse and extract quantitative information by hand from these contour maps, but also by the poor spatial availability of the data, with no elevation data present between contours [Grieve, 2016].

In the early 1990s, increasing computational processing power led to the development of novel techniques for producing digital representations of topography. Initially, these techniques focused on digitising existing contour maps, with a particular emphasis on hydrology and flow routing [O'Loughlin, 1986; Moore *et al.*, 1988; Moore and Grayson, 1991; Moore *et al.*, 1991]. However, digitised contour maps are difficult to analyse computationally, due to the irregular data structure, and the large amount of interpolation required between contours. Furthermore,

the availability, resolution, and production of these digitised contour maps was inconsistent, making it difficult to compare the statistical properties and geometry of different landscapes. The launch of satellite platforms, such as NASA's Shuttle Radar Topography Mission [SRTM, Rabus *et al.*, 2003; Farr *et al.*, 2007], or the Advanced Space-borne Thermal Emission and Reflection Radiometer [ASTER, Yamaguchi *et al.*, 1998; San and Suzen, 2005], allowed the production of gridded DEMs on a global scale at 30 m resolution. Many workers have since tested the accuracy and validation of these datasets for the extraction of geomorphic information [e.g. Fisher *et al.*, 2013; Purinton and Bookhagen, 2017]. Alongside these global data, the United States Geological Survey (USGS) produced the National Elevation Dataset (NED), providing a seamless 10 m resolution DEM for the conterminous US [Gesch *et al.*, 2002]. For a comprehensive review of the development of digital elevation models, the reader is referred to Grieve [2016].

2.2 Lidar and high resolution topography

Currently satellite platforms are able to produce digital elevation data at a scale of tens of metres, but for higher resolution data, on the metre to sub-metre scale, ground and airborne-based techniques are typically required. The most widespread form of such data is derived from lidar. This name of this technology originally derived from an acronym for Light Detection And Ranging (LiDAR) but has become so ubiquitous that it has graduated to an English word, much like radar.

2.2.1 Acquisition and distribution of lidar data

In the past 30 years, the development of lidar technology for generating elevation data from the Earth's surface has dramatically increased both the accuracy and resolution of topographic data. Collection of lidar data involves firing pulses of laser light with a defined waveform at a surface. These pulses of light are either partially or fully reflected by the surface, and the return of these pulses are then analysed by a sensor, mounted on either airborne or terrestrial platforms. The travel time between the surface and the sensor is analysed and converted to a distance, resulting in the elevation of the surface when compared to a fixed datum [Carter *et al.*, 2001].

In order to examine geomorphic processes over relatively large spatial scales, lidar machines are often mounted on planes, helicopters, or unmanned aerial vehicles (UAVs). This results in an irregular cloud of points: modern airborne lidar data can consist of tens of points per square metre, providing an extremely high-resolution representation of the land surface with grid resolutions typically ≤ 2 m [Slatton *et al.*, 2007; Glennie *et al.*, 2013; Roering *et al.*, 2013]. Lidar sensors can also be mounted onto terrestrial platforms, such as Terrestrial Laser Scanners (TLS), in order to achieve even higher resolution representations of the Earth surface. These sensors are much closer to the surface of interest, and therefore point densities can reach 1000s of points per square metre, leading to DEMs with centimetre-scale resolution [e.g. Milan *et al.*, 2007; Heritage and Hetherington, 2007; Hodge *et al.*, 2009]. Figure 2.1 shows an example of varying DEM resolutions from the USGS Natural Debris Flow Laboratory at Chalk Cliffs, CO, ranging from 10 m NED data to 2 cm TLS data. In addition, lidar sensors capable of collecting the full waveform returns of light pulses can give fully two dimensional information about objects along the path of a light pulse [Mallet and Bretar, 2009]; these data have proven useful for ecological applications [e.g. Morsdorf *et al.*, 2009;

Woodhouse *et al.*, 2011; Wallace *et al.*, 2012]. This thesis will specifically focus on the use of pulsed lidar point clouds from airborne platforms, as these data are the most ubiquitously used for analysing geomorphic processes over large scales.

The first airborne lidar data for geomorphic applications was developed in the 1990s, but the expense of hiring private contractors meant that these data covered very small areas, and were not widely used [Roering *et al.*, 2013]. The first institutes to acquire a lidar instrument specifically for research were the Universities of Florida and Florida International University in 2000, greatly increasing the amount of lidar data available to the geomorphic community [Carter *et al.*, 2001]. Shortly afterwards, in 2003, the National Science Foundation in the United States provided funding for the National Center for Airborne Laser Mapping (NCALM), with the primary aim of making state-of-the-art lidar datasets available for both research and teaching. NCALM has since obtained over 100 lidar datasets (Figure 2.2), which are all freely available for research purposes [`ncalm.org`]. Alongside NCALM, the National Science Foundation also funded OpenTopography, a portal for facilitating the distribution of high-resolution topographic data for Earth surface processes research [`http://www.opentopography.org`, Krishnan *et al.*, 2011]. OpenTopography is based at the San Diego Supercomputer Center at the University of California, San Diego, and compiles lidar data from various sources throughout the United States as well as globally. These data can be available either as lidar point clouds or DEMs, depending on the location. Furthermore, many countries throughout Europe have undertaken large-scale airborne lidar campaigns in the past 10 years, with national lidar now freely available for many countries such as England and Wales [`https://data.gov.uk/dataset/lidar-composite-dtm-1m1`], Spain [`ftp://ftp.geo.euskadi.net/lidar/`], and Denmark [`https://download.kortforsyningen.dk/`]. A comprehensive review on the use of lidar for geomorphic applications is presented by Roering *et al.* [2013].

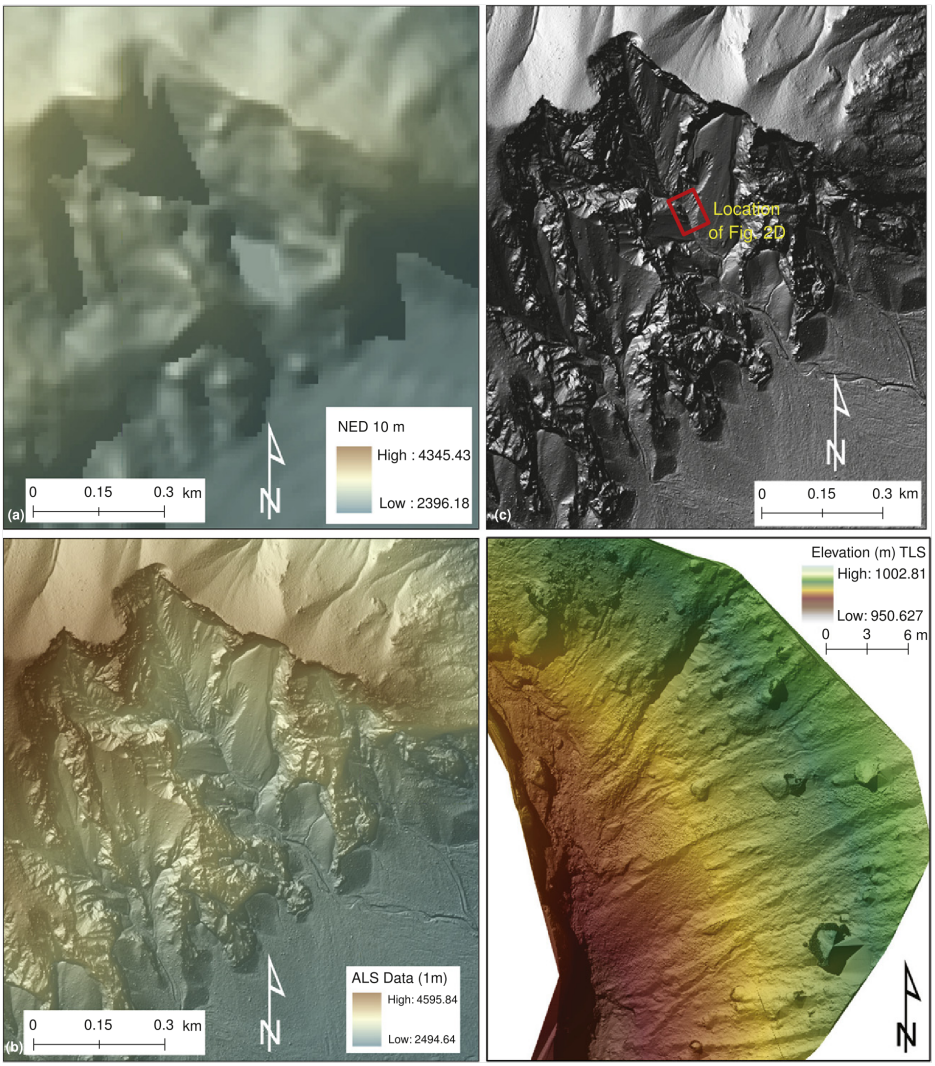

Figure 2.1: Varying DEM resolutions from the USGS Natural Debris Flow Laboratory at Chalk Cliffs, CO, showing (a) the 10 m NED DEM; (b) 1 m resolution DEM generated from airborne lidar; (c) hillshaded lidar DEM; and (d) 2 cm DEM from terrestrial laser scanning, matching location of red box in (c). Modified from Wasklewicz *et al.* [2013].

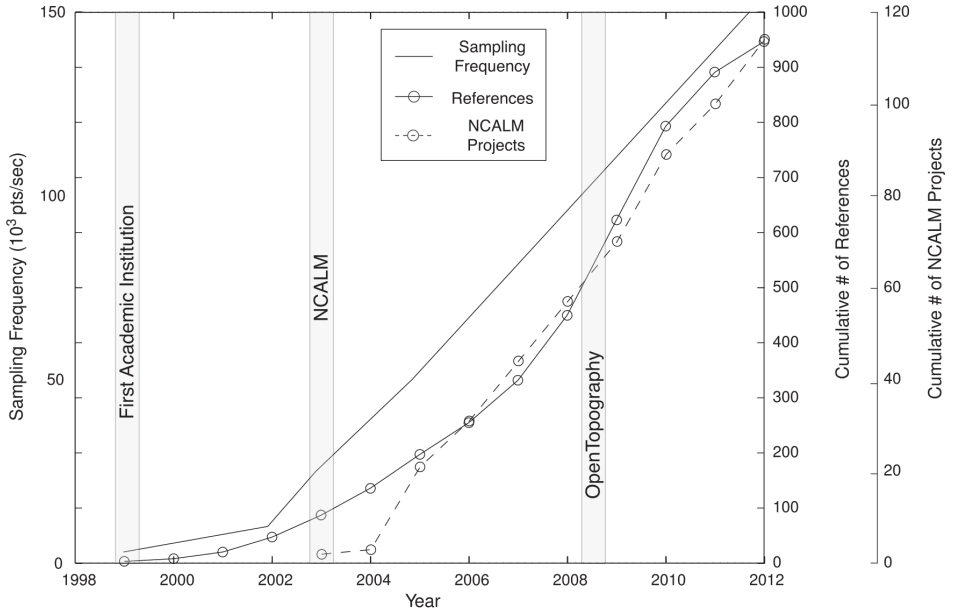

Figure 2.2: The development of geomorphological research using lidar-derived datasets. The solid line shows the sampling frequency of the lidar datasets (a proxy for the point spacing) from Slatton *et al.* [2007]. The solid line with circles shows the cumulative number of references in the literature with the keywords 'lidar' and 'geomorphology' through time. The dashed line shows the cumulative number of airborne lidar datasets collected by the National Center for Airborne Laser Mapping (NCALM) from 1990 to 2013, showing the dramatic increase over the past 30 years. Reproduced from Roering *et al.* [2013].

2.2.2 Production of digital elevation models

In order to extract signatures of geomorphic processes from lidar data, point clouds are typically filtered and then gridded to produce a bare-earth DEM of the Earth's surface. The production of DEMs from lidar data offers many potential advantages over traditional methods, such as photogrammetry or automated image mapping [Meng *et al.*, 2010]. The density of the point cloud data allows the generation of accurate, high-resolution DEMs, as well as enabling the mapping of subtle variations in topographic form [Baltsavias, 1999; Lin and Mills, 2010].

Furthermore, the ability of lidar pulses to penetrate through vegetation canopies enables the mapping of the ground surface even in densely vegetated landscapes [Baltsavias, 1999], as well as providing information on the structure of the canopy itself [Kraus and Pfeifer, 1998; Raber *et al.*, 2002; Stoker *et al.*, 2006; Meng *et al.*, 2009].

The first step in this process is the removal of any spurious points from the point cloud dataset, and the classification of the remaining data as either i) ground, or ii) non-ground [Meng *et al.*, 2010]. This is crucial for obtaining accurate DEMs from the original point cloud [Axelsson, 1999; Vosselman, 2000; Zhang *et al.*, 2003; Zhang and Whitman, 2005; Shan and Aparajithan, 2005]. Many algorithms have been developed in order to perform this filtering step: a comprehensive review of these algorithms can be found in Meng *et al.* [2010].

Once the point cloud data have been filtered, they are then interpolated, transforming the irregular cloud of X, Y, and Z points into a regularly spaced array of Z values. Many interpolation methods exist for the production of digital elevation models, which can be applied to multiple sources of topographic data [e.g. Mitášová and Mitáš, 1993; Mitášová and Hofierka, 1993; Mitáš and Mitášová, 1999]. However, specific algorithms have been developed for gridding lidar point clouds due to the extremely high data densities. For example, Kim *et al.* [2006] developed Points2Grid, which is a local binning algorithm that searches for points in a circular window radius defined by the desired resolution of the grid (R_G):

$$Radius = [\sqrt{2}R_G]. \tag{2.1}$$

After identifying points within this radius, an elevation value is calculated for each cell using an inverse distance-weighting approach. Points2Grid has been used extensively for the gridding of lidar point clouds, and has been implemented

within the OpenTopography framework, allowing the distribution and processing of the lidar data in one step.

2.3 Geomorphic applications of airborne lidar

Although the use of lidar is widespread within many fields, due to the high resolution and accuracy of lidar-derived DEMs, this thesis will focus on the specific applications of airborne lidar for geomorphic research. One of the key goals within geomorphological research is to quantify and understand the processes involved in landscape formation, and lidar data has been applied extensively for this aim [e.g. Lashermes *et al.*, 2007; Roering *et al.*, 2007; Booth *et al.*, 2009; Tarolli and Dalla Fontana, 2009; DiBiase *et al.*, 2010, 2012; Passalacqua *et al.*, 2010a; Thommeret *et al.*, 2010; Orlandini *et al.*, 2011; Sofia *et al.*, 2011; Milodowski *et al.*, 2015b; Grieve *et al.*, 2016a,b].

2.3.1 Base mapping

An important research question in geomorphology is quantifying the interactions between geological substrates and the Earth's surface [e.g. Duvall *et al.*, 2004; Roering *et al.*, 2005; Hartmann and Moosdorf, 2012; Hurst *et al.*, 2013b; Braun *et al.*, 2014]. In order to understand the links between lithology and geomorphic processes, accurate and high-resolution geological maps are essential. Traditionally, geological mapping was based on contour maps, suffering from the same problems as described in Section 2.1. Furthermore, the digitisation of these geological maps can often result in errors, with features such as lithologic contacts or structural lineations often offset by hundreds of metres [Roering *et al.*, 2013]. Therefore, many geological surveys have invested in the collection of lidar to serve

as improved geological base maps, particularly on a state-wide scale in the United States (e.g. North Carolina, South Carolina, Oregon, Minnesota, Kentucky, Pennsylvania, Virginia).

Lidar data have also been used as base maps in geomorphic research for a number of different purposes, such as for channel mapping [Devauchelle *et al.*, 2012], terrace delineation [Fuller *et al.*, 2009; Bowles and Cowgill, 2012; Gran *et al.*, 2013], identification of landslide scars [Mackey and Roering, 2011], and examination of bedrock structures [Martel, 2011; Pavlis and Bruhn, 2011]. Furthermore, more accurate underlying base maps has dramatically improved the ability of workers to perform landslide inventories for natural hazards over large areas [Schulz, 2007; Van Den Eeckhaut *et al.*, 2007; Guzzetti *et al.*, 2012]. Base maps created from lidar data are also particularly useful in the field as they allow the accurate pinpointing of sample locations, measurements, or geomorphic features within their topographic context.

2.3.2 Geomorphic feature extraction

One of the major advantages of the increasing availability of high resolution topographic data is our improved ability to extract features of geomorphological interest on an appropriate scale. For example, processes such as channelisation [Tarolli and Dalla Fontana, 2009], bioturbation [Gabet *et al.*, 2003; Roering *et al.*, 2010], or hillslope sediment transport [Roering *et al.*, 2007] often occur on metre to sub-metre scales. Therefore, detecting the signature of these processes in the landscape requires the use of high resolution topographic data.

Existing algorithms for topographic analysis which were developed for coarser resolution (30 m) data are often unsuitable for use with lidar data due to the dramatic increase in data density, requiring the use of much more computing

power and memory. Therefore, many authors have published new methods which are designed for maximum computational efficiency [Han *et al.*, 2012; Braun and Willett, 2013], or modified existing algorithms to take advantage of modern parallel processing techniques [Wu *et al.*, 2011; Tesfa *et al.*, 2011; Qin and Zhan, 2012].

A key first step in many geomorphic studies is the accurate delineation of channel networks, which is essential for landscape evolution modelling [e.g. Willgoose *et al.*, 1991; Howard, 1994] and predicting the flux of water, sediment, and pollutants through catchments [e.g. Montgomery and Dietrich, 1989; Novotny, 2002; Julian *et al.*, 2012]. Traditionally, channel networks were identified from coarse resolution DEMs based on either contributing area thresholds [O'Callaghan and Mark, 1984; Band, 1986; Tarboton *et al.*, 1991], or by quantifying the relationship between local gradient and drainage area within catchments [Montgomery and Dietrich, 1988; Dietrich *et al.*, 1992; Dietrich and Dunne, 1993]. However, these scaling relationships may be difficult to determine in steep landscapes where sediment transport is highly non-linear [Montgomery and Foufoula-Georgiou, 1993], and are strongly dependent on the grid resolution of the topographic data [Orlandini *et al.*, 2011].

The introduction of lidar data has led to the development of many new techniques for identifying channel networks within landscapes using local topographic metrics. For example, Sofia *et al.* [2011] developed an algorithm for identifying the upstream extent of channels using topographic openness, a metric that quantifies the degree of enclosure of a location on an irregular surface. Additional methods have been proposed that use tangential curvature to identify concave valleys within the landscape. Tangential curvature (κ_t) can be calculated from the DEM as the second derivative of elevation:

$$\kappa_t = \frac{z_{xx}z_y^2 - 2z_{xy}z_x z_y + z_{yy}z_x^2}{(z_x^2 + z_y^2)\sqrt{1 + z_x^2 + z_y^2}}, \tag{2.2}$$

where z is the elevation of the surface, and the subscripts represent derivatives [Mitášová and Hofierka, 1993]. One such technique is GeoNet, a software package developed by Passalacqua *et al.* [2010a,b, 2012] and Sangireddy *et al.* [2016b]. GeoNet filters the DEM using a non-linear diffusive filter [Perona and Malik, 1990], then identifies a threshold of tangential curvature for channelisation using a quantile-quantile technique. This produces an initial map of channel locations, which is then refined using thresholds of tangential curvature and drainage area (Figure 2.3). Although originally developed for natural landscapes, GeoNet has also been tested on landscapes which have a significant anthropogenic influence [Passalacqua *et al.*, 2012]. Pelletier [2013] published an alternative method, which involves filtering the DEM using an optimal Wiener filter [Wiener, 1949; Press, 2007], then applying a tangential curvature threshold to identify the upstream extent of concave valleys. Flow is then routed from these upstream points using a multi-directional flow routing algorithm [Freeman, 1991].

Lidar data have also proven useful in the remote detection of floodplains and fluvial terraces. Traditionally, areas prone to flood inundation were predicted using hydraulic modelling studies [e.g. Noman *et al.*, 2001; Grimaldi *et al.*, 2013], which can be computationally intensive. Predictions of flood inundation derived from these techniques can be highly detailed; in some cases predictions can be made at the level of a single building [e.g. Horritt and Bates, 2002; Cobby *et al.*, 2003; Guzzetti *et al.*, 2005; Hunter *et al.*, 2007; Kim *et al.*, 2012]. However, these models require the calibration of large numbers of parameters, which frequently are poorly constrained [e.g. Beven, 1993; Horritt and Bates, 2002; Liu and Gupta, 2007]. The introduction of lidar has provided ways of mapping floodplains rapidly over large spatial extents, by analysing topographic metrics

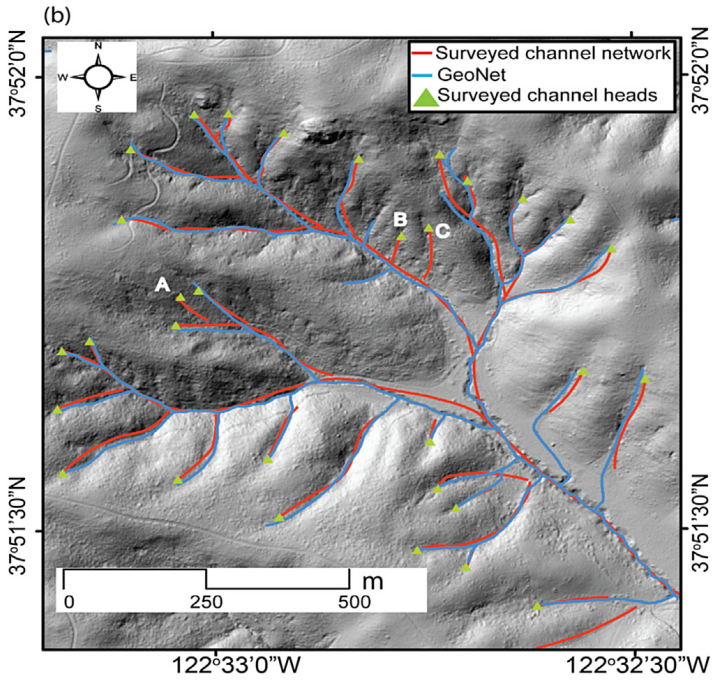

Figure 2.3: Example of channel networks extracted using the GeoNet software (blue) compared to surveyed channel network (red) and channel heads (green triangles) in Tennessee Valley, CA. A, B, and C represent channel heads missed by GeoNet. Modified from Sangireddy *et al.* [2016b].

from DEMs. These topographic metrics include drainage area and local slope [Kirkby, 1975; Beven and Kirkby, 1979; Beven *et al.*, 1995; Quinn *et al.*, 1995; Beven, 1997; Manfreda *et al.*, 2011, 2014]; elevation and distance from the nearest channel [Degiorgis *et al.*, 2012]; and floodplain and channel geometries [Dodov and Foufoula-Georgiou, 2006].

Many authors have also developed techniques to remotely map fluvial terrace features using high-resolution DEMs. These techniques generally identify terraces surfaces based on a combination of local slope, and the height of each pixel compared to the nearest channel [Demoulin *et al.*, 2007; Stout and Belmont, 2014]. Demoulin *et al.* [2007] developed a method to reconstruct previous channel

long profiles from terraces surfaces by using these topographic metrics, but this method was not designed to map terraces spatially over the landscape. Therefore, following on from this approach, Stout and Belmont [2014] published a semi-automated toolbox, TerEx, which can be applied as a plugin to GIS software. TerEx identifies terraces based on thresholds of distance from the channel, minimum terrace area, and local relief, which are set by the user. Once a draft terrace map is produced, the tool allows the user to manually clip and edit the terrace surfaces based on comparison with field data (Figure 2.4). Although these methods provide new opportunities for mapping floodplain and terrace features rapidly, all of these methods require significant user input, and calibration with independent datasets, such as flood hazard maps or field-mapped terraces. At present, no method exists to map floodplain or terrace features based on topographic data alone.

The analysis of surface roughness on the metre to sub-metre scale from lidar data has also been exploited by many workers to detect and extract hillslope features, such as the signature of landsliding. Subtle topographic variability resulting from hummocks, scarps, and pressure ridges has been shown to reflect the spatial distribution of landslides and landslide deformation processes [McKean and Roering, 2004; Glenn *et al.*, 2006]. This topographic variability was exploited by Booth *et al.* [2009] to determine a characteristic spatial scale of deep-seated landsliding, which enabled the accurate mapping of landslides across the Pacific Northwest, USA. Recent studies have built upon these methods to develop new techniques for large-scale landslide mapping [Tarolli *et al.*, 2012; Van Den Eeckhaut *et al.*, 2012; Berti *et al.*, 2013], a comprehensive review of which can be found in Tarolli [2014]. Surface roughness from lidar data has also been used to map the emergence of bedrock on hillslopes across steep landscapes [Milodowski *et al.*, 2015b], building on previous slope-based methods [DiBiase *et al.*, 2012; DiBiase and Lamb, 2013; Marshall and Roering, 2014].

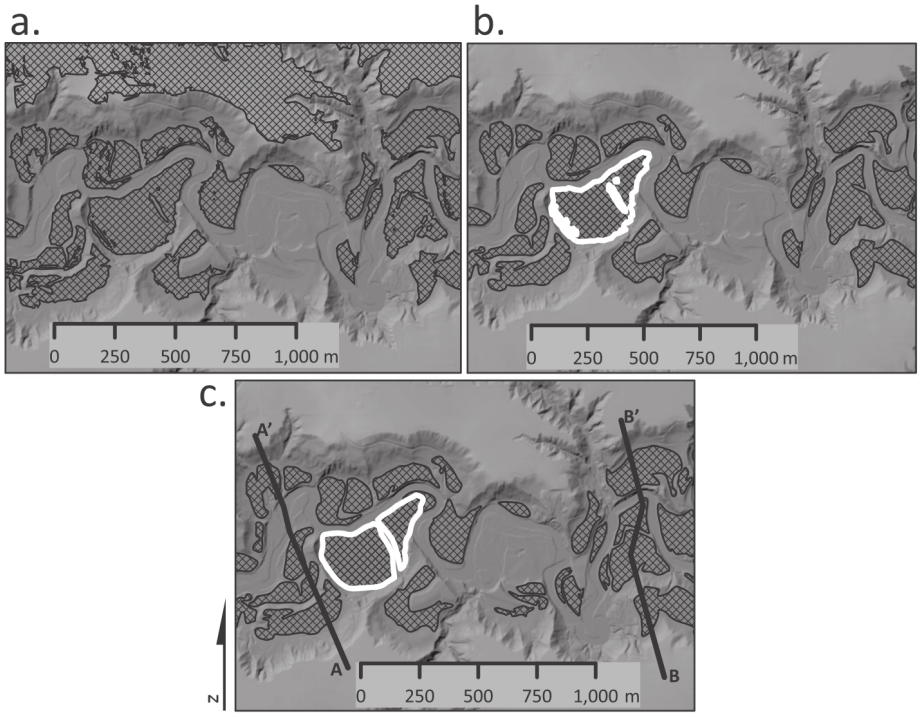

Figure 2.4: Example of terraces extracted using the TerEx toolbox for part of the Le Sueur River, MN, showing (a) initial extracted terraces; (b) selection of a terrace for modification; and (c) terrace feature after the manual editing process. Reproduced from Stout and Belmont [2014].

2.3.3 Understanding controls on topographic form

A central goal in Earth surface research is to understand the relationship between the shape of the landscape and the geomorphic processes that act within it. Achieving this goal requires falsifiable, process-based models simulating landscape evolution [Dietrich *et al.*, 2003]. To be falsifiable, a model must produce predictions that can be tested against topographic data: this testing often requires the extraction of geomorphic features as described in Section 2.3.2. Pioneering early studies of landscape evolution compared the predictions of topographic form to real landscapes, but in a qualitative sense [Ahnert, 1976]. Following on from this, many workers used DEMs with resolutions of $\sim$ 10 m to calibrate

and evaluate landscape evolution models more quantitatively, by using metrics such as slope-area analysis, hypsometry, and cumulative area distributions [e.g. Tucker and Bras, 1998; Hancock and Willgoose, 2001; Hancock *et al.*, 2002].

The resolution of topographic data derived from lidar is often finer than that of common landscape evolution models, allowing accurate testing, validation, and evaluation [Roering *et al.*, 2007, 2013]. This has been particularly useful for the testing of models of hillslope sediment transport, which is often performed using measurements of topographic curvature or local gradient. These metrics are strongly dependent on the scale at which they are measured, and therefore high-resolution DEMs are necessary to detect the subtle changes in gradient and curvature associated with hillslope processes such as rainsplash, bioturbation, or tree throw [Heimsath *et al.*, 1999; Lashermes *et al.*, 2007; Roering *et al.*, 2010; Hurst *et al.*, 2012; Grieve *et al.*, 2016c]. For example, different models of hillslope sediment flux have been tested by analysing hillslope profiles from lidar [Roering *et al.*, 1999, 2001; Grieve *et al.*, 2016a], and by comparing lidar-derived measurements of local relief with erosion rate [Roering *et al.*, 2007; Hurst *et al.*, 2012, 2013a; Grieve *et al.*, 2016b]. Roering [2008] tested the topographic predictions of a series of different soil transport equations, which were evaluated using lidar-derived DEMs. Similar techniques have been used to test predictions of soil depth across landscapes, and to understand the relationship between soil depth and sediment transport [Pelletier and Rasmussen, 2009; Pelletier *et al.*, 2011].

Lidar data has also proven useful in examining the relationship between these hillslope sediment transport processes and fluvial incision. For example, Perron *et al.* [2008a] developed a numerical model predicting that the spacing of ridges and valleys in the landscape was controlled by the relative rates of advective processes, such as fluvial incision, and diffusive processes, such as soil creep (Section 1.2.3). These predictions result in a characteristic hillslope length scale,

which can be directly tested from topographic data. Perron *et al.* [2008b, 2009] used spectral analysis to determine this characteristic length scale from five landscapes with varying valley spacings. They found that the length scale was directly proportional to those predicted by the numerical modelling, and therefore suggested that the spacing of valleys and ridges is a fundamental parameter recording the relative influence of advection and diffusion.

A long-standing problem in Earth surface processes research is understanding the influence of tectonics on the shape of the topography [e.g. Wobus *et al.*, 2006]. Tectonic processes are often difficult to measure directly, requiring detailed field studies and extensive geochronologic work [England and Molnar, 1990]. Therefore, determining a link between tectonics and topographic structure provides an exciting opportunity to map uplift rates over large spatial scales from topographic data alone.

Intuitively, we might expect that the steepest landscapes on Earth are associated with the highest rates of surface rock uplift, suggesting that hillslope morphology may potentially record meaningful tectonic information. However, hillslopes have been shown to reach a threshold gradient, where erosion rates become fast enough to outpace the rate of soil production [Burbank *et al.*, 1996; Heimsath *et al.*, 1997; Montgomery and Brandon, 2002; Binnie *et al.*, 2007], limiting the ability of hillslope gradient to record changes in uplift rate. Therefore, recent work has exploited measurements of hilltop curvature from lidar data, which have been shown to remain sensitive to increasing erosion rate over several orders of magnitude [Hurst *et al.*, 2012, 2013a]. Hurst *et al.* [2013a] examined hillslope length, gradient, and hilltop curvature along the Dragon's Back Pressure Ridge (DBPR), a section of the San Andreas Fault in California (Figure 2.5), and showed that hillslope curvature reflected patterns of uplift rate measured along the fault [Hilley and Arrowsmith, 2008]. DiBiase *et al.* [2012] used a combination of aerial photographs and lidar-derived DEMs to identify bedrock exposure in a region with

a gradient of uplift rates in the San Gabriel Mountains, southern California. They showed that the percentage of bedrock exposure and colluvial channel density in the landscape was positively correlated with uplift rate.

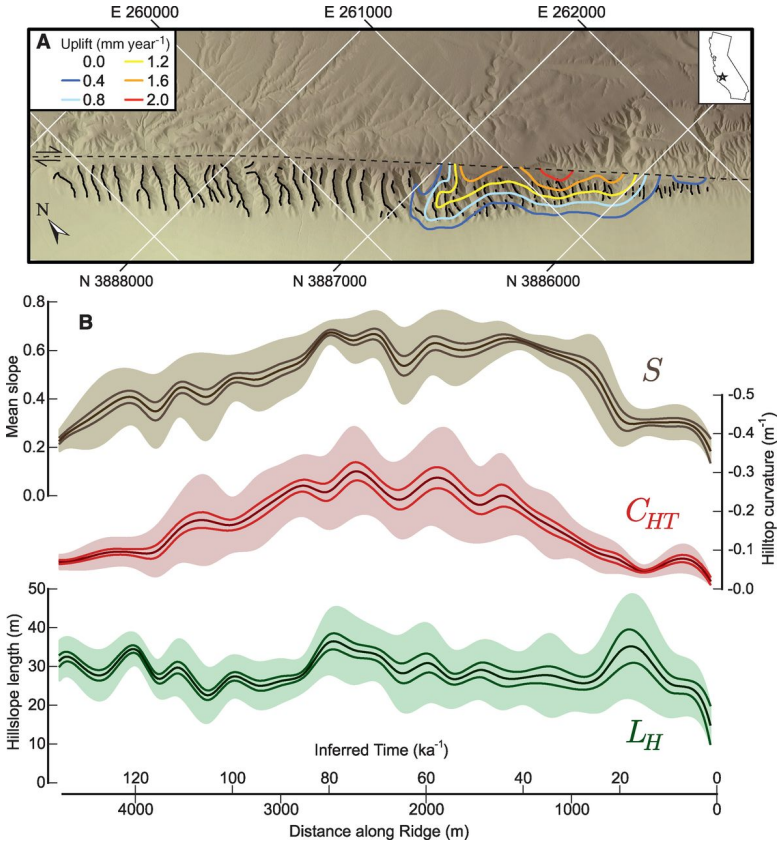

Figure 2.5: Correlation between hillslope morphology and uplift rates along the Dragon's Back Pressure Ridge, CA. (a) Shaded relief map of the ridge showing the uplift field (UTM Zone 11°N); black lines indicate hilltops sampled. (b) Distribution of hillslope gradient, hilltop curvature, and hillslope length along the ridge, showing that hilltop curvature continues to increase along the ridge while gradient is limited at around 900 m. Reproduced from Hurst *et al.* [2013a].

Another important factor controlling topographic form is the influence of biological processes. Biotic activity can be instrumental in driving hillslope sediment production and transport in soil-mantled landscapes, and therefore may leave behind a detectable topographic signature [e.g. Dietrich and Perron, 2006; Corenblit

and Steiger, 2009; Reinhardt *et al.*, 2010]. Dietrich and Perron [2006] suggested that these biotic processes should be included explicitly within geomorphic transport laws, in order to model and develop testable predictions of the impact of life on landscape evolution. Following on from their work, Roering *et al.* [2010] used lidar-derived DEMs to examine the role of trees in shaping topographic form and the production of soil in the Oregon Coast Range, a steep forested landscape. They calculated hillslope curvature across the landscape using a range of different window sizes, and found a prominent scaling break in the topographic data at a window radius of $\sim$ 7.5 m. They suggested that hillslope curvature calculated over small scales therefore represents the signature of pit and mound topography, created from tree throw and bioturbation. Gabet *et al.* [2014] combined numerical modelling of gopher burrowing with high-resolution topographic data to show that the topographic predictions of sediment transport by gophers correlated well with the surface metrics of a mima mound field in Merced, California. Lidar data have also been used to demonstrate relationships between ecosystem structure and geomorphology, such as the distribution of above-ground biomass [Milodowski *et al.*, 2015a].

2.4 An open-source framework for topographic analysis

Section 2.3 reviews the many advantages of the development of high-resolution topographic data for geomorphic research. However, the large volume of data involved in the analysis of these topographic datasets also leads to some challenges, particularly as these datasets are still relatively new within the field. Therefore,

an important goal for Earth surface processes research is to make these algorithms for topographic analysis reproducible, accessible, and easy to use by the community.

Traditional topographic analysis methods for use with coarser resolution DEMs are normally implemented within Geographical Information Systems (GIS) software, which can be either commercial or open-source. These GIS packages provide easy to use, powerful approaches for spatial analysis, but also result in some problems related to automation and reproducibility. For example, techniques to perform intensive computational analyses on topographic data are often missing from these packages. Due to the emphasis on a well-developed graphical user interface (GUI), these GIS packages are often not equipped to deal with the density of data and large file sizes associated with analysing high-resolution topography. Furthermore, the underlying code behind these software packages may not be available for the user to inspect, especially if the software is commercial, meaning that it is difficult for the user to determine the exact processing being performed. If plugins or add-ons to these software packages are developed for research, then these may not be easily accessible by other users in the community, due to the need to purchase the software or appropriate licences.

Alongside these problems, the 'point and click' approach of traditional GIS packages which have extensive GUIs can lead to issues with the reproducibility of topographic analysis. Reproducibility is a fundamental goal within any scientific discipline. Currently, many fields are experiencing severe problems in ensuring that past studies can be repeated and validated appropriately [Ioannidis *et al.*, 2009; Open Science Collaboration, 2015]. Within geomorphology, the complex steps involved in performing topographic analysis using GIS software means that users may get different results each time they perform the analysis. This makes it difficult for authors to reproduce the results of even their own work, let alone that of another researcher.

In order to address these issues, a key part of the research for this thesis has been developing new algorithms for extracting information from high-resolution topography within a reproducible, open-source framework. This software development has been done in collaboration with other researchers at the Universities of Edinburgh, Glasgow, and Manchester. I have therefore set out the following guiding principles for 'best practice' topographic analysis, in collaboration with the other software developers:

1. All software should be **open source** and readily accessible by other researchers in the community.

2. Algorithms should be developed to maximise **computational efficiency**, in terms of both the development language and code structure.

3. The analysis should **minimise user input**, to avoid the 'point and click' approach of traditional software. Users should be able to re-run the analysis multiple times and produce identical output.

4. The software should be **fully version-controlled**, to allow transparent documentation of code development and retain functionality of previous versions.

5. All routines should be **thoroughly documented** and contain tutorials to instruct users on how to perform the analyses themselves. This should help to allow other researchers to use the code, and maintain transparency about the processing steps within the code.

6. The routines that are used for research should be **reproducible**. In order to achieve this, all code used for topographic analysis should be fully archived and citable with a digital object identifier (DOI).

The software developed during my PhD research has been based on these guiding

principles. In order to achieve this, the software is written using fully open-source languages, including C++ and Python. This ensures that no licences or propriety software are required for running the topographic analysis routines. Furthermore, the code has been specifically developed for use with high-resolution topographic data, and the use of C++ for manipulating the data ensures optimum computational efficiency, compared with a higher level language such as MATLAB or Python. This also allows the implementation of efficient routines for DEM processing, such as calculation of stream power [Braun and Willett, 2013] and filling of pits and sinks [Wang and Liu, 2006]. After processing of the topographic data in C++, Python is used for visualisation to ensure that the figures produced in each study are reproducible [e.g. Mudd, 2017].

In order to ensure that the software is fully version controlled and the results of the analysis are reproducible, the software used for each of the analysis is stored on GitHub within its own repository (`https://github.com/LSDtopotools`). This ensures an online record of all changes made to the code and allows anyone within the community to download and use the software for their own research. Alongside ensuring that the software is publicly available online, I have also worked in collaboration with the other software developers to write thorough documentation and tutorials for downloading, installing, and running the software for topographic analysis. This documentation can be found at `http://lsdtopotools.github.io/LSDTT_book/`.

A stable version of the software is also released onto Zenodo, a data sharing platform developed to encourage open-source practices within scientific research (`https://zenodo.org/communities/lsdtopotools/`). This means that the software associated with each analysis receives its own DOI and is therefore fully citable within the community.

Chapter 3

Methods of channel extraction

The work presented in this chapter was published in Water Resources Research:

Clubb, F.J., Mudd, S.M., Milodowski, D.T., Hurst, M.D., and Slater, L.J. (2014) Objective extraction of channel heads from high-resolution topographic data, *Water Resources Research* **50**, 4283-4304, doi:10.1002/2013WR015167

The software used and developed in this chapter is available at:

Clubb, F. J., Mudd, S. M., Milodowski, D. T., Grieve, S.W.D., and Hurst, M. D. (2017) LSDChannelExtraction v 1.0. *Zenodo*, doi:10.5281/zenodo.824198

This research was conducted in collaboration with the named co-authors, who helped to edit the final manuscript and contributed to software development. I wrote the topographic analysis algorithms, performed the analyses, created the figures, and wrote the manuscript.

Abstract

Fluvial landscapes are dissected by channels, and at their upstream termini are channel heads. Accurate reconstruction of the fluvial domain is fundamental to understanding runoff generation, storm hydrology, sediment transport, biogeochemical cycling and landscape evolution. Many methods have been proposed for predicting channel head locations using topographic data, yet none have been tested against a robust field dataset of mapped channel heads across multiple landscapes. In this study, four methods of channel head prediction were tested against field data from four sites with high-resolution DEMs: slope-area scaling relationships; two techniques based on landscape tangential curvature; and a new method presented here, which identifies the change from channel to hillslope topography along a profile using a transformed longitudinal coordinate system. This method requires only two user-defined parameters, determined via independent statistical analysis. Slope-area plots are traditionally used to identify the fluvial-hillslope transition, but I observe no clear relationship between this transition and field-mapped channel heads. Of the four methods assessed, one of the tangential curvature methods and the new method presented here most accurately reproduce the measured channel heads in all four field sites (Feather River CA, Mid Bailey Run OH, Indian Creek OH, Piedmont VA), with mean errors between the mapped and predicted channel heads of 11, 7, 5 and 24 m and 34, 3, 12 and 58 m respectively. Negative values indicate channel heads located upslope of those mapped in the field. Importantly, these two independent methods produce mutually consistent estimates, providing two tests of channel head locations based on independent topographic signatures.

3.1 Introduction

Fluvial landscapes are dissected by channels and at the upstream termini of these channels are channel heads. Their position controls the total length of channels in the stream network, which sets drainage density and therefore influences biogeochemical cycling, and water and sediment flux to the river system [Montgomery and Dietrich, 1989; Julian *et al.*, 2012; Jefferson and McGee, 2013]. Their location also determines the speed at which pollutants may enter the river network if located close to areas of anthropogenic land use such as industry or mining [Novotny, 2002]. Therefore, determining the location of channel heads is essential for flood forecasting, mitigation of pollution, prediction of ecosystem functioning, and landscape evolution.

Channel heads can be defined morphologically as 'the upslope limit of erosion and concentration of flow within steepened banks' [Montgomery and Dietrich, 1989]. Field identification of channel heads is difficult and time consuming, so many authors have suggested methods to identify these landscape features using topographic data [O'Callaghan and Mark, 1984; Band, 1986; Montgomery and Dietrich, 1988; Tarboton *et al.*, 1991; Dietrich *et al.*, 1992, 1993; Dietrich and Dunne, 1993; Montgomery and Foufoula-Georgiou, 1993; Molloy and Stepinski, 2007; Tarolli and Dalla Fontana, 2009; Passalacqua *et al.*, 2010a; Thommeret *et al.*, 2010; Sofia *et al.*, 2011; Henkle *et al.*, 2011; Orlandini *et al.*, 2011; Pelletier, 2013]. A clear distinction exists between the 'channel network', which represents parts of the landscape responding to fluvial incision, and the 'valley network', defined as areas of convergent topography [Howard, 1994]. In this study I focus on methods of extracting the channel network from digital elevation models (DEMs).

Traditionally, channel heads were identified using methods founded on process-based models, such as contributing area thresholds [O'Callaghan and Mark, 1984; Band, 1986; Tarboton *et al.*, 1991] or slope-area scaling relationships [Montgomery

and Dietrich, 1988; Dietrich *et al.*, 1992, 1993]. Montgomery and Dietrich [1988] suggested that channels initiate where drainage area is large enough to support a channel and that there is an inverse relationship between slope and drainage area downstream of the channel head. However, in steep, rocky landscapes, it may be difficult to distinguish between fluvial channels and steep threshold hillslopes using these scaling relationships [Montgomery and Foufoula-Georgiou, 1993]. Furthermore, the analysis of channel head locations using coarse-resolution (30m) DEMs may result in error, as the processes involved in channel initiation act on a metre to sub-metre scale. Orlandini *et al.* [2011] extracted slope and drainage area threshold conditions for channel initiation across DEMs of varying resolutions using observed channel heads, and found that the value of the threshold parameters strongly depended on the grid size.

The recent introduction of high resolution topographic data, such as Airborne Light-Detection and Ranging data (lidar) has revolutionised the study of geomorphology, and has allowed fundamental questions about landscape form and evolution to be reassessed. Recent methods of channel head prediction have used lidar to predict channel head locations directly from local topographic characteristics. For example, Sofia *et al.* [2011] used topographic openness, a morphometric character that quantifies the degree of openness or enclosure of a location on an irregular surface, to predict channel heads. Other methods use the tangential curvature to identify the start of the fluvial network from DEMs. The GeoNet software, developed by Passalacqua *et al.* [2010a], combines a Perona-Malik filter, to smooth the DEM whilst preserving hillslope-valley transitions, and a curvature threshold to produce a draft map of the channel head locations. This is improved by creating a valley network based on pathways which minimise a cost function inversely proportional to the threshold curvature and drainage area [Passalacqua *et al.*, 2010a]. Another curvature-based method utilises an algorithm created by Pelletier [2013], which involves filtering the DEM using an optimal Wiener filter

[Wiener, 1949; Press, 2007] and a threshold tangential curvature for channelisation. These methods are similar in that they search for a tangential curvature signature in the landscape for the location of the channel network; however, the Pelletier [2013] method requires two user-defined parameters, whereas GeoNet Passalacqua *et al.* [2010a] requires three.

In order to demonstrate the success of a method as a predictive tool, it must be tested against a robust field dataset. Sofia *et al.* [2011] tested their algorithm on 57 channel heads across two alpine headwater catchments. Passalacqua *et al.* [2010a] mapped seven channel heads in a sub-catchment of the South Fork Eel River basin in northern California to test the GeoNet algorithm. Pelletier [2013] tested his algorithm using a synthetic dataset in which channel heads were proscribed within a simple landscape evolution model. Although these previous tests suggest these methods could be used to detect channel heads from DEMs alone, the test datasets had relatively few data points to compare with algorithm output and, crucially, they were not tested across multiple landscapes.

In this study I test several proposed methods of channel head prediction against field-mapped channel head data from multiple field sites. I test both methods that incorporate theoretical process-based models and those that predict channel heads directly from geometric characteristics of high-resolution DEMs. The methods of channel head identification I evaluate are slope-area scaling relationships [Montgomery and Dietrich, 1988; Orlandini *et al.*, 2011]; the GeoNet drainage network extraction algorithm [Passalacqua *et al.*, 2010a]; tangential curvature mapping [Pelletier, 2013]; and a new, process based method of channel head identification that uses a coordinate transformation of flow distance, which I describe in Section 3.3.4. I call my new method the Drainage Extraction by Identifying Channel Heads (DrEICH) method. I test these methods against a total of 167 mapped channel heads in three field areas that are co-located with 1m resolution lidar data.

3.2 Field setting

I report channel head locations mapped for this study across two sites in Northern California and two in Southern Ohio, and I also assimilate data from a previous study that was conducted in the Piedmont physiographic region, Virginia, with 1 m resolution lidar [Julian *et al.*, 2012].

3.2.1 Feather River, Sierra Nevada, California

Channel head mapping was undertaken in the lower part of the Middle Fork Feather River in the northern Sierra Nevada, California (Figure 3.1). Airborne Laser Swath Mapping (ALSM)-derived topographic data was undertaken in the region on 25th - 27th September 2008 by the National Center for Airborne Laser Mapping [NCALM, www.ncalm.org], with a vertical accuracy of 0.05 m to 0.3 m and a mean horizontal accuracy of 0.3 m. The metadata were made available online by the National Science Foundations OpenTopography service [www.opentopography.org].

The landscape is largely forested and soil mantled, with a semi-arid climate and a strong precipitation gradient from the Sierra Nevada mountain range to the drier Central Valley of California [Hurst *et al.*, 2012]. The mean annual precipitation is around 1650 mm and the mean annual temperature is 12.5°C [National Climatic Data Center and National Oceanic and Atmospheric Administration (NCDC/NOAA)].

During the Pleistocene, the uppermost sections of the catchment underwent glaciation while the lower areas remained mainly unaffected [Clark, 1995]; the mapping was conducted exclusively in sub-catchments unaffected by glaciers. The underlying geology consists of a series of granite, granodiorite and tonalite plutons

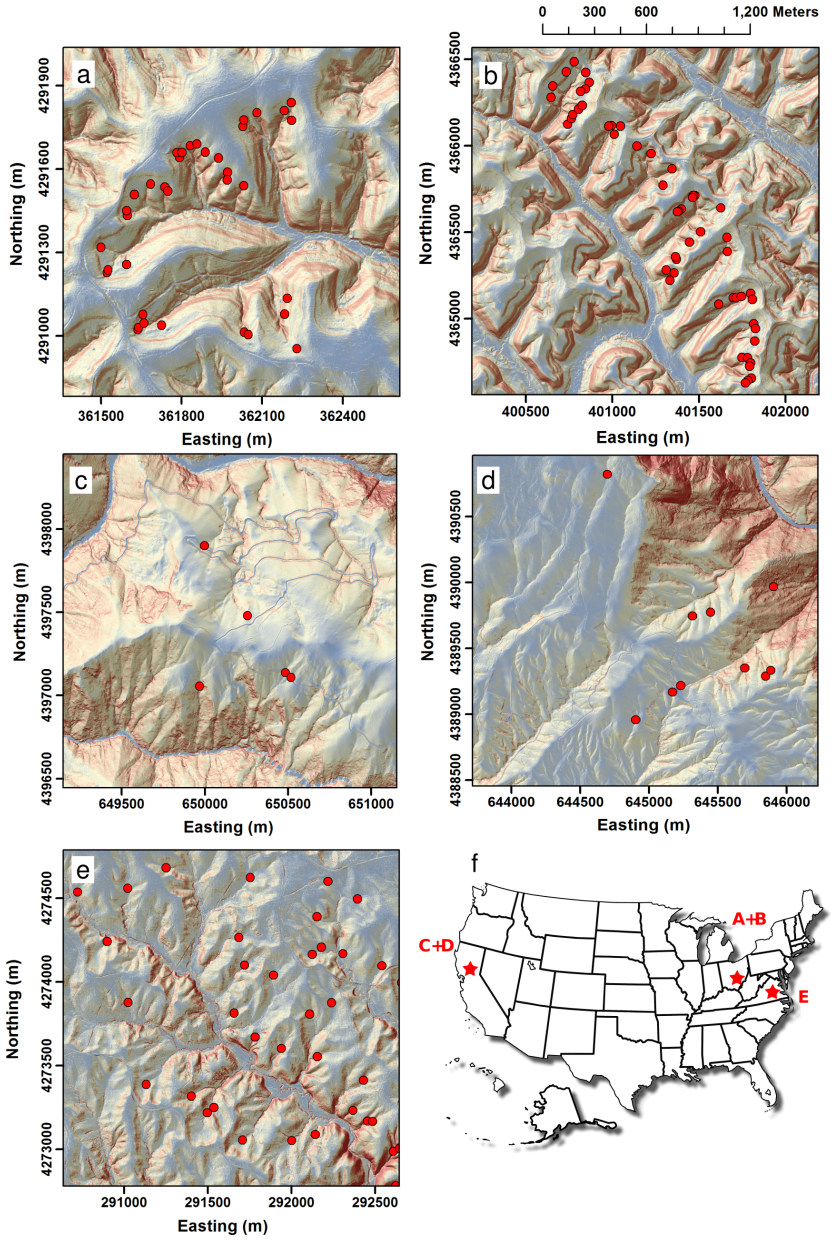

Figure 3.1: Shaded slope map of each field site with mapped channel heads, along with their location in the USA. (a) Indian Creek, Wayne National Forest, OH, UTM Zone 17°N. (b) Mid Bailey Run, Wayne National Forest, OH, UTM Zone 17°N. (c) Cascade Ridge, Sierra Nevada, CA,UTM Zone 10°N. (d) Bald Rock Basin, Sierra Nevada, CA, UTM Zone 10°N. (e) Piedmont, VA, UTM Zone 18°N. (f) Map of the USA showing locations of sites in (a)-(e).

(part of the Sierra Nevada batholith) that were emplaced during Cretaceous arc volcanism [Unruh, 1991]. This surface was then dissected by the Feather River, forming deep canyons. This incision is evident from the slope distribution in which the steepest hillslopes are found next to the Feather River and its main tributaries (Figure 3.1). In turn, this has led to an order of magnitude variation in erosion rates across the landscape, with erosion rates on low relief surfaces of < 20 mm ka^{-1} that contrast with erosion rates in and near the canyon exceeding 200 mm ka^{-1} [Riebe *et al.*, 2000; Hurst *et al.*, 2012, 2013b]. The distribution of slopes and erosion rates throughout the catchments allow testing of the drainage network extraction algorithms in a landscape of varying topographic form. Two different sub-basins of the main Feather River catchment were chosen for analysis in this study: Cascade Ridge and Bald Rock Basin (Figure 3.1).

3.2.2 Wayne National Forest, Ohio

The second field site used in this study is located in Wayne National Forest, south-eastern Ohio, within the southern, unglaciated Allegheny Plateau (Figure 3.1). The site remained free of glacial ice during the Pleistocene [Peltier, 2004]. Lidar data for the site was collected via ALSM mapping by the Ohio Statewide Imagery Program during 2008 and 2009 [OSIP, http://ogrip.oit.ohio.gov/ServicesData/StatewideImagery/tabid/86/Default.aspx], with a vertical accuracy of 0.3 m and a mean horizontal accuracy of 0.3 m.

The forest is divided into three distinct eco-regions: the Marietta Unit, the Athens Unit and the Ironton Unit [Hix and Pearcy, 1997]. Channel head location data were collected for two catchments in this area: Mid Bailey Run, in the Athens Unit; and Indian Creek, in the Ironton Unit, between 26 May and 7 June 2011. Major flooding in the region had occurred in the month preceding the field mapping. The Athens Unit is the most northerly unit of

Wayne National Forest (Figure 3.1), and has a temperate, continental climate with distinct seasons [Small and McCarthy, 2001]. Precipitation is generally evenly distributed throughout the year, with the wettest month being July and the driest being October. The mean annual precipitation is 1025 mm and the mean annual temperature is 10.7°C [NCDC/NOAA]. The Athens Unit consists of Carboniferous and Permian sediments laid down in shallow seas. These consist of sandstones, shales, siltstones, limestones, and frequent coal seams, which form an eastwards-dipping anticline [Goebel and Hix, 1996]. The landscape forms a mature dissected plateau, with moderate to steep slopes, narrow ridges, and stream valleys [Goebel and Hix, 1996]. The width of the ridges is strongly controlled by the underlying lithology, with narrow ridges underlain by sandstone and broad ridges underlain by siltstones and shales. Elevations range from 642 to 1044 m above mean sea level (AMSL). The soils can be classified as moderate- to well-drained loam or silt loam soils [Goebel and Hix, 1996]. The Ironton Unit is the most southerly of the districts of the Wayne National Forest (Figure 3.1). It has similar underlying geology, soil types, and climate to that of the Athens Unit [Martin *et al.*, 2011], and elevations range from 652 to 979 m AMSL.

3.2.3 Piedmont, Virginia

Channel head data in the Piedmont, eastern Virginia (Figure 3.1), was publicly available online from mapping carried out by Julian *et al.* [2012]. ALSM was carried out on forty flight missions between April 3rd and May 10th, 2011 by Geodigital/Terrapoint, with a vertical accuracy of between 0.083 m and 0.101 m and a mean horizontal accuracy of 0.99 m, and providing a 1 m resolution DEM. Although additional channel head mapping was carried out by Julian *et al.* [2012] at other regions across Virginia and West Virginia, freely available lidar could not be obtained for these regions.

The Piedmont is a transitional zone between the mountainous regions of the Appalachians to the west, and the Coastal Plain to the east at the Atlantic Ocean (Figure 3.1). The landscape is forested, with thick, clay-rich soils and deeply weathered bedrock [Julian *et al.*, 2012]. From November 1946 to April 2012, mean annual precipitation in the region was 1121 mm, and the mean annual temperature was 13.2°C [NCDC/NOAA]. The Piedmont is made up of Proterozoic to Palaeozoic igneous and metamorphic rocks which form the core of the Appalachians, arranged as a series of distinct terrains separated by thrusts or normal faults [Conley, 1985]. The study area is located within the Fork Mountain Formation which consists of mica schist, biotite gneiss, amphibolite and quartzite [Conley, 1985]. The topography of the study area is characterised by rolling plains, with moderate relief.

3.3 Methods

3.3.1 Field mapping of channel heads

Field mapping of channel heads was carried out in the Feather River, California in June 2012. A channel head was defined as 'the upslope limit of erosion and concentration of flow within steepened banks', following Montgomery and Dietrich [1989]. I determined this upslope limit using features such as sediment sorting, alignment of pine needles, bedrock polishing, and the overall valley shape. Channel heads were then mapped using a Garmin GPS 60 with an average spatial accuracy of 6 m. The particular characteristics of each channel head were noted, and photographs were taken upstream and downstream of the location. Positions of the upstream limit of concentration of flow were taken and dominant valley features were mapped, including evidence of fluvial bedrock incision, or lack of evidence of fluvial action. In cases where upstream access was restricted due

to dense vegetation cover, the furthest accessible point of fluvial activity was mapped. Figure 3.2 shows annotated field photographs of the features mapped as channel heads in this site. Many of the mapped channel heads were initiated by tree throw or were downstream of colluvial hollows. A total of 15 channel heads were mapped in this area along with 7 locations of clear bedrock incision, 6 locations of valleys with no evidence of fluvial activity, and 4 valleys with restricted access due to vegetation.

Mapped channel head data were also collected at two sites in Wayne National Forest, Ohio, in May-June 2011. Channel heads were mapped using a Trimble GeoXM GeoExplorer 2008 series GPS with 6 m accuracy, with the same criteria as at the Feather River site. A total of 53 channel heads were mapped in the Mid Bailey Run catchment and 36 channel heads in the Indian Creek catchment.

The third set of channel head data was made publicly available by Julian *et al.* [2012] from the Piedmont region. Their study focused on channel head mapping in forested watersheds, using Google Earth to ensure complete forest cover. Channel heads were mapped using a WAAS-enabled Garmin GPSmap 60CSx. Their identification was based on the definition of Dietrich and Dunne [1993], where channel heads were classified as the furthest upslope location of bed load sorting within definable banks. A total of 63 channel heads were mapped in the Piedmont physiographic province.

3.3.2 Processing of DEMs and field data

Bare-earth DEMs with 1 m resolution were obtained from the National Science Foundation OpenTopography project for the Feather River catchment (California). Bare-earth DEMs were obtained for Indian Creek and Mid Bailey Run (Ohio) from the OSIP program [DEMs are available online

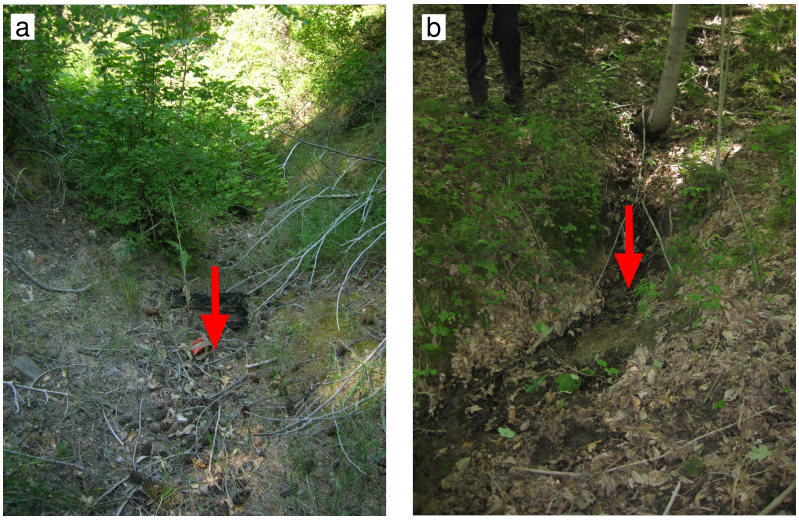

Figure 3.2: Field photographs of channel heads mapped in the Feather River, CA, and Wayne National Forest, OH. Red arrow indicates the position of the channel head. (a) Channel head mapped in Bald Rock Basin, CA; channel width is approximately 1 m. (b) Channel head mapped in Mid Bailey Run, OH; channel width is approximately 80 cm.

at http://ogrip.oit.ohio.gov/ProjectsInitiatives/OSIPDataDownloads.aspx]. A bare-earth DEM with a resolution of 2.5 feet for the Piedmont region was obtained from the Center for Geospatial Analysis at the College of William and Mary [available online at http://www.wm.edu/as/cga/About/index.php]. This was converted to UTM Zone 18°N with a resolution of 1 m using cubic interpolation. The DEMs were filled using the filling algorithm of Wang and Liu [2006]. Flow routing was then performed using the D infinity algorithm [Tarboton, 1997]. The field mapped channel heads were then plotted on the DEM of each site. The varying accuracy of the GPS measurements occasionally caused these channel heads to be located in areas of divergent topography. Therefore, each of the points was manually pinned to the nearest DEM-derived flow accumulation line, guided by field notes and slope maps to constrain the process. This resulted in the movement of channel head locations on average by 8.49 m in the Feather River, 2.10 m in Mid Bailey Run, 0.97 m in Indian Creek, and 3.11 m

in the Piedmont region. A possible reason for the discrepancy is the dense forest cover reducing GPS accuracy, which is a common cause of differences between field-located channel heads and their corresponding GPS coordinates [Jefferson and McGee, 2013].

3.3.3 Geometric techniques of identifying channel heads

I tested two geometric techniques for identifying channel heads: the method of Passalacqua *et al.* [2010a] and that of Pelletier [2013].

GeoNet

The first method of locating channel heads that was evaluated in this study is GeoNet (version 2.0), which is software based on algorithms developed by Passalacqua *et al.* [2010a]. GeoNet filters the DEM based on anisotropic nonlinear diffusion using a Perona-Malik filter. This filter uses the diffusion equation:

$$\partial_t z(x, y, t) = \bigtriangledown.[p(|\bigtriangledown z|) \bigtriangledown z], \tag{3.1}$$

where $z(x, y, t)$ represents the elevation at the location (x, y) and at time t, $\bigtriangledown z$ is the gradient, and $p(\bigtriangledown z)$ represents the edge-stopping function, which prevents diffusion across channel boundaries [Passalacqua *et al.*, 2010a]. Nonlinear filtering allows the smoothing of high-frequency, low-relief noise while enhancing the hillslope-to-valley transition.

Passalacqua *et al.* [2010a] define a channel head as occurring when an erosion threshold has been crossed after which fluvial incision takes place, and their method therefore extracts the channel network rather than the valley network.

The channel heads are predicted using a tangential-curvature threshold, illustrated in Figure 3.3a. However, the drainage network resulting from the use of a curvature threshold often results in a series of disconnected segments. In order to improve the drainage network, the algorithm defines the network by minimising a cost function which is inversely proportional to threshold curvature and contributing drainage area [Passalacqua *et al.*, 2010a]. The GeoNet algorithm therefore requires the input of three user-defined parameters: (i) time of forward diffusion; (ii) a contributing area threshold; and (iii) a search box for automatic identification of channel end points (or search box size). In this study, the default parameters were used for each of the field sites analysed. Selection of the appropriate curvature threshold or contributing area threshold parameters requires a priori knowledge of the channel head positions, which undermines the programs ability to predict the locations. Therefore, the same parameters were used for each field site in order to test the success of the algorithm at predicting channel head locations across a variety of different landscapes. GeoNet was run for each of the field sites, creating a map of the predicted channel head locations and resulting drainage network.

Pelletier method

The second method evaluated for channel head prediction in this study is based on mapping of the landscape tangential curvature, followed by the use of a threshold tangential curvature value, proposed by Pelletier [2013] and illustrated in Figure 3.3a. This method requires the input of two user defined parameters, rather than the three parameters used by the GeoNet algorithm. There are three main steps involved in identifying the channel heads from this method, followed by three additional steps to extract the full channel network. As this study focuses on channel head identification, the three principal steps will be described here, but the full method is described in detail by Pelletier [2013]. The first step uses an

optimal Wiener filter (OWF) [Wiener, 1949; Press, 2007] to remove high frequency microtopographic noise by distinguishing the signal of the large scale hillslope-valley morphology and amplifying this signal relative to the noise. The filter uses the transfer function:

$$\Phi(v) = \frac{|H(v)^2|}{|H(v)^2| + |N(v)^2|}, \tag{3.2}$$

where $|H(v)^2|$ represents the power-law radially averaged spectrum which characterises the large scale valley morphology, and $|N(v)^2|$ represents a flat power spectrum with equal power at all frequencies, characterising the white noise component. At low frequencies, where $|H(v)^2|$ is much greater than $|N(v)^2|$, equation 3.2 approaches unity and the input data are not modified. At high frequencies, where $|N(v)^2|$ is greater than $|H(v)^2|$, the amplitude of the noise is reduced according to the ratio of the noise to the amplitude of the signal. Filtering with an OWF therefore differs from diffusion filtering, in that it does not require any user input as to how much filtering should be performed: the filter weights are instead calculated from the structure of the power spectrum [Press, 2007]. After smoothing the landscape with the OWF, the tangential curvature is mapped: pixels with positive curvature are identified as part of the channel network; while pixels with negative curvature are identified as hillslopes. The tangential curvature (k_t) is calculated using the following equation, defined by Mitášová and Hofierka [1993]:

$$k_t = \frac{z_{xx}z_y^2 - 2z_{xy}z_xz_y + z_{yy}z_x^2}{(z_x^2 + z_y^2)\sqrt{1 + z_x^2 + z_y^2}}, \tag{3.3}$$

where $z(x, y)$ represents the elevation, and the subscripts represent derivatives. The final step involves identifying each pixel with a k value higher than that of a user-defined threshold tangential curvature value, k_{th}. The valley network

may be identified by the transition from negative to positive curvature. Hillslope segments close to the channel network often have positive curvature associated with overland flow, and therefore a low positive threshold value for tangential curvature is more appropriate for determining the start of true channelisation [Pelletier, 2013]. Pelletier [2013] tested this algorithm on synthetic valley networks in which the position of the drainage network is known, as well as on two field sites, and suggested that a k_{th} value of 0.1 m^{-1} produces accurate results for a variety of landscapes. Therefore, this suggested value of k_{th} was used to extract the channel head positions from each of the field sites and compared with the field mapped data.

3.3.4 Process-based techniques of identifying channel heads

I also tested two process-based techniques: slope-area scaling and the DrEICH method which was developed for this study.

Slope-area scaling relationships

Identifying scaling breaks in slope-area plots has traditionally been used to identify channel head locations [Montgomery and Dietrich, 1988]. Many different relationships have been proposed that define a threshold slope and area at which channel initiation occurs [e.g. Montgomery and Dietrich, 1992; Istanbulluoglu *et al.*, 2002]. Jefferson and McGee [2013] suggest that this relationship takes the general form of:

$$c = A^{\mu} S^{\beta}, \tag{3.4}$$

where c represents the threshold value (depending on climate, lithology, vegetation, land use and soil type), A represents the upslope contributing area (generally in m^2) and S represents the local slope (typically in m/m). The area exponent μ is often assumed to be 1, which allows the normalisation of the slope exponent to $\frac{1}{\mu}$, referred to as the relative exponent [Jefferson and McGee, 2013]. This threshold can be identified using slope-area plots, as the different process regimes occurring above and below the threshold result in different relationships between slope and drainage area. Figure 3.3b illustrates the slope-area plot method of identifying channel heads. Where fluvial processes are dominant (below the channel head) slope can be expressed as a power law function of drainage area such that:

$$S = k_{sn} A^{-\theta}, \tag{3.5}$$

where S is the local slope (m/m), k_{sn} is the channel steepness index, A is the upslope drainage area (m^2), and θ is the concavity index [Flint, 1974].

Where hillslope processes are dominant, gradient increases with drainage area, giving rise to a boomerang shape in the slope-area plot [e.g. Roering *et al.*, 2007]. In steep landscapes, however, debris-flow processes may cause a plateau at the transition between hillslope and fluvial processes [Stock and Dietrich, 2006]. This may lead to difficulty in identifying the transition in landscapes with high erosion rates. In order to test whether this method was successful in predicting channel head locations for the study areas, slope-area plots were constructed for each field site. The slope was calculated based on a polynomial fit with a circular window with a radius of 7 m, and the contributing area calculated using the D-infinity flow routing algorithm [Tarboton, 1997]. A window radius of 7 metres was chosen to minimise microtopographic noise influencing local slope on a metre to sub-metre scale [Roering *et al.*, 2007; Hurst *et al.*, 2012].

Slope and area data for each pixel were sorted into logarithmically-spaced bins with a width of 0.1 in log-space, and the standard deviation and standard error of each bin were computed. Graphs of the binned slope-area data were then constructed for each field site to compare the position of the scaling break to the slope and contributing area of the mapped channel heads. Furthermore, the relationship between slope and drainage area between the mapped channel heads was also determined to extract a threshold value (equation 3.4). A first set of threshold values were extracted from the mapped channel heads by averaging the contributing area of the mapped channel heads for each field site (setting μ as 1 and β as 0 in equation 3.4, referred to as a threshold value of A). Other analysts have suggested that a threshold based on both slope and contributing area for channel identification may be calculated by setting μ as 1 and β as 2 in equation 3.4 [Orlandini *et al.*, 2011], referred to as a threshold value of AS^2. These threshold values were then used to predict the channel head locations across the landscape.

DrEICH method

The last method of predicting channel head locations is a new algorithm presented in this study based on transformation of river long profiles. This algorithm has two principal stages: first, the basins in which the channel heads are to be identified are selected based on the tangential curvature (the geometry of the valley); and second, the exact position of the channel heads within these basins is calculated using the longitudinal profiles of the channels and hillslopes (a process-based method). Chi transformations involve integrating drainage area along a channel. The method, first proposed by Royden *et al.* [2000], allows comparison of the steepness of channels, normalised for drainage area, and suffers less from errors and uncertainties in topographic data than slope-area analysis [Perron and Royden, 2013]. The transformed coordinate, χ (or chi), can be calculated from

any topographic dataset, but is best understood in the context of the stream power equation [e.g. Howard, 1994], the predictions of which are broadly consistent with observed channel geometries [e.g. Kirby and Whipple, 2012]. The stream power equation is a detachment-limited model that proposes that the fluvial incision rate is proportional to stream power, which represents the energy expenditure of the flow [Sklar and Dietrich, 1998]. It does not describe overland flow in valley bottoms, or sediment transport on hillslopes by processes such as rainsplash and soil creep. The steady-state stream power equation results in the following expression for channel slope:

$$\frac{dz}{dx} = \left(\frac{U}{K}\right)^{\frac{1}{n}} A(x)^{-\frac{m}{n}}, \tag{3.6}$$

where z represents elevation [L], x is the horizontal upstream distance [L], U is rock uplift rate relative to a reference elevation value [L T^{-1}], K is an erodibility coefficient, A is drainage area [L^2], and m and n are constants. Integrating equation 3.6 leads to the following equation for a river profile, if spatially constant uplift rates and erodibility are assumed:

$$z(x) = z(x_b) + \left(\frac{U}{K}\right)^{\frac{1}{n}} \int_{x_b}^{x} \frac{dx}{A(x)^{\frac{m}{n}}}, \tag{3.7}$$

where the integration is performed in the upstream direction from the base level x_b to the observation point x [Perron and Royden, 2013]. It is performed in the upstream direction to allow integration through tributary junctions, as the tributaries will have the same elevation as the main stem at their confluence. A reference drainage area (A_0) is then introduced in order to create profiles with units of length on both axes, leading to:

$$z(x) = z(x_b) + \left(\frac{U}{K {A_0}^m} \right)^{\frac{1}{n}} \chi, \tag{3.8}$$

where the longitudinal coordinate, χ, is given by:

$$\chi = \int_{x_b}^{x} \left(\frac{A_0}{A(x)} \right)^{m/n} dx. \tag{3.9}$$

Perron and Royden [2013] plot equation 3.8 as a line, where the independent variable is χ and the dependent variable is z, both with units of distance. The gradient of the line is represented by $(U/K)^{1/n}/A_0^{m/n}$ and the y-intercept by $z(x_b)$. A river profile represented by a plot of z against χ is referred to as a chi-plot [Perron and Royden, 2013]. The ratio m/n can be constrained using this method by performing statistical tests to determine the ratio that best linearises profile data [Perron and Royden, 2013; Mudd *et al.*, 2014].

In this study, chi-plots are used to predict the channel head locations with an algorithm that assumes that the chi-plot is composed of two different segments: a channel segment and a hillslope segment. The channel head is predicted to occur at the transition point between these two segments (Figure 3.3c). The relationship between z and χ is assumed to be linear in the fluvial segment, where channels conform to the stream power law. However, in the divergent hillslope segment the relationship is non-linear, due to the change in process regime.

Before the DrEICH algorithm can be used, the best fit m/n value must be obtained for the field site in question, as shown by equation 3.9. This value is found using routines presented in Mudd *et al.* [2014]. These routines loop through the potential m/n values and perform a linear regression on the chi profile for each value. For each regression, the Akaike information criterion (AIC) is calculated

[Akaike, 1974], which is a measure of how well the data fits the linear regression, while penalising overfitting. The best fit m/n is assumed to be the value with the lowest AIC value.

In order to locate basins for channel head identification, I identify concave portions of the landscape based on a methodology for drainage network extraction created by Peucker and Douglas [1975] and described by Band [1986]. Valleys are identified if the stretch of landscape is at least 10 m long and has a tangential curvature of at least 0.1 m^{-1}, which is the same threshold value used by Pelletier [2013]. I use this tangential curvature threshold value to distinguish between the stream network and threshold hillslopes, as the latter may have a small positive curvature associated with overland flow [Pelletier, 2013; Furbish and Roering, 2013]. The chi segment fitting algorithm is then run from each of the first-order valley outlets identified by the tangential curvature to the hilltop. Following identification of suitable basins, the valley outlet to hilltop profile is transformed into χ-elevation space. The algorithm then loops through the possible combinations of channel and hillslope segment lengths and performs a linear regression on each segment. This allows the calculation of both the R^2 value for the linear regression and the Durbin-Watson statistic. The Durbin-Watson statistic (d) is a test for autocorrelation between residuals from the regression analysis [Durbin and Watson, 1950]. The value of d always lies between 0 and 4; if d is greater than 2 there is statistical evidence that the residuals correspond to a linear fit; if d is less than 2 then the data are non-linear. Within the chi-plot, the channel segment should be linear, and thus have a high value of R^2, whereas the hillslope segment should be non-linear, and therefore have a low value of d. For each combination of segment lengths, a test value η was calculated using these two statistics such that:

$$\eta = R_c^2 - \frac{d_h - 2}{2}, \tag{3.10}$$

where R_c^2 is the R^2 value of the channel segment, and d_h is the Durbin-Watson statistic of the hillslope segment. If d_h is low, then $(d_h - 2)/2$ will be negative. If d_h is greater or equal to 2, then $(d_h - 2)/2$ will be positive. The second term allows comparison across the two different statistics: R^2, which varies between 0 and 1; and d which values between 0 and 4. The maximum value of η will occur with a highly linear channel segment and a non-linear hillslope segment, with η varying between 2 and -1. This defines the predicted position of the channel head, from which flow routing generates the channel network. This method therefore provides a process-based technique for identifying the onset of fluvial incision. This channel network is distinct from the valley network, which includes all areas of topographic convergence.

3.3.5 Comparison of predictions to field data

For each of the four different methods tested in this study (two geometric techniques and two process-based techniques) the predicted channel heads were compared to the field-mapped locations, with the horizontal distance between the predicted and mapped locations noted for each channel head. The mean distance and standard deviation were also calculated for each of the field sites.

I also assessed the ability of the four methods to accurately predict the number of channel heads in a landscape. Three analyses of the quality of each of the methods were carried out in order to test the number of extracted channel heads. These analyses require every channel head in the basin to be mapped and were performed on 3 basins in Indian Creek, 8 basins in Mid Bailey Run, and 3 basins in the Piedmont. Difficulty with the terrain and dense thickets of *Toxicodendron diversilobum* (common name: poison oak) and other woody shrubs in the Feather River meant it was not possible to map every channel head in the catchment. Predictions of channel head locations can be divided into three classes: true

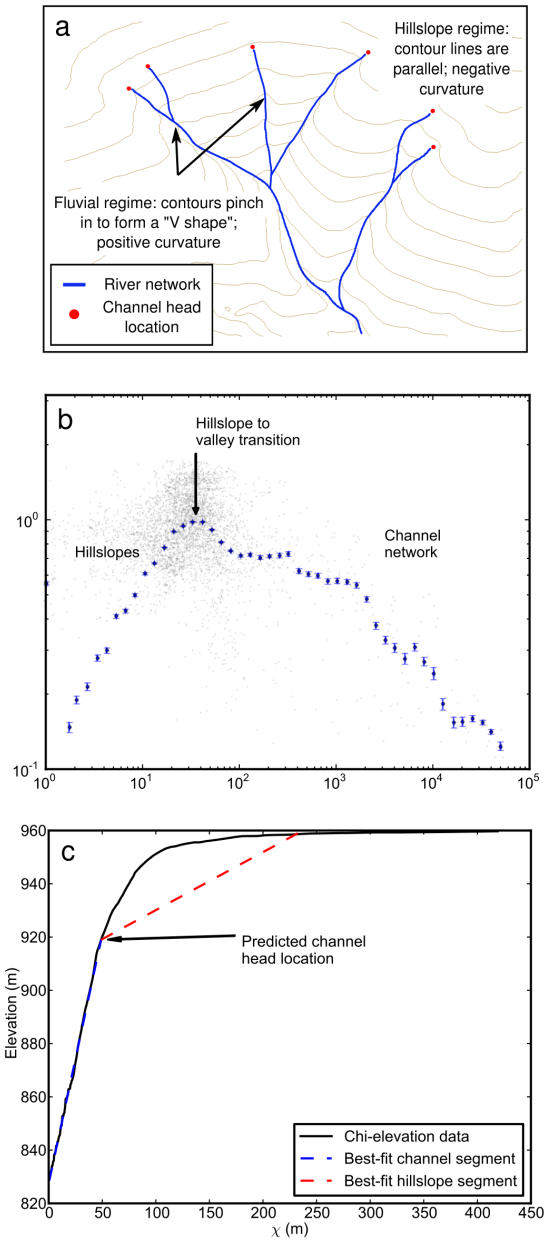

Figure 3.3: Schematic diagrams of each method showing how they predict channel heads. (a) Both GeoNet and the Pelletier method predict channel heads based on tangential curvature, where contour lines form a 'V shape' directly below the channel head. (b) The slope-area plot method identifies the transition from fluvial to hillslope scaling forming a 'boomerang' shape. The data cloud first must be binned logarithmically (blue). (c) The DrEICH method identifies channel heads based on the transition point between a best-fit linear channel segment (blue) and a non-linear hillslope segment (red).

positives (TP), false positives (FP), and false negatives (FN) [Orlandini *et al.*, 2011]. TPs are defined as occurring when a predicted channel head is found in the same first order basin as a mapped channel head. FPs occur when a predicted channel head is located in a first order basin with no mapped channel head. FNs occur when a channel head is not predicted in a first order basin where there is a mapped channel head. In order to quantify the ability of a method to accurately predict channel head locations, the reliability and sensitivity indices of Orlandini *et al.* [2011] were used. The reliability of a method can be defined as:

$$r = \frac{\sum TP}{\sum TP + \sum FP}, \tag{3.11}$$

where $\sum TP$ and $\sum FP$ are the total numbers of true and false positives [Orlandini *et al.*, 2011]. This measures the methods capacity not to generate FPs. The sensitivity of a method can be defined as:

$$s = \frac{\sum TP}{\sum TP + \sum FN}, \tag{3.12}$$

where $\sum TP$ and $\sum FN$ are the total numbers of true positives and false negatives. This measures the methods ability not to generate FNs, or to predict all mapped channel heads [Orlandini *et al.*, 2011].

A third analysis was also performed by calculating the drainage density of each basin from the observed channel heads, and comparing this with the drainage density predicted from each of the methods. The drainage density can be defined as the total length of channels within the basin divided by the basin area, and is an essential parameter for hydrologic modelling. A FP located at the downstream end of the first order basin will have less impact on the drainage density than a

FP at the upstream end of the basin. The percentage error between the mapped and predicted drainage densities for each catchment (ϵ_{D_d}) was calculated by:

$$\epsilon_{D_d} = \left(\frac{D_{dm} - D_{dp}}{D_{dm}} \right) 100, \tag{3.13}$$

where D_{dm} represents the mapped drainage density and D_{dp} represents the predicted drainage density. The mean ϵ_{D_d} for each field site was then computed.

3.3.6 Sensitivity analysis

All of the channel network extraction methods tested here require user-defined parameters, the value of which may influence the position of the resulting channel heads. A robust method which is applicable across a range of different landscapes should ideally have as few user-defined parameters as possible. Furthermore, the sensitivity of the results to these parameters is an important factor that must be considered. In order to test the sensitivity of the methods to the parameters chosen, I varied the main parameters for the GeoNet algorithm, the tangential curvature mapping and the chi analysis for the Indian Creek field site in Ohio. Although GeoNet has three user-defined parameters, the main parameter that influences the position of the channel heads in the GeoNet algorithm is the contributing area parameter. The default value in the program is set to 3000 m^2. Additional runs were performed with a contributing area value of both 1000 m^2 and 5000 m^2 to test the effect on the channel head locations. The tangential curvature mapping algorithm proposed by Pelletier [2013] uses only 2 user-defined parameters, the most influential of which I hypothesised to be the tangential curvature threshold k_{th}, which determines the pixels selected as channel heads before flow routing. The second user-defined parameter of the Pelletier [2013] method is the discharge per pixel used to connect discontinuous valley segments.

Pelletier [2013] suggests that a value of $k_{th} = 0.1$ m^{-1} is appropriate across a variety of landscapes, whereas other workers have suggested using a multiple of the standard deviation of contour curvature (σ) as the threshold value, as this can be extracted directly from the DEM [Tarolli and Dalla Fontana, 2009]. Therefore additional runs were performed using a threshold value of 2σ and 3σ to determine the effect on channel head locations.

The chi analysis methodology proposed in this study requires two user-defined parameters: the m/n value, which can be estimated statistically using independent routines created by Mudd *et al.* [2014] and the number of linked pixels used for valley identification. These user-defined parameters can be determined directly from the DEM alone and do not need to be calculated based on observed channel head locations. Whipple and Tucker [1999] suggest that for most channels, m/n falls within a range of 0.35 and 0.6, although values of up to 0.79 have been reported [Anthony and Granger, 2007]. In order to test the sensitivity of the algorithm, the m/n value was altered from 0.525 (the value suggested by the statistical test) to 0.425 and 0.625. The number of linked pixels required before a valley is identified may also impact the results of the channel head identification: if this value is too small, the resulting channel network will be feathered; whereas if this value is too large, first order tributaries may be missed by the algorithm. Therefore a sensitivity analysis was performed by varying the number of linked pixels used as a threshold value between 5 and 25 pixels.

3.4 Results

3.4.1 Geometric techniques

Figure 3.4a shows channel head locations calculated using the GeoNet algorithm. The mean and standard deviation of the horizontal distance between measured and predicted channel heads was calculated for each field site to assess the accuracy of channel head predictions (Figure 3.5). In some cases, GeoNet did not identify a valley in which a channel head had been mapped. This occurred in 22 tributaries out of the 53 with mapped channel heads in Mid Bailey Run, and in 14 out of 36 in Indian Creek. No tributaries with mapped channel heads were missed in the Feather River or Piedmont field sites. In general, the GeoNet algorithm predicted the channel head location well in Mid Bailey Run and Indian Creek (with a mean distance between mapped and predicted channel heads of 22 m and 18 m respectively), but was less accurate in the Feather River (-31 m) and the Piedmont region (-129 m). The predicted channel heads were mainly downstream of the mapped positions in the two Ohio field sites, upstream of the mapped positions in the Piedmont, and varied in the Feather River. Channel head locations from the Pelletier method were predicted using a threshold tangential curvature value of 0.1 m^{-1}, as described in Section 3.3.3. Figure 3.4b shows the drainage network created with the Pelletier algorithm, along with its relationship to the mapped channel heads. In general, the Pelletier method was extremely successful in predicting the channel head locations. The mean distance between the mapped and predicted channel heads was -11 m in the Feather River, -7 m in Mid Bailey Run, 5 m in Indian Creek, and -24 m in the Piedmont. The predicted channel heads were located upstream of the mapped channel heads at every field site, with the exception of Indian Creek (Figure 3.5). Channel heads could not always be mapped using the Pelletier method if they were located in valleys which did not exceed the curvature threshold. This occurred in 6 tributaries out of the

53 with mapped channel heads in Mid Bailey Run, 5 out of 36 in Indian Creek, and 3 out of 63 in the Piedmont. No tributaries with mapped channel heads were missed in the Feather River.

3.4.2 Process-based techniques

Slope-area plots at the field sites indicate that slope-area scaling relationships are generally a poor predictor of the location of the mapped channel heads (Figure 3.6). For the Cascade Ridge, Mid Bailey Run and Indian Creek field sites, channel heads are located at a lower drainage area than the point of transition into fluvial scaling where slope decreases with increasing drainage area (Figure 3.3b). In Bald Rock Basin the channel heads have a much lower gradient than the mean for the binned data, and in the Piedmont region the channel heads occur within the fluvial scaling regime.

Figure 3.7 shows the average contributing area and gradient of the channel heads at each location. For each of the field sites, a power law regression was performed on the contributing area and gradient of the channel heads. The R^2 values of these regressions were 0.0009 for the Feather River, 0.0391 for Mid Bailey Run, 0.1342 for Indian Creek, and 0.1196 for Virginia. Contrary to other studies [Montgomery and Dietrich, 1992; Istanbulluoglu *et al.*, 2002; Jefferson and McGee, 2013], which state that there is a threshold for channel head initiation (based on equation 3.4), I find no statistically significant relationship between the slope and drainage area of the mapped channel heads, implying that a slope-area threshold is not effective in identifying channel head locations. Threshold values of A and AS^2 were also tested to determine their success at predicting channel head locations across the field sites. The average thresholds for these two methods respectively for the field sites were: 12262 m^2 and 1805 m^2 for the Feather River; 413 m^2 and 278 m^2 for Mid Bailey Run; 1035 m^2 and 640 m^2 for Indian Creek; and 20816 m^2 and

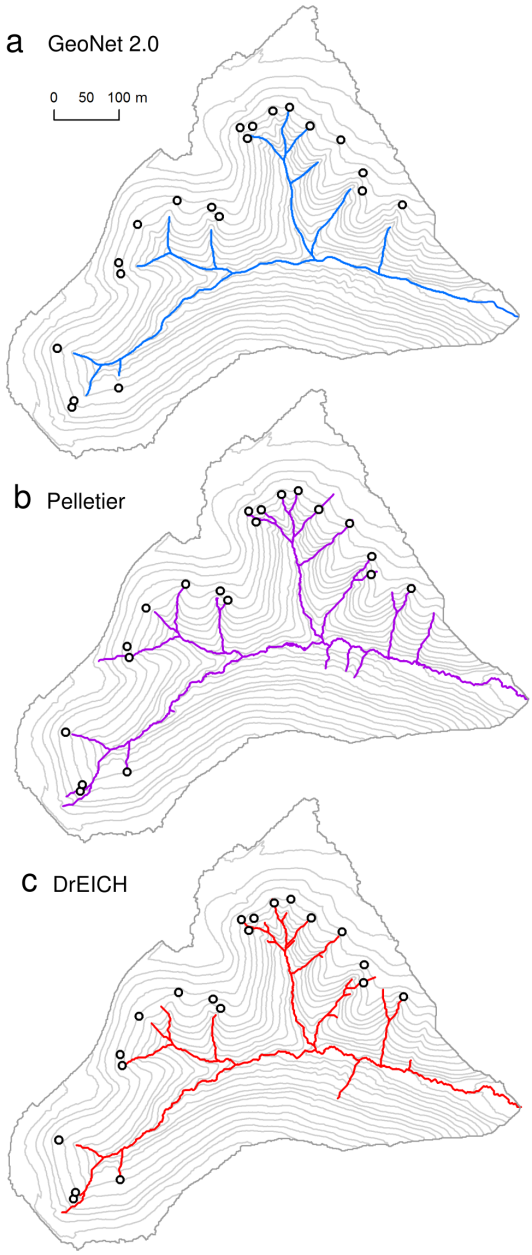

Figure 3.4: Contour maps showing the results of each method for a catchment in Indian Creek, OH. The circles indicate the field mapped channel heads and the contour intervals are 10 m. (a) Stream network resulting from GeoNet shown in blue. (b) Stream network resulting from Pelletier method shown in purple. (c) Stream network resulting from DrEICH method shown in red.

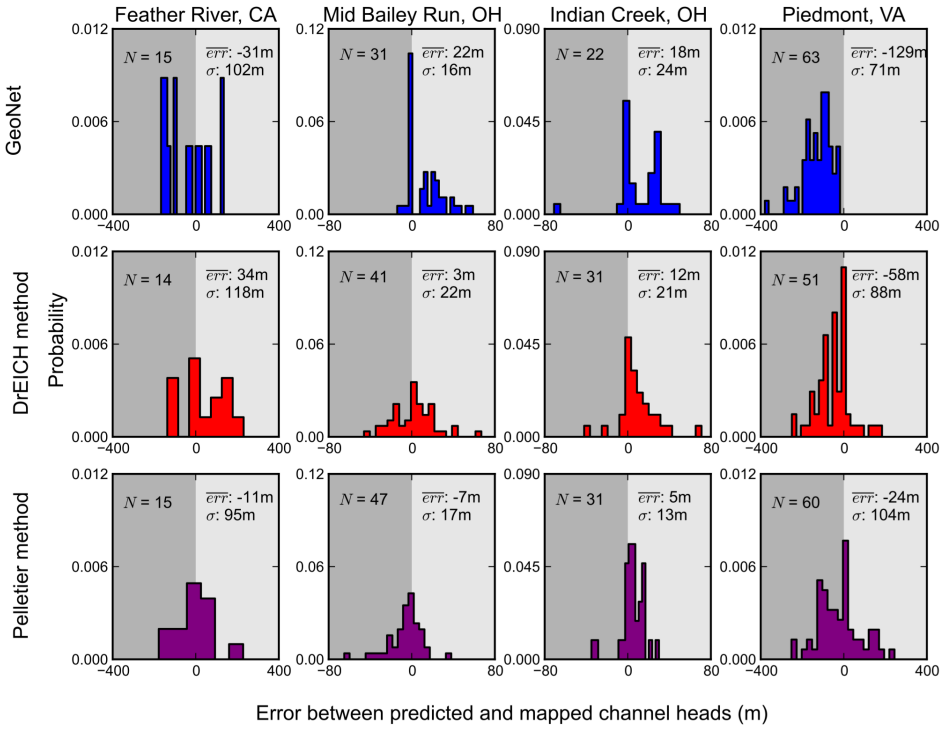

Figure 3.5: Histograms showing the distance and direction of error between the mapped and predicted channel heads for each field site and method. The GeoNet method is shown in blue; the DrEICH method is shown in red; and the Pelletier method is shown in purple. The dark grey shading represents areas where the predicted channel heads were located upstream of the mapped (negative); the light grey shading represents areas where the predicted were downstream of the mapped channel heads (positive). The mean and standard deviation of the error are also shown.

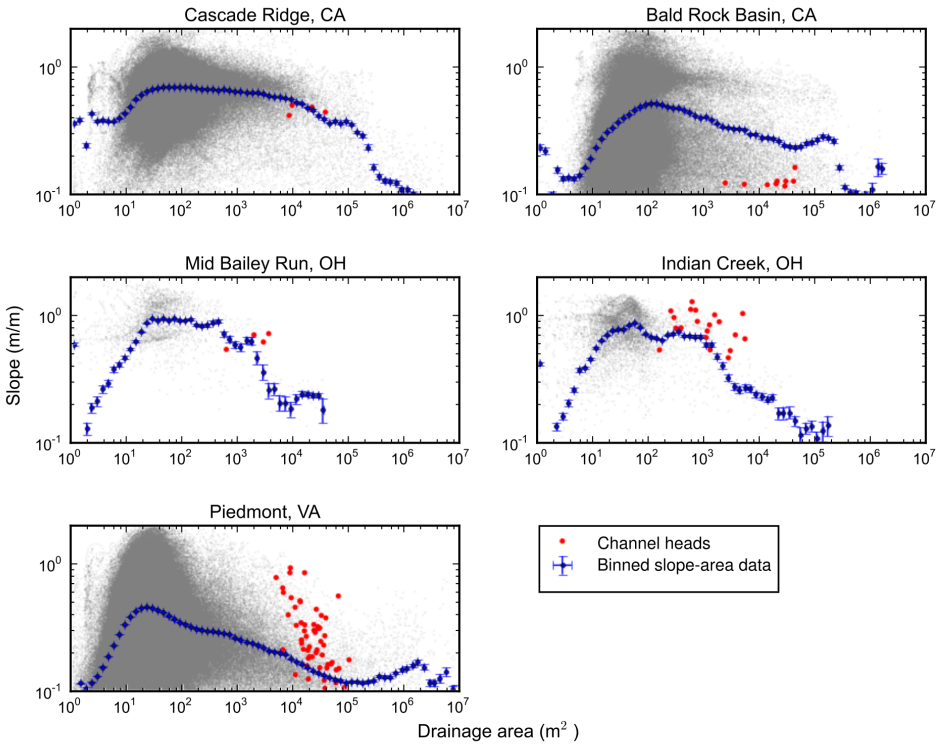

Figure 3.6: Slope-area plots for each field site. The log-binned slope-area data is shown in blue (with 95% confidence interval) with a bin width of 0.1; the data cloud with every pixel included is shown in grey, and the field mapped channel heads are shown in red. The data clouds were thinned for visualisation (every 10th pixel was selected).

1721 m^2 in Virginia. The A threshold resulted in errors between the mapped and predicted channel heads of -39 m in the Feather River, -26 m in Mid Bailey Run, -26 m in Indian Creek, and -94 m in Virginia. The AS^2 threshold resulted in errors of -51 m, -29 m, -18 m and -65 m for the same field sites.

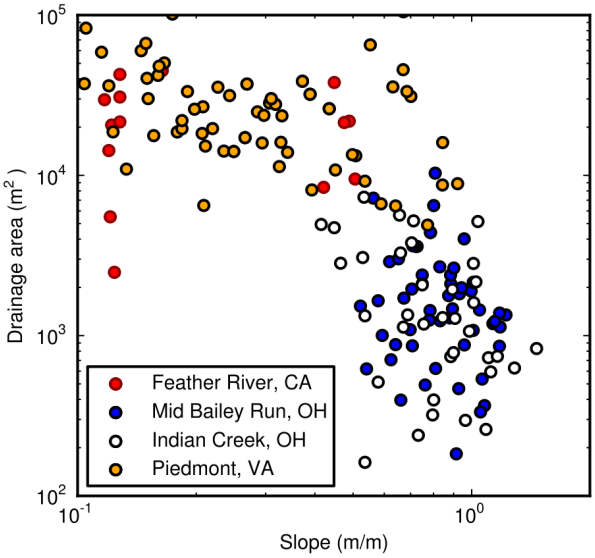

Figure 3.7: Relationship between slope and drainage area in log space for the mapped channel heads at each field site. There is no clear inverse relationship between slope and drainage area at each individual field site.

The m/n ratio for each of the field sites for use with the DrEICH method was constrained using the routines of Mudd *et al.* [2014]. This was estimated to be 0.3 for the Feather River, 0.525 for each of the sites in Ohio, and 0.375 in Virginia. Figure 3.8 shows examples of chi-plots for the Indian Creek field site. The linear regressions of the fitted channel and hillslope segments were also plotted in order to identify the predicted channel head location, as well as the corresponding field-mapped channel head. Figure 3.4c shows the resulting drainage network for the Indian Creek field site. In some cases, a basin with a mapped channel head could not be analysed due to the valley extraction algorithm threshold used in this study, which only identified valleys with more than 10 linked pixels with a tangential

curvature greater than 0.1 m^{-1}. Such small valleys prevented the analysis of: 1 channel head in the Feather River, 9 out of 53 channel heads in Mid Bailey Run, 10 out of 36 in Indian Creek, and 13 out of 63 channel heads in the Piedmont region. The mean distance between mapped and predicted channel heads was 12 m in the Feather River, 3 m in Mid Bailey Run, 12 m in Indian Creek, and 58 m in the Piedmont.

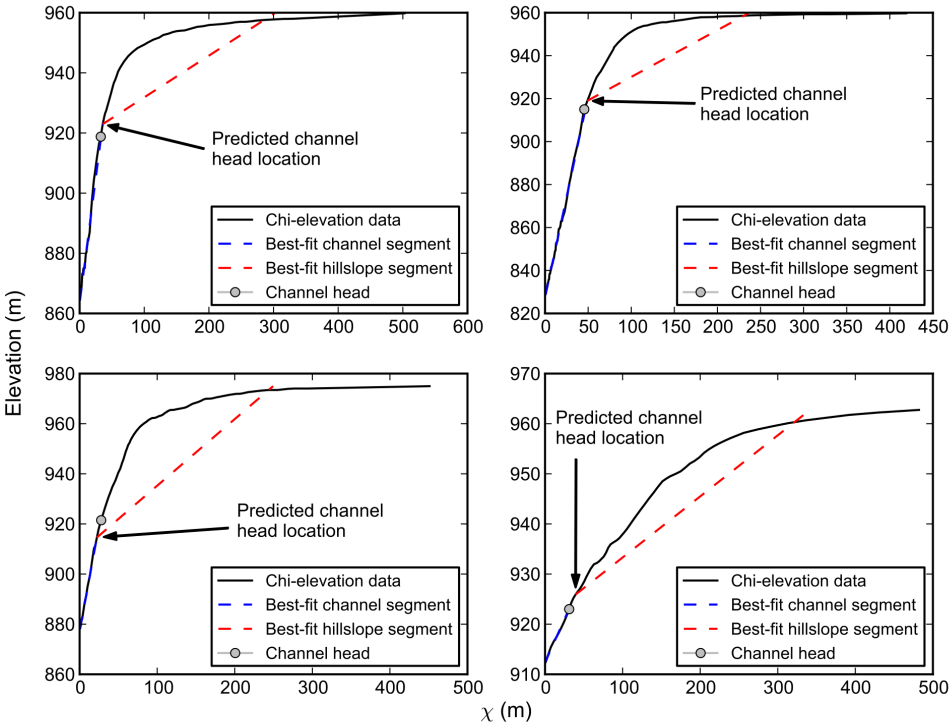

Figure 3.8: Example chi plots for basins with mapped channel heads in Indian Creek, OH. The transformed river profile is shown in black, with the location of the field-mapped channel head shown in grey. The blue line represents the best-fit channel segment and the red line represents the best-fit hillslope segment, with the transition point between them identifying the predicted location of the channel head.

A comparison of the results from the three methods (Figure 3.5), excluding the slope-area analysis, indicates that the tangential curvature method of Pelletier

[2013] and the DrEICH method were the most successful at locating the channel heads as mapped in the field. The distribution of errors was generally similar in each case, both in terms of magnitude and direction, with the Pelletier [2013] method generally producing the smallest errors across the field sites. This suggests that these two techniques identify similar features as channel heads despite completely different methodologies. In comparison, the errors associated with GeoNet were typically larger, with the exception of the Feather River site, at which the results were comparable to those of the DrEICH method.

3.4.3 Analysis of quality

Three analyses of the quality of each method were performed as described in Section 3.3.5. The reliability index describes the methods ability not to predict false positives, whereas the sensitivity index describes the methods capacity not to allow false negatives [Orlandini *et al.*, 2011]. The average error between the mapped and predicted drainage density for each of the field sites was also calculated. Negative values indicate that the predicted drainage density was greater than the mapped drainage density. The values of these indices for each of the field sites are reported in Table 3.1.

3.4.4 Sensitivity analysis

Sensitivity analyses were performed as described in Section 3.3.6. Figure 3.9 shows the results of the sensitivity analysis for the Indian Creek field site after altering the parameters for the GeoNet algorithm, the Pelletier algorithm and the DrEICH algorithm. The GeoNet algorithm is relatively sensitive to changing the contributing area threshold, with the mean error between the mapped and predicted channel heads changing from 18 $\pm$ 24 m downstream of the mapped

Table 3.1: Analysis of quality for each of the field sites [1]

Field site	GeoNet			DrEICH			Pelletier		
	r	s	ϵ_{D_d}	r	s	ϵ_{D_d}	r	s	ϵ_{D_d}
Mid Bailey Run	0.727	0.453	-204.84	0.489	0.830	-48.17	0.52	0.736	-26.05
Indian Creek	0.783	0.5	2.7	0.509	0.75	-17.38	0.531	0.722	-37.60
Piedmont	0.245	1.0	-138.67	0.306	0.756	-64.24	0.324	0.8	-47.14

[1] r is the reliability index, s is the sensitivity index, and ϵ_{D_d} is the error between the mapped and predicted drainage densities (%)

channel heads with a threshold of 3000 m^2, to 1 $\pm$ 29 m upstream with a threshold of 1000 m^2, to 39 $\pm$ 15 m downstream with a threshold of 5000 m^2. The Pelletier algorithm is less sensitive to changing parameters, although it results in a mean error change from 5 $\pm$ 13 m downstream with $k_{th} = 0.1$, to 6 $\pm$ 15 m downstream with $k_{th} = 2\sigma k_t$, and 15 $\pm$ 10 m downstream with $k_{th} = 3\sigma k_t$. The DrEICH method was found to be relatively insensitive to changing the m/n value. The mean error changes from 12 $\pm$ 21 m downstream with $m/n = 0.525$, to 11 $\pm$ 21 m downstream with $m/n = 0.425$, to 12 $\pm$ 22 m downstream with $m/n = 0.625$.

The second user-defined parameter used by the DrEICH method is the number of linked pixels used to identify first order basins (section 3.3.4). Changing this threshold value illustrated that a small threshold value (e.g. 5 m) caused the channel network to be 'feathered', where the algorithm identified channel heads in small first order basins that do not exist. However if the threshold value is too large (>20 m) then the algorithm misses some first order tributaries with mapped channel heads. Therefore a standard value of 10 m is suggested when analysing 1 m-resolution lidar with this method, to balance spurious feathering of the network with missing first order tributaries.

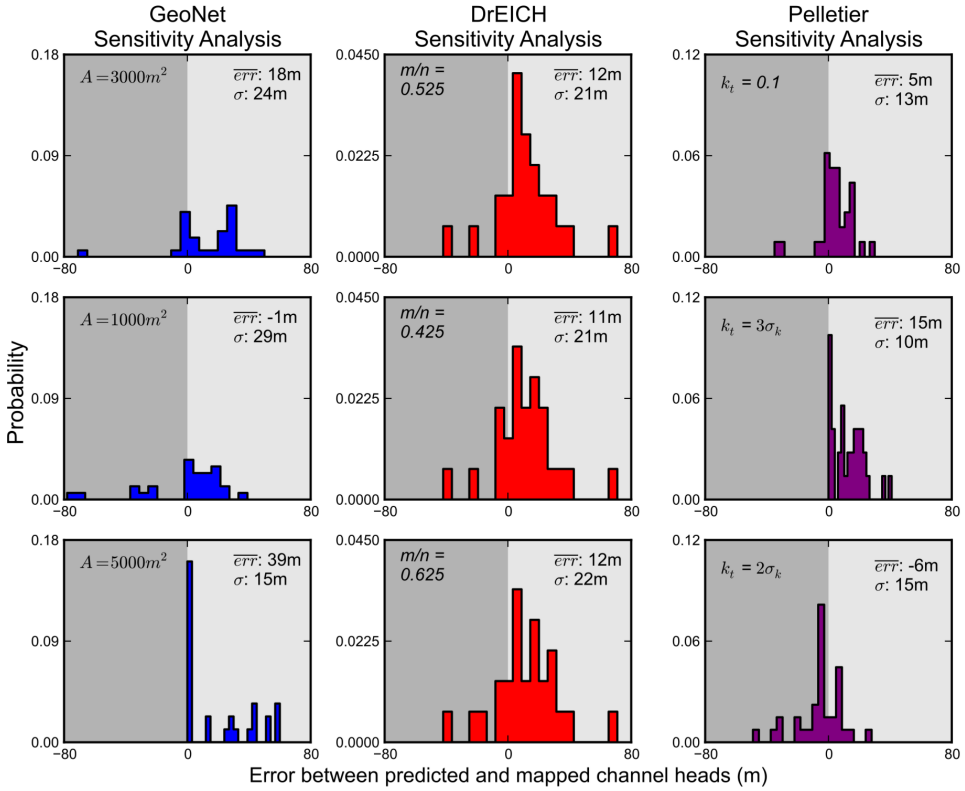

Figure 3.9: Sensitivity analysis for each of the methods at Indian Creek. Each panel shows the value of the parameter than was altered, the resulting mean distance of error between the mapped and predicted channel heads, and the standard deviation. The GeoNet method is shown in blue, where the contributing area parameter was changed from 3000 m^2 to 1000 m^2 and 5000 m^2. The DrEICH method is shown in red, where the m/n value was changed from 0.525 to 0.425 and 0.625. The Pelletier method is shown in purple, where the threshold curvature was changed from 0.1 m^{-1} to multiples of the standard deviation of the curvature.

3.5 Discussion

3.5.1 Field mapping of channel heads

Testing methods of drainage network extraction from high-resolution topographic data requires mapping of channel heads in the field, however, the exact location of a channel head in the field may be difficult to determine, and may result in subjectivity between different workers. A channel head may be defined morphologically as 'the upslope limit of erosion and concentration of flow within steepened banks'[Montgomery and Dietrich, 1989], but the point at which concentration of flow begins within a channel in the field may be unclear, and more importantly may be inherently transient. Channel head mapping in the Feather River was undertaken using a set of identifying criteria, as described in Section 3.3.1. However the assimilation of data from the two Ohio field sites and from the Piedmont region [Julian *et al.*, 2012] may have led to slight differences in the features being mapped as the channel head. This may be the cause of some error surrounding the channel head locations, and is a recurring problem in mapping of channel heads.

Furthermore, the position of the upstream limit of overland flow will vary temporally depending on many factors [e.g. Dietrich *et al.*, 1993]. Differences in the precipitation volume and intensity (storm frequency) can impact the position of the channel head. I expect that the channel heads would migrate further upstream in years with a high volume of rainfall, and vice versa for years with less rainfall. Changes in vegetation cover, for example due to anthropogenic land use or wildfires, will also influence the partitioning of precipitation into overland flow and thus change the position of the channel head in the field. Evidence of this was observed in the channel heads mapped at the Feather River field site. Channel heads were mapped both in a forested catchment (Cascade Ridge) and a

catchment which had recently undergone clearing due to fire (Bald Rock Basin). In general, the channel heads in the cleared catchment were located further up the valley than in the forested catchment. I suggest that the reduction of interception, driven by the reduced canopy extent in the recently burned areas, leads to greater partitioning of precipitation into overland flow, which in turn causes a transient upstream shift of the channel head, which will gradually relax as the canopy recovers.

In contrast, the topographic signatures used to extract channel heads from topographic data (i.e., the longitudinal profile of valleys and hillslopes, or the convergence of topographic contours) represent the time-integrated balance of hillslope and fluvial sediment transport. Thus the channel heads predicted from these methods reflect the transition from the hillslope domain to the fluvial domain at timescales significant to landscape evolution. While comparisons to field data should be consistent with prediction of channel heads, and repeating the analysis across multiple landscapes should increase the reliability of the results, additional confidence can be gained if different topographic signatures of channel forming processes used by the different methods are consistent in their indication of the location of channel heads.

3.5.2 Geometric techniques

At the Mid Bailey Run, Indian Creek and Feather River field sites the GeoNet algorithm was successful in predicting channel heads within 22 m, 18 m, and -31 m respectively. However, the error between the predicted and mapped channel heads was greater at the Piedmont field site (-129 m). Figure 3.5 shows differences in the direction of error between the field sites. In general, the predicted channel heads were located further downstream than the mapped channel heads in the two Ohio field sites, whereas they were further upstream in the Feather River,

and furthest upstream in the Piedmont. This difference between the field sites may be explained by the potential differences in channel head mapping between the sites, as previously discussed. For example, as the channel heads in the Piedmont are further downstream compared to the other field sites, this would suggest that channel heads were systematically mapped further downstream than in the other field sites, corresponding with the results from the slope-area plots. This may be due to the different identification criteria used in comparison with the other sites. GeoNet requires three user-defined parameters in its analysis: time of forward diffusion, a contributing area threshold, and a search box for automatic identification of channel end points. In particular, the contributing area parameter may affect the position of the predicted channel heads. As drainage density is inversely proportional to the contributing area upstream of a valley, the predicted stream network will be heavily influenced by the contributing area threshold used in the analysis [Pelletier, 2013].

Figure 3.9 shows that increasing or decreasing the contributing area threshold moved the location of the predicted channel heads further downstream or upstream respectively. However, correcting the algorithm for the appropriate value of the parameter requires knowledge of the location of the channel heads in the field. Therefore, this leads to a problem if the drainage network is extracted purely from topographic data with no field information. The quality analysis of the GeoNet software showed that this algorithm had a high reliability and lower sensitivity in the two Ohio field sites, suggesting that in these sites few false positives were identified, but many false negatives. This was the opposite in the Piedmont field site, where many false positives were identified but few false negatives. This suggests that the quality of this method varies significantly with field site and would need to be carefully considered when using the GeoNet algorithm to extract drainage networks. The drainage density analysis suggested that the GeoNet algorithm over-predicted the drainage density significantly in the Mid

Bailey Run and Piedmont field sites and under-predicted drainage density slightly in Indian Creek. This is important to take into account when considering flow routing, as a large difference between mapped and predicted drainage densities suggests the predicted channel network may differ significantly from the observed.

The distance of error between the mapped and predicted channel heads when using the Pelletier algorithm was less than 25 m for each of the field sites (Figure 3.5). The predicted channel heads are generally upstream of the mapped channel heads at each field site, with the exception of Indian Creek, where the predicted channel heads are similar to those identified by the GeoNet method. This suggests that this algorithm identifies similar geometric features across the field sites. The quality analysis of the Pelletier algorithm suggested that this method has a higher sensitivity than reliability across the field sites (Table 4.4), predicting more false positives than false negatives. The drainage density quality analysis shows this method over-predicts drainage density in all locations but provides a more realistic representation of the drainage network than that of the GeoNet method.

One of the benefits of this algorithm is the smaller number of user-defined parameters, rather than the three required by the GeoNet software. However, the sensitivity analysis performed in this study (Figure 3.9) suggests that the algorithm is relatively sensitive to the tangential curvature threshold, k_{th}. Figure 3.9 shows that changing the threshold value to $3\sigma k_t$ increases the mean error to 15 m downstream, while changing the value to $2\sigma k_t$ alters the direction of error, with the mean error changing to 6 m upstream. The threshold value based on the standard deviation may be more objective, as it uses the geometric properties of the landscape to identify the threshold rather than using the same value for each landscape.

3.5.3 Process-based techniques

The comparison of the binned slope-area data from each field site with the slope and drainage area of the channel heads shows that there is no clear relationship between the predicted transition point on the slope-area curve and the channel heads (Figure 3.6). Furthermore, there is no clear inverse relationship between the slope and drainage area of the field-mapped channel heads as would be predicted by the use of a slope-area threshold (Figure 3.7). Although these relationships have previously been observed [Montgomery and Dietrich, 1988; Tarboton *et al.*, 1992; Montgomery and Foufoula-Georgiou, 1993] these studies generally used DEMs with a resolution of 30 m or coarser. As the processes involved in channel initiation generally act on a metre to sub-metre scale, using topographic information from DEMs on this scale to predict channel heads is not reliable [e.g. Orlandini *et al.*, 2011; DiBiase *et al.*, 2012]. Furthermore, the use of slope-area scaling relationships has been shown to be successful in low-relief, soil-mantled landscapes, but in steep landscapes headwater channels are difficult to distinguish from threshold hillslopes when using slope-area plots [Montgomery and Foufoula-Georgiou, 1993]. The recent introduction of higher-resolution DEMs allows these relationships to be examined more robustly. The A threshold and AS^2 threshold analysis performed on the 1 m DEMs shows that these methods are less accurate in predicting channel head locations across the landscape than the DrEICH algorithm or the contour curvature technique of Pelletier [2013]. Furthermore, these methods require the presence of field mapped channel heads in order to extract the threshold values, unlike the other methods evaluated in this study.

Figure 3.6 shows that the channel heads are generally located in the fluvial regime on the slope-area plot, where slope is inversely proportional to drainage area. There is a wide variation of several orders of magnitude in the drainage areas of

the mapped channel heads, ranging from 1,000 m^2 to 100,000 m^2. Therefore any method using drainage area to identify channel initiation will be limited because of the uncertainty in the threshold drainage area. Furthermore, the slopes of the mapped channel heads vary between field sites, with the channel heads in Bald Rock Basin occurring at much lower slopes than the binned values or the channel heads from the other field sites. The variation in both the slope and drainage area of the mapped channel heads across the field sites may be due to different processes responsible for channel initiation. Three runoff processes have been suggested to primarily control channel head location: Hortonian or overland flow; the intersection of subsurface flow (e.g. springs) with the land surface; and mass failure [Dietrich and Dunne, 1993]. These processes will occur at different slope angles and drainage areas. This is a key limitation of the slope-area method of predicting channel head locations.

The last method evaluated for channel head prediction was the DrEICH algorithm, a new method presented in this study. It predicted the channel head locations to within on average -2 m in Indian Creek, -10 m in Mid Bailey Run, -34 m in the Feather River and -66 m in the Piedmont (Figure 3.5). All predicted channel heads were upstream of the mapped heads. The higher error in the Piedmont dataset may again be due to systematic differences in the field mapping strategy between this site and the others. In general the DrEICH method predicts the channel head locations with less error than the GeoNet method and with a similar margin of error compared to the Pelletier method. The quality analysis of the DrEICH algorithm showed that this method has a higher sensitivity index than reliability, suggesting that it is more effective at avoiding false negatives than false positives, similar to the Pelletier algorithm. The drainage density quality validation suggested that the DrEICH algorithm over-predicts drainage density across all of the field sites, similar to the Pelletier algorithm, but provides a more accurate channel network than the GeoNet method.

Identifying relationships when using slope-area plots can be extremely difficult due to the impact of low-frequency noise within the topographic data when slope is estimated [Perron and Royden, 2013]. In order to remove the topographic noise, techniques such as logarithmically binning the data (as used in this study) have to be used. However, although these techniques have been used successfully [Wobus *et al.*, 2006], they introduce bias and uncertainty into the results obtained. The transformation of river profiles into chi-space does not suffer from this noise as it does not use an estimate of channel slope [Perron and Royden, 2013]. The DrEICH algorithm is based on the steady-state stream power equation, and therefore can be used when the headwaters of the catchment are undergoing bedrock erosion (detachment-limited). It will not predict channel head locations accurately if the landscape is under transport-limited conditions. However, I would argue that in most upland landscapes where channel heads are initiated, the headwaters will be detachment-limited rather than transport-limited as bedrock incision occurs. In order to obtain a plot of chi vs. elevation for a river channel, an m/n ratio must be assigned (see equation 3.9). A statistical test to determine the most likely m/n ratio can be performed [Mudd *et al.*, 2014]; this test is independent of any field mapping of channel heads. The results, however, were found to be insensitive to variation in m/n (Figure 3.9). The second user-defined parameter in the DrEICH method is the number of linked pixels used to identify first order basins: a threshold value of 10 metres is suggested in this study.

The mean values and direction of error between the mapped and predicted channel heads is similar between the DrEICH method and the Pelletier method, despite the differences in the approaches. The DrEICH method is based on a theoretical change in process domain from a fluvial segment which obeys the stream power law, to a non-linear hillslope segment. The Pelletier method, on the other hand, uses a geometrical property of the landscape to identify where the channel heads should occur [Pelletier, 2013]. The general agreement between the

two independent methods suggests that I can be confident that these predicted locations truly represent a significant geomorphic feature. Although geometric methods of predicting channel head locations are useful, process-based methods provide a means of examining the fundamental controls on stream initiation. Furthermore, using a process-based method may allow investigation of the factors which determine the length between valley heads and channel heads, yielding insight into the long term position of process transitions, i.e. between fluvial erosion and hillslope erosion, including diffusion-like and debris flow sediment transport. Therefore, the DrEICH method provides a new, accurate, process-based method which may lead to an increased understanding of the mechanisms governing channel head formation.

3.6 Conclusions

I evaluated different methods commonly used to predict channel head locations from high resolution topographic data. Traditional process-based methods using slope-area scaling relationships or thresholds were less effective than the DrEICH method in all of the field areas. This may be due to the impact of low-frequency topographic noise obscuring the process domain transitions [Perron and Royden, 2013] or the difficulty of distinguishing steep, threshold hillslopes from fluvial channels using slope-area plots [Montgomery and Foufoula-Georgiou, 1993]. Although the GeoNet algorithm predicted channel head locations within less than 40 m for all field sites (excepting the Piedmont field site), it requires a contributing area threshold which must be specified by the user, and the value that is chosen strongly affects the location of the predicted channel heads. An alternative method developed by Pelletier [2013] uses the tangential curvature without a contributing area threshold. Although this method requires two user-defined parameters, most notably the tangential curvature threshold k_{th},

it predicted the channel head locations to within a small margin of error at each of the field sites using a standard value of 0.1 m^{-1}. Furthermore, a threshold value of a multiple of the standard deviation [Tarolli and Dalla Fontana, 2009] may provide a method of estimating this tangential curvature threshold directly from DEMs.

The new DrEICH algorithm presented in this study consistently identified the mapped channel head with a small margin of error. This technique requires two user-defined parameters: the m/n value, and the number of linked pixels for valley identification. The sensitivity analysis performed in this study shows that this method is insensitive to changing the m/n value. The number of linked pixels affects the density of the resulting stream network, and must be carefully selected in order to use this method. All techniques tested in this analysis search for a topographic signature of channel heads, and results were compared to channel heads identified in the field. Channel heads identified by human observations can be ambiguous, however, due to subtle differences in the criteria used by different operators to define channel heads, and due to temporal variability in the channel head location induced by, for example, seasonal changes in precipitation or time since last major fire or storm. Furthermore, the coordinates of mapped channel heads may be affected by the accuracy of the GPS device used during field surveying. Despite these uncertainties, the GeoNet, Pelletier [2013] and DrEICH methods all identify channel head locations that are consistent, on the order of tens of metres, with channel heads identified in the field.

I believe that process-based channel head detection methods, such as the DrEICH algorithm, can ultimately be used to examine fundamental aspects of landscape evolution, because they quantify geomorphic process transitions averaged over geomorphic timescales, defined as the time it takes geomorphic processes to reconfigure topography. A number of authors have noted that the valley network is not the same as the channel network [e.g. Dietrich *et al.*, 1993; Rinaldo *et al.*,

1995]. Separation of the extent of the valley network from the extent of the landscape that has a fluvial topographic signature could help determine the formation, stability, and temporal dynamics of the un-channelled portions of the valley network, hypothesised to be caused by climate change [e.g. Rinaldo *et al.*, 1995], chemical weathering [e.g. Mudd and Furbish, 2004] or a transition to landslide susceptibility [e.g. Dietrich *et al.*, 1986]. I show that the DrEICH algorithm can produce consistent, objective estimates of channel head locations, and thus can provide reproducible estimates of channel network extent.

Chapter 4

Geomorphometric delineation of floodplains and terraces from slope and channel relief thresholds

The work presented in this chapter has been published in Earth Surface Dynamics:

Clubb, F.J., Mudd, S.M., Milodowski, D.T., Valters, D.A., Slater, L.J., Hurst, M.D., and Limaye, A.B. (2017) Geomorphometric delineation of floodplains and terraces from objectively defined topographic thresholds, *Earth Surf. Dynam.* **5**, 369-385, doi:10.5194/esurf-5-369-2017

The software used and developed in this chapter is available at:

Clubb, F.J., Mudd, S.M., Grieve, S.W.D., Milodowski, D.T., Valters, D.A., and Hurst, M.D. (2017) LSDTerraceModel v1.0. *Zenodo*, doi:10.5281/zenodo.824205

This research was conducted in collaboration with the named co-authors, who helped to edit the final manuscript and contributed to software development. I wrote the algorithms for floodplain and terrace extraction, performed the analyses, created the figures, and wrote the manuscript.

Abstract

Floodplain and terrace features can provide information about current and past fluvial processes, including channel response to varying discharge and sediment flux; sediment storage; and the climatic or tectonic history of a catchment. Previous methods of identifying floodplain and terraces from digital elevation models (DEMs) tend to be semi-automated, requiring the input of independent datasets or manual editing by the user. In this study I present a new method of identifying floodplain and terrace features based on two thresholds: local gradient, and elevation compared to the nearest channel. These thresholds are calculated statistically from the DEM using quantile-quantile plots and do not need to be set manually for each landscape in question. I test the method against field-mapped floodplain initiation points, published flood hazard maps, and digitised terrace surfaces from seven field sites from the US and one field site from the UK. For each site, I use high-resolution DEMs derived from light detection and ranging (lidar) where available, as well as coarser resolution national datasets to test the sensitivity of the method to grid resolution. I find that the method is successful in extracting floodplain and terrace features compared to the field-mapped data from the range of landscapes and grid resolutions tested. The method is most accurate in areas where there is a contrast in slope and elevation between the feature of interest and the surrounding landscape, such as confined valley settings. My method provides a new tool for rapidly and objectively identifying floodplain

and terrace features on a landscape scale, with applications including flood risk mapping, reconstruction of landscape evolution, and quantification of sediment storage and routing.

4.1 Introduction

Identifying the location of floodplains and fluvial terrace features can provide important insights into geomorphic and hydrological processes. Understanding the controls on floodplain inundation carries increasing societal importance, as the frequency of flood events is predicted to increase with the rise in global temperatures and varying patterns of precipitation caused by climate change [Schreider *et al.*, 2000; Booij, 2005; Hartmann *et al.*, 2013]. Although there are still large uncertainties regarding the impacts of climate change on flood frequency [Booij, 2005], identifying floodplains is crucial for forecasting and planning purposes. On longer timescales, the morphology and structure of fluvial terraces can provide important information on channel response to climatic, tectonic, and base-level variations [Bull, 1991; Merritts *et al.*, 1994; Pazzaglia *et al.*, 1998]; the relative importance of lateral and vertical channel incision [Finnegan and Dietrich, 2011]; and sediment storage and dynamics [Pazzaglia, 2013; Gran *et al.*, 2013].

Attempts to identify floodplains can be classified into two broad families of methods: (i) flood risk mapping and hydrological modelling, and (ii) geometric terrain classification. Traditionally, identification of floodplains has relied upon the creation of flood hazard maps, produced through detailed hydraulic modelling studies [e.g. Noman *et al.*, 2001; Grimaldi *et al.*, 2013]. These studies tend to incorporate historical flood event information, hydrological analyses, and hydraulic flow propagation models [Degiorgis *et al.*, 2012]. These mature techniques can lead to

accurate flood inundation predictions down to the level of a single building [e.g. Horritt and Bates, 2002; Cobby *et al.*, 2003; Guzzetti *et al.*, 2005; Hunter *et al.*, 2007; Kim *et al.*, 2012]. However, these models can be computationally expensive and time-consuming to run, even in one dimension, requiring the calibration of large numbers of parameters, all with their own uncertainties [e.g. Beven, 1993; Horritt and Bates, 2002; Liu and Gupta, 2007]. This means that hydraulic simulations are usually performed at cross sections across the channel and interpolated to cover the rest of the stream network [Noman *et al.*, 2001; Dodov and Foufoula-Georgiou, 2006]. For example, floodplain mapping tools have been developed that incorporate either field-based or modelled stage-duration information at multiple cross sections along the channel, and interpolate a three-dimensional water surface between these sections [e.g Yang *et al.*, 2006; Belmont, 2011].

The introduction of high-resolution digital elevation models (DEMs) has provided the opportunity to map floodplain features much more rapidly and over larger spatial scales than previously possible [Noman *et al.*, 2001]. This had led to the development of many different methods that rely on extracting a variety of topographic indices from DEMs, such as local slope, contributing area, and curvature [Manfreda *et al.*, 2014]. One common metric used to predict floodplains is the topographic index ($\phi = ln(A/(tan\beta))$), where A is the contributing area to each cell (m^2) and β is the local slope in degrees [e.g. Kirkby, 1975; Beven and Kirkby, 1979; Beven *et al.*, 1995; Quinn *et al.*, 1995; Beven, 1997]. The contributing area term reflects the tendency of water to accumulate at certain regions of the basin, whereas the slope term represents the tendency for gravity to transport water downhill. Therefore, high values of the topographic index represent areas which are likely to saturate first, as they have a large contributing area compared to local slope [Beven, 1997]. Manfreda *et al.* [2011] suggested a modified version of the topographic index, changing the weighting on the area term by raising it to an exponent n. This modification allows the

relative importance of slope or contributing area to be changed by varying the n parameter. They proposed that floodplains can be identified as cells with a modified topographic index (ϕ_m) greater than a threshold value, τ. However, this method requires calibration of the parameters τ and n through comparing the output floodplain map with a pre-existing hazard map, and noting the occurrence of true and false positives and negatives [Manfreda *et al.*, 2011].

Another geometric method that has been developed to identify floodplains uses a series of linear binary classifiers for a number of topographic metrics [Degiorgis *et al.*, 2012]. Five different parameters are sampled from the DEM (slope, contributing area, elevation from nearest channel, distance from nearest channel, and curvature), and each cell is classified as either 1 (floodplain) or 0 (non-floodplain) depending on whether these parameters are above or below threshold values. Each of these five metrics can be considered in isolation or in pairs. The thresholds are calibrated using flood hazard maps, where the number of true and false positives and negatives are noted, similar to the approach of Manfreda *et al.* [2011]. For each parameter and threshold value the Receiver Operating Characteristics (ROC) curve [e.g. Fawcett, 2006] is calculated, which is defined by the number of true and false positives. The maximum area under the curve is determined to allow the threshold value for each parameter to be calibrated, as well as comparisons between each parameter to be found. The pair of best-performing features was identified as the distance (D) and elevation (H) from the nearest channel (m). This method is also semi-automated, as it requires the existence of flood hazard maps for at least some part of the catchment in order to select the correct binary classifiers for floodplain identification.

Dodov and Foufoula-Georgiou [2006] present an algorithm for identifying floodplains over large scales based on information on bankfull channel depths. They suggest that the morphology of the floodplain is defined by the lateral channel

migration rate through time, and is controlled by the transport of water and sediment by the channel. Therefore, they assume that the geometry of the floodplain is related to that of the channel, and demonstrate a relationship between bankfull channel depths and floodplain inundation depths which is linear over a range of scales [Dodov and Foufoula-Georgiou, 2006]. Floodplain delineation is carried out by locally filling the DEM up to the depth of inundation, which is determined based on bankfull channel depths, calibrated using data from United States Geological Survey (USGS) gauging stations across Oklahoma and Kansas, along with field measurements. The depth of inundation at points along the channel network is then used to find the lateral extent of the floodplain by using the planform curvature of the channel. This method also requires significant user input, as the channel bankfull depths are required in order to estimate the inundation depth.

The extraction of fluvial terraces (the remnants of previous floodplains) represents a closely related problem to the delineation of presently active floodplain surfaces. Previous studies have also used a geometric approach to identify terrace features from DEMs. For example, Demoulin *et al.* [2007] identified terrace surfaces based on local slope and height of each pixel compared to the channel. They used these attributes in order to reconstruct palaeo-channel profiles from terrace surfaces, but their methodology was not designed to produce a map of terrace extents on a wider landscape scale. Therefore, following on from their approach, Stout and Belmont [2014] presented the TerEx toolbox, a semi-automated tool to identify potential terrace surfaces based on thresholds of local relief, minimum area, and maximum distance from the channel. After potential terrace surfaces are identified, their area and height above the local channel are measured. The tool then allows the user to edit the terrace surfaces based on comparison with field data. Hopkins and Snyder [2016] evaluated the TerEx toolbox, along with two other semi-automated methods for identifying terrace surfaces [Wood, 1996; Walter *et al.*, 2007] at the Sheepscot River, Maine. They found that all of the methods over-predicted terrace

areas compared to the field-mapped terraces, and the accuracy of the methods decreased in lower relief landscapes. These semi-automated methods allow the user to manually clip over-predicted terrace surfaces based on field data and DEM observations, and remove selected surfaces that do not represent terraces, such as roads, alluvial fans, or water bodies [Stout and Belmont, 2014].

The geomorphic methods of mapping both terraces and floodplains outlined above are all semi-automated, requiring independent datasets and significant user input. For example, the method proposed by Manfreda *et al.* [2011] requires the parameters to be optimised using flood inundation maps from hydraulic simulations. The linear binary classifiers outlined by Degiorgis *et al.* [2012] and tested by Manfreda *et al.* [2014] use flood hazard maps to select the correct threshold for floodplain prediction from the geomorphic indices. The TerEx toolbox, developed by Stout and Belmont [2014], requires significant user input in order to manually edit the predicted terrace surfaces. No existing approach to mapping either floodplains or terraces from topographic data includes objective criteria for setting the thresholds that identify floodplains and terraces. As a result, the different thresholds that a user might select can result in varying floodplain and terrace maps for the same input DEM, complicating efforts to consistently map geomorphic features between different landscapes.

Here I introduce a new method of identifying floodplain and terrace surfaces from topographic data. This method uses two geometric thresholds that can be readily extracted from DEMs: the gradient of each pixel, and the elevation of each pixel relative to the nearest channel. Importantly, this method does not require calibration using any independent datasets, as the thresholds are statistically calculated from the DEM using quantile-quantile plots. I test the method against field-mapped floodplain initiation points, published flood hazard maps, and digitised terrace surfaces from seven field sites throughout the US

and one site in the UK (Figure 4.1). For each site, where available, I use high-resolution lidar-derived DEMs, as well as the corresponding national elevation datasets (10 m resolution for the US and 5 m for the UK) in order to test the sensitivity of the method to grid resolution.

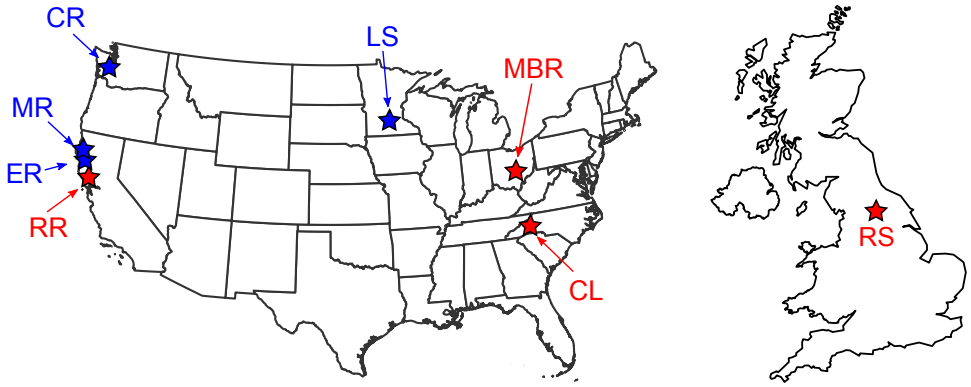

Figure 4.1: Maps of the US and UK showing the location of the eight field sites in the study. Red stars represent floodplain sites; blue stars represent terrace sites. RR = Russian River, CA; ER = South Fork Eel River, CA; MR = Mattole River, CA; CR = Clearwater River, WA; LS = Le Sueur River, MN; MBR = Mid Bailey Run, OH; CL = Coweeta Hydrologic Laboratory, NC; RS = River Swale, Yorkshire, UK.

4.2 Methodology

Floodplain and terrace surfaces can be defined as low relief, quasi-planar areas capped by alluvium and found proximal to the modern river channel. Therefore, field mapping campaigns typically identify these surfaces as spatially continuous areas with low gradients that occur next to the channel. I present a new geometric method which replicates this field approach as closely as possible by using two metrics which can be readily extracted from the DEM: elevation compared to

the nearest channel, and local gradient. My method is efficient to run and is based on the statistical selection of topographic thresholds, requiring no input of independent datasets or field mapping. I outline below the DEM pre-processing steps followed by the methodology for identifying floodplain and terrace features.

4.2.1 DEM pre-processing

The first step of the algorithm is to smooth the DEM in order to remove micro-topographic noise. Gaussian filters are often used to smooth DEMs, where the smoothing can be described by linear diffusion. A Gaussian filter results in the DEM being smoothed uniformly at all locations and in all directions [e.g. Lashermes *et al.*, 2007]. However, one consequence of the Gaussian filtering is the loss of information where there are sharp boundaries between features due to the uniform smoothing. Therefore, I filter the input DEM using a non-linear filter proposed by Perona and Malik [1990], and applied to channel extraction from high-resolution topography by Passalacqua *et al.* [2010a]. The Perona-Malik filter is an adaptive filter in which the degree of smoothing decreases as topographic gradient increases [Perona and Malik, 1990; Passalacqua *et al.*, 2010a]. This non-linear diffusion equation can be described as:

$$\partial_t z(x, y, t) = \bigtriangledown.[p(|\bigtriangledown z|) \bigtriangledown z], \tag{4.1}$$

where z is the elevation at location (x, y) and time t, $\bigtriangledown$ is the gradient operator, and $p(|\bigtriangledown z|)$ is an edge-stopping function that specifies where to stop diffusion across feature boundaries, where:

$$p(|\bigtriangledown z|) = \frac{1}{1 + (|\bigtriangledown z|/\lambda)^2}, \tag{4.2}$$

and λ is a constant. Importantly for the identification of low-gradient surfaces, the Perona-Malik filtering enhances the transitions between features, such as the low-gradient valley floor and the surrounding hillslopes, while preferentially smoothing low gradient reaches of the DEM. Following the methodology of Passalacqua *et al.* [2010a], I set the number of iterations (t) to 50 and calculate λ from the 90% quantile of the probability distribution function of the landscape gradient, following Perona and Malik [1990]. I keep these parameters constant across each site tested in the study. A full explanation of these parameters and derivation of the Perona-Malik filter is described by Passalacqua *et al.* [2010a].

After the DEM is smoothed, I then extract the channel network. Many studies have proposed different methods for identifying channel networks from high-resolution topography [e.g. Lashermes *et al.*, 2007; Tarolli and Dalla Fontana, 2009; Passalacqua *et al.*, 2010b, 2012; Pelletier, 2013; Clubb *et al.*, 2014]. Grieve *et al.* [2016a] tested the validity of channel extraction algorithms at coarsening DEM resolution, and found that a geometric method of channel extraction was consistent up to DEM resolutions of 30 m. This method, described by Grieve *et al.* [2016b], uses an Optimal Wiener filter to remove micro-topographic noise from the DEM [Wiener, 1949; Pelletier, 2013]. The Optimal Wiener filter is only used to extract the channel network: I use the Perona-Malik filtering to extract the floodplains and terraces. Channelised portions of the landscape are selected using a tangential curvature threshold [Pelletier, 2013], which is defined using quantile-quantile plots as described by Lashermes *et al.* [2007] and Passalacqua *et al.* [2010a]. These channelised portions of the landscape are combined into a channel network using a connected components algorithm outlined by He *et al.* [2008], and thinned using the algorithm of Zhang and Suen [1984]. I chose this algorithm for channel extraction to allow consistency when running the method on DEMs of varying grid resolutions.

4.2.2 Floodplain and terrace identification

After smoothing the DEM, the user can choose to run the terrace and floodplain mapping algorithm across the whole DEM, or to extract the floodplains and terraces relative to a specific channel of interest. If the algorithm is run on the whole DEM, the local gradient, S, and relief relative to the nearest channel, R_c, are calculated for each pixel. These two parameters were chosen on the basis that floodplains and terraces tend to form low-gradient regions that are close to the elevation of the modern channel. Local gradient has been used in previous geometric methods of floodplain and terrace identification, both in the calculation of the topographic index [Kirkby, 1975; Manfreda *et al.*, 2011], and in combination with other topographic metrics [e.g. Degiorgis *et al.*, 2012; Stout and Belmont, 2014; Limaye and Lamb, 2016]. Local gradient was calculated by fitting a second order polynomial surface to the DEM with a circular window [e.g. Lashermes *et al.*, 2007; Roering *et al.*, 2010; Hurst *et al.*, 2012; Grieve *et al.*, 2016c]. The radius of the window is calculated by identifying breaks in the standard deviation and interquartile range of curvature with increasing window size, following Grieve *et al.* [2016c]. This allows the window size to be calculated for each DEM to ensure that the slope values are representative at the hillslope scale, rather than being influenced by smaller-scale variations from vegetation [e.g. Roering *et al.*, 2010; Hurst *et al.*, 2012]. R_c has also been used in previous geometric methods [e.g. Degiorgis *et al.*, 2012; Manfreda *et al.*, 2014; Limaye and Lamb, 2016], and is calculated as the difference in elevation between the starting pixel and the nearest channel pixel, identified using a steepest descent flow routing algorithm [O'Callaghan and Mark, 1984; Braun and Willett, 2013]. A threshold Strahler stream order is set by the user such that the nearest channel must have a stream order greater than the threshold. This is necessary so that each pixel is mapped to the main channel along which floodplains or terraces have formed, rather than narrow tributary valleys. I found that a threshold of

third order channels was appropriate for each of the field sites, based on a visual inspection of the DEM. One of the outputs of the software package is a raster of the channel network labelled by the Strahler stream order. The user can identify an appropriate threshold stream order based on visual inspection of floodplain and terrace surfaces compared to this network.

As well as running the algorithm on the whole landscape, the user can also choose to extract floodplains or terraces relative to a specific channel of interest. The user must provide the latitude and longitude of two points defining the upstream and downstream end of the channel. The algorithm then defines a channel network between these points using a steepest descent flow routing algorithm [O'Callaghan and Mark, 1984; Braun and Willett, 2013]. After the identification of the channel, a swath profile is created along it following the method outlined in Hergarten *et al.* [2014] and applied by Dingle *et al.* [2016]. The user must specify the width of the swath, which can be estimated by a visual inspection of the DEM, to provide a sufficiently wide swath compared to the valleys in the landscape. The same two parameters (S and R_c) are used for feature classification for each pixel in the swath profile, except that R_c is calculated compared to the nearest point on the reference channel.

After the calculation of slope and R_c, I identify thresholds for each metric in order to provide a binary classification of each pixel as either floodplain/terrace (1) or hillslope (0). A key feature of the new method is that the thresholds for R_c and local gradient do not need to be set by the user based on independent validation, but are calculated statistically from the DEM. Many methods of channel extraction employ statistical selection of topographic thresholds [e.g. Lashermes *et al.*, 2007; Thommeret *et al.*, 2010; Passalacqua *et al.*, 2010a; Pelletier, 2013; Clubb *et al.*, 2014], but this has yet to be developed for the identification of floodplains or terraces. I identify thresholds for R_c and S using quantile-quantile plots, which have previously been used in the detection of

hillslope-valley transitions [e.g. Lashermes *et al.*, 2007; Passalacqua *et al.*, 2010a]. Quantile-quantile plots are used to determine if a probability density function of real data can be described by a Gaussian distribution. The transition between process domains can be determined by the value at which the probability density function of the real data deviates from the Gaussian function [Lashermes *et al.*, 2007]. The real data are plotted against the corresponding standard normal variate, which indicates how many standard deviations an element is from the mean. For example, if a value has a standard normal variate (or z-score) of 1, then it is one standard deviation above the mean, which has a z-score of 0. A Gaussian distribution plots as a straight line on a quantile-quantile plot, and is modelled for each DEM based on a lower and upper percentile of the real data. The percentiles chosen to represent the reference Gaussian distribution can be set by the user based on the landscape in question, but are generally set as the 25^{th} and 75^{th} percentile [Passalacqua *et al.*, 2010a]. For each value of the real data, I calculate the difference between the real data and the Gaussian distribution as a fraction of the range of the real data (Figure 4.2).

The threshold values for R_c and slope are then identified as the lowest value at which there is less than 1% difference between the two distributions. Figure 4.3 shows an example of the channel relief and slope maps for the Russian River field site, with the calculated thresholds for each field site presented in Table 4.1. If the user wishes to extract only the terraces, then a threshold height above the modern river channel must be set: any pixels below this height will be identified as floodplain, and any pixels above this height will be identified as terraces. This threshold height can also be determined based on a visual inspection of the DEM. My method allows the analysis of spatial extent of floodplain and terrace features (if run across the whole DEM) as well as the distribution along a specific channel of interest (if run with the swath mode). For example, in swath mode, the elevation and slope of the terraces can be mapped as a function of distance upstream

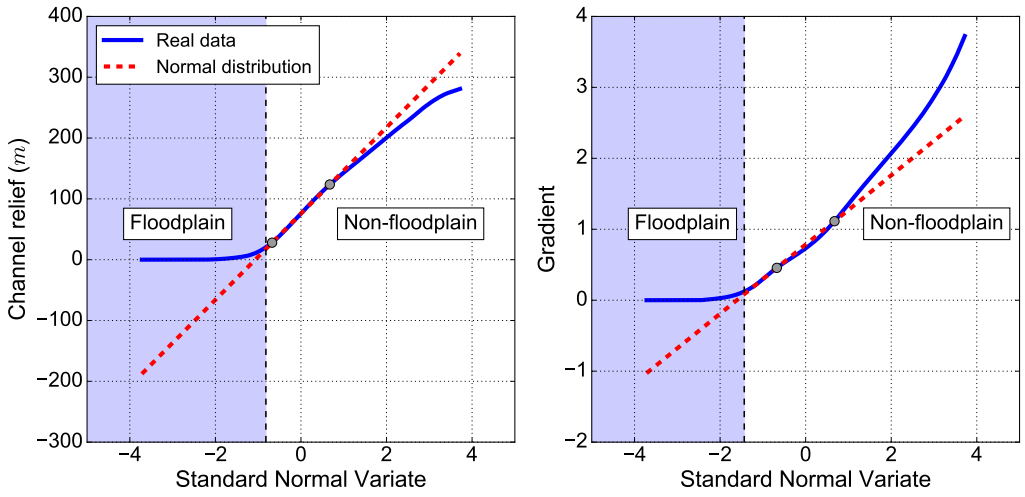

Figure 4.2: Example quantile-quantile plots for Mid Bailey Run, Ohio, showing probability density function of relief relative to the channel and slope. The probability density function of each is shown in blue, with the reference normal distribution shown by the red dashed line. The threshold (black dashed line) is selected where there is less than 1% difference between the real and reference distributions. The blue box highlights the portion of the distribution identified as floodplain. The grey points represent the 25^{th} and 75^{th} percentiles of the real data.

along the channel network. This provides numerous potential applications of the method for understanding controls on terrace formation and morphology.

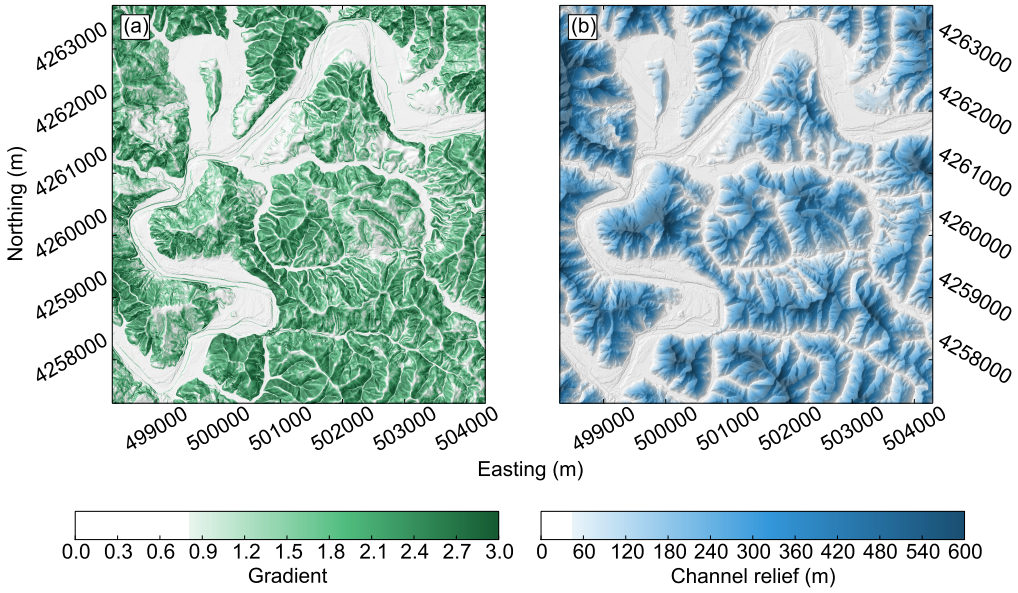

Figure 4.3: Maps showing (a) gradient and (b) relief relative to the nearest channel, R_c, for the Russian River field site. The areas of the landscape identified as below the threshold are shown in white, with values above the threshold then grading to darker colours. In order to be selected as floodplain, each pixel must be below the threshold for both gradient and R_c. The coordinate system is UTM Zone 10°N.

4.2.3 Comparison with published data

In order to test the results of the method I compare the predicted floodplain and terrace locations to field-mapped floodplain initiation points, published flood hazard maps, and digitised terrace surfaces. In order to quantify the performance of the methods compared to these datasets, I assess the rates of true positives (TP), false positives (FP), true negatives (TN), and false negatives (FN) [e.g. Heipke *et al.*, 1997; Molloy and Stepinski, 2007; Tarolli *et al.*, 2012; Orlandini

Table 4.1: Channel relief and slope threshold for each field site

Field site	Channel relief threshold (m)	Slope threshold
Mid Bailey Run, OH	23.69	0.15
Coweeta, NC	32.80	0.11
Russian River, CA	43.51	0.81
River Swale, UK	39.40	0.05
South Fork Eel River, CA	42.96	0.05
Le Sueur River, MN	9.42	0.05
Mattole River, CA	50.25	0.17
Clearwater River, WA	12.67	0.06

et al., 2011; Manfreda *et al.*, 2014; Clubb *et al.*, 2014]. Each pixel is assigned to one of the four categories:

1. True positive TP: The pixel is identified as floodplain/terrace by both the geomorphic method and the independent dataset.

2. False positive FP: The pixel is identified as floodplain/terrace by the geomorphic method, but not by the independent dataset.

3. True negative TN: The pixel is not identified as floodplain/terrace by either dataset.

4. False negative FN: The pixel is identified as floodplain/terrace by the independent dataset but not by the geomorphic method.

I report the reliability (r), sensitivity (s), and overall quality (Q_t) for each field site:

$$r = \frac{\sum TP}{\sum TP + \sum FP}, \tag{4.3a}$$

$$s = \frac{\sum TP}{\sum TP + \sum FN}, \tag{4.3b}$$

$$Q_t = \frac{\sum TP}{\sum TP + \sum FP + \sum FN}. \tag{4.3c}$$

The reliability, r, is a measure of the ability of the method to not generate false positives. The r value can vary between 0 and 1: if the r value is low, then the method is predicting a large amount of pixels as floodplain or terrace which are not identified by the independent dataset, whereas a high r value indicates that the majority of pixels mapped as floodplain or terrace are also identified by the independent map. The sensitivity, s, is a measure of the ability of the method to not generate false negatives: a low s value indicates that the method is not identifying many of the floodplain or terrace pixels selected by the published maps. The overall quality, Q_t, combines both the number of false positives and false negatives to give an overall 'goodness' of the feature classification. It also varies between 0 and 1, where 0 represents no correlation between the predicted and observed features, and 1 represents a perfect match [Heipke *et al.*, 1997].

4.3 Study areas

I ran the new method on a total of eight field sites, located in Figure 4.1. Four of these field sites (the Russian River, CA; Mid Bailey Run, OH; Coweeta NC; and the River Swale, UK) were selected to test the ability of the algorithm to

identify floodplains, using published flood maps for the regions. The remaining four sites were selected to validate the algorithm against digitised terrace maps (South Fork Eel River, CA; Le Sueur River, MN; Clearwater River, WA, and Mattole River, CA). Table 4.2 summarises the mean annual precipitation and mean annual temperature of each site, based on data from the PRISM Climate Group (`http://prism.oregonstate.edu`) for the US sites and the Met Office (`http://www.metoffice.gov.uk/public/weather/climate/`) for the UK site. It also summarises the underlying lithology, the source of the data used for validation, and the grid resolution. The algorithm was run based on topographic data derived from 1 m lidar data for the sites where these were available (the Russian River, CA; Mid Bailey Run, OH; Coweeta, NC; the South Fork Eel River, CA; and the Le Sueur River, MN). For the remaining field sites the topographic data were generated from the United States Geological Survey National Elevation Dataset 1/3 arc sec DEM, sampled at 10 m resolution for the US sites, and from the Ordnance Survey Terrain 5 dataset for the UK site, sampled at 5 m resolution. All DEMs were converted to the Universal Transverse Mercator (UTM) coordinate system using the WGS84 datum.

4.4 Results

4.4.1 Comparison with mapped floodplains

I compare the floodplain extent predicted by the method to field mapped floodplain initiation points (FIPs) from two of the four study areas: Mid Bailey Run, OH, and Coweeta, NC. A FIP was defined as the upstream limit of low gradient surfaces at the same elevation as the channel banks. As the valley opens out from its more confined upper reaches, these surfaces transition from discontinuous depositional pockets to more continuous floodplain surfaces [Jain

Table 4.2: Details of climate and lithology for each field site

Field site	UTM Zone	MAP (mm)	MAT (°C)	Lithology	Comparison datasets	R_G (m)
Russian River, CA	10° N	1396	14.1	Sandstones and shales; Quaternary alluvial deposits	FEMA flood hazard maps	1
Mid Bailey Run, OH	17° N	1005	10.9	Sandstones, siltstones, shales	FEMA flood hazard maps; Field-mapped FIPs	1
Coweeta, NC	17° N	1792	12.3	Meta-sedimentary units	FEMA flood hazard maps; Field-mapped FIPs	1
River Swale, UK	30 ° N	898	8.4	Limestones and sandstones	EA flood hazard maps	5
South Fork Eel River, CA	10° N	2009	12.7	Greywackes and shales	Digitised terraces [Seidl and Dietrich, 1992]	1
Le Sueur River, MN	15° N	793	7.5	Pleistocene tills and Ordovician dolostones	Digitised terraces [Gran *et al.*, 2009]	1
Mattole River, CA	10° N	2593	12.8	Sandstones and shales; Quaternary alluvial deposits	Digitised terraces [Dibblee and Minch, 2008; Limaye and Lamb, 2016]	10
Clearwater River, WA	10° N	3126	9.9	Sandstones with interbedded shales	Digitised terraces [Wegmann and Pazzaglia, 2002; Limaye and Lamb, 2016]	10

et al., 2008]. In this study I consider the FIP to start at the onset of alluviation outside the channel banks: therefore, I mapped the start of the discontinuous floodplain pockets at the FIPs in each channel. The onset of alluviation often occurred at multiple locations along the same channel: in these cases I took the location of each FIP downstream along the channel.

A total of 19 FIPs were mapped in Mid Bailey Run, OH, during May–June 2011, and eight FIPs were mapped in the Coweeta catchment, NC, in May 2014. FIPs in the Mid Bailey Run catchment were mapped using a Trimble GeoXM GeoExplorer 2008 series GPS with a mean horizontal accuracy of 6 m. Point locations in the Coweeta catchment were mapped using a Trimble GeoXR GeoExplorer 6000 series GPS with a mean horizontal accuracy of 1.01 m and a mean precision of 1.3 m. Figure 4.4 shows the relationship between the field mapped initiation points and predicted floodplain extent. In order to compare these field mapped FIPs to the predicted floodplain extents, I measured the flow distance between the field mapped point and the furthest upstream point of the nearest predicted floodplain patch. The distances for each FIP are reported in Table 4.3, where negative values indicate that the predicted floodplain initiation was upstream of the mapped, and vice versa for positive values. I also report the r, s, and Q_t values for the predicted floodplain initiation points. Following the methodology of Orlandini *et al.* [2011], I classify a point as a TP if the predicted FIP is within a 30 m radius of the mapped FIP. The comparison with the mapped FIPs resulted in $r = 0.83$, $s = 0.67$, and $Q_t = 0.59$ for Mid Bailey Run, and $r = 0.78$, $s = 1$, and $Q_t = 0.78$ for Coweeta.

Along with these field mapped floodplain initiation points, I also compare the predicted floodplain extent to published flood risk maps for three out of the four study areas. For the sites in the US, flood risk maps were obtained from the Federal Emergency Management Agency (FEMA)'s National Flood Hazard Layer (https://msc.fema.gov/portal/). The National Flood Hazard Layer is a

Table 4.3: Flow distances between the field-mapped FIPs and predicted floodplain extents

Field site	Mapped FIP	Easting (m)	Northing (m)	Flow distance (m)[1]
Mid Bailey Run, OH	T2FPI1	401513	4364940	59
	T3FPI1	401622	4364773	85
	T3FPI2	401661	4364732	-49
	WBT1FPI	400090	4363977	-23
	WBT2FPI1	399865	4364215	-1
	T4FPI	401342	4365472	28
	T5FPI2	401072	4365675	0
	T7FPI2	400670	4366152	2
	T5FPI1	401208	4365807	0
	T1FPI1	401443	4365150	0
	TX3D3-FPI0	400718	4366277	-42
	TX3FPI1	400644	4366126	-5
	MBFPI	400449	4366130	-34
	T7FPI1	400600	4366074	-19
	T4FPI2	401391	4365514	92
	T6FPI1	400900	4365921	-20
Coweeta, NC	SF5	277212.380	3882554.000	-51
	BC1	276326.800	3880661.200	-3
	HCW	277641.5	3881694.2	2
	BC3	277584.633	3881138.653	-3
	HW1	278252.652	3881715.719	13
	CB1	278089.041	3882301.638	12
	HB1	277444.900	3882919.685	-16
	CC2	277098.745	3882348.108	-2

[1] The distance between the mapped FIP and the upstream extent of the nearest floodplain patch predicted by the geomorphic method

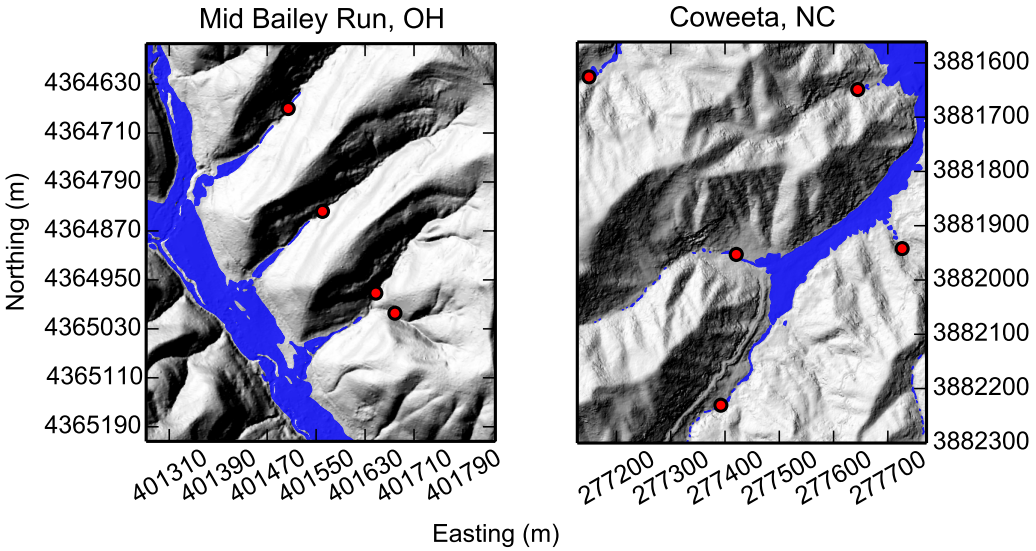

Figure 4.4: Shaded relief maps of Mid Bailey Run and Coweeta field sites showing the relationship between the predicted floodplain (blue) and the mapped floodplain initiation points (red). The UTM zone is 17°N.

compilation of GIS data consisting of a US-wide Flood Insurance Rate map. It contains information on the flood zone, base flood elevation, and floodway status for a location. Floodplain extents are calculated using a hydraulic model, such as HEC-RAS (Hydrologic Engineering Center-River Analysis System), incorporating discharge data, cross sectional survey data, and stream characteristics. These studies can be expensive, with a detailed survey on a mile-long reach typically costing between $10,000 and $25,000 [Committee on FEMA Flood Maps, 2009]. The original data were in the geographic projection NAD1983, and were converted to the projected UTM WGS84 coordinate system (Ohio and NC Zone 17°N, Russian River Zone 10°N). I separate the flood zones into two categories: areas within the 100 year flood (blue), with a 1% annual chance of flooding, and areas with a greater than 100 year flood risk (less than 1% annual risk of flooding). In order to compare these maps to the method, I gridded the FEMA flood risk maps with a resolution of 1 m. The Coweeta field site in North Carolina did not have

a complete flood risk map for the catchment and therefore could not be included in this analysis.

For the River Swale field site in the UK, flood risk maps were obtained from the Environment Agency's (EA) Risk of Flooding from Rivers and Sea dataset, which divides the landscape into 50 by 50 m cells (`https://data.gov.uk/dataset/risk-of-flooding-from-rivers-and-sea1`). Each cell is categorised into one of four flood risk likelihood categories: high (3.3% annual chance of flooding); medium (between 3.3% and 1%); low (between 1% and 0.1%); or very low (<0.1%). The dataset is created by hydraulic modelling, including information about the state of flood defences and local stage heights as inputs to the model. The data were re-projected from the British National Grid coordinate system to the UTM WGS84 datum, Zone 30°N. In order to keep the comparison consistent with the sites from the US, each pixel was classified into the same two categories as for the FEMA maps, with areas of flood risk identified as having greater than 1% annual chance of flooding. The dataset is provided as vector data: to compare with the floodplain identified by the the method, I gridded the vector dataset at 5 m resolution (the same as the input DEM). Figure 4.5 shows examples of the FEMA and EA flood maps for each study area.

The r, s, and Q_t values for each site are reported in Table 4.4, with a visual comparison between the method and the published flood maps shown in Figure 4.6. I also report the quality values for floodplains extracted from the United States Geological Survey's 1/3 arc second National Elevation Dataset (NED), gridded at 10 m, in order to test the sensitivity of the method to grid resolution. The USGS NED is a seamless dataset created for the conterminous US, using a variety of elevation products which is updated on a two-month cycle. The method was most similar to the flood risk maps for the Russian River, CA with the highest overall quality value ($Q_t = 0.67$ for the 1 m DEM and 0.68 for the 10 m DEM). The method has a higher sensitivity than reliability for both DEM datasets, with

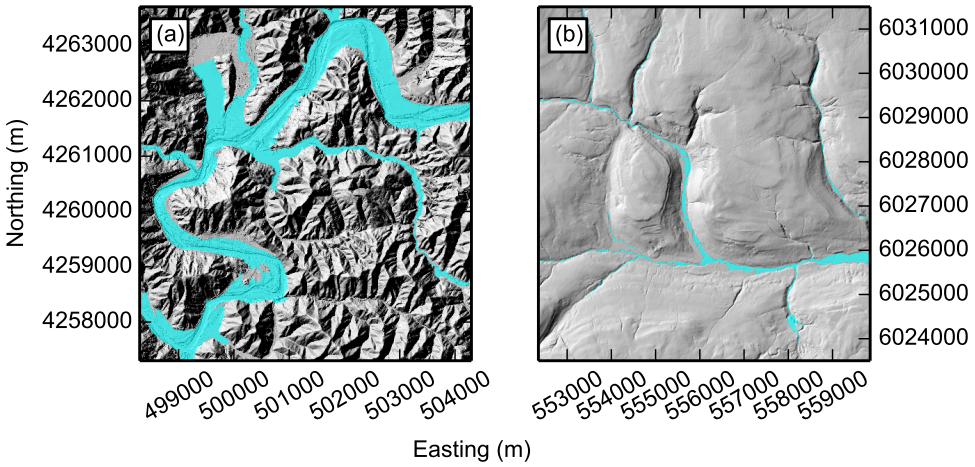

Figure 4.5: Shaded relief maps showing (a) FEMA flood risk map for the Russian River, CA, UTM Zone 10°N and (b) EA flood risk map for the River Swale, UK, UTM Zone 30°N. In some parts of the landscape the published flood maps do not extend all the way up the catchments.

$s = 0.97$ and $r = 0.74$ for the 1 m DEM; compared to $s = 0.96$ and $r = 0.70$ for the 10 m DEM. For both the Mid Bailey Run and Russian River field sites, the sensitivity is higher than the reliability for all of the DEM resolutions tested (Table 4.4). However for the River Swale site, the reliability is higher than the sensitivity ($r = 0.84, s = 0.65$).

4.4.2 Comparison with mapped terraces

I also compare the features extracted by the method to field-mapped terraces from four field sites throughout the US: the South Fork Eel River, CA [Seidl and Dietrich, 1992]; the Le Sueur River, MN [Gran *et al.*, 2009]; the Mattole River, CA [Dibblee and Minch, 2008]; and the Clearwater River, WA [Wegmann and Pazzaglia, 2002]. Two of these sites had 1 m lidar-derived DEMs (the South

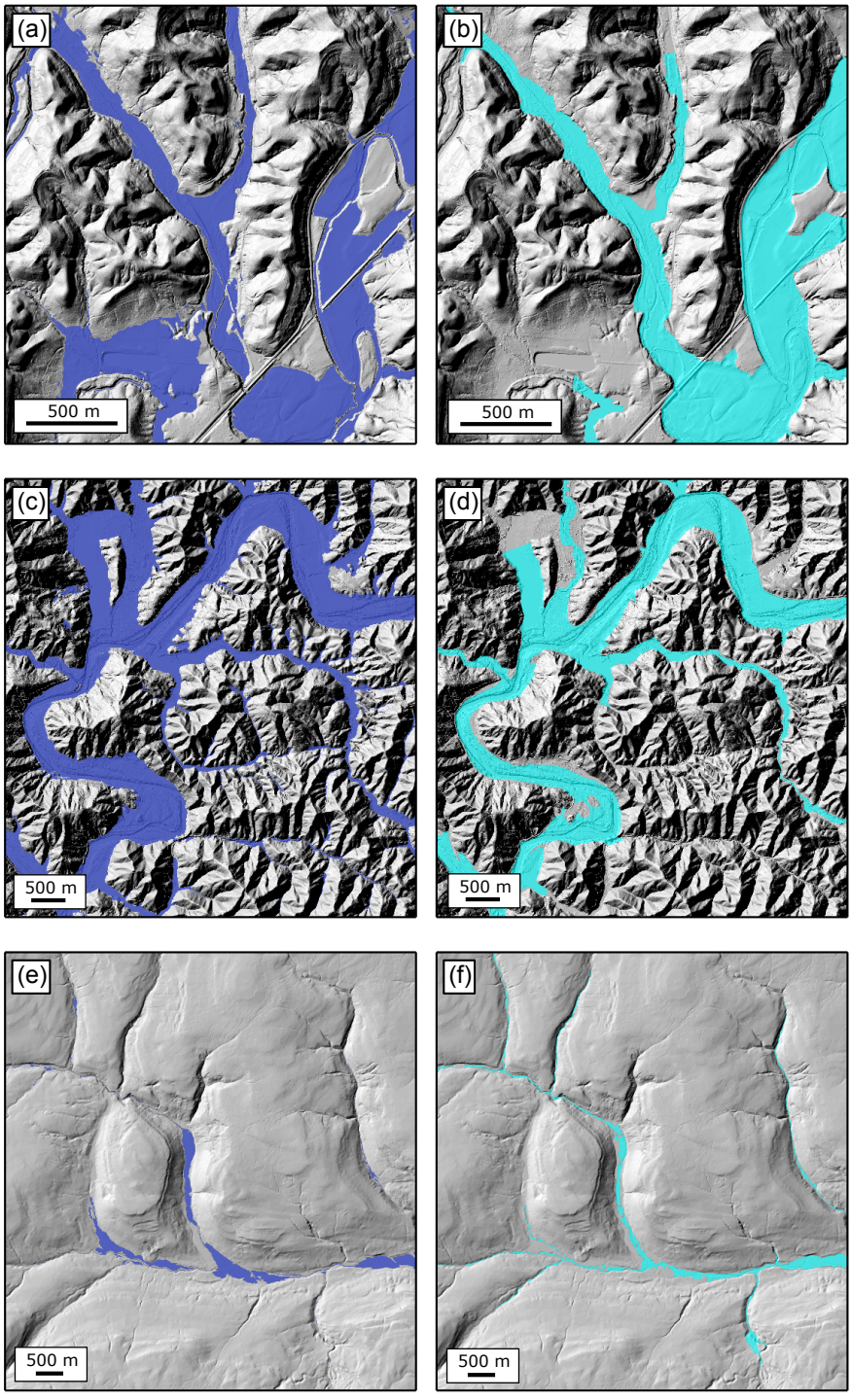

Figure 4.6: Shaded relief maps for each field site showing a comparison between the predicted floodplains (first column) and the published FEMA/EA maps (second column). (a) - (b) Mid Bailey Run, OH. (c) - (d) Russian River, CA. (e) - (f) River Swale, UK.

Table 4.4: Results of the reliability (r), sensitivity (s), and overall quality (Q_t) analysis for each site

Field site	Grid resolution (m)	r	s	Q_t
Mid Bailey Run, OH	1	0.73	0.76	0.59
	10	0.77	0.80	0.65
Russian River, CA	1	0.74	0.97	0.67
	10	0.70	0.96	0.68
River Swale, UK	5	0.84	0.65	0.58
South Fork Eel River, CA	1	0.65	0.72	0.52
Le Sueur River, MN	1	0.58	0.54	0.39
Mattole River, CA	10	0.58	0.65	0.44
Clearwater River, WA	10	0.56	0.55	0.39

Fork Eel and Le Sueur Rivers). For the remaining two sites, 10 m DEMs were derived from the USGS 1/3 arc second NED, following Limaye and Lamb [2016]. Terraces in the South Fork Eel River and the Le Sueur River were digitised from field mapping carried out in previous studies [Seidl and Dietrich, 1992; Gran *et al.*, 2009], constrained by the hillshaded DEMs. Terraces from the Mattole River and the Clearwater River were digitised by Limaye and Lamb [2016] from geological maps, with the terraces mapped by Dibblee and Minch [2008] for the Mattole River, and Wegmann and Pazzaglia [2002] for the Clearwater River. I ran the method in the swath setting for each of these sites, so that the terraces were mapped compared to the main stem channel of interest in each site. The thresholds for terrace identification (R_c and S) were set statistically for each site using the quantile-quantile plots. In order to quantify the difference between the method and the digitised terraces, I calculated the r and s values following the same methodology as for the floodplain comparison (Table 4.4).

Figure 4.7 shows a visual comparison of the predicted and digitised terraces from the two sites with 1 m lidar-derived DEMs. In general there was good spatial correlation between the two terrace datasets for each field site, although in

some cases the automated method did not identify all terraces at high elevations compared to the modern channel. The South Fork Eel River had the highest values of both r (0.65) and s (0.72). The comparison between the two terrace datasets for the field sites with 10 m DEMs is shown in Figure 4.8. These sites had lower r and s values than that of the South Fork Eel River, but were comparable to the values for the Le Sueur River (e.g. Table 4.4).

4.5 Discussion

4.5.1 Floodplains

The results outlined above compare the method of automatic feature extraction to various datasets of both floodplains and terraces. In order to test the ability of the method in identifying floodplains, I compared the delineated geomorphic floodplain to both field-mapped floodplain initiation points and hydrological modelling predictions. I found that the method predicts the location of the field-mapped FIPs to within tens of metres for both field sites (Mid Bailey Run, OH; and Coweeta, NC). The reliability and sensitivity values were highest for the Coweeta field sites, with a value of $r = 0.78$ and $s = 1$, which indicates that there were no false negatives in this field site. Table 4.3 shows that in many cases the error between the mapped and predicted FIPs is within the same order of magnitude as the error on the field-mapped coordinates ($\approx$ 1 m for Coweeta and $\approx$ 6 m for Mid Bailey Run). In isolated cases in the Mid Bailey Run site, the error was higher between the mapped and predicted FIPs (around 90 m for two of the points), where the mapped FIP was located in narrow headwater valleys (Figure 4.4). Furthermore, the predicted floodplain in the majority of cases was located downstream of the mapped FIPs in Mid Bailey Run (Table 4.3). This is not surprising, as my method is based on identifying areas of low gradient, which

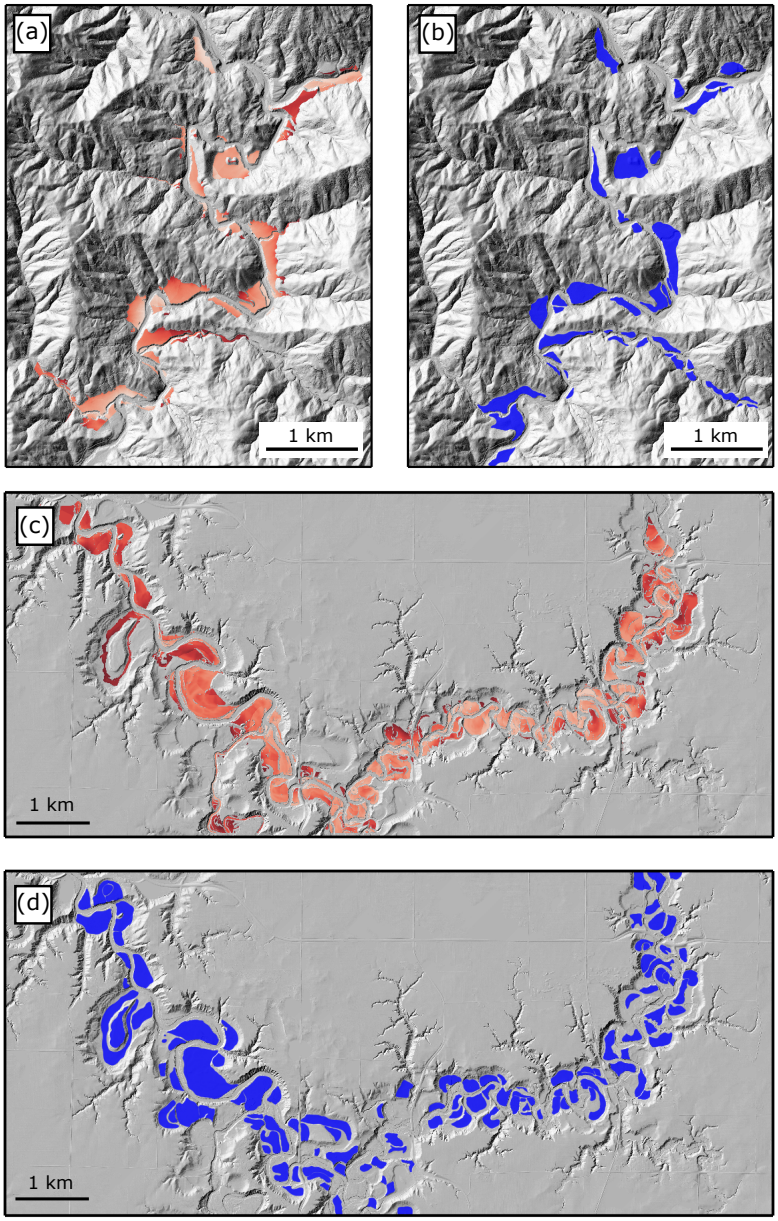

Figure 4.7: Shaded relief maps for the two field sites with lidar-derived DEMs showing a comparison between the predicted terraces (red) and the digitised terraces (blue). The predicted terraces are coloured by elevation compared to the channel, where darker red indicates higher elevation. (a) - (b) South Fork Eel River, CA. Maximum terrace height is 43 m. (c) - (d) Le Sueur River, MN. Maximum terrace height is 9.5 m.

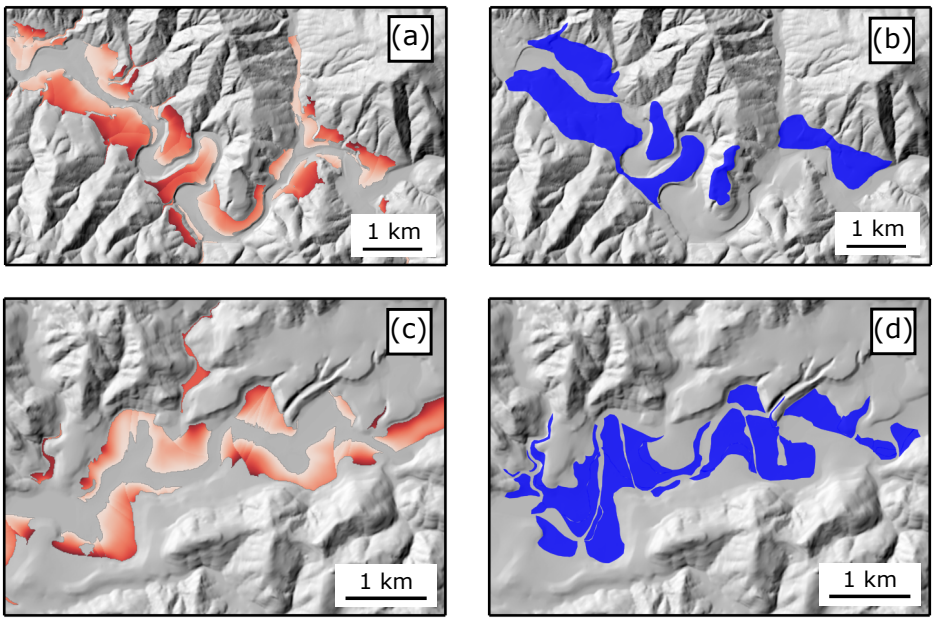

Figure 4.8: Shaded relief maps for the two field sites with 10 m resolution DEMs from the USGS NED showing a comparison between the predicted terraces (red) and the digitised terraces (blue). The predicted terraces are coloured by elevation compared to the channel, where darker red indicates higher elevation. (a) - (b) Mattole River, CA. Maximum terrace height is 50 m. (c) - (d) Clearwater River, WA. Maximum terrace height is 13 m.

is calculated based on polynomial surface fitting with a specified window radius (Section 4.2.2). Small pockets of alluviation in narrow valleys may therefore be missed by the method if the width of the floodplain is less than that of the window radius or the DEM resolution.

I also validated the method against published flood maps for three of the field sites (Mid Bailey Run, OH; Russian River, CA; and River Swale, UK). The quality analysis for this comparison (Table 4.4 and Figure 4.6) suggests that there is in general a good correlation between the method and the published flood maps, with high values for reliability ($r \geq 0.7$), sensitivity ($s \geq 0.65$), and overall quality ($Q \geq 0.58$) for each field site. The results for both the Russian River and Mid Bailey Run showed higher sensitivity values than reliability, suggesting that the the method predicted more false positives than false negatives. In each field site, the published flood maps were classified to define the 1% annual chance of flooding, or the 100 year return period flood event. It may therefore be expected that the geomorphic-based method would delineate a larger floodplain than is flooded in a 100 year return period event. The results for the River Swale, however, show a higher reliability than sensitivity, suggesting that more false negatives were predicted than false positives. This may be due to methodological differences in the production of this flood map by the Environment Agency (UK) compared to the US sites. Figure 4.6f shows the published flood map for the River Swale site which, in comparison to the FEMA flood maps (Figures 4.6b and 4.6d) extends into the headwaters of the channel network. As these areas do not have low gradient surfaces next to the channel, they may not be selected by the method. This may account for the higher number of false negatives predicted at this site.

Published flood maps are useful in providing an independent estimate of likely floodplains in each field site. However, there are potential limitations to these maps which must be carefully considered, and may result in some of the differences

compared to geomorphic floodplain prediction techniques. Hydrodynamic models have a large number of parameters, which require careful calibration with field and hydraulic data, such as channel roughness and discharge data from gauging stations. Furthermore, due to the time-consuming and expensive nature of these studies, flood maps are often not produced for small catchment sizes, and may therefore be incomplete on a landscape-scale (e.g. Figure 4.5). There may also be differences in the methodology used in producing these maps for each site, depending on the input topographic data and modelling software used. However, despite these discrepancies between the flood maps I find a good spatial correlation between these and the predictions from my method (Figure 4.6).

In order to test the sensitivity of the method to grid resolution, I also ran the floodplain extraction using 10 m DEMs derived from the USGS NED for two of the field sites (Russian River, CA, and Mid Bailey Run, OH), as well as testing it on the River Swale in the UK (5 m resolution DEM). I found there was little difference in the reliability and sensitivity results when compared to the 1 m DEMs (Table 4.4). This suggests that the method is relatively insensitive to grid resolution, allowing the identification of floodplain features on coarser-resolution DEMs. Furthermore, in the Mid Bailey Run field site, the method performed better on the 10 m data compared to the 1 m DEM. High-resolution topographic data may contain both small-wavelength topographic noise caused by tree throw and biotic activity [Roering *et al.*, 2010; Marshall and Roering, 2014], as well as synthetic noise from point cloud processing [Liu, 2008; Meng *et al.*, 2010]. This noise may affect the calculation of topographic metrics [Grieve *et al.*, 2016a], potentially leading to differences in the location of extracted floodplains or terraces compared to the lower resolution data.

4.5.2 Terraces

I also tested the ability of the method to identify fluvial terraces in four field sites (South Fork Eel River, CA; Le Sueur River, MN; Mattole River, CA; and Clearwater River, WA) by comparing to digitised terrace maps. Two of these field sites had 1 m lidar-derived DEMs (Figure 4.7) whereas two had 10 m DEMs from the USGS NED (Figure 4.8). The quality analysis for the 1 m DEMs showed the higher reliability and sensitivity values for the South Fork Eel River site ($r = 0.65$ and $s = 0.72$), with comparable values for the remaining three field sites. This may be due to the influence of topographic structure on terrace identification. The portion of the Eel River DEM analysed here has higher relief, with a maximum elevation of 290 m above the nearest channel, compared to the lower-relief landscape covered by the DEM for the Le Sueur River, with a maximum elevation of 40 m above the nearest channel. As the method relies on the distribution of relief relative to the channel in order to select the threshold for terrace identification, it will work best in areas where there is a greater contrast between the slope and relief of the terrace surfaces compared to the surrounding topography, such as steep mountainous areas. This is similar to other semi-automated terrace extraction methods [e.g. Stout and Belmont, 2014; Hopkins and Snyder, 2016]. The Le Sueur River is currently incising through Pleistocene tills, forming a low-gradient surface or plateau [Fisher, 2003; Gran *et al.*, 2009; Belmont *et al.*, 2011a]. High-altitude, low-gradient surfaces, such as relict plateaus, may result in error in the method due to the difficulty in distinguishing the distribution of terrace elevations from these low-relief surfaces. The Le Sueur River basin is also heavily influenced by human land use, which makes feature extraction challenging [Passalacqua *et al.*, 2012]. The results of the quality analysis for the eight field sites (Table 4.4) showed that the method performed better in the floodplain identification compared to the terrace identification. This may be due to the fact that, with the exception of the South Fork Eel River, the sites used for

terrace extraction are lower relief than those used to test the floodplain extraction (e.g. Figures 4.6 - 4.8).

Another potential cause of error between the predicted and digitised terrace locations may be problems in distinguishing whether features represent the modern floodplain or terraces. In the method a minimum height above the modern channel is set, where pixels above this height are classified as terrace, and below this height are classified as floodplain. In some cases, particularly where the terraces are at a similar elevation to that of the modern channel, the method may mistakenly identify terraces as being part of the modern floodplain, or vice versa. An example of this may be the Clearwater River site, where the method had lower indices of r and Q_t (Figures 4.8c and d and Table 4.4). In this site, the digitised terraces are close in elevation to the modern channel, with a maximum terrace height of 13 m. Furthermore, in some cases the method did not select all of the terraces identified by the field mapping, particularly at the highest elevations compared to the modern channel (e.g. Figure 4.7c and d). This may be the case if the threshold for elevation compared to the channel selected by the quantile-quantile plot is lower than that of the highest terrace elevations. This can be examined for the landscape in question by a visual inspection of the quantile-quantile plots and the location of the threshold compared to the distribution of channel relief (e.g. Figure 4.2). My method fits a Gaussian distribution to the quantile-quantile plots, and selects the thresholds as the deviation of the real data from this distribution, as a simple general model of elevation distributions that can be applied across multiple landscapes. However, in some landscapes, the distribution of elevations may not be accurately represented by a Gaussian distribution. A future avenue for development of this method may be to include multiple models for elevation distributions from which to select the thresholds of elevation and gradient.

However, despite these limitations, the selection of the threshold from quantile-quantile plots means that the method does not require the input of any independent datasets or field-mapping. Semi-automated methods of terrace identification, where the terrace polygons are manually edited by the user, are particularly useful in areas where independent datasets of terrace locations are available for calibration, and may be more appropriate than the method on site-specific scales [e.g. Stout and Belmont, 2014]. However, the selection of thresholds based on a statistical approach means that the method can be applied in areas where these data do not exist, on a broader landscape scale, or as a rapid first-order predictor of terrace locations.

In addition to the field sites with lidar-derived DEMs, I also tested the method against digitised terraces from two sites with 10 m DEMs gridded from the USGS NED, to examine the performance of the method at lower grid resolution. Figure 4.8 shows the results of the terrace identification on the 10 m resolution data. The reliability and sensitivity of the method for these two sites (Table 4.4) was lower than that of the South Fork Eel River, but comparable to that of the Le Sueur River. This suggests that the method is able to successfully select terraces at lower grid resolutions. Although there are some differences between the terraces predicted by the method and those digitised in the field, the majority of the terrace features evident from a visual inspection of the hillshaded DEMs are correctly identified by the algorithm (Figure 4.8). In some cases, some terrace-like features that can be seen on the hillshaded DEMs are not identified in the digitised terrace maps (e.g. Figure 4.8b). This may be due to error in the mapping of terrace surfaces in the field, or discrepancies resulting from the digitisation process.

An objective, landscape-scale method of identifying floodplain and terrace features has numerous applications in the geomorphological and hydrological communities. For example, terrace surfaces have been used to examine the response of fluvial systems to tectonic and climatic perturbations [e.g. Merritts *et al.*, 1994],

and to investigate the relative importance of lateral and vertical channel incision [e.g. Finnegan and Dietrich, 2011]. Analysis of terrace areas can be used to quantify sediment budgets and estimate storage volumes over millennial timescales [e.g. Trimble, 1999; Brown *et al.*, 2009; Belmont *et al.*, 2011b; Blöthe and Korup, 2013]. My new method facilitates the rapid extraction of terrace surfaces either across the whole landscape or compared to a representative channel of interest. It allows the user to investigate how various metrics, such as elevation compared to the channel, slope, and curvature, vary both within and between individual terrace surfaces (e.g. Figure 4.7). These metrics could be used in order to examine how terrace heights vary with distance along channel profiles, for example, or to identify signatures of deformation corresponding to tectonic processes [Avouac and Peltzer, 1993; Lavé and Avouac, 2000; Pazzaglia and Brandon, 2001; Viveen *et al.*, 2014].

4.5.3 Research needs: fully-automated feature extraction

A key goal for the Earth surface research community is to develop fully-automated methods of feature extraction from DEMs in order to avoid expensive and time consuming field-mapping, and to investigate the controls on geomorphic processes at a landscape scale. My new method of floodplain and terrace delineation attempts to meet some of these research needs, by allowing the statistical determination of the thresholds for feature extraction. However, the method still requires the input of some user-defined parameters. If the method is run across the whole landscape, the user must set a threshold stream order for the calculation of elevation compared to the nearest channel. This is necessary so that each pixel is mapped to the main channel along which floodplains or terraces have formed, rather than narrow tributary valleys. This threshold can be determined by the user based on a visual inspection of the DEM compared to the channel

network. If the user runs the method based on the swath mode, the width of the swath profile must be set. This can also be done based on a visual inspection of the DEM to provide a sufficiently wide swath compared to the valleys in the landscape. Furthermore, if the method is run in the swath mode, then a minimum terrace height must be set in order to delineate between floodplains and fluvial terraces.

However, future development of new algorithms, such as extraction of valley widths, would allow these parameters to be set based on the topographic data alone. My method represents a first step towards this goal of fully-automated geomorphic feature identification, which can be improved upon with future research. The combination of different algorithms for terrain analysis, such as hillslope flow routing, channel network extraction, floodplains, and fluvial terraces, would allow an objective landscape-scale investigation of the controls on geomorphic processes.

4.6 Conclusions

I have presented a novel method for the geomorphometric delineation of floodplain and fluvial terrace features from topographic data. Unlike previous methods, which tend to require calibration with additional datasets, the method selects floodplain and terrace features using thresholds of local gradient and elevation compared to the nearest channel, which are calculated statistically from the DEM. Furthermore, the floodplain or terrace surfaces do not need to be manually edited by the user at any point during the process. My method can be run either across the whole landscape, or from a topographic swath profile where features can be compared to a specific channel of interest.

In order to test the performance of the method I have compared it to field-mapped

floodplains and terraces from eight field sites with a range of topographies and grid resolutions. I find that the method performs well when compared to field-mapped floodplain initiation points, published flood risk maps, and digitised terrace surfaces. My method works particularly well in higher relief areas, such as the Russian and South Fork Eel Rivers (CA), where the floodplain and terrace features are constrained within valleys. It is relatively insensitive to grid resolution, allowing the successful extraction of floodplain and terrace features at resolutions of 1 - 10 m.

My new method has numerous applications in both the hydrological and geomorphological communities. It can allow the rapid extraction of floodplain features in areas where the data required for detailed hydrological modelling studies are unavailable, facilitating investigation of flood response, sediment transport, and alluviation. Furthermore, the automated extraction of terrace locations, heights, and other metrics could be used to examine the response of fluvial systems to climatic and tectonic perturbations, as well as the relative importance of lateral and vertical channel incision.

Chapter 5

The relationship between drainage density, erosion rate, and hilltop curvature

The work presented in this chapter was published in the Journal of Geophysical Research: Earth Surface:

Clubb, F.J., Mudd, S.M., Attal, M., Milodowski, D.T., and Grieve, S.W.D. (2016) The relationship between drainage density, erosion rate, and hilltop curvature: implications for sediment transport processes, *Journal of Geophysical Research: Earth Surface* **121**, 1724-1745, doi:10.1002/2015JF003747

The software used and developed in this chapter is available at:

Clubb, F.J., Mudd, S.M., Milodowski, D.T., and Grieve, S.W.D. (2017) LSDDrainageDensity v1.0. *Zenodo*, doi:10.5281/zenodo.824423

This research was conducted in collaboration with the named co-authors, who helped to edit the final manuscript and contributed to software development. I wrote the topographic analysis algorithms, performed the analyses, created the figures, and wrote the manuscript.

Abstract

Drainage density is a fundamental landscape metric describing the extent of the fluvial network. Here I compare the relationship between drainage density (D_d) and erosion rate (E) using the Channel-Hillslope Integrated Landscape Development (CHILD) numerical model. I find that varying the channel slope exponent (n) in detachment-limited fluvial incision models controls the relationship between D_d and E, with $n > 1$ resulting in increasing D_d with E if all other parameters are held constant. This result is consistent when modelling both linear and non-linear hillslope sediment flux. I also test the relationship between D_d and E in five soil-mantled landscapes throughout the USA: Feather River, CA; San Gabriel Mountains, CA; Boulder Creek, CO; Guadalupe Mountains, NM; and Bitterroot National Forest, ID. For two of these field sites I compare D_d to cosmogenic radionuclide (CRN)-derived erosion rates, and for each site I use mean hilltop curvature as a proxy for erosion rate where CRN-derived erosion rates are not available. I find that there is a significant positive relationship between D_d, E, and hilltop curvature across every site, with the exception of the San Gabriel Mountains, CA. This relationship is consistent with an n exponent greater than 1, suggesting that at higher erosion rates, the transition between advective and diffusive processes occurs at smaller contributing areas in soil-mantled landscapes.

5.1 Introduction

One of the most distinctive features of soil-mantled upland landscapes is the repeating patterns of ridges and valleys. The spacing of these ridges and valleys is fundamentally controlled by the competition between creep-like sediment transport processes, which tend to smooth the landscape, and fluvial processes, which incise the landscape [Tarboton *et al.*, 1992; Tucker and Bras, 1998; Perron *et al.*, 2012]. Perron *et al.* [2008a] elegantly demonstrated that the spacing of valleys reflects the relative efficacy of advective (e.g. fluvial) and diffusive (e.g. hillslope) transport processes, both of which may be influenced by climate. Sweeney *et al.* [2015] used laboratory experiments to further demonstrate that the competition between hillslope and valley-forming sediment transport processes controls the degree of landscape dissection. The erosion rate of the landscape plays a major role in controlling the spacing of ridges and valleys, by affecting the relative efficacy of fluvial and hillslope transport processes [Tucker and Bras, 1998; Perron *et al.*, 2008a].

How valley spacing, and the associated landscape properties of hillslope length and drainage density (D_d), change with erosion rates has been predicted to be sensitive to parameters in common fluvial incision models. Fluvial incision can be modelled using a detachment-limited scenario in which the incision rate E is a power-law function of upstream drainage area A and channel slope S_{CH} [e.g. Whipple and Tucker, 1999]:

$$E = KA^m {S_{CH}}^n, \tag{5.1}$$

where K is an erodibility coefficient [T^{-1} L^{1-2m}], and m and n are constant exponents. The m and n exponents in the stream power model have been shown

to control the relationship between erosion rate and topographic gradient [Kirkby, 1980, 1993; Howard, 1997; Tucker and Bras, 1998; Perron *et al.*, 2008a]. This relationship has important implications for how landscapes respond to changing tectonic forcing. Royden and Perron [2013] showed analytically that if the parameters are such that the fluvial incision model forecasts a linear relationship between erosion rate and slope, then river profiles will retain features that reflect changes in erosion rates (such as knickpoints). This is assumed in many studies, and means that river profiles can be inverted to obtain uplift histories over millions of years, for example [e.g. Whittaker *et al.*, 2008; Roberts and White, 2010], under the assumption that knickpoints are not structurally controlled. If the relationship is non-linear, however, channels will be imperfect recorders of channel uplift history as the rate of knickpoint migration becomes a function of incision rate [Royden and Perron, 2013]. The value of these parameters in fluvial incision models also controls whether drainage density is sensitive to changing erosion rates [Tucker and Bras, 1998]. D_d also affects the transit time of water through the landscape and thus exerts a primary control on catchment flood response [Chorley and Morgan, 1962; Carlston, 1963; Gregory and Walling, 1968].

Several authors have predicted, based on numerical and analytical models, the relationship between D_d and metrics describing valley morphology, including slope, erosion rate, and sediment transport process [Kirkby, 1980, 1993; Willgoose *et al.*, 1991; Tucker and Bras, 1998]. Here I build on previous studies that have attempted to examine the relationship between D_d and erosion rate directly [Montgomery and Dietrich, 1989; Oguchi, 1997; Talling and Sowter, 1999; DiBiase *et al.*, 2012]. These studies used varying methods for identifying the channel to hillslope transition, including slope-area scaling relationships. However, such methods can lack precision due to noise when extracting slope from digital elevation models (DEMs). Recently developed methods of channel head identification allow the

extraction of accurate drainage networks from high-resolution DEMs [Passalacqua *et al.*, 2010a,b, 2012; Pelletier, 2013; Clubb *et al.*, 2014]. In addition, early studies were limited by the coarse resolution of the DEMs available at the time.

In this study I aim to evaluate potential controls on the relationship between drainage density and erosion rate, using both numerical modelling and analysis of real landscapes with high-resolution topographic data. I develop a 1D analytical model using linear and non-linear hillslope sediment flux laws, along with detachment-limited fluvial incision models, to examine the effect of different parameters on the relationship between drainage density and erosion rate. I then use the Channel-Hillslope Integrated Landscape Development (CHILD) model [Tucker *et al.*, 2001a] to test my analytical predictions, using both steady-state and transient scenarios. I constrain channel network density using a recently developed technique for extracting channel networks that takes advantage of high-resolution (1 m) light detection and ranging (lidar) datasets in order to test the model predictions on real landscapes. I compare drainage density to basin-averaged erosion rates obtained from detrital cosmogenic radionuclide (CRN) analyses. In sites where CRN-derived erosion rates are not available, I calculate the mean hilltop curvature (C_{HT}) of each basin. Mean C_{HT} has been demonstrated by Hurst *et al.* [2012] to vary linearly with erosion rate in high-relief soil mantled landscapes.

5.2 Theoretical background

The relationship between D_d and erosion rate can be predicted by combining models of river incision with models of hillslope sediment transport [Tarboton *et al.*, 1992; Tucker and Bras, 1998]. Here I model fluvial incision using the stream power model, a common detachment-limited scenario (equation 5.1). Depending

on the values chosen for the exponents m and n, this model can represent fluvial erosion rate as a function of shear stress, for example, or unit stream power [Whipple and Tucker, 1999]. There are significant limitations to this detachment-limited model formulation. It assumes that channel width scales with contributing area, and it does not take into account the effects of sediment flux or the impact of stochasticity and thresholds, all of which can modulate fluvial incision for a given channel geometry [Lague, 2014]. However, Gasparini and Brandon [2011] found that sediment flux and threshold effects can be cast in the general form of equation 5.1. It is often used to examine fluvial response to changing climatic and tectonic conditions, for example, by solving for the relationship between channel slope and contributing area, assuming uniform incision [Hack, 1973; Flint, 1974; Howard and Kerby, 1983; Sklar and Dietrich, 1998; Wobus *et al.*, 2006]:

$$S_{CH} = \left(\frac{E}{K}\right)^{\frac{1}{n}} A^{-m/n}. \tag{5.2}$$

Choosing correct values of the exponents m and n is important in landscape evolution studies, because these values control the relationship between landscape steepness and erosion rates, as well as the competition between advective (fluvial) and diffusive (hillslope) processes. Although the m/n ratio has been reported for many landscapes [Stock and Montgomery, 1999; Whipple and Tucker, 1999; Anthony and Granger, 2007; Perron and Royden, 2013; Mudd *et al.*, 2014], relatively few studies have reported individual values for the m and n exponents, as the erosion rate and K coefficient must be known. In particular, the slope exponent n is a critical parameter as it largely controls the timescale and magnitude of fluvial response to perturbations [Whipple and Tucker, 1999]. Howard and Kerby [1983] studied a gradient in erosion rates across badlands in Virginia and suggested values of $m = 0.45$ and $n = 0.7$. Whittaker and Boulton [2012] examined knickpoint retreat rates above active faults in the Mediterranean

and found that increasing channel steepening with fault throw rate may be explained only if the n exponent is greater than 1.3. Lague [2014] reanalysed data from a range of studies, and suggested that $m \approx 1$ and $n \approx 2$ in most cases, with a few exceptions. Data from the Siwaliks in the Himalayas [Lavé and Avouac, 2001], Eastern Tibet [Ouimet *et al.*, 2009], and the Mendocino triple junction in the Western USA [Snyder *et al.*, 2000] suggest values of $m = 0.55$, 0.85, and 2 and $n = 1.1$, 1.7, and 4 respectively [Lague, 2014]. Whipple *et al.* [2000] argued that the n exponent depends on the dominant erosion process and varies between $\sim 2/3$ and $\sim 5/3$. Royden and Perron [2013] used transformed river long profiles along with previously-determined uplift rates for the Rio Torto in the central Apennines to estimate an n value of approximately 0.5. Mudd *et al.* [2014] analysed the gradient (M_χ) of these transformed profiles to estimate $0.52 < n < 0.82$ for the Rio Torto. A recent global study of the stream power law parameters by Harel *et al.* [2016] found that in most landscapes the exponent n is greater than 1.

The n exponent may be constrained by examining the relationship between D_d and erosion rate [Tucker and Bras, 1998]. I represent drainage density using the downslope distance from the hilltop to the valley head, L_h, at which the slopes above and below the valley head are equal. The equilibrium slope for linear hillslope diffusion (S_H) can be expressed as [e.g., Roering *et al.*, 2001]:

$$S_H = \frac{E}{D} L_h, \tag{5.3}$$

where D represents a diffusivity coefficient [$\mathrm{L}^2\ \mathrm{T}^{-1}$]. I assume that D and K do not vary with erosion rate. In order to equate the channel slope, S_{CH}, given by equation 5.2, with S_H, I assume that the contributing area A at the channel head is given by a flow strip of length L_h [L] and width w [L], where $A = L_h b$:

$$S_{CH} = \left(\frac{E}{Kw^m}\right)^{\frac{1}{n}} L_h^{-m/n}. \tag{5.4}$$

I can equate the slopes above and below the channel head, given by S_H and S_{CH} respectively (equations 5.3 and 5.4), to obtain the mean length of overland flow:

$$L_h = D^{1/(1+(m/n))} k_f^{-1/(m+n)} E^{(1-n)/(m+n)}, \tag{5.5}$$

where $k_f = Kw^m$. This reduces to $k_f = K$ [T^{-1} L^{1-3m}] if I assume a rectangular flow strip of unit width (i.e., $w = 1$ m). The mean length of overland flow is approximately equal to half the reciprocal of D_d [Horton, 1945], and therefore equation 5.5 can be converted to:

$$\frac{1}{2D_d} = D^{1/(1+(m/n))} K^{-1/(m+n)} E^{\psi}, \tag{5.6}$$

where $\psi = (1-n)/(m+n)$. The relationship between D_d and erosion rate E depends on the slope exponent n, shown in Figure 5.1a. If $n > 1$, the contributing area at the channel head will decrease with increasing erosion rate and D_d will therefore increase. However if $n < 1$ then D_d will decrease with increasing erosion rate [Tucker and Bras, 1998]. Performing a power-law regression on a plot of mean length of overland flow against erosion rate allows the calculation of the n exponent, assuming the m/n ratio is known, as ψ is the gradient of the regression.

The theory outlined above assumes that hillslope sediment transport occurs by linear diffusion (equation 5.3). However, in many high-relief landscapes hillslope sediment transport has been suggested to become nonlinear, increasing rapidly as

the gradient approaches a critical value [Roering *et al.*, 1999]. Nonlinear hillslope sediment flux (q_s, $L^3/L/T$) can be modelled according to:

$$q_s = \frac{DS_H}{1-(S_H/S_c)^2}, \tag{5.7}$$

where S_c is a threshold slope gradient beyond which q_s tends to infinity [Roering *et al.*, 1999, 2001]. Under this regime, hillslope gradient can be stated as [e.g. Roering *et al.*, 2001]:

$$S_H = \frac{DS_c^2}{2EL_h}\left(\sqrt{1+\left(\frac{2EL_h}{DS_c}\right)^2}-1\right). \tag{5.8}$$

Due to the non-linearity of equation 5.8, there is no analytical solution equivalent to equation 5.6. Instead I show numerical results for D_d as a function of E in the case of non-linear hillslope sediment transport in Figure 5.1b.

The analytical model outlined above is the simplest case scenario, with a number of assumptions. For example, I assume a linear relationship between A and L_h. Alternative model formulations are possible, such as that of a power-law relationship, where $A = bL_h{}^y$ [Pelletier *et al.*, 2016]. However, using this alternative power-law relationship predicts the same relationship between D_d and E as that of the simpler scenario (see Appendix). Furthermore, this model scenario neglects colluvial infilling of the channel head (equation 5.4). Pelletier *et al.* [2016] present a transport-limited model for predicting drainage density, calibrated for the Walnut Gulch Experimental Watershed, Arizona, where they assume that the channel head occurs where the fluvial erosion rate is greater than the colluvial deposition rate by an amount equal to the net erosion rate E. In the model outlined above, I follow a similar approach to Tucker and Bras [1998] by assuming that the channel head occurs where the fluvial erosion rate is greater

than colluvial erosion. Including colluvial deposition at the channel head in my analytical model may lead to decreased absolute values of drainage density. In order to test these simple 1D predictions I therefore carried out 2D numerical modelling, described in Section 5.3.1.

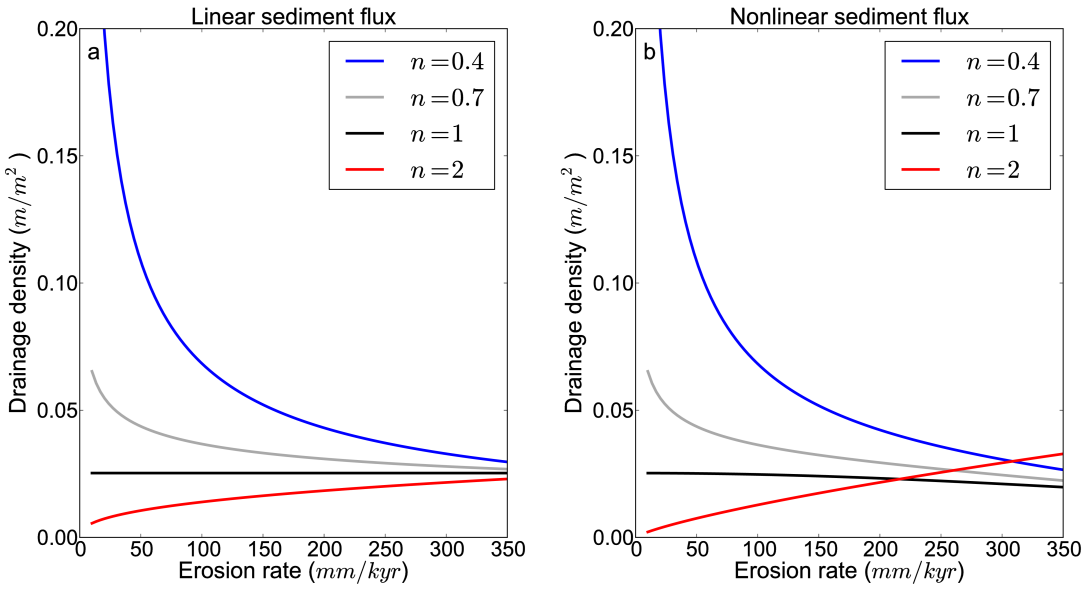

Figure 5.1: Analytical predictions of the relationship between drainage density and erosion rate for a) linear hillslope sediment flux, b) nonlinear hillslope sediment flux. I set parameters in equations 5.6 and 5.8 to the following: $D = 0.0088$ m^2 yr^{-1}, $K = 1 \times 10^{-4}$ m yr^{-1}, $m = 0.5$, and $S_c = 1.25$. The values of these parameters are the same as for the numerical modelling runs (Table 5.1). The relationship depends on the value of n in the stream power law: I predict a positive relationship for $n > 1$, a negative relationship for $n < 1$, and no relationship between D_d and E for $n = 1$.

5.3 Methodology

5.3.1 Landscape evolution modelling

In order to test whether the theory outlined by equations 5.1 - 5.8 is applicable in 2D, I analyse a series of model landscape evolution scenarios created using the Channel-Hillslope Integrated Landscape Development (CHILD) model [Tucker *et al.*, 2001a]. In the model, topography evolves based on a combination of fluvial incision using the stream power law (equation 5.1), as well as linear and non-linear diffusive hillslope sediment transport (equations 5.3 and 5.7). The model domain is 500 m by 500 m with a node spacing of 5 m, comparable to the size of the catchments extracted and the DEM resolution of the real datasets respectively. Although the real datasets have a DEM resolution of 1 m, I could not run the numerical models at the same resolution due to computational constraints. The domain has one boundary set to a fixed elevation ($z = 0$ m) and three boundaries set to no flux. I detail the model setup and the values of all parameters used in the Appendix and Table 5.1.

I ran three different series of scenarios with different values of n. My first scenario set $n = 1$ and $m = 0.5$, where erosion is proportional to specific stream power. I then kept all other parameters constant while changing the value of n. I ran further scenarios with $n = 0.4$, $n = 0.7$, and $n = 2$. I chose these values of n in order to run scenarios with different values of ψ. For each scenario, several runs were performed with uplift rates varying between 10 and 320 mm/kyr. I ran each simulation for 5×10^6 years to allow the topography to reach steady state, which I determined as occurring when the volume of rock above sea level in the modelled domain became constant. Figures 5.2a and 5.2b show examples of the topography generated during these runs with high and low erosion rates. The CHILD model uses a triangulated irregular network (TIN). I converted the

Table 5.1: Parameter values chosen for CHILD model runs

Parameter	Value	Justification
Mean precipitation rate	0.75 mm hr^{-1}	Preserved from Mudd *et al.* [2014]
Mean storm duration	22 h	Preserved from Mudd *et al.* [2014]
Mean interstorm duration	260 h	Preserved from Mudd *et al.* [2014]
Specific weight of water, k_g	9810 kg m^{-2} s^{-2}	Preserved from Mudd *et al.* [2014]
Channel width coefficient, k_w	4.6 $m^{-1/2}$ $s^{1/2}$	Preserved from Mudd *et al.* [2014]
Erodibility coefficient, k_b	1×10^{-4} m yr^{-1} (W $m^{-2})^{-1}$	Adjusted from Mudd *et al.* [2014] to account for varying n values
Hillslope transport coefficient, D	0.0088 m^2 yr^{-1}	Calculated by Hurst *et al.* [2013b] for Feather River CA
Critical slope S_c (nonlinear runs)	1.25	Calculated by Roering *et al.* [1999] for Oregon Coast Range

output TINs to rasters and performed the same topographic analysis as with the real datasets, described in the following sections. I extracted the channel network and calculated the drainage density for the whole catchment generated; the methodology for channel extraction is described in Section 5.3.4. I also computed mean C_{HT} for each run following the methodology outlined in Section 5.3.5. I further wished to examine the effect of different hillslope transport laws on the relationship between D_d and C_{HT} for varying values of n. Therefore all my steady-state scenarios have been run twice, using linear and non-linear hillslope sediment flux laws (equations 5.3 and 5.7, respectively).

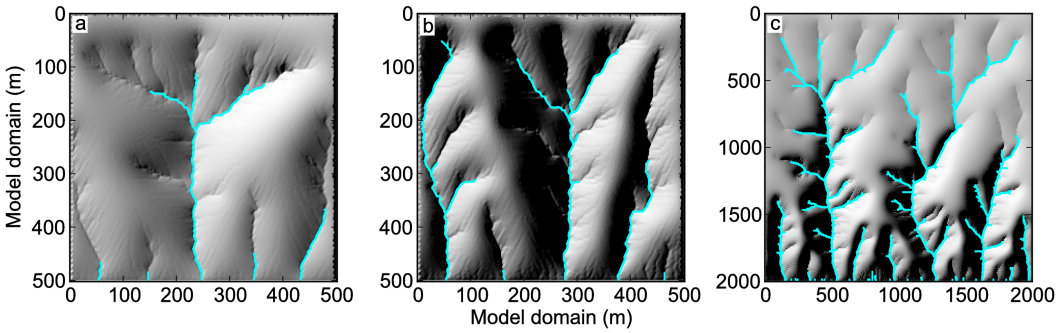

Figure 5.2: Example of topography and channel networks extracted from CHILD runs for n = 2. The lower boundary of the model is fixed, with the other boundaries set to no flux. (a) Steady state run with U = 110 mm/kyr, maximum elevation of 163 m. (b) Steady state run with U = 320 mm/kyr, maximum elevation of 351 m. (c) Transient run with U = 40 mm/kyr for 60 Ma then increased to 320 mm/kyr for 1 Ma, maximum elevation of 595 m.

In addition to steady state runs, I examined a transient scenario for three values of n: $n = 1$, $n = 2$, and $n = 0.7$ with linear hillslope sediment transport. I ran these scenarios to test whether such landscapes conform to the same theory, and whether spatial changes in drainage density resulting from varying erosion rates can be detected. These were performed with a larger model domain (2000 m by 2000 m) in order to examine the variation in drainage density across different basins in the same landscape (Figure 5.2c). The model was run at a low uplift rate

(40 mm/kyr) for 20×10^6 years, then the uplift rate was increased to 320 mm/kyr for 1×10^6 years. This allowed me to compare basins responding to different uplift rates in the same model landscape. The transient scenarios were analysed following the same procedures (Sections 5.3.4 and 5.3.5), with the drainage density and hilltop curvature extracted for different basins in the domain.

A potential limitation of using the CHILD model is that the hillslope sediment transport term does not account for flow width (equation 5.3) [Howard, 1994; Pelletier, 2010]. Pelletier [2010] suggested that, if the grid resolution of the model (R_G) is greater that that of the valley width (w_v), the diffusive transport term should be scaled by a ratio of R_G/w_v. This is not accounted for in CHILD, suggesting that my model runs may underestimate the colluvial deposition rate and potentially predict higher drainage densities. In order to test the sensitivity of my model scenarios to grid resolution, I ran the steady-state scenarios at grid resolutions of 2.5 m, 7.5 m, and 10 m, along with the original 5 m runs. I found that the predicted relationship between D_d and E was independent of grid resolution (Appendix, Figures 7.3 - 7.5).

5.3.2 Study areas

As well as testing these predictions on model landscapes, I report D_d and hilltop curvature for five field sites with 1 m resolution lidar data: two sites in California, one site in Colorado, one site in New Mexico, and one site in Idaho (Figure 5.3). These sites were chosen based on the following criteria: (i) the availability of 1 m resolution lidar data; (ii) relatively uniform lithology across the site; and (iii) a gradient in erosion rates across the landscape, either measured or inferred based on highly variable slopes and ridgetop curvatures. Table 5.2 summarises the mean annual temperature and mean annual precipitation of each site [PRISM Climate Group, http://prism.oregonstate.edu], the underlying lithology, and the

elevation range. These sites are predominantly soil-mantled, as shown in Table 5.2, although some of these sites have bedrock outcrops, such as the Guadalupe Mountains and the San Gabriel Mountains, which becomes bedrock-dominated in the rapidly eroding parts of the landscape [DiBiase *et al.*, 2010]. Debris flows are also prevalent at the San Gabriel Mountains site [DiBiase *et al.*, 2012].

Table 5.2: Details of climate and lithology for each field site[1]

Field site	UTM Zone	MAP (mm)	MAT (°C)	Lithology	Elevations (m AMSL)	Soil ridgetops (%)[2]	Difference in gradient (%)[3]
Feather River, CA	10°N	1796	13.8	Granite, granodiorites, tonalite	225-1549	94	24.3
San Gabriel Mts, CA	11°N	685	13.7	Granite	1076-2010	87	19.5
Boulder Creek, CO	13°N	566	5.9	Gneiss and granite	1652-3519	85	13.8
Guadalupe Mts, NM	13°N	454	13.5	Limestone, dolomite	1536-1980	98	9.9
Bitterroot National Forest, ID	11°N	830	3.9	Mica schist and gneiss	816-2497	70	11.3

[1] MAP = mean annual precipitation; MAT = mean annual temperature [PRISM Climate Group]

[2] Calculated following Milodowski *et al.* [2015b]

[3] Mean percentage difference between gradients 2 m above and below channel heads

5.3.3 Cosmogenic radionuclide (CRN)-derived erosion rates and study basins

In order to examine the relationship between D_d and erosion rate, published CRN-derived erosion rates were compiled from two sites: Feather River, CA [Riebe *et al.*, 2000; Hurst *et al.*, 2012] and Boulder Creek, CO [Dethier *et al.*,

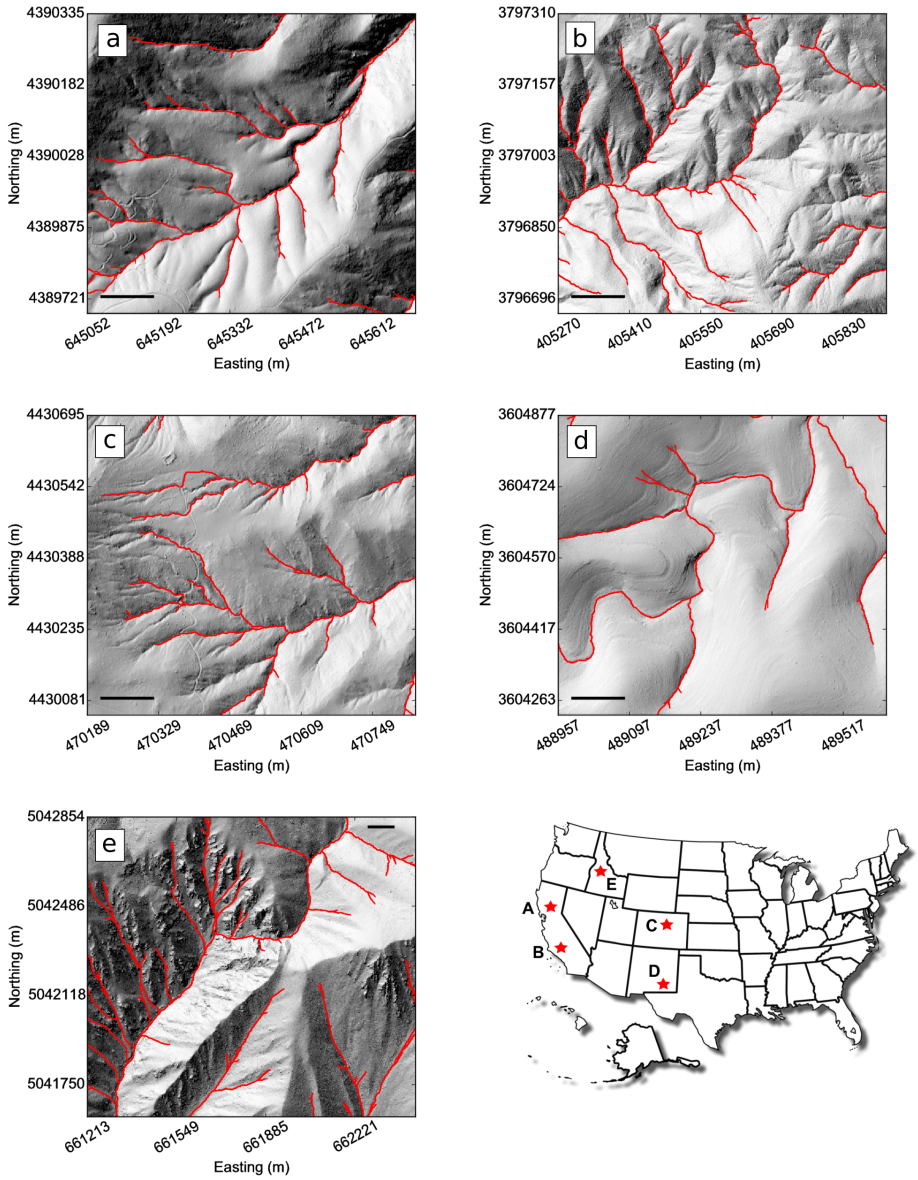

Figure 5.3: Shaded relief maps of part of each field site with drainage network extracted using the DrEICH algorithm. The scale bar on each map is 100 m. (a) Feather River, CA. UTM Zone 10°N. (b) San Gabriel Mountains, CA. UTM Zone 11°N. (c) Boulder Creek, CO. UTM Zone 13°N. (d) Guadalupe Mountains, NM. UTM Zone 13°N. (e) Bitterroot National Forest, ID, UTM Zone 11°N. (f) USA state map showing location of field sites (a)-(e).

2014] summarised in Table 5.3. No CRN data are available for the other sites. The catchment-averaged erosion rates for the Feather River field site were derived using ^{10}Be concentrations from fluvial sands, assumed to have minimal storage in the fluvial system, by Riebe *et al.* [2000] and Hurst *et al.* [2012]. A total of 21 CRN-derived erosion rates are available for the Feather River. These erosion rates span an order of magnitude, varying from 12.5 ± 1.4 mm/kyr to 253.8 ± 66.6 mm/kyr. CRN-derived erosion rates for the Boulder Creek field site were also calculated by measuring ^{10}Be concentrations from quartz in alluvial channel sediments by Dethier *et al.* [2014]. Within the Boulder Creek catchment there are twelve basins for which a CRN-derived erosion rate is available, ranging from 14.97 ± 1.25 mm/kyr to 62.92 ± 5.96 mm/kyr.

Two sets of study basins were used in the analysis. The first set of study basins included all catchments for which there were CRN-derived erosion rates available (the two sites above). The second set of study basins, extracted for each of the five sites, included all third order basins. I chose to use third order basins to sample across a large number of catchments at different erosion rates in each site. I obtained the mean hilltop curvature for each of these basins to use as a proxy for erosion rate where CRN-derived erosion rates were not available, as previous work by Hurst *et al.* [2012] demonstrated that hilltop curvature scales linearly with erosion rate.

5.3.4 Drainage density

D_d was calculated for each of the study basins using the DrEICH method, a channel head extraction algorithm [Clubb *et al.*, 2014]. The DrEICH method extracts channel heads based on transforming river profiles into χ-elevation space [Perron and Royden, 2013], identifying the upstream transition between fluvial and hillslope processes [Clubb *et al.*, 2014]. Perron and Royden [2013] showed

Table 5.3: Compiled CRN samples from Feather River, CA, and Boulder Creek, CO[1]

Field site	Basin ID	Easting	Northing	Erosion rate (mm/kyr)	Standard deviation (mm/kyr)	Author
FR	FR-2	640504.27	4391321.67	125.9	23.2	Hurst et al. 2012
FR	FR-4	647490.78	4388656.03	253.8	66.6	Hurst et al. 2012
FR	FR-5	648350.75	4388752.06	133.3	31.9	Hurst et al. 2012
FR	FR-6	643053.99	4388961.32	25.2	2.7	Hurst et al. 2012
FR	FR-7	643117.49	4389018.47	18.5	2.0	Hurst et al. 2012
FR	FR-8	643790.59	4391155.89	12.5	1.4	Hurst et al. 2012
FR	FR-9	643346.09	4390768.54	14.4	1.6	Hurst et al. 2012
FR	FR-10	642298.33	4389824.92	24.3	2.7	Hurst et al. 2012
FR	BRB-2	645334.53	4389864.62	38.6	3.4	Hurst et al. 2012
FR	BRB-6	645336.52	4389843.51	35.7	4.7	Hurst et al. 2012
FR	BRB-8	645547.44	4390101.49	90.3	8.5	Hurst et al. 2012
FR	BEAN-1	643390.54	4386092.39	43.8	3.7	Hurst et al. 2012
FR	BEAN-2	643479.44	4387197.29	44.8	3.7	Hurst et al. 2012
FR	BEAN-4	643536.59	4387349.69	65	5.3	Hurst et al. 2012
FR	BEAN-5	643333.39	4388156.14	45.1	3.8	Hurst et al. 2012
FR	BEAN-7	643511.19	4387851.34	90.7	7.2	Hurst et al. 2012
FR	FT-3	644875.52	4392651.31	26.2	2.3	Hurst et al. 2012
FR	FT-4	644872.88	4392628.56	24.9	2.2	Hurst et al. 2012
FR	FT-6	644462.24	4393416.23	23.6	2.1	Hurst et al. 2012
FR	BS-1	650229.72	4397969.15	99.9	9.7	Riebe et al. 2000
FR	SB-1	650758.89	4398041.91	75.4	6.6	Riebe et al. 2000
BC	DC-01-01	459127.15	4424213.09	31.4	2.56	Dethier et al. 2014
BC	DC-01-03	470265.96	4411862.60	18.48	1.55	Dethier et al. 2014
BC	DC-01-04	463608.27	4401576.01	23.3	1.96	Dethier et al. 2014
BC	DC-01-05	471610.16	4399252.56	20.72	1.78	Dethier et al. 2014
BC	DC-01-06	465526.88	4423375.63	32.77	2.7	Dethier et al. 2014
BC	DC-01-09	459882.61	4445285.94	18.98	1.6	Dethier et al. 2014
BC	DC-01-11	472690.03	4450295.82	22.39	1.88	Dethier et al. 2014
BC	DC-01-12	467600.04	4459486.53	14.86	1.26	Dethier et al. 2014
BC	DC-01-14	466043.22	4473501.55	17.14	1.45	Dethier et al. 2014
BC	DC-01-16	470649.89	4503943.49	21.62	1.78	Dethier et al. 2014
BC	DC-01-19	347619.84	4466934.06	29.51	2.43	Dethier et al. 2014
BC	OW-01-07	337088.69	4568762.91	30.75	2.57	Dethier et al. 2014
BC	JFC-02-03	429688.04	4450427.15	37.67	3.35	Dethier et al. 2014
BC	MJ-BC-01	445725.68	4421257.71	19.48	1.68	Dethier et al. 2014
BC	MJ-BC-17	449479.18	4433367.11	28.94	2.41	Dethier et al. 2014
BC	JFW-02-13	471124.81	4562497.45	22.81	1.92	Dethier et al. 2014
BC	DC-09-18	460869.07	4429299.65	19.41	1.58	Dethier et al. 2014
BC	DC-09-20	459448.16	4429799.91	14.97	1.25	Dethier et al. 2014
BC	DC-01-17	427084.65	4525460.09	37.11	3.02	Dethier et al. 2014
BC	DC-01-18	343228.15	4477463.60	47.58	3.85	Dethier et al. 2014
BC	OW-01-08	384303.27	4695037.67	286.62	31.09	Dethier et al. 2014

[1] FR = Feather River, UTM Zone 10°N; BC = Boulder Creek, UTM Zone 13°N.

that river profiles are linearised when transformed into χ-elevation space. The DrEICH algorithm identifies channel heads as the point at which these profiles become non-linear, representing the transition to hillslope processes [Clubb *et al.*, 2014]. In order to extract channel networks for each field site via the DrEICH methodology, the m/n value for the landscape must be calculated. This was done using the independent statistical collinearity tests described by Mudd *et al.* [2014] which assume channel profiles are made up of a number of different segments depending on heterogeneities and spatial variations in incision rate within the river profile. The collinearity test loops through all potential m/n values and performs a piecewise linear regression on the profile. For each regression the Akaike information criterion (AIC) is calculated [Akaike, 1974], which measures how well the data fit the regression whilst penalizing for over-fitting. The best fit m/n is selected at the minimum AIC value.

I ran the test described by Mudd *et al.* [2014] on two catchments at each field site using 10 m DEMs derived from the United States Geological Survey's National Elevation Dataset. I used the National Elevation Dataset instead of the lidar data at each field site to provide a larger area for calculation of the m/n ratio and to reduce computational cost. The Mudd *et al.* [2014] algorithms require four user-defined parameters: the target skip value, the standard deviation of the elevation data (σ), the minimum segment length, and the number of target nodes (for a detailed description of each of these parameters see Mudd *et al.* [2014]). The value of these parameters can influence the result of the m/n analysis. I performed a sensitivity analysis by changing each parameter and examining the variation in m/n ratios extracted. In total I ran 54 combinations of the parameters to determine the best fit m/n. I varied the skip parameter between 1 and 3, the number of target nodes between 80 and 100, and the minimum segment length between 10 and 20 nodes. I used a σ value of 3 m for all field sites, as analyses performed by Mudd *et al.* [2014] showed that the most reliable m/n ratios were

calculated when σ values were $\leq$ 3 m. I used the mean value of the sensitivity analyses as the best fit m/n for the sites; mean, median and standard deviation of the analyses are reported in Table 5.4.

Table 5.4: Calculated best-fit m/n ratios for each field site

Field site	Mean m/n	Median m/n	Standard deviation
Feather River, CA	0.30	0.25	0.141
San Gabriel Mountains, CA	0.42	0.438	0.146
Boulder Creek, CO	0.42	0.425	0.037
Guadalupe Mountains, NM	0.39	0.275	0.129
Bitterroot National Forest, ID	0.31	0.325	0.02

The DrEICH algorithm first identifies concave portions of the landscape using a curvature threshold, which is calculated using the quantile-quantile method of Passalacqua *et al.* [2010a]. First of all, the DEM is smoothed using optimal Wiener filtering, which distinguishes the large scale signal of the fluvial-hillslope system from microtopographic noise [Pelletier, 2013]. After smoothing the DEM, the curvature threshold is calculated based on a quantile-quantile plot of the distribution of curvature in each landscape (for more details on this methodology see Passalacqua *et al.* [2010a,b, 2012]). The DrEICH algorithm identifies the upstream extent of fluvial incision within the valleys based on χ-transformed longitudinal profiles [Clubb *et al.*, 2014]. It assumes that the channel profile will be made up of two segments in χ-elevation space: a linear channel segment and a non-linear hillslope segment. The channel head in each valley is calculated as the transition point between the best-fit linear channel segment and non-linear hillslope segment. The DrEICH algorithm was tested against 167 field-mapped channel heads from a variety of landscapes by Clubb *et al.* [2014], and was found to accurately reproduce the field-mapped channel networks when compared to other channel extraction methods. The analytical model described in Section 5.2

relies on equating the channel and hillslope gradient at the channel head. In order to test whether these were comparable, I extracted the gradient 2 m above and below each channel head for every field site, and calculated the percentage difference between the two gradients. I then calculated the mean percentage difference across each landscape (Table 5.2). For each field site there was less than 25% mean difference in the gradients above and below the channel heads, suggesting that the assumption of equating the slopes in the analytical model is valid.

For each basin of interest, I then extracted the total length of channels via the DrEICH method, and divided it by the basin contributing area to calculate the D_d (expressed in m/m^2). I extracted the drainage density for two different sets of basins: all basins with CRN-derived erosion rates where these were available (the Feather River and Boulder Creek field sites), and all third order basins for every field site to investigate the relationship between D_d and mean C_{HT}.

5.3.5 Mean hilltop curvature

Mean C_{HT} may be used to infer the distribution of erosion rates across the landscape [Roering *et al.*, 2007; Hurst *et al.*, 2012]. Hurst *et al.* [2012] demonstrated that mean C_{HT} continues to vary linearly with erosion rate after hillslope gradient has become insensitive to increasing erosion rate. Mean C_{HT} has been demonstrated to respond rapidly to changing channel steepness in soil-mantled landscapes, and can therefore be used as a proxy for erosion rate in areas where CRN-derived erosion rates are not available [Hurst *et al.*, 2013a]. In order to ensure the landscapes were dominantly soil-mantled, I calculated the percentage of ridgetops that were soil-mantled in each field site using the surface roughness algorithm described in Milodowski *et al.* [2015b]. I detect patches of bedrock from the lidar DEMs, using a surface roughness ratio of 0.015 as the threshold for

bedrock, following Milodowski *et al.* [2015b]. The roughness ratio is a measure of the local variability of the surface normal vectors, which has been shown to correspond to the outcrop of bedrock [Milodowski *et al.*, 2015b]. The percentage of ridgetops identified as soil-mantled are reported in Table 5.2, and is $\geq 70\%$ for every field site. In some circumstances, C_{HT} may not reflect the variability of erosion rates across the landscape. In transient landscapes, some basins may contain knickpoints, leading to differing erosion rates within the same basin. Therefore, hilltops connected to the channel above and below the knickpoint may not be adjusted to the same channel incision rate [e.g., Mudd and Furbish, 2007; Reinhardt *et al.*, 2007; Anderson *et al.*, 2012; Hurst *et al.*, 2012, 2013a]. In addition, the presence of landslides in some high-relief basins may lead to decoupling of hilltops from the channel network. To avoid such issues, I visually excluded basins with landslides or knickpoints evident from the lidar DEM.

Ridgetops were mapped as the intersecting margins of basins from zeroth stream order and upwards, following the methodology of Hurst *et al.* [2012] and Grieve *et al.* [2016c]. Only hilltops internal to each study basin were considered, in order to ensure that C_{HT} was adjusted to the erosion rate within each basin. Curvature was calculated using polynomial surface fitting with a circular window radius of 7 m [Hurst *et al.*, 2012]. The polynomial surface has the form:

$$z = ax^2 + by^2 + cxy + dx + ey + f, \tag{5.9}$$

where curvature (C) and slope (S) can be determined from the fitted coefficients:

$$C = 2a + 2b, \tag{5.10a}$$

$$S = \sqrt{d^2 + e^2}. \tag{5.10b}$$

The size of the window radius is determined through identifying scaling breaks in the interquartile range and standard deviation of the curvature [Lashermes *et al.*, 2007; Roering *et al.*, 2010; Hurst *et al.*, 2012]. This ensures that curvature is sampled over a length scale characteristic of hillslope to valley transitions. Mean C_{HT} was computed for each third order basin. The relationship between C_{HT} and D_d was then examined across each field site.

5.3.6 Constraints on the n exponent

Theoretically the n exponent in the detachment-limited incision model (equation 5.1) may be calculated using the relationship between the mean length of overland flow (inversely proportional to drainage density) and the erosion rate, if known. I fitted a power-law to the relationship between mean length of overland flow and erosion rate for the two field sites with CRN-derived erosion rates available: Feather River, California, and Boulder Creek, Colorado. I used the gradient of the regression, ψ to calculate the n exponent based on equation 5.6.

5.4 Results

5.4.1 Landscape evolution modelling

For each of the steady state modelling scenarios ($n = 0.4$, $n = 0.7$, $n = 1$, and $n = 2$) the relationship between D_d and uplift rate was plotted for both linear and non-linear hillslope sediment transport (Figures 5.4 and 5.5). Figure 5.4 shows that in the scenarios with linear hillslope sediment transport, there is a positive relationship between drainage density and uplift rate (and therefore erosion rate as the scenarios are at steady state) for $n = 2$; a negative relationship for $n = 0.7$

and $n = 0.4$; and that drainage density is invariant with uplift rate for $n = 1$. The negative relationship between D_d and U is steeper for $n = 0.4$ than $n = 0.7$, as would be expected from equation 5.6 and Figure 5.1.

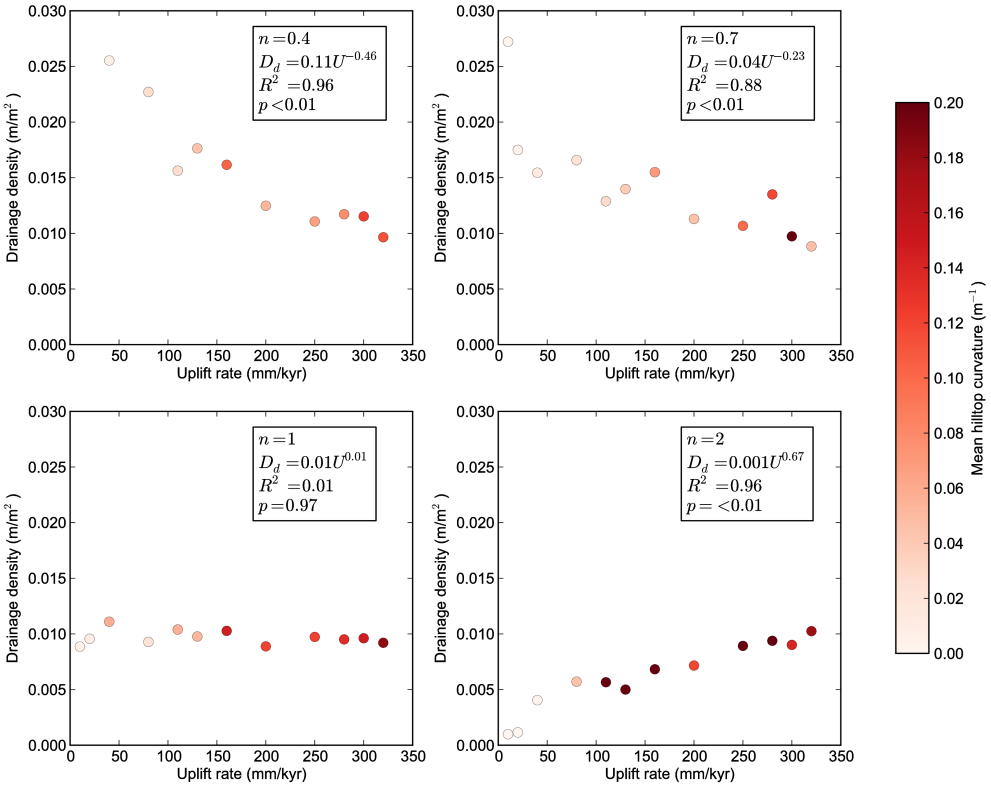

Figure 5.4: Results of CHILD modelling for steady state scenarios with linear hillslope sediment transport. Plots indicate measured relationship between drainage density and uplift rate where $n = 0.4$, $n = 0.7$, $n = 1$, and $n = 2$. The points are coloured by mean hilltop curvature: lighter colours indicate low curvature values and darker colours indicate high values.

I fit a linear regression to the relationship between hilltop curvature and uplift rate based on the predictions of erosion rate and mean C_{HT} set out by Roering *et al.* [2007] and following the methodology of Hurst *et al.* [2012], shown in Figure

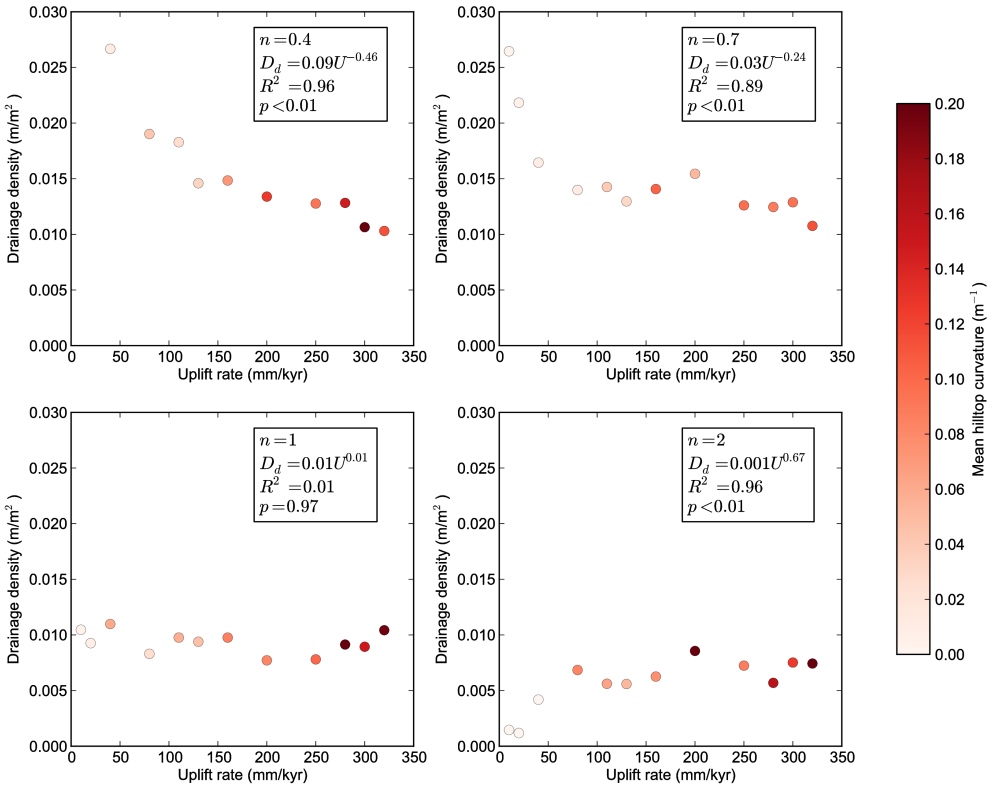

Figure 5.5: Results of CHILD modelling for steady state scenarios with non-linear hillslope sediment transport. Plots indicate measured relationship between drainage density and uplift rate where $n = 0.4$, $n = 0.7$, $n = 1$, and $n = 2$. The points are coloured by mean hilltop curvature: lighter colours indicate low curvature values and darker colours indicate high values.

5.6. I find a significant positive relationship between mean C_{HT} and uplift rate for both the linear and non-linear hillslope sediment transport scenarios.

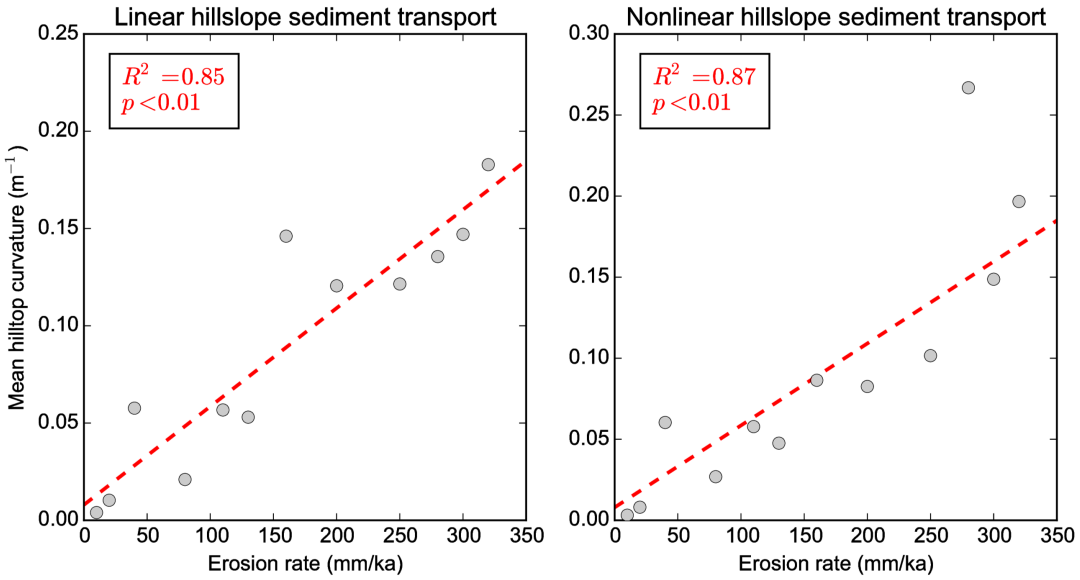

Figure 5.6: Scatter plots of mean hilltop curvature against uplift rate for steady-state CHILD modelling scenarios where n = 1, showing both linear and non-linear hillslope sediment flux. A significant positive linear relationship is found for both sediment transport scenarios, with R^2 values of 0.85 and 0.87 respectively.

These results in an ideal landscape mirror those from the theory (Section 5.2) and justify the use of C_{HT} as an indicator of erosion rate in soil-mantled landscapes. The same general trends between D_d and U are apparent for non-linear sediment transport (Figure 5.5). Figure 5.1b suggests that the relationship between D_d and uplift rate should be steeper for $n = 2$ for non-linear sediment transport, which is not evident from the modelling results. My transient simulations (Figure 5.7) show the same trends as the steady-state runs, suggesting that the same theory can be applied to transient landscapes.

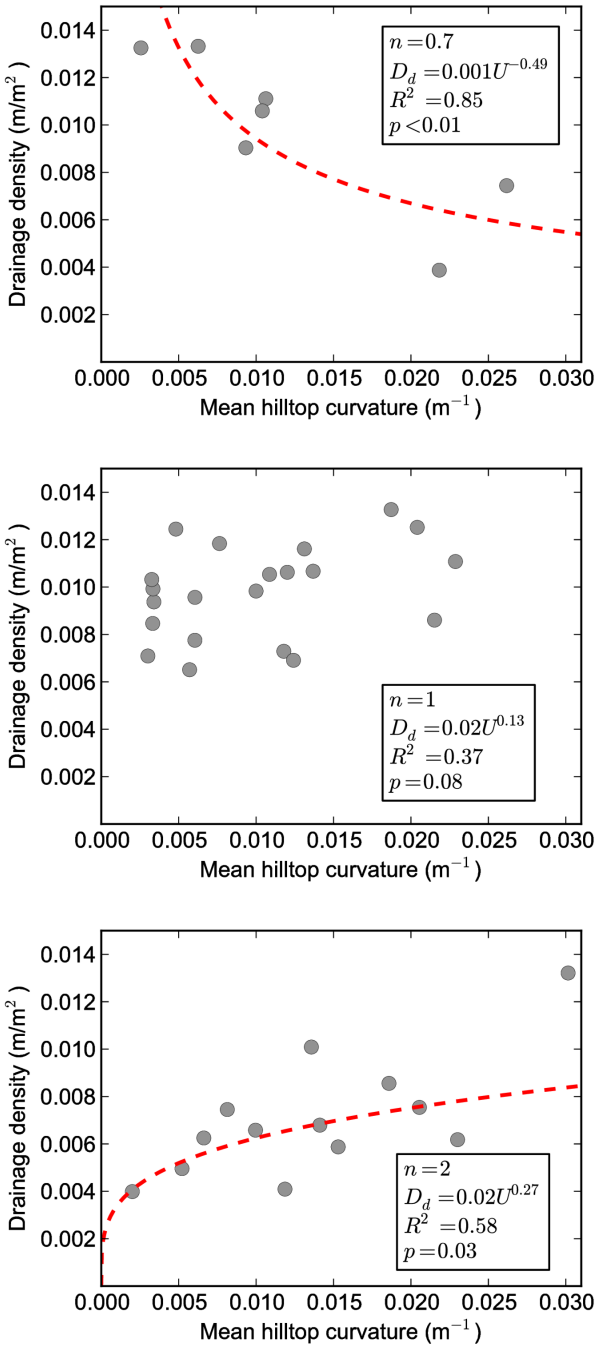

Figure 5.7: Results of CHILD modelling for transient scenarios with linear hillslope sediment flux. Plots indicate measured relationship between drainage density and mean hilltop curvature where $n = 0.7$, $n = 1$, and $n = 2$.

5.4.2 CRN-derived erosion rates and drainage density

For the real landscapes, I created scatter plots of D_d against CRN-derived erosion rates for the two field sites with available CRN data: Feather River, CA, and Boulder Creek, CO. A power-law regression was fitted to the raw data for each of the field sites (Figure 5.8). A regression was deemed to be significant if the p value was less than 0.01 (99% confidence interval). Figure 5.8 shows that for both the Feather River and Boulder Creek field sites there is a positive relationship between erosion rate and D_d. The regressions for the Feather River and Boulder Creek both have p values <0.01, and R^2 values of 0.76 and 0.82 respectively. The exponents on the power-law relationships (ψ) are 0.91 and 1.37 respectively.

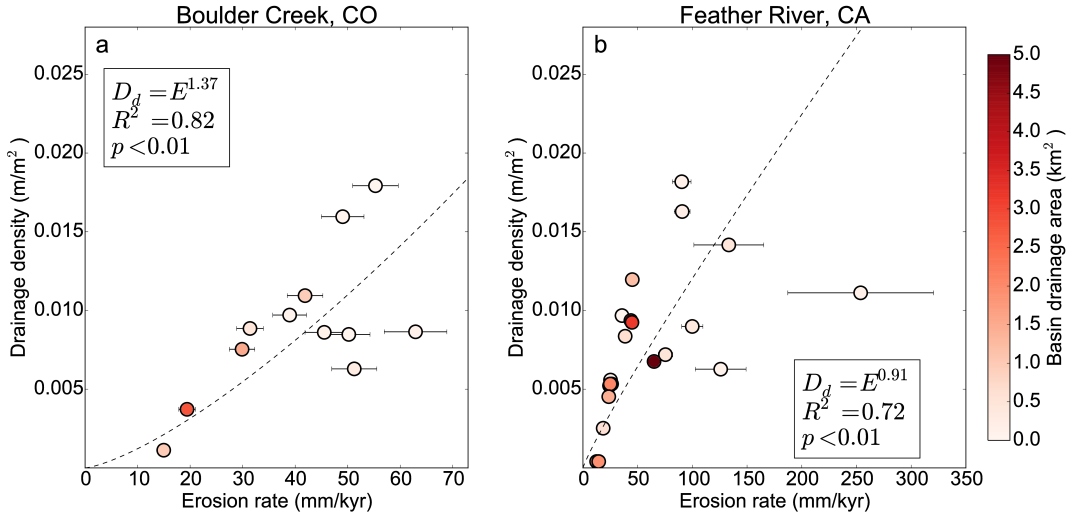

Figure 5.8: Scatterplots showing relationship between CRN-derived erosion rate and drainage density (D_d) with a fitted power-law relationship. The R^2 and p value of the regressions are also shown. The points are coloured based on the contributing area of the basin, with white representing low contributing areas and dark red representing high contributing areas. (a) Scatterplot for the Boulder Creek field site, Colorado. (b) Scatterplot for the Feather River field site, California.

5.4.3 Mean hilltop curvature and drainage density

Mean hilltop curvature was calculated for every third order basin in each of the five study sites and compared to drainage density. Figure 5.9 shows an example of the spatial distribution of hilltop curvature and drainage density for the Guadalupe Mountains field site.

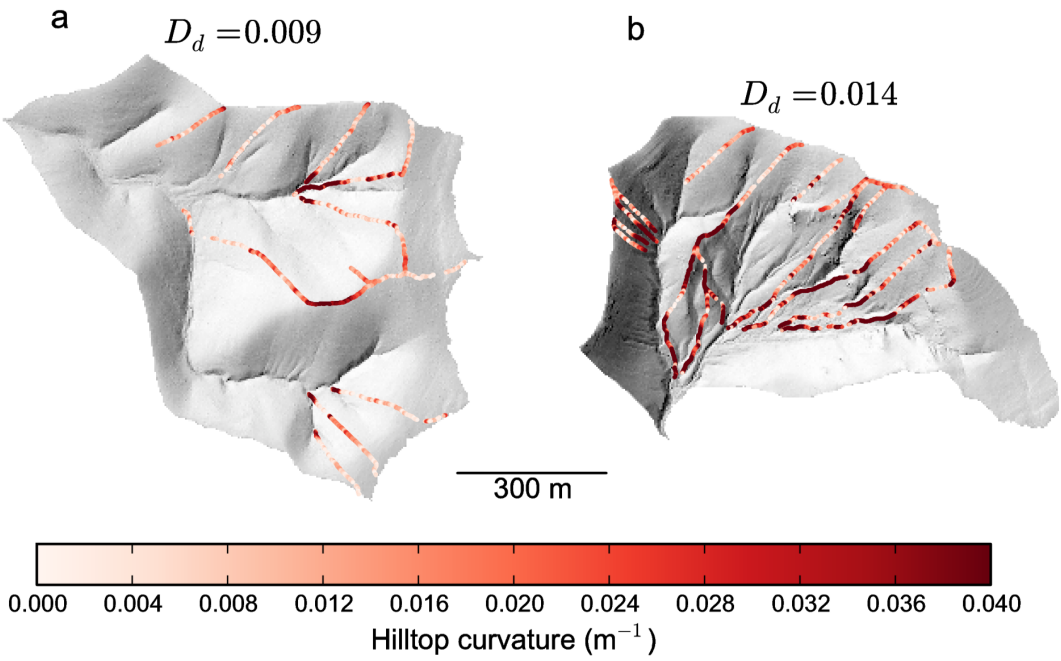

Figure 5.9: Shaded relief map showing spatial distribution of mean hilltop curvature across Guadalupe Mountains, NM for (a) a low drainage density basin, and (b) a high drainage density basin. The hilltop curvature is shown in red.

Scatter plots were created of D_d against mean C_{HT} for each of these basins (Figure 5.10), and the data were also binned with a bin width of 0.005 m^{-1}. A power-law relationship was fit through all of the data points for each field site, and the p value and R^2 were reported (see Figure 5.10).

A significant positive relationship between mean C_{HT} and D_d was observed for four out of the five field sites analysed in this study, with the exponent in the

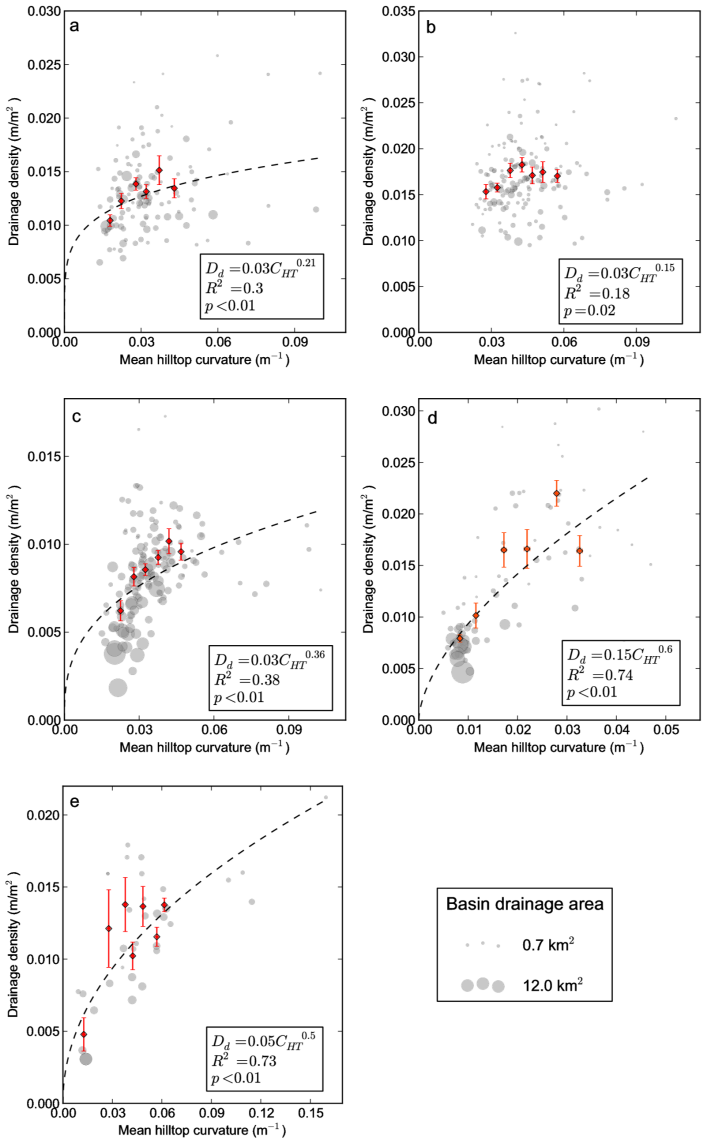

Figure 5.10: Scatterplots of the relationship between mean C_{HT} and D_d for each field site. The full dataset is shown in grey, with the size of the points representing the contributing area. The binned data are shown in red, with a bin width of 0.005 m^{-1}. A polynomial fit of the full dataset is represented by the dashed line. (a) Feather River, CA. (b) San Gabriel Mountains, CA. (c) Boulder Creek, CO. (d) Guadalupe Mountains, NM. (e) Bitterroot National Forest, ID.

power-law relationship varying between 0.15 and 0.6. There was no significant relationship observed between C_{HT} and D_d for the San Gabriel Mountains field site, with a p value of 0.02 and an R^2 of 0.18. Mean C_{HT} may only be used as a proxy for erosion rate if the ridgetops are soil-mantled. Therefore the percentage of bedrock ridgetops as a function of mean C_{HT} was also plotted for each field site (Figure 5.11). I found a positive linear relationship between the percentage of bedrock ridgetops and mean C_{HT} for each field site. The vast majority of basins in each site had a low percentage of bedrock ridgetops (Figure 5.11), although one basin in the Bitterroot National Forest site had an anomalously high percentage (70%).

5.4.4 Constraints on the n exponent

The relationship between D_d and erosion rate can theoretically be used to calculate the n exponent. The scatter plots of D_d against CRN-derived erosion rate show a positive relationship for the Feather River and Boulder Creek (Figure 5.8). Furthermore, there is also a positive relationship between D_d and mean C_{HT} for four out of the five field sites (Figure 5.10). This suggests that $n > 1$ at each of these sites. The relationship between the mean length of overland flow (inversely proportional to D_d) and erosion rate can be used to calculate n if the m/n ratio is known using equation 5.6. However, I find that varying the gradient of the regression within the range of acceptable values results in a wide variation in the calculated n exponent. Therefore it was not possible to further constrain the value of the n exponent using this technique.

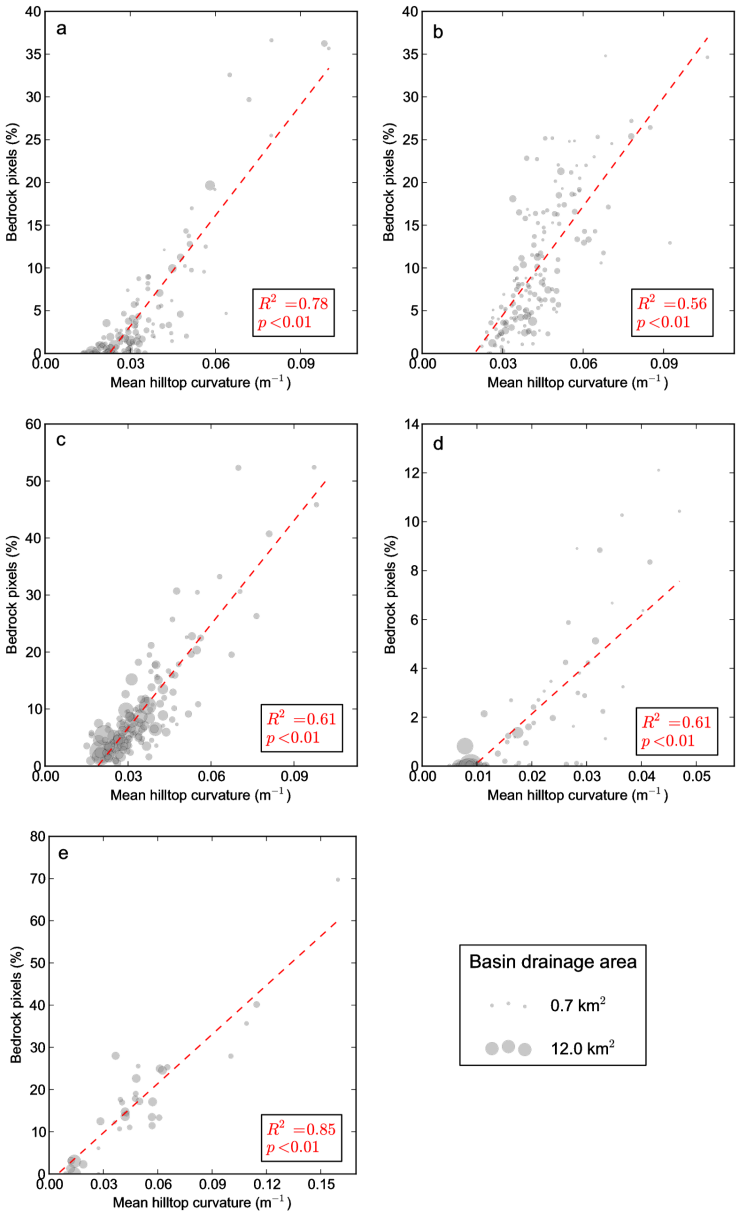

Figure 5.11: Scatterplots of the relationship between mean C_{HT} and the percentage of ridgetops identified as bedrock for third order basins in each field site. The size of the points represents the contributing area of the basin, and the dashed line shows a linear regression through the dataset. (a) Feather River, CA. (b) San Gabriel Mountains, CA. (c) Boulder Creek, CO. (d) Guadalupe Mountains, NM. (e) Bitterroot National Forest, ID.

5.5 Discussion

The results of the landscape evolution modelling show that the theoretical concepts outlined in Section 5.2 are applicable in a 2D domain. I find that the nature of the relationship between D_d and E in the model scenarios vary with the value of the slope exponent in the detachment-limited incision model, n. The steady state modelling runs (Figures 5.4 - 5.5) show that if $n > 1$, there is a positive relationship between D_d and C_{HT}, whereas if $n < 1$ there is a negative relationship. Modelling of transient scenarios also supports this, showing that the theory is still applicable in these landscapes. There was a significant trend between drainage density and mean hilltop curvature for the transient model runs with $n = 0.7$ and $n = 2$, with R^2 values of 0.85 and 0.58 respectively (Figure 5.7).

These modelling results also have implications for examining the impact of non-linear hillslope sediment transport on length scales in landscapes. As relief increases and hillslopes approach threshold gradients, hillslope sediment transport becomes increasingly non-linear, as sediment flux becomes dominated by mass wasting and landslides [Roering *et al.*, 1999]. The landscape evolution modelling scenarios where hillslope sediment transport was non-linear (Figure 5.5) exhibited the same relationships between drainage density and erosion rate as scenarios in which hillslope sediment transport was linear. However, my analytical solution (Figure 5.1) predicted a steeper relationship between D_d and uplift rate with non-linear transport for $n = 2$. This may be due to noise in the modelling results (Figures 5.4 - 5.7). This noise may be caused by the extraction of hilltop curvature from the model domain, as well as the loss of information when transforming a TIN network onto a regular grid. The model has a grid spacing of 5 m due to computational constraints, but this resolution may not be fine enough to perfectly capture the variation in curvature along the ridgetops. Despite the noise, a clear significant trend between drainage density and uplift rate is observed from the

steady state model runs using linear and non-linear sediment flux laws, with R^2 values ranging from 0.88 - 0.96. (Figures 5.4 - 5.5).

It may be expected that the effect of the non-linear sediment flux law will increase with erosion rates in higher-relief landscapes. In the CHILD model runs I tested a maximum erosion rate of 320 mm/kyr in order to compare these results to the real landscapes with CRN-derived erosion rates in this order of magnitude (Table 5.3). At higher erosion rates, where landscapes transition from soil-mantled to bedrock-dominated, C_{HT} cannot be used as an indicator of erosion rate as soil production can no longer keep pace with transport rates [Hurst *et al.*, 2012]. Therefore the results of this study are applicable to landscapes with soil-mantled ridgetops where C_{HT} can be used as a proxy for erosion rate across the landscape. Figure 5.11 shows that in each field site with the exception of Bitterroot National Forest, the majority of basins had below 20% of ridges identified as bedrock. In the Bitterroot site the majority of basins had less than 35% bedrock ridgetops, although with more variability than the other field sites. This may lead to more noise in the relationship between D_d and C_{HT} in this site, although a significant positive relationship was still observed (Figure 5.10). In regions with much higher erosion rates, a positive relationship between D_d and erosion rate may not be observed. Previous studies by Oguchi [1997] in the mountainous region of central Japan, and by Talling and Sowter [1999] in the Southern San Joaquin Valley, California, found lower drainage densities corresponding to higher relief. These authors concluded that the dominance of mass-wasting processes on steep slopes in these regions resulted in a negative relationship between D_d and relief. In contrast, Sangireddy *et al.* [2016a] found that across a wide range of humid landscapes D_d was positively correlated with relief.

I also tested the predictions on real landscapes, using lidar-derived DEMs for five field sites in the USA. My results show a positive relationship between D_d and erosion rate, using CRN-derived erosion rates for two of the field sites,

and mean C_{HT} for four out of the five sites. Drainage density has profound implications for the transit time of runoff through catchments, and maximum storm runoff has been demonstrated to be a function of drainage density [Chorley and Morgan, 1962; Gregory and Walling, 1968]. My results suggest that increasing erosion rates will therefore result in more rapid catchment response to storms or precipitation events. Furthermore, an increase in drainage density with erosion rate may increase the rapidity of sediment supply to the fluvial network. This is an important control on downstream fluvial morphology, influencing the transition between braided and meandering channels, for example, as stable meandering channels are more likely to develop with low rates of sediment transport [Church, 2006]. Furthermore, based on the landscape evolution modelling results, this positive relationship between drainage density and erosion rate is consistent with a value of n in the stream power law (equation 5.1) greater than 1. In landscapes with linear hillslope sediment transport, if n is greater than 1 and other parameters are constant, as slope increases (in response to an increase in uplift, for example) fluvial processes will out-compete diffusive processes. This would lead to channel incision occurring further upstream and an increase in D_d. However, where hillslope sediment transport is non-linear, this relative efficiency of advective and diffusive processes may also depend on the critical gradient, S_c. I set S_c constant in the modelling scenarios but acknowledge that the value of S_c may vary spatially [Grieve *et al.*, 2016c,b], which could affect the observed relationship between drainage density and erosion rate.

The value of the n exponent also has important implications for how the landscape responds to transient forcing. The slope of river profiles may be used to extract information about the uplift history of the channel [Pritchard *et al.*, 2009; Roberts and White, 2010]. However, complete uplift histories can only be extracted from channel profiles if $n = 1$, when knickpoint retreat rates should be independent of erosion rate. Royden and Perron [2013] demonstrated that if $n > 1$, rapid

incision signals should propagate upstream more rapidly than slow incision (with the converse true for $n < 1$). Steep segments in river profiles are predicted to lengthen when $n > 1$, consuming lower gradient segments and therefore progressively destroying the record of the preceding uplift history. My results are consistent with $n > 1$ for four of the field sites analysed, and $n \geq 1$ for all of the field sites. This agrees with Lague [2014], who found that $n \approx 2$ in the majority of cases. These results therefore imply that channels in these landscapes will be imperfect recorders of tectonic forcing, and complete uplift histories cannot be extracted from these river profiles.

The competition between the parameters D and K has been shown to exert a first order control on valley spacing [e.g. Perron *et al.*, 2008a, 2009; Sweeney *et al.*, 2015]. Perron *et al.* [2008a] showed that valley spacing is also predicted to vary with the parameters m, n, and relief (ζ). They define the Péclet number, Pe as:

$$Pe = \frac{K L_c^{2(m+1)-n}}{D\zeta^{1-n}}, \tag{5.11}$$

where L_c is the horizontal length of a drainage basin. Perron *et al.* [2008a] suggest that, assuming the other parameters are constant, higher erosion rates will increase Pe through an increase in relief, ζ, if $n > 1$. This leads to narrower valley spacing and increased drainage density. However, if $n = 1$, Pe is independent of relief. This theory is consistent with the results of this study, where I find a positive relationship between drainage density and erosion rate, consistent with $n > 1$.

However, a key assumption of this study is that the D and K parameters in equations 5.1 and 5.3 are constant. The competition between these parameters has been shown to exert a first order control on valley spacing [e.g. Perron *et al.*, 2008a, 2009; Sweeney *et al.*, 2015]. However, the values of D and K may vary

both spatially and temporally. The hillslope diffusion coefficient, D, is a function of hillslope sediment properties, such as soil thickness, cohesion, and grain size [Furbish *et al.*, 2009]. Both soil thickness and grain size are thought to vary with erosion rate [Heimsath *et al.*, 1997; Attal *et al.*, 2015; Riebe *et al.*, 2015]. D has also been shown to vary with climate through controls on soil transport processes [e.g. Carson and Kirkby, 1972; Yoo *et al.*, 2005], and lithology, which affects material properties and soil particle sizes [Hurst *et al.*, 2013b]. If soil thickness decreases with erosion rate, the models of depth-dependent sediment transport suggest that D may also vary with erosion rate [e.g. Braun *et al.*, 2001]. The channel erodibility coefficient, K, is a function of many parameters such as lithology, climate, sediment cover, and channel width [Whipple and Tucker, 1999]. K may vary with erosion rate through channel width adjustments, as channels have been demonstrated to narrow in response to steepened reaches from increased uplift rates [e.g. Finnegan *et al.*, 2005; Amos and Burbank, 2007]. If $n = 1$ then equation 5.6 simplifies so that D_d is dependent on D/K. This suggests that, if $n = 1$, a positive relationship between D_d and E may result from a decreasing D/K ratio with erosion rate (Figure 7.2, Appendix). This may be caused by a decrease in D; an increase in K; or K increasing faster than D such that the ratio decreases. However, as no field evidence has demonstrated how K or D vary with E, these three scenarios cannot be distinguished. With these limitations, I suggest that these results are consistent with the hypothesis that $n > 1$ for four out of the five field sites, although acknowledge that there may be other possible explanations for the observed relationship.

A further assumption of my analytical predictions is that of detachment-limited fluvial incision (see equation 5.1). Detachment-limited incision assumes that the erosion rate is related to the shear stress, velocity, or power of overland flow, and that sediment is transported by the channel without being deposited. It has been assumed in many studies modelling evolution of soil-mantled landscapes

[e.g. Howard, 1994, 1997; Perron *et al.*, 2008a, 2009]. Other studies, however, suggest that erosion in soil-mantled landscapes is transport-limited, where erosion rate is proportional to the divergence of sediment flux [e.g. Tucker and Bras, 1998; Simpson and Schlunegger, 2003; Istanbulluoglu *et al.*, 2003]. Pelletier [2012] demonstrated through analysis of field measurements, along with numerical modelling, that at small spatial scales, both detachment- and transport-limited conditions may apply depending on the texture of the eroding soil. The assumption of detachment-limited conditions is a simplifying one that I make in this study to generate simple predictions that are testable against real landscapes. However, Tucker and Bras [1998] present a purely transport-limited model of the drainage density in soil-mantled landscapes, and predict similar relationships between D_d and E as I find in my detachment-limited model.

Previous studies have suggested that the underlying lithology has an effect on D_d [Oguchi, 1997]. Three of the sites analysed (Feather River, Boulder Creek, and the San Gabriel Mountains) were situated on granitic lithologies; the Guadalupe Mountains site was primarily composed of limestone; and the Bitterroot National Forest site was composed of schist and gneissic bedrock. Despite these variations, the relationship between D_d and erosion rate was positive for four of these sites (Figures 5.8 and 5.10). The San Gabriel Mountains is the only site to show no relationship between drainage density and erosion rate. DiBiase *et al.* [2012] analysed the same DEM, and found that fluvial drainage density decreased with increasing erosion rate, while colluvial channels become denser, leading to the total drainage density remaining constant across the landscape. This contrasts with my analysis, as I found that fluvial drainage density was invariant with erosion rate. The difference between these results may be due differences in channel extraction: DiBiase *et al.* [2012] used slope-area plots to identify fluvial channels, whereas in my analysis I used the DrEICH algorithm, which identifies channels based on transformed river long profiles. My results are consistent

with the n value in this landscape being close to 1, as implied by my numerical modelling results. As shown by the San Gabriel Mountains site, the presence of colluvial channels in steep landscapes formed through debris flow processes [Stock and Dietrich, 2003] may complicate the results of this analysis. These colluvial channels can impact the results of channel extraction algorithms, and therefore the calculation of drainage density across the landscape, as the DrEICH algorithm is focused on identifying the extent of the fluvial channel network.

Furthermore, although I link changing drainage density to erosion rate, there are various other factors in the landscape that may affect both D_d and E. Several landscape metrics have been shown to vary with erosion rate, such as soil thickness [Heimsath *et al.*, 1997, 2012; Gabet *et al.*, 2015] and vegetation [Milodowski *et al.*, 2015a]. In many landscapes, sediment flux has been suggested to be depth-dependent [Heimsath *et al.*, 2005; Roering, 2008], and bioturbation efficiency may be reduced as the amount of biomass supported by the landscape decreases [Gabet *et al.*, 2003]. Reduced vegetation cover may also result in increased susceptibility to erosion by overland flow [Istanbulluoglu and Bras, 2005]. Therefore, while I attribute changes in drainage density to fluvial processes, I acknowledge that drainage density variations may be driven by other processes. Although these factors may complicate the interpretation, I observe a consistent trend between drainage density and erosion rate across four of the sites, which vary from low-relief landscapes, such as Guadalupe Mountains, to higher-relief landscapes, such as the Bitterroot National Forest and Boulder Creek sites.

5.6 Conclusions

My results show a consistent positive relationship between D_d and erosion rate across four field sites in the USA with varying lithologies and climates. I compared

D_d with CRN-derived erosion rates at two field sites; and with hilltop curvature at all field sites. There was a significant positive relationship between D_d and CRN-derived erosion rates, as well as with C_{HT}, whereas one field site demonstrated no relationship between D_d and mean C_{HT}. Modelling results confirm that C_{HT} may be used to reflect the spatial variability of erosion rates across multiple landscapes [Hurst *et al.*, 2012]. The positive relationship between D_d and erosion rate constrains fundamental parameters in theoretical models of fluvial incision, particularly the n exponent. My results are consistent with a value of n exceeding unity across four of the sites, assuming that K and D are invariant with erosion rate. This suggests that, all else being equal, advection out-competes diffusion in higher-relief landscapes, leading to fluvial incision occurring further up-valleys and resulting in an increase in D_d. However, this relationship may not be apparent in landscapes dominated by debris flow processes, such as in the San Gabriel Mountains site. Furthermore, river profiles will not be perfect recorders of uplift histories in landscapes where $n > 1$, as more rapidly eroding reaches will migrate upstream at a faster rate, progressively consuming the erosion history encoded into the upstream portion of the channel network [Royden and Perron, 2013]. I constrain this topographic analysis with landscape evolution modelling, which shows that both linear and non-linear hillslope sediment transport predict similar relationships between drainage density and erosion rate at steady state within the range of erosion rates tested. I also test a transient scenario of rapid uplift with linear hillslope sediment transport, showing the same predicted relationships to that of the steady state scenarios.

Chapter 6

Discussion and Conclusions

One of the main motivations behind geomorphological research is to understand the processes that shape the Earth's surface. To do this, we need to answer two key questions: firstly, how can we quantify landscape morphology; and secondly, what are the key factors that determine it?

This thesis has contributed to these questions by using high-resolution topographic data to explore the structure and evolution of river networks in upland landscapes. My thesis was split into two sections: firstly, the development of new algorithms to extract geomorphic features from lidar-derived DEMs (Chapters 3 and 4); and secondly, the application of these algorithms to quantify and explore controls on the density of fluvial networks (Chapter 5).

In Chapter 3 I presented a new method of identifying the upstream extent of channel processes, or channel heads, from high-resolution topographic data, using transformed integral analysis of river profiles. I tested this new method against three other methods of identifying channel heads: slope-area scaling relationships; and two curvature-based methods (GeoNet, developed by Passalacqua *et al.* [2010a,b, 2012] and a method developed by Pelletier [2013]). I compared these

methods with a total of 167 field-mapped channel heads from four different landscapes with high-resolution lidar-derived DEMs. My analysis demonstrated that the new algorithm presented here (the DrEICH algorithm) along with the algorithm presented by Pelletier [2013] consistently identified the mapped channel heads with a small margin of error across each field site. The GeoNet algorithm [Passalacqua *et al.*, 2010a,b, 2012; Sangireddy *et al.*, 2016b] also predicted channel head locations with an error of less than 40 m for three of the four field sites, but requires a contributing area threshold which must be specified by the user, and affects the location of the predicted channel heads.

Following on from this work, in Chapter 4 I developed and tested a new method of identifying the spatial extent of floodplains and fluvial terraces from DEMs, based on thresholds of elevation compared to the nearest channel and local gradient. Unlike previous methods, which tend to require calibration with additional datasets, this method calculates these thresholds statistically from the DEM using quantile-quantile plots. This method can be run by the user either across the whole landscape, or as a swath profile allowing the comparison of the features to a specific channel of interest. I compared this method to field-mapped floodplains and terraces from eight field sites using a range of topographies and grid resolutions. I found that the method performed well compared to field-mapped floodplain initiation points, flood hazard maps, and digitised terrace surfaces. The method extracted features most accurately in higher relief areas where the floodplains and terraces are constrained within valleys. The method was also found to be relatively insensitive to grid resolution, allowing the extraction of these features from DEMs of 1 - 10 m resolution.

Chapter 5 involved the application of these techniques for automated feature extraction from lidar-derived DEMs to analyse the drainage density, D_d, of catchments across multiple upland landscapes with a gradient in erosion rates. I found a consistent positive relationship between D_d and erosion rate across four

out of the five landscapes with varying climate and lithological characteristics, using both cosmogenic radionuclide derived erosion rates, and mean hilltop curvature as a proxy. Through comparison with analytical and numerical modelling, I demonstrated that this positive relationship can be used to constrain fundamental parameters in theoretical models of fluvial incision, particularly the slope exponent, n, in the stream power incision model. My results are consistent with $n > 1$ across these sites, in contrast to the commonly-held assumption that $n = 1$ in many studies of landscape evolution.

The rest of this chapter contains a discussion of the main findings and wider implications of this thesis, both for topographic analysis from high-resolution DEMs; and for theories of landscape evolution and fluvial incision into bedrock. This is followed by a discussion of some potential future research directions, including constraining fundamental parameters in common models of fluvial incision, and exploring controls on the formation and morphology of fluvial terraces in mountainous regions.

6.1 Topographic analysis

6.1.1 Choosing an appropriate method for delineating channels

Determining the upstream extent of channel networks is a fundamental first step in many geomorphic studies, and is essential for understanding storm hydrology, flow routing, biogeochemical cycling, sediment transport, and landscape evolution. In this thesis, I tested three different methods that have been proposed for identifying channel networks from high-resolution topographic data, as well as developing a new technique using integral analysis of river profiles (the DrEICH algorithm).

The results of this comparison and these new techniques were used as a starting point for both the identification of floodplains and terraces in Chapter 4, and for the analysis of channel network density in Chapter 5. The accurate identification of the upstream extent is particularly important for the calculation of drainage density, which is sensitive to the channel extraction method used.

Along with the methods tested in Chapter 3, there are many other techniques which have been published for extracting channel networks from high-resolution DEMs, mostly based on the analysis of topographic curvature [e.g. Lashermes *et al.*, 2007; Thommeret *et al.*, 2010; Orlandini *et al.*, 2011; Sofia *et al.*, 2011; Liu *et al.*, 2015; Hooshyar *et al.*, 2016]. The wealth of methods available may make it challenging for researchers to select an appropriate method for their study.

Here I divide these techniques into two different categories: i) geometric techniques; and ii) process-based techniques. I define geometric methods as those which directly predict channel head locations from topographic metrics which can be extracted from the DEM, such as curvature [Lashermes *et al.*, 2007; Passalacqua *et al.*, 2010a,b, 2012; Pelletier, 2013; Hooshyar *et al.*, 2016], or topographic openness [Sofia *et al.*, 2011]. These techniques are based around the search for concave areas in the landscape where overland flow is likely to be concentrated. Process-based techniques, on the other hand, are defined here as methods which identify channel heads based on theoretical laws of fluvial incision, such as predictions of the relationship between channel gradient and drainage area at channel heads [O'Callaghan and Mark, 1984; Band, 1986; Tarboton *et al.*, 1991; Montgomery and Dietrich, 1988; Dietrich *et al.*, 1992, 1993]. The DrEICH method presented here is also process-based, in that it searches for linear segments in plots of χ against elevation along channels, representing domains in the landscape which obey theoretical models of fluvial incision.

Some methods of extracting channel heads may be more appropriate than

others, depending on both the landscape and the aim of the study in question. Geometric techniques of measuring curvature are able to pick out the signatures of concave valleys, and therefore studies which are interested in identifying valley networks may be more suited to using a geometric technique, such as GeoNet or the curvature method of Pelletier [2013]. Furthermore, in landscapes heavily influenced by the presence of roads or artificial features, these geometric methods may be more appropriate than process-based techniques, as channels in these landscapes may be less likely to obey the predictions of fluvial erosion models. Extraction techniques such as GeoNet have been tested and shown to work well in human-impacted landscapes [Passalacqua *et al.*, 2012; Sangireddy *et al.*, 2016b].

However, these geometric techniques cannot distinguish between the valley network and the channel network: in many landscapes, especially those which are high-relief, debris flows and colluvial channels can form concave regions at the tips of the drainage network [e.g. Stock and Dietrich, 2003, 2006; DiBiase *et al.*, 2010], which will not be distinguished from the fluvial network using geometric techniques. Many field studies of channel networks have shown that the initiation of overland flow and fluvial processes can occur tens to hundreds of metres downstream of the valley head [e.g. Dietrich and Dunne, 1993]. Therefore, in order to quantify and analyse controls on fluvial drainage density, discussed in Chapter 6, it is essential to use a technique which aims to detect the signature of fluvial processes, rather than simply concave valleys. Previously, the only process-based method of identifying the onset of fluvial processes was looking for scaling breaks in slope-area plots. However, I have shown that this method was not appropriate in identifying channel head locations across the field sites analysed. The DrEICH algorithm, on the other hand, provides a novel process-based method of identifying the transition to fluvial processes which was accurate to within tens of metres across each field site tested. The results of this thesis should therefore allow researchers to make an informed choice on the most appropriate

method of extracting channel networks from DEMs, based on the study aims and characteristics of the landscape in question.

6.1.2 Fully automated feature extraction

A key goal for the Earth surface research community is to develop fully-automated methods of feature extraction from DEMs. These techniques would allow us to detect the signature of geomorphic processes on a broader landscape scale, as well as significantly saving both time and expense in field mapping studies.

Techniques designed to extract geomorphic signatures from the topography generally require calibration by the user, either through the input of independent datasets or the manual tuning of parameters. This applies to both methods of identifying channel networks, discussed in Chapter 3, and methods of delineating floodplains and terraces, discussed in Chapter 4. For example, methods of channel extraction generally require user-defined parameters, such as a curvature threshold for channel head identification [Pelletier, 2013], or contributing area thresholds for channel network thinning [Passalacqua *et al.*, 2010a,b, 2012]. Optimising these parameters for a particular landscape requires *a priori* knowledge of the channel head locations, which can restrict the ability of the methods to predict accurate channel networks over large spatial scales. Previous techniques for the identification of floodplains and terraces discussed in Chapter 5 generally require calibration using independent datasets, such as flood risk maps [Dodov and Foufoula-Georgiou, 2006; Manfreda *et al.*, 2011; Degiorgis *et al.*, 2012; Manfreda *et al.*, 2014], or manual editing by the user after feature detection [Stout and Belmont, 2014].

The techniques presented in this thesis for the identification of channel networks, floodplains, and terraces have been designed with the aim of minimising the

number of user-defined parameters and need for calibration with independent datasets. The DrEICH method for extracting channel heads requires only two user-defined parameters: the value of m/n, and the number of linked pixels for valley identification. In Chapter 3 I demonstrated that the performance of the method is insensitive to varying the m/n value, although the number of linked pixels can affect the density of the resulting channel network and should therefore be carefully selected. The method for extracting floodplains and fluvial terraces presented in Chapter 4 attempts to minimise user input, by allowing the statistical determination of the thresholds for gradient and elevation compared to the channel. However, this method still requires the input of some user-defined parameters, such as a threshold stream order, the width of the swath profile, and a minimum terrace height. The selection of these parameters can generally be performed by a visual inspection of the DEM prior to running the analysis.

Although the methods presented in this thesis provide a first step towards the goal of fully automating feature extraction, further development is needed to reduce potential error, and allow these parameters to be set based on the topographic data alone. For example, the development of techniques to map valley widths would allow the width of the swath profile in the floodplain and terrace method to be determined automatically. Totally automated feature extraction would mean that geomorphologists could perform reproducible analyses of the spatial variation in landscape features on regional and continental scales.

6.2 Implications for landscape evolution

New techniques for extracting signatures of geomorphic processes provide unique and exciting opportunities for understanding controls on the morphology and evolution of fluvial landscapes. One such opportunity is the ability to add both

rigour and reproducibility to testing of theoretical models of landscape evolution. Many workers have derived elegant equations for the behaviour of fluvial systems in upland landscapes, based on our understanding on the physics of sediment transport, as well as empirical observations of fluvial morphology, outlined in Chapter 1. These equations contain predictions of landscape shape: the new techniques outlined in this thesis, along with the ever-growing availability of lidar data, allow us to validate these predictions at both higher resolution and greater spatial scales than previously possible.

In Chapter 5, I combined analytical theories of sediment transport on hillslopes with a common model of fluvial incision (the stream power incision model) to predict where in the landscape channels should initiate, and therefore fluvial network density. These predictions, using models of both linear and nonlinear hillslope sediment transport, showed that drainage density should be correlated with landscape erosion rate, but that the nature of this correlation depended strongly on the parameters set within the stream power model, particularly the channel slope exponent, n. Using lidar-derived DEMs and the channel network extraction technique I developed in Chapter 3, I showed that there was a positive relationship between drainage density and erosion rate across four out of five landscapes tested, consistent with a value of n greater than unity for each of these landscapes.

Many workers have used the stream power incision model to understand controls on fluvial networks, such as to extract uplift histories [e.g. Pritchard *et al.*, 2009; Roberts and White, 2010; Goren *et al.*, 2014; Fox *et al.*, 2014], to explore the role of divide organisation and stability [Willett *et al.*, 2014], or to predict drainage migration [Pelletier, 2004]. These studies all require the specification of the parameters m and n, most commonly as $m/n = 0.5$ and $n = 1$. The results of this thesis show that this assumption is not necessarily correct, and that in general $n \neq 1$ for the majority of the landscapes tested. Royden and Perron [2013]

demonstrated numerically that, if $n > 1$, the propagation of transient signals along river profiles will be dependent on the fluvial erosion rate, and therefore these channels will not record complete histories of tectonic forcing. Therefore, one of the key implications of this thesis is that the parameters of fluvial incision models, such as the value of n, need to be more carefully constrained before river profiles can be used to extract meaningful information about allogenic forcings.

The parameters K (fluvial erodibility) and D (hillslope diffusivity) are also important unknowns in these theoretical predictions of landscape evolution. In Chapter 5, we assume that m/n, K, and D are constant, both spatially and temporally. However, both K and D may be expected to vary with erosion rate, for example if channels adjust their width in response to increased uplift rates [Finnegan *et al.*, 2005; Amos and Burbank, 2007]; or by varying soil thickness and grain size [Heimsath *et al.*, 1997; Attal *et al.*, 2015; Riebe *et al.*, 2015]. No field evidence has yet demonstrated if there is a link between either K or D and erosion rate. Furthermore, no studies at present have attempted to constrain how the values of m/n, K, or D vary within a landscape, due to local variations in climate or lithology, for example. These are key problems which need to be addressed in order to better understand the links between geomorphic processes, topographic form, and landscape evolution.

6.3 Future research directions

Based on the key results of this thesis and the wider implications discussed above, I have defined a series of questions which I aim to address in future research, in order to improve our understanding of the controls on fluvial network structure and organisation, as well as landscape evolution more generally.

6.3.1 How does concavity vary across a landscape?

The results of Chapter 5 show that in order to link theoretical predictions of fluvial incision to topography, it is essential to have better constraints on parameters in landscape evolution models, such as concavity (m/n), channel erodibility (K), or hillslope diffusivity (D). The concavity index θ, or m/n, is of particular importance, and describes the variation of discharge with drainage area along a channel profile: the higher m/n is, the more concave the profile will be. The values of m and n are major unknowns, and have been suggested to reflect the fundamental process driving fluvial incision: if incision is driven by stream power, theory suggests that $m = 0.5$ and $n = 1$, whereas if it is driven by shear stress, then $m = 0.3$ and $n = 0.7$ [e.g. Howard and Kerby, 1983; Sklar and Dietrich, 1998; Whipple and Tucker, 1999].

Remarkably, both of these incision models predict that the ratio of these two parameters, m/n, should equal approximately 0.5, although this has been suggested to lead to unrealistic topography in recent numerical modelling studies [Kwang and Parker, 2017]. Attempts to quantify the concavity index from different landscapes using both field data and topographic analysis suggested that the m/n ratio appears to fall within a relatively narrow range, where $0.4 < m/n < 0.6$ [Howard and Kerby, 1983; Whipple and Tucker, 1999; Harel *et al.*, 2016]. The value of the concavity index is of particular importance for studies which attempt to use river profiles to obtain uplift histories [Pritchard *et al.*, 2009; Roberts and White, 2010; Goren *et al.*, 2014; Fox *et al.*, 2014]; as indicators of tectonic processes [Wobus *et al.*, 2006; Whittaker *et al.*, 2008]; or to detect signals of drainage divide migration [Willett *et al.*, 2014]

Traditional methods of estimating the concavity index of channel profiles involved performing a linear regression on plots of slope against drainage area and calculating the gradient of the regression (Section 1.2.2 and Figure 1.5) [e.g.

Howard and Kerby, 1983; Whipple *et al.*, 2000; Snyder *et al.*, 2000; Wobus *et al.*, 2006]. However, it is often difficult to determine an appropriate concavity index using slope-area plots due to the inherent noise within topographic data, which is amplified when deriving the surface to calculate gradient [Perron and Royden, 2013; Wang *et al.*, 2017]. Slope-area plots therefore require extensive smoothing and binning the data in order to determine the concavity [Wobus *et al.*, 2006]. New techniques using the integral method of channel profile analysis [e.g. Perron and Royden, 2013; Mudd *et al.*, 2014] allow the calculation of the best-fit m/n for a landscape by linearising channel profiles in χ-elevation space (Figure 1.6). These methods do not rely on calculating channel gradient, meaning there is much less noise within the data and a more accurate m/n can be determined.

Both slope-area plots and integral profile analysis are generally used to calculate the mean best-fit m/n for a landscape as a whole [Perron and Royden, 2013; Mudd *et al.*, 2014; Harel *et al.*, 2016]. This approach was also taken in Chapters 3 and 5 to constrain the m/n ratio for channel extraction. However, we may expect that the concavity index varies within a landscape based on local controls: m/n should be controlled by the relationships between drainage area, discharge, and channel width (e.g. equation 1.7 - 1.8). These relationships should be dependent on the underlying lithology, which is theoretically represented through K. No studies have yet shown in the field whether there is a significant link between m/n ratio and lithology, or K, on a local scale. I plan to use the new integral analysis techniques for calculating concavity indices for individual basins within the landscape: initial work suggests that there is a significant spatial heterogeneity in m/n (Figure 6.1).

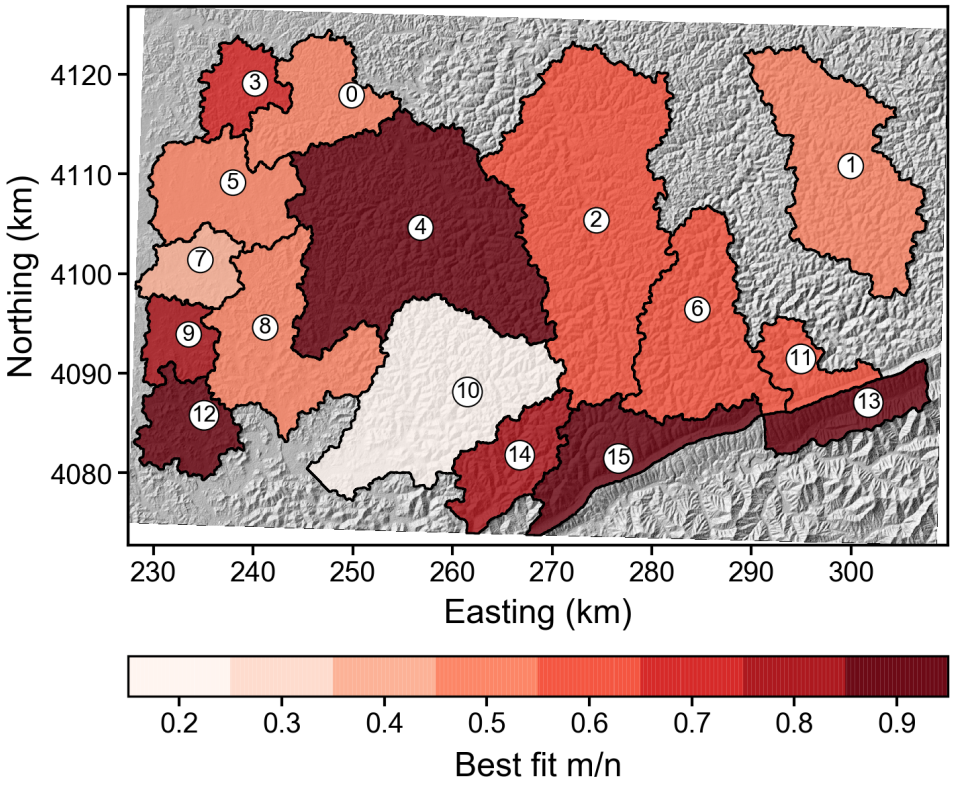

Figure 6.1: Shaded relief map of part of the Allegheny Plateau, Kentucky, showing a series of drainage basins coloured by the best-fit m/n ratio (darker colours represent a higher concavity index). The m/n ratio varies significantly within this landscape despite no active tectonic forcing.

6.3.2 Where does the transition between bedrock and alluvial rivers occur?

The theoretical models of fluvial incision described in Chapter 1, and applied in Chapters 3 - 5, require the assumption that channels in these landscapes are detachment-limited, and therefore erosion rate is proportional to the shear stress, velocity, or power of overland flow with no significant sediment deposition. This assumption is commonly used to make theoretical predictions of landscape evolution in mountainous landscapes [e.g. Howard *et al.*, 1994; Howard, 1997; Whipple and Tucker, 1999; Perron *et al.*, 2008a, 2009]. However, it breaks down as rivers transition from bedrock-dominated to alluvial-dominated along their length. Past this transition point to alluvial channels, incision becomes proportional to the divergence of sediment flux [Howard, 1980; Whipple and Tucker, 2002]. Many authors have attempted to predict the transition between detachment- and transport-limited regimes, either through analytical models [Howard, 1980, 1987; Sklar and Dietrich, 1998; Whipple and Tucker, 2002] or based on empirical observations [Howard and Kerby, 1983; Montgomery *et al.*, 1996]. Whipple and Tucker [2002] set out a theory for predicting a critical gradient along which channels should transition from bedrock to alluvial, outlined in Section 1.2.4.

However, identifying process domain transitions using gradient is problematic due to the noise within the data, as discussed in Chapter 3 and Section 6.3.1. Perron and Royden [2013] presented a method of transforming river profiles for bedrock channels using the stream power incision model. I plan to develop a similar approach for transforming alluvial channels based on equations for alluvial channel geometry [Whipple and Tucker, 2002], outlined in Section 1.2.4 to investigate the predicted concavity of alluvial rivers. For example, equation 1.26 presents a representation of channel gradient for alluvial rivers, where the concavity, θ_t, is equal to $(m_t - 1)/n_t$. If I integrate this equation:

$$\int dz = \int \left(\frac{B(x)E(x)}{K_t(x)A(x)^{(m_t-1)}} \right)^{\frac{1}{n_t}} dx, \tag{6.1}$$

and perform the integration upstream from the base level x_b to the observation point x, this leads to the following equation for a river profile, similar to equation 1.14:

$$z(x) = z(x_b) + \int_{x_b}^{x} \left(\frac{B(x)E(x)}{K_t(x)A(x)^{(m_t-1)}} \right)^{\frac{1}{n_t}} dx. \tag{6.2}$$

If I assume that that B, E, and K_t are spatially uniform this leads to:

$$z(x) = z(x_b) + \left(\frac{BE}{K_t} \right)^{\frac{1}{n_t}} \int_{x_b}^{x} \frac{dx}{A(x)^{\frac{m_t-1}{n_t}}}. \tag{6.3}$$

A reference drainage area can then be introduced to remove the influence of drainage area on the steepness of the channel:

$$z(x) = z(x_b) + \left(\frac{BE}{K_t A_0^{(m_t-1)}} \right)^{\frac{1}{n_t}} \chi_t, \tag{6.4a}$$

$$\chi_t = \int_{x_b}^{x} \frac{A_0}{A(x)}^{\frac{m_t-1}{n_t}} dx. \tag{6.4b}$$

The transformed longitudinal coordinate, χ_t, is directly comparable to the transformed coordinate χ for bedrock rivers derived by Perron and Royden [2013]. This technique provides a potential method for estimating the best-fit concavity

of alluvial rivers, using similar techniques for bedrock rivers proposed by Perron and Royden [2013] and Mudd *et al.* [2014]. The bedrock-alluvial transition should represent the point along a channel profile where the profile changes from obeying theoretical laws of bedrock incision (with a concavity represented by θ), to obeying laws of sediment transport (with a concavity represented by θ_t). Therefore, I plan to use techniques for identifying best-fit concavity from channel profiles, such as slope-area plots and the integral analysis described in equations 6.1 - 6.4, to search for scaling breaks in concavity along channel profiles. This should provide a method of identifying the transition from bedrock to alluvial reaches along channels, which can be tested against these theoretical predictions [e.g. Whipple and Tucker, 2002]. This will help to improve our understanding of the spatial patterns of erosion and deposition along river channels, which is important for both short term applications, such as flood risk or the assessment of stream habitat characteristics [Montgomery *et al.*, 1996], and for modelling long-term landscape evolution.

6.3.3 What are the controls on fluvial terrace distribution and morphology?

The methods presented in Chapters 3 and 4 provide exciting new opportunities for detecting and quantifying the signatures of geomorphic processes over larger spatial scales than previously possible. For example, these methods allow the analysis of the distribution of fluvial terraces, which have been extensively used to investigate channel response to changes in both climate and tectonics [e.g. Gilbert, 1877; Merritts and Bull, 1989; Bull, 1991; Merritts *et al.*, 1994; Pazzaglia *et al.*, 1998; Lavé and Avouac, 2000, 2001; Wegmann and Pazzaglia, 2002; Gran *et al.*, 2009], to examine sediment storage and dynamics within river systems [Pazzaglia,

2013; Gran *et al.*, 2013], and to quantify lateral channel mobility [Finnegan and Dietrich, 2011].

A debated topic within geomorphology is the formation of fluvial strath terraces, which are primarily composed of bedrock (Figure 1.10b), and therefore represent periods of fluvial incision. Many workers have suggested that strath terraces may form due to an increase in channel sediment supply, driven by climate (the Gilbert hypothesis) [e.g. Gilbert, 1877; Personius *et al.*, 1993; Hancock and Anderson, 2002; Wegmann and Pazzaglia, 2002]. This sediment results in armouring of the channel bed, hindering vertical incision and therefore causing the channel to carve out its valley laterally. Alternatively, strath terraces may preserved through progressive tectonic uplift or base-level fall, leading to a 'terrace staircase' [Burbank *et al.*, 1996; Pazzaglia and Brandon, 2001; Cunha *et al.*, 2008; Viveen *et al.*, 2014]. These different formation mechanisms should hypothetically result in different distribution of terrace elevations along channels: if terraces are formed through climate-driven variations in sediment supply, we might expect that terrace elevations would be random, whereas fluvial incision through base level fall or tectonic uplift should result in a series of terraces with a systematic elevation pattern [e.g. Pazzaglia and Brandon, 2001].

I plan to use the new method of remotely identifying terraces from DEMs presented in Chapter 4 to quantify and detect the signatures of fluvial terraces on a larger scale than previously possible with traditional field mapping methods. This technique allows the analysis of terrace metrics such as elevation, area, and height compared to the modern channel. A potential site for this research is the coast of California, where previous workers have looked at terrace distributions on a more local scale [e.g. Merritts *et al.*, 1994; Fuller *et al.*, 2009]. I aim to extend this analysis to every channel along the coast to provide a regional analysis of controls on terrace formation, channel dynamics, and landscape evolution.

6.4 Conclusions

The main conclusions of this thesis are as follows:

1. *New methods of analysing high-resolution topography provide novel opportunities to quantify the signatures of geomorphic processes.*

   The development of techniques to rapidly and objectively extract geomorphic features from lidar, such as channel networks, floodplains, and terraces, allows us to detect the signature of geomorphic processes at both higher resolutions and larger spatial scales than previously possible. These techniques have numerous applications across diverse fields such as geomorphology, hydrology, and ecology.

2. *Fluvial network density is positively related to landscape erosion rate.*

   Fluvial drainage density was shown to increase with erosion rate across multiple landscapes, with a variety of climatic and lithological characteristics. This suggests that in higher-relief landscapes, advection out-competes diffusion leading to fluvial incision occurring further up valleys and resulting in an increase in drainage density. Therefore, more rapidly eroding landscapes will respond faster to extreme precipitation events, and will transport sediment more rapidly through catchments.

3. *The channel slope exponent in the stream power incision model is greater than unity.*

   The positive relationship between drainage density and erosion rate across these landscapes is consistent with an n exponent in the stream power incision model greater than unity, in contrast to the assumptions made in many studies of landscape evolution. Therefore, care must be taken when using fluvial profiles to extract complete uplift histories, as these channels will be imperfect recorders of tectonic forcings.

4. *More research is needed to constrain major unknowns in theoretical predictions of fluvial incision.*

   As yet, it is not well understood how fundamental parameters in models of fluvial incision, such as the stream power model, vary spatially and temporally. More research is needed to explore how profile concavity, channel erodibility, and hillslope diffusivity vary with local controls such as lithology, climate, and erosion rate.

Chapter 7

Appendix

This appendix contains the supporting information for Chapter 5, published in the *Journal of Geophysical Research: Earth Surface*.

Section 7.1 sets out an alternative modelling scenario for predictions of the relationship between drainage density (D_d) and erosion rate (E) which is a more complex version of the analytical model presented in the Chapter 5. The model is set out below and the resulting predictions are shown in Figure 7.1. Section 7.2 sets out the details of the CHILD landscape evolution model used in Chapter 5, along with a description of each of the parameters. I also show an alternative explanation for the positive relationship found between D_d and E, where the n exponent in the detachment-limited fluvial incision model is equal to 1, but hillslope diffusivity (D) and channel erodibility (K) vary with erosion rate (Figure 7.2). Figures 7.3-7.5 show the results of the sensitivity analysis of the model runs to grid resolution (resolutions varying between 2.5 and 10 m.)

7.1 Alternative analytical model formulation

The model presented in the main text combines a simple detachment-limited model of fluvial incision with both linear and non-linear hillslope sediment transport models to predict the theoretical relationship between D_d and E. In this supporting information I present an alternative model formulation where I assume a different relationship between the drainage area at the channel head, A, and the distance from the divide, L_h. I model fluvial incision following the same detachment-limited model as in the main text [e.g. Whipple and Tucker, 1999]:

$$E = K A^m {S_{CH}}^n, \tag{7.1}$$

where K is an erodibility coefficient [$\mathrm{T}^{-1}\ \mathrm{L}^{1-2m}$], S_{CH} is the channel slope, and m and n are constant exponents. I rearrange this equation to solve for S_{CH} [Hack, 1973; Flint, 1974; Howard and Kerby, 1983; Sklar and Dietrich, 1998; Wobus *et al.*, 2006]:

$$S_{CH} = \left(\frac{E}{K}\right)^{\frac{1}{n}} A^{-m/n}. \tag{7.2}$$

I represent drainage density using the downslope distance from the hilltop to the channel head, L_h, at which the slopes above and below the channel head are equal. The equilibrium slope for linear hillslope diffusion (S_H) can be expressed as [e.g. Roering *et al.*, 2001]:

$$S_H = \frac{E}{D} L_h, \tag{7.3}$$

where D represents a diffusivity coefficient [L^2 T^{-1}]. In my in-text model, I assume that the drainage area at the channel head, A, is linearly related to the distance from the divide L_h. However in this alternative formulation, I instead assume a power law relationship between A and L_h thus where $A = bL_h{}^y$. I can therefore substitute A for L_h in the detachment-limited fluvial model:

$$S_{CH} = \left(\frac{E}{Kb^m}\right)^{\frac{1}{n}} L_h^{-ym/n}. \tag{7.4}$$

I equate the slopes above and below the channel head, given by S_H and S_{CH} respectively (equations 7.3 and 7.4), to obtain the mean length of overland flow:

$$L_h = D^{1/(1+(ym/n))} k_f^{-1/(ym+n)} E^{(1-n)/(ym+n)}, \tag{7.5}$$

where $k_f = Kb^m$. The mean length of overland flow is approximately equal to half the reciprocal of D_d [Horton, 1945], and therefore equation 7.5 can be converted to:

$$\frac{1}{2D_d} = D^{1/(1+(ym/n))} k_f^{-1/(ym+n)} E^{\psi}, \tag{7.6}$$

where $\psi = (1-n)/(ym+n)$. This alternative model formulation results in a similar expression to that of the simpler model presented in the main text. I also modify the model for non-linear sediment transport to include the power law relationship between A and L_h. Nonlinear hillslope sediment flux (q_s) can be modelled according to:

$$q_s = \frac{DS_H}{1-(S_H/S_c)^2}, \tag{7.7}$$

where S_c is a threshold slope gradient beyond which q_s tends to infinity [Roering *et al.*, 1999, 2001]. Under this regime, hillslope gradient can be stated as [e.g. Roering *et al.*, 2001]:

$$S_H = \frac{DS_c^2}{2EL_h}\left(\sqrt{1+\left(\frac{2EL_h}{DS_c}\right)^2}-1\right). \tag{7.8}$$

Due to the nonlinearity of equation 7.8 there is no analytical solution: I instead show it numerically in Figure 7.1b. Figure 7.1 shows that the predicted relationship varies with n in a similar way to that of the simpler model formulation presented in the main text. The pattern of the relationship is the same, with a slight variation in the absolute value of D_d predicted.

7.2 Description of parameters used in the CHILD model

In the CHILD model, topography evolves based on equation 7.1, and either equation 7.3 or equation 7.7 [Tucker *et al.*, 2001a; Attal *et al.*, 2011]. The scenarios we present model purely detachment-limited erosion, where there are neither erosion thresholds nor adjustment in channel geometry. Erosion driven by soil creep is computed based on equation 7.3. We also examine scenarios where hillslope erosion is driven by nonlinear sediment flux, calculated by equation 7.7. Fluvial erosion rate E [L T^{-1}] is calculated following:

$$E = k_b \tau_b^{pb}, \tag{7.9}$$

where k_b is a specific bedrock erodibility coefficient (in L T^{-1} per "stress quantity"

in SI units), τ_b [M L^{-1} T^{-2}] is a fluvial shear stress quantity, and pb is a dimensionless constant. The erosion rate calculated for both hillslope and fluvial processes is compared at each time step for each node, and the elevation of the node is lowered by the largest amount predicted by either of the two processes. Beyond a given contributing area, fluvial processes become dominant, and equation 7.9 prevails. The shear stress quantity (the unit of which depends on the values chosen for exponents mb and nb) is calculated according to:

$$\tau_b = k_g (Q/W)^{mb} S^{nb}, \tag{7.10}$$

where Q is water discharge [L^3 T^{-1}], W [L] is channel width, k_g is a coefficient, and mb and nb are constants. Here, channel width is calculated using the simplest form of hydraulic scaling available in CHILD [Leopold and Maddock, 1953]:

$$W = k_w Q^{1/2}, \tag{7.11}$$

where k_w is a hydraulic scaling coefficient [$L^{-1/2}$ $T^{1/2}$]. In the model, we assume no infiltration so that discharge is only the product of precipitation rate P in [L T^{-1}] by contributing area:

$$Q = PA. \tag{7.12}$$

Combining equations 7.9 to 7.12 gives:

$$E = k_b k_t^{pb} k_w^{(pb.mb)} P^{(pb.mb/2)} A^{(pb.mb/2)} S^{(pb.nb)}. \tag{7.13}$$

This equation is equivalent to equation 7.1, with $m = pb.mb/2$, $n = pb.nb$, and $K = k_b k_t^{pb} k_w^{(-pb.mb)} P^{(pb.mb/2)}$. Note that the exponents mb, nb, and pb can be set to simulate different fluvial incision laws (i.e. incision rate proportional to fluvial shear stress, cross-section-averaged stream power, or specific stream power). We start our initial scenario with $nb = mb = pb = 1$ where erosion is proportional to specific stream power. This leads to $m = 0.5$ and $n = 1$ in equation 7.1. We then vary n in each scenario, while leaving m constant. Table 5.1 details the value of each parameter in the model runs.

7.3 Figures

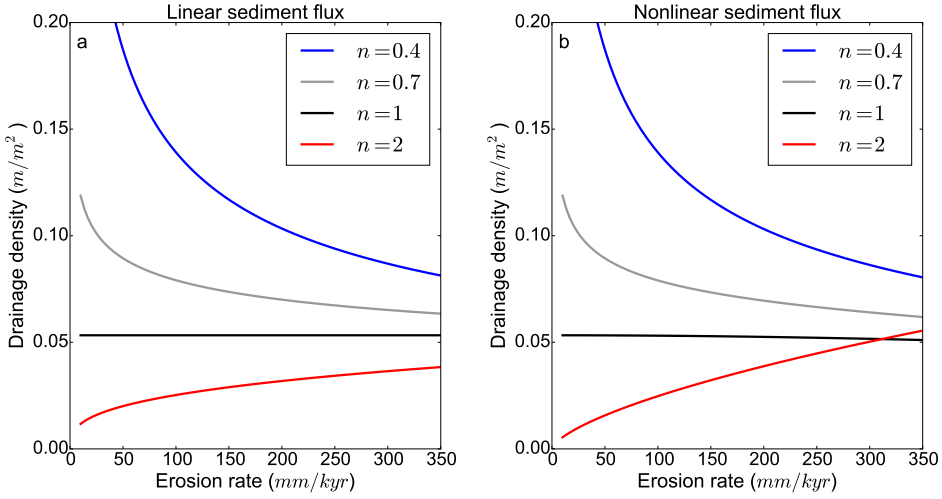

Figure 7.1: Analytical predictions of the relationship between drainage density and erosion rate for a) linear hillslope sediment flux, and b) nonlinear hillslope sediment flux with the alternative model formulation. I set parameters in equations 7.6 and 7.8 to the following: $D = 0.0088$ m^2 yr^{-1}, $K = 1 \times 10^{-4}$ m yr^{-1}, $m = 0.5$, and $S_c = 1.25$. The relationship depends on the value of n in the stream power law: we predict a positive relationship for $n > 1$, a negative relationship for $n < 1$, and no relationship between D_d and E for $n = 1$.

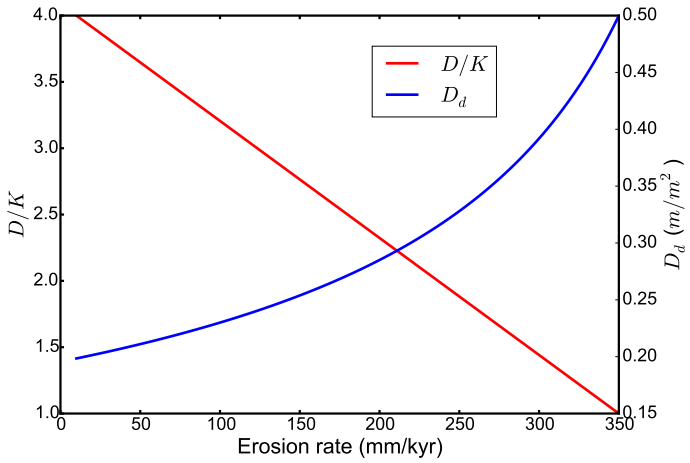

Figure 7.2: Hypothetical relationship between D_d and E for $n = 1$ if the ratio of D/K varies with erosion rate. D/K in this example is set to vary linearly with erosion rate. This results in an exponential increase in D_d with E.

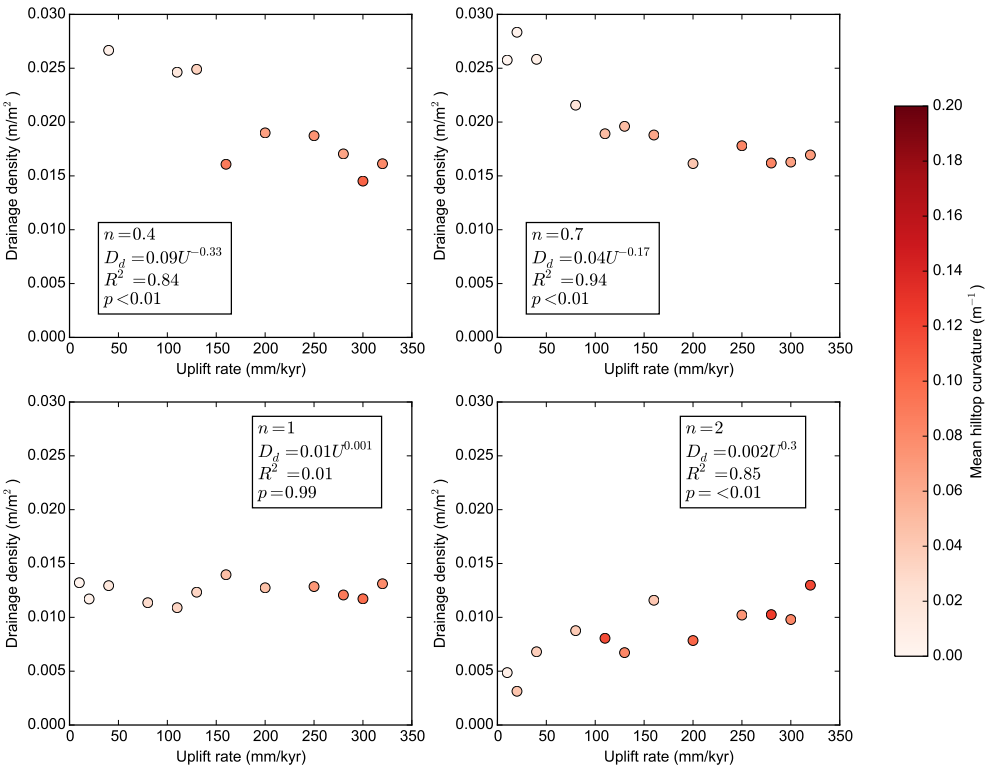

Figure 7.3: Results of CHILD modelling for steady state scenarios with linear hillslope sediment transport with 2.5 m grid resolution. Plots indicate measured relationship between drainage density and uplift rate where $n = 0.4$, $n = 0.7$, $n = 1$, and $n = 2$. The points are coloured by mean hilltop curvature: lighter colours indicate low curvature values and darker colours indicate high values.

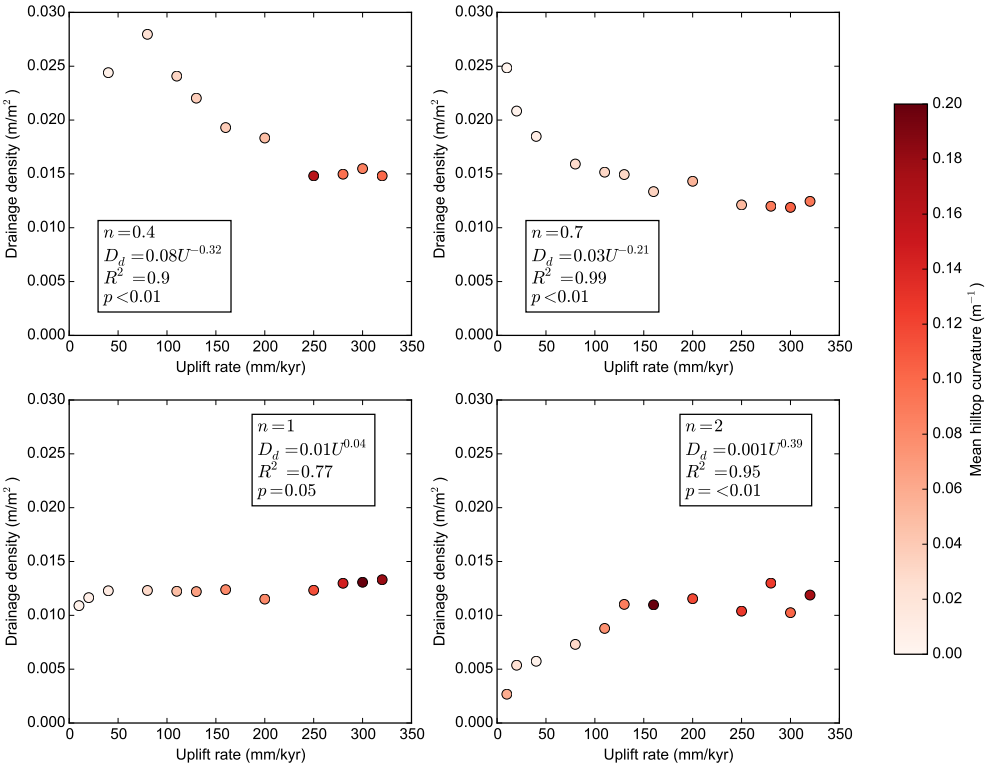

Figure 7.4: Results of CHILD modelling for steady state scenarios with linear hillslope sediment transport with 7.5 m grid resolution. Plots indicate measured relationship between drainage density and uplift rate where $n = 0.4$, $n = 0.7$, $n = 1$, and $n = 2$. The points are coloured by mean hilltop curvature: lighter colours indicate low curvature values and darker colours indicate high values.

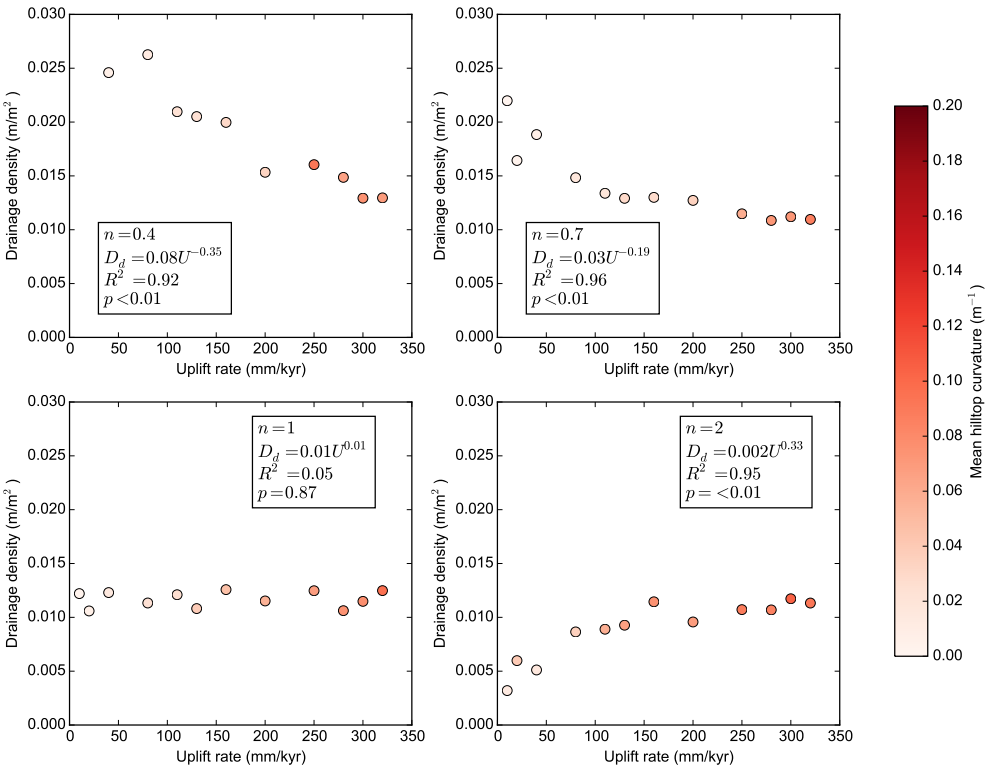

Figure 7.5: Results of CHILD modelling for steady state scenarios with linear hillslope sediment transport with 10 m grid resolution. Plots indicate measured relationship between drainage density and uplift rate where $n = 0.4$, $n = 0.7$, $n = 1$, and $n = 2$. The points are coloured by mean hilltop curvature: lighter colours indicate low curvature values and darker colours indicate high values.

References

Abrahams, A.D. (1984). Channel Networks: A Geomorphological Perspective. *Water Resources Research*, **20**, 161–188.

Abrahams, A.D. and Flint, J.J. (1983). Geological controls on the topological properties of some trellis channel networks. *Geological Society of America Bulletin*, **94**, 80–91.

Ahnert, F. (1970). Functional relationships between denudation, relief, and uplift in large, mid-latitude drainage basins. *American Journal of Science*, **268**, 243–263.

Ahnert, F. (1976). Brief description of a comprehensive three-dimensional process-response model for landform development. *Zeitschrift fur Geomorphologie, N. F., Supplementband*, **25**, 29–49.

Akaike, H. (1974). A new look at the statistical model identification. *Automatic Control, IEEE Transactions on*, **19**, 716–723.

Amos, C.B. and Burbank, D.W. (2007). Channel width response to differential uplift. *Journal of Geophysical Research: Earth Surface*, **112**, F02010.

Anderson, S.P., Anderson, R.S. and Tucker, G.E. (2012). Landscape scale linkages in critical zone evolution. *Comptes Rendus Geoscience*, **344**, 586–596.

Andrews, D.J. and Bucknam, R.C. (1987). Fitting degradation of shoreline scarps by a nonlinear diffusion model. *Journal of Geophysical Research: Solid Earth*, **92**, 12857–12867.

Anthony, D.M. and Granger, D.E. (2007). An empirical stream power formulation for knickpoint retreat in Appalachian Plateau fluviokarst. *Journal of Hydrology*, **343**, 117–126.

Attal, M., Cowie, P.A., Whittaker, A.C., Hobley, D., Tucker, G.E. and Roberts, G.P. (2011). Testing fluvial erosion models using the transient response of bedrock rivers to tectonic forcing in the Apennines, Italy. *Journal of Geophysical Research: Earth Surface*, **116**, F02005.

Attal, M., Mudd, S.M., Hurst, M.D., Weinman, B., Yoo, K. and Naylor, M. (2015). Impact of change in erosion rate and landscape steepness on hillslope and fluvial sediments grain size in the Feather River basin (Sierra Nevada, California). *Earth Surface Dynamics*, **3**, 201–222.

Avouac, J.P. and Peltzer, G. (1993). Active tectonics in southern Xinjiang, China: Analysis of terrace riser and normal fault scarp degradation along the Hotan-Qira Fault System. *Journal of Geophysical Research: Solid Earth*, **98**, 21773–21807.

Axelsson, P. (1999). Processing of laser scanner data—algorithms and applications. *ISPRS Journal of Photogrammetry and Remote Sensing*, **54**, 138–147.

Baltsavias, E.P. (1999). A comparison between photogrammetry and laser scanning. *ISPRS Journal of Photogrammetry and Remote Sensing*, **54**, 83–94.

Band, L.E. (1986). Topographic Partition of Watersheds with Digital Elevation Models. *Water Resources Research*, **22**, 15–24.

Belmont, P. (2011). Floodplain width adjustments in response to rapid base level fall and knickpoint migration. *Geomorphology*, **128**, 92–102.

Belmont, P., Gran, K., Jennings, C.E., Wittkop, C. and Day, S.S. (2011a). Holocene landscape evolution and erosional processes in the Le Sueur River, central Minnesota. *Field Guides*, **24**, 439–455.

Belmont, P., Gran, K.B., Schottler, S.P., Wilcock, P.R., Day, S.S., Jennings, C., Lauer, J.W., Viparelli, E., Willenbring, J.K., Engstrom, D.R. and Parker, G. (2011b). Large Shift in Source of Fine Sediment in the Upper Mississippi River. *Environmental Science & Technology*, **45**, 8804–8810.

Benda, L. and Dunne, T. (1987). Sediment routing by debris flows. In R.L. Beschta, R. Blinn, G.E. Grant, G. Ice and F.J. Swanson, eds., *Erosion and sedimentation in the Pacific rim*, International Association of Hydrological Sciences Publication 165, 213–223.

Berti, M., Corsini, A. and Daehne, A. (2013). Comparative analysis of surface roughness algorithms for the identification of active landslides. *Geomorphology*, **182**, 1–18.

Beven, K. (1993). Prophecy, reality and uncertainty in distributed hydrological modelling. *Advances in Water Resources*, **16**, 41–51.

Beven, K. (1997). TOPMODEL: A critique. *Hydrological Processes*, **11**, 1069–1085.

Beven, K.J. and Kirkby, M.J. (1979). A physically based, variable contributing area model of basin hydrology / Un modèle à base physique de zone d'appel variable de l'hydrologie du bassin versant. *Hydrological Sciences Bulletin*, **24**, 43–69.

Beven, K.J., Lamb, R., Quinn, P., Romanowicz, R. and Freer, J. (1995). TOPMODEL. In V.P. Singh, ed., *Computer Models of Watershed Hydrology*, 627–668, Water Resource Publications, Colorado.

Binnie, S.A., Phillips, W.M., Summerfield, M.A. and Fifield, L.K. (2007). Tectonic uplift, threshold hillslopes, and denudation rates in a developing mountain range. *Geology*, **35**, 743–746.

Blöthe, J.H. and Korup, O. (2013). Millennial lag times in the Himalayan sediment routing system. *Earth and Planetary Science Letters*, **382**, 38–46.

Booij, M.J. (2005). Impact of climate change on river flooding assessed with different spatial model resolutions. *Journal of Hydrology*, **303**, 176–198.

Booth, A.M., Roering, J.J. and Perron, J.T. (2009). Automated landslide mapping using spectral analysis and high-resolution topographic data: Puget Sound lowlands, Washington, and Portland Hills, Oregon. *Geomorphology*, **109**, 132–147.

Bowles, C.J. and Cowgill, E. (2012). Discovering marine terraces using airborne LiDAR along the Mendocino-Sonoma coast, northern California. *Geosphere*, **8**, 386–402.

Braun, J. and Willett, S.D. (2013). A very efficient O(n), implicit and parallel method to solve the stream power equation governing fluvial incision and landscape evolution. *Geomorphology*, **180–181**, 170–179.

Braun, J., Heimsath, A.M. and Chappell, J. (2001). Sediment transport mechanisms on soil-mantled hillslopes. *Geology*, **29**, 683–686.

Braun, J., Simon-Labric, T., Murray, K.E. and Reiners, P.W. (2014). Topographic relief driven by variations in surface rock density. *Nature Geoscience*, **7**, 534–540.

Brierley, G.J. and Fryirs, K.A. (2013). *Geomorphology and River Management: Applications of the River Styles Framework*. John Wiley & Sons.

Brown, A.G., Carey, C., Erkens, G., Fuchs, M., Hoffmann, T., Macaire, J.J., Moldenhauer, K.M. and Walling, D.E. (2009). From sedimentary records to sediment budgets: Multiple approaches to catchment sediment flux. *Geomorphology*, **108**, 35–47.

Bull, W.B. (1991). *Geomorphic responses to climatic change*. Oxford University Press, New York.

Burbank, D.W. (1992). Causes of recent Himalayan uplift deduced from deposited patterns in the Ganges basin. *Nature*, **357**, 680–683.

Burbank, D.W., Leland, J., Fielding, E., Anderson, R.S., Brozovic, N., Reid, M.R. and Duncan, C. (1996). Bedrock incision, rock uplift and threshold hillslopes in the northwestern Himalayas. *Nature*, **379**, 505–510.

Carlston, C.W. (1963). *Drainage density and streamflow*. U.S. Govt. Print. Off.

Carson, M.A. and Kirkby, M.J. (1972). *Hillslope Form and Process*. Cambridge University Press, Cambridge, UK.

Carter, W., Shrestha, R., Tuell, G., Bloomquist, D. and Sartori, M. (2001). Airborne laser swath mapping shines new light on Earth's topography. *Eos, Transactions American Geophysical Union*, **82**, 549–555.

Chorley, R.J. (1957). Illustrating the Laws of Morphometry. *Geological Magazine*, **94**, 140–150.

Chorley, R.J. and Morgan, M.A. (1962). Comparison of Morphometric Features, Unaka Mountains, Tennessee and North Carolina, and Dartmoor, England. *Geological Society of America Bulletin*, **73**, 17–34.

Church, M. (2006). Bed Material Transport and the Morphology of Alluvial River Channels. *Annual Review of Earth and Planetary Sciences*, **34**, 325–354.

Clark, D. (1995). *Extent, timing, and climatic significance of latest Pleistocene and Holocene glaciation in the Sierra Nevada, California*. PhD thesis, University of Washington, Seattle.

Clubb, F.J., Mudd, S.M., Milodowski, D.T., Hurst, M.D. and Slater, L.J. (2014). Objective extraction of channel heads from high-resolution topographic data. *Water Resources Research*, **50**, 4283–4304.

Cobby, D.M., Mason, D.C., Horritt, M.S. and Bates, P.D. (2003). Two-dimensional hydraulic flood modelling using a finite-element mesh decomposed according to vegetation and topographic features derived from airborne scanning laser altimetry. *Hydrological Processes*, **17**, 1979–2000.

Collins, D.B.G. and Bras, R.L. (2010). Climatic and ecological controls of equilibrium drainage density, relief, and channel concavity in dry lands. *Water Resources Research*, **46**, W04508.

Committee on FEMA Flood Maps (2009). *Mapping the Zone: Improving Flood Map Accuracy*. The National Academies Press, 500 Fifth Street, N.W. Washington, DC 20001.

Conley, J. (1985). Geology of the Southwestern Virginia Piedmont. Tech. Rep. 59, Department of Mines, Minerals and Energy, Charlottesville, Virginia.

Cook, K.L., Turowski, J.M. and Hovius, N. (2013). A demonstration of the importance of bedload transport for fluvial bedrock erosion and knickpoint propagation. *Earth Surface Processes and Landforms*, **38**, 683–695.

Corenblit, D. and Steiger, J. (2009). Vegetation as a major conductor of geomorphic changes on the Earth surface: toward evolutionary geomorphology. *Earth Surface Processes and Landforms*, **34**, 891–896.

Cox, K.G. (1989). The role of mantle plumes in the development of continental drainage patterns. *Nature*, **342**, 873–877.

Culling, W.E.H. (1960). Analytical Theory of Erosion. *The Journal of Geology*, **68**, 336–344.

Culling, W.E.H. (1963). Soil Creep and the Development of Hillside Slopes. *The Journal of Geology*, **71**, 127–161.

Cunha, P.P., Martins, A.A., Huot, S., Murray, A. and Raposo, L. (2008). Dating the Tejo river lower terraces in the Ródão area (Portugal) to assess the role of tectonics and uplift. *Geomorphology*, **102**, 43–54.

Davis, W.M. (1892). The convex profile of badland divides. *Science*, **20**, 245–245.

Degiorgis, M., Gnecco, G., Gorni, S., Roth, G., Sanguineti, M. and Taramasso, A.C. (2012). Classifiers for the detection of flood-prone areas using remote sensed elevation data. *Journal of Hydrology*, **470–471**, 302–315.

Demoulin, A., Bovy, B., Rixhon, G. and Cornet, Y. (2007). An automated method to extract fluvial terraces from digital elevation models: The Vesdre valley, a case study in eastern Belgium. *Geomorphology*, **91**, 51–64.

Densmore, A.L., Ellis, M.A. and Anderson, R.S. (1998). Landsliding and the evolution of normal-fault-bounded mountains. *Journal of Geophysical Research: Solid Earth*, **103**, 15203–15219.

Desmet, P.J.J., Poesen, J., Govers, G. and Vandaele, K. (1999). Importance of slope gradient and contributing area for optimal prediction of the initiation and trajectory of ephemeral gullies. *CATENA*, **37**, 377–392.

Dethier, D.P., Ouimet, W., Bierman, P.R., Rood, D.H. and Balco, G. (2014). Basins and bedrock: Spatial variation in 10be erosion rates and increasing relief in the southern Rocky Mountains, USA. *Geology*, G34922.1.

Devauchelle, O., Petroff, A.P., Seybold, H.F. and Rothman, D.H. (2012). Ramification of stream networks. *Proceedings of the National Academy of Sciences*, **109**, 20832–20836.

Dibblee, T.W. and Minch, J.A. (2008). Geologic Map of the Point Delgada and Garberville 15 minute Quadrangles, Humboldt and Mendocino Counties, California.

DiBiase, R.A. and Lamb, M.P. (2013). Vegetation and wildfire controls on sediment yield in bedrock landscapes. *Geophysical Research Letters*, **40**, 1093–1097.

DiBiase, R.A., Whipple, K.X., Heimsath, A.M. and Ouimet, W.B. (2010). Landscape form and millennial erosion rates in the San Gabriel Mountains, CA. *Earth and Planetary Science Letters*, **289**, 134–144.

DiBiase, R.A., Heimsath, A.M. and Whipple, K.X. (2012). Hillslope response to tectonic forcing in threshold landscapes. *Earth Surface Processes and Landforms*, **37**, 855–865.

Dietrich, W.E. and Dunne, T. (1978). Sediment budget for a small catchment in mountainous terrain. *Z. Geomorphol. Suppl.*, **29**, 191–206.

Dietrich, W.E. and Dunne, T. (1993). The channel head. In K. Beven and M.J. Kirkby, eds., *Channel Network Hydrology*, 175–219, J. Wiley and Sons.

Dietrich, W.E. and Perron, J.T. (2006). The search for a topographic signature of life. *Nature*, **439**, 411–418.

Dietrich, W.E., Wilson, C.J. and Reneau, S. (1986). Hollows, colluvium and landslides in soil-mantled landscapes. In A.D. Abrahams, ed., *Hillslope Processes*, Sixteenth Annual Geomorphology Symposium, 361–388, Allen and Unwin.

Dietrich, W.E., Wilson, C.J., Montgomery, D.R., McKean, J. and Bauer, R. (1992). Erosion thresholds and land surface morphology. *Geology*, **20**, 675–679.

Dietrich, W.E., Wilson, C.J., Montgomery, D.R. and McKean, J. (1993). Analysis of Erosion Thresholds, Channel Networks, and Landscape Morphology Using a Digital Terrain Model. *The Journal of Geology*, **101**, 259–278.

Dietrich, W.E., Bellugi, D.G., Sklar, L.S., Stock, J.D., Heimsath, A.M. and Roering, J.J. (2003). Geomorphic Transport Laws for Predicting Landscape form and Dynamics. In P.R. Wilcock and R.M. Iverson, eds., *Prediction in Geomorphology*, 103–132, American Geophysical Union.

Dingle, E.H., Sinclair, H.D., Attal, M., Milodowski, D.T. and Singh, V. (2016). Subsidence control on river morphology and grain size in the Ganga Plain. *American Journal of Science*, **316**, 778–812.

Dodds, P.S. and Rothman, D.H. (1999). Unified view of scaling laws for river networks. *Physical Review E*, **59**, 4865–4877.

Dodov, B. and Foufoula-Georgiou, E. (2006). Floodplain morphometry extraction from a high-resolution digital elevation model: a simple algorithm for regional analysis studies. *IEEE Geoscience and Remote Sensing Letters*, **3**, 410–413.

Dunne, T. (1980). Formation and controls of channel networks. *Progress in Physical Geography*, **4**, 211–239.

Durbin, J. and Watson, G.S. (1950). Testing for Serial Correlation in Least Squares Regression. I. *Biometrika*, **37**, 409–428.

Duvall, A., Kirby, E. and Burbank, D. (2004). Tectonic and lithologic controls on bedrock channel profiles and processes in coastal California. *Journal of Geophysical Research: Earth Surface*, **109**, F03002.

England, P. and Molnar, P. (1990). Surface uplift, uplift of rocks, and exhumation of rocks. *Geology*, **18**, 1173–1177.

Farr, T.G., Rosen, P.A., Caro, E., Crippen, R., Duren, R., Hensley, S., Kobrick, M., Paller, M., Rodriguez, E., Roth, L., Seal, D., Shaffer, S., Shimada, J., Umland, J., Werner, M., Oskin, M., Burbank, D. and Alsdorf, D. (2007). The Shuttle Radar Topography Mission. *Reviews of Geophysics*, **45**, RG2004.

Fawcett, T. (2006). An introduction to ROC analysis. *Pattern Recognition Letters*, **27**, 861–874.

Finnegan, N.J. and Dietrich, W.E. (2011). Episodic bedrock strath terrace formation due to meander migration and cutoff. *Geology*, **39**, 143–146.

Finnegan, N.J., Roe, G., Montgomery, D.R. and Hallet, B. (2005). Controls on the channel width of rivers: Implications for modeling fluvial incision of bedrock. *Geology*, **33**, 229–232.

Finnegan, N.J., Sklar, L.S. and Fuller, T.K. (2007). Interplay of sediment supply, river incision, and channel morphology revealed by the transient evolution of an experimental bedrock channel. *Journal of Geophysical Research: Earth Surface*, **112**, F03S11.

Fisher, G.B., Bookhagen, B. and Amos, C.B. (2013). Channel planform geometry and slopes from freely available high-spatial resolution imagery and DEM fusion: Implications for channel width scalings, erosion proxies, and fluvial signatures in tectonically active landscapes. *Geomorphology*, **194**, 46–56.

Fisher, T.G. (2003). Chronology of glacial Lake Agassiz meltwater routed to the Gulf of Mexico. *Quaternary Research*, **59**, 271–276.

Flint, J.J. (1974). Stream gradient as a function of order, magnitude, and discharge. *Water Resources Research*, **10**, 969–973.

Fox, M., Goren, L., May, D.A. and Willett, S.D. (2014). Inversion of fluvial channels for paleorock uplift rates in Taiwan. *Journal of Geophysical Research: Earth Surface*, **119**, 1853–1875.

Freeman, T.G. (1991). Calculating catchment area with divergent flow based on a regular grid. *Computers & Geosciences*, **17**, 413–422.

Fuller, T.K., Perg, L.A., Willenbring, J.K. and Lepper, K. (2009). Field evidence for climate-driven changes in sediment supply leading to strath terrace formation. *Geology*, **37**, 467–470.

Furbish, D.J. and Roering, J.J. (2013). Sediment disentrainment and the concept of local versus nonlocal transport on hillslopes. *Journal of Geophysical Research: Earth Surface*, **118**, 937–952.

Furbish, D.J., Haff, P.K., Dietrich, W.E. and Heimsath, A.M. (2009). Statistical description of slope-dependent soil transport and the diffusion-like coefficient. *Journal of Geophysical Research: Earth Surface*, **114**, F00A05.

Gabet, E.J., Reichman, O. and Seabloom, E.W. (2003). The Effects of Bioturbation on Soil Processes and Sediment Transport. *Annual Review of Earth and Planetary Sciences*, **31**, 249–273.

Gabet, E.J., Perron, J.T. and Johnson, D.L. (2014). Biotic origin for Mima mounds supported by numerical modeling. *Geomorphology*, **206**, 58–66.

Gabet, E.J., Mudd, S.M., Milodowski, D.T., Yoo, K., Hurst, M.D. and Dosseto, A. (2015). Local topography and erosion rate control regolith thickness along a ridgeline in the Sierra Nevada, California. *Earth Surface Processes and Landforms*, **40**, 1779–1790.

Gangodagamage, C., Belmont, P. and Foufoula-Georgiou, E. (2011). Revisiting scaling laws in river basins: New considerations across hillslope and fluvial regimes. *Water Resources Research*, **47**, W07508.

Gasparini, N.M. and Brandon, M.T. (2011). A generalized power law approximation for fluvial incision of bedrock channels. *Journal of Geophysical Research: Earth Surface*, **116**, F02020.

Gesch, D.B., Oimoen, M.J., Greenlee, S.K., Nelson, C.A., Steuck, M.J. and Tyler, D.J. (2002). The national elevation data set. *Photogrammetric Engineering and Remote Sensing*, **68**, 511.

Gilbert, G. (1877). Geology of the Henry Mountains. USGS Unnumbered Series, Government Printing Office, Washington, D.C.

Gilbert, G. (1909). The Convexity of Hilltops. *The Journal of Geology*, **17**, 344–350.

Glenn, N.F., Streutker, D.R., Chadwick, D.J., Thackray, G.D. and Dorsch, S.J. (2006). Analysis of LiDAR-derived topographic information for characterizing and differentiating landslide morphology and activity. *Geomorphology*, **73**, 131–148.

Glennie, C.L., Carter, W.E., Shrestha, R.L. and Dietrich, W.E. (2013). Geodetic imaging with airborne LiDAR: the Earth's surface revealed. *Reports on Progress in Physics*, **76**, 086801.

Goebel, P. and Hix, D.M. (1996). Development of mixed-oak forests in south-eastern Ohio: a comparison of second-growth and old-growth forests. *Forest Ecology and Management*, **84**, 1–21.

Goren, L., Fox, M. and Willett, S.D. (2014). Tectonics from fluvial topography using formal linear inversion: Theory and applications to the Inyo Mountains, California. *Journal of Geophysical Research: Earth Surface*, **119**, 1651–1681.

Gran, K.B., Belmont, P., Day, S.S., Jennings, C., Johnson, A., Perg, L. and Wilcock, P.R. (2009). Geomorphic evolution of the Le Sueur River, Minnesota, USA, and implications for current sediment loading. *Geological Society of America Special Papers*, **451**, 119–130.

Gran, K.B., Finnegan, N., Johnson, A.L., Belmont, P., Wittkop, C. and Rittenour, T. (2013). Landscape evolution, valley excavation, and terrace development following abrupt postglacial base-level fall. *Geological Society of America Bulletin*, **125**, 1851–1864.

Gray, D.M. (1961). Interrelationships of watershed characteristics. *Journal of Geophysical Research*, **66**, 1215–1223.

Gregory, K.J. and Walling, D.E. (1968). The Variation of Drainage Density Within a Catchment. *International Association of Scientific Hydrology Bulletin*, **13**, 61–68.

Grieve, S.W., Mudd, S.M. and Hurst, M.D. (2016a). How long is a hillslope? *Earth Surface Processes and Landforms*, **41**, 1039–1054.

Grieve, S.W.D. (2016). *Uncovering signatures of geomorphic process through high resolution topography*. PhD thesis, University of Edinburgh.

Grieve, S.W.D., Mudd, S.M., Hurst, M.D. and Milodowski, D.T. (2016b). A nondimensional framework for exploring the relief structure of landscapes. *Earth Surface Dynamics*, **4**, 309–325.

Grieve, S.W.D., Mudd, S.M., Milodowski, D.T., Clubb, F.J. and Furbish, D.J. (2016c). How does grid-resolution modulate the topographic expression of geomorphic processes? *Earth Surface Dynamics*, **4**, 627–653.

Grimaldi, S., Petroselli, A., Arcangeletti, E. and Nardi, F. (2013). Flood mapping in ungauged basins using fully continuous hydrologic–hydraulic modeling. *Journal of Hydrology*, **487**, 39–47.

Guzzetti, F., Stark, C.P. and Salvati, P. (2005). Evaluation of Flood and Landslide Risk to the Population of Italy. *Environmental Management*, **36**, 15–36.

Guzzetti, F., Mondini, A.C., Cardinali, M., Fiorucci, F., Santangelo, M. and Chang, K.T. (2012). Landslide inventory maps: New tools for an old problem. *Earth-Science Reviews*, **112**, 42–66.

Hack, J. (1957). Studies of longitudinal profiles in Virginia and Maryland. U.S. Geological Survey Professional Paper 294-B, United States Government Printing Office, Washington, D.C.

Hack, J. (1960). Interpretation of Erosional Topography in Humid Temperate Regions. *American Journal of Science*, **258**, 80–97.

Hack, J. (1973). Stream-profile analysis and stream-gradient index. *Journal of Research of the US Geological Survey*, **1**, 421–429.

Han, S., Kim, S., Hoon Jung, J., Kim, C., Yu, K. and Heo, J. (2012). Development of a hashing-based data structure for the fast retrieval of 3d terrestrial laser scanned data. *Computers & Geosciences*, **39**, 1–10.

Hancock, G. and Willgoose, G. (2001). Use of a landscape simulator in the validation of the SIBERIA Catchment Evolution Model: Declining equilibrium landforms. *Water Resources Research*, **37**, 1981–1992.

Hancock, G.R., Willgoose, G.R. and Evans, K.G. (2002). Testing of the SIBERIA landscape evolution model using the Tin Camp Creek, Northern Territory, Australia, field catchment. *Earth Surface Processes and Landforms*, **27**, 125–143.

Hancock, G.S. and Anderson, R.S. (2002). Numerical modeling of fluvial strath-terrace formation in response to oscillating climate. *Geological Society of America Bulletin*, **114**, 1131–1142.

Hancock, G.S., Anderson, R.S. and Whipple, K.X. (1998). Beyond Power: Bedrock River Incision Process and Form. In K.J. Tinkler and E.E. Wohl, eds., *Rivers Over Rock: Fluvial Processes in Bedrock Channels*, 35–60, American Geophysical Union.

Harel, M.A., Mudd, S.M. and Attal, M. (2016). Global analysis of the stream power law parameters based on worldwide 10be denudation rates. *Geomorphology*, **268**, 184–196.

Harkins, N., Kirby, E., Heimsath, A., Robinson, R. and Reiser, U. (2007). Transient fluvial incision in the headwaters of the Yellow River, northeastern Tibet, China. *Journal of Geophysical Research: Earth Surface*, **112**, F03S04.

Hartmann, D., Klein Tank, A., Rusticucci, M., Alexander, L.V., Bronnimann, S., Charabi, Y., Dentener, F., Dlugokencky, E.J., Easterling, D.R., Kaplan, A., Soden, B.J., Thorne, P.W., Wild, M. and Zhai, P.M. (2013). Observations: Atmosphere and Surface. In T.F. Stocker, D. Qin, G. Plattner, M. Tignor, S. Allen, J. Boschung, A. Nauels, Y. Xia, V. Bex and P. Midgley, eds., *Climate Change 2013: The Physical Science Basis. Contribution of Working Group I to the Fifth Assessment Report of the Intergovernmental Panel on Climate Change*, Cambridge University Press, Cambridge, United Kingdom and New York, NY, USA.

Hartmann, J. and Moosdorf, N. (2012). The new global lithological map database GLiM: A representation of rock properties at the Earth surface. *Geochemistry, Geophysics, Geosystems*, **13**, Q12004.

He, L., Chao, Y. and Suzuki, K. (2008). A Run-Based Two-Scan Labeling Algorithm. *IEEE Transactions on Image Processing*, **17**, 749–756.

Heimsath, A.M., Dietrich, W.E., Nishiizumi, K. and Finkel, R.C. (1997). The soil production function and landscape equilibrium. *Nature*, **388**, 358–361.

Heimsath, A.M., E. Dietrich, W., Nishiizumi, K. and Finkel, R.C. (1999). Cosmogenic nuclides, topography, and the spatial variation of soil depth. *Geomorphology*, **27**, 151–172.

Heimsath, A.M., Furbish, D.J. and Dietrich, W.E. (2005). The illusion of diffusion: Field evidence for depth-dependent sediment transport. *Geology*, **33**, 949–952.

Heimsath, A.M., DiBiase, R.A. and Whipple, K.X. (2012). Soil production limits and the transition to bedrock-dominated landscapes. *Nature Geoscience*, **5**, 210–214.

Heipke, C., Mayer, H., Wiedemann, C. and Jamet, O. (1997). Automated reconstruction of topographic objects from aerial images using vectorized map information. *International Archives of Photogrammetry and Remote Sensing*, **23**, 47–56.

Henkle, J.E., Wohl, E. and Beckman, N. (2011). Locations of channel heads in the semiarid Colorado Front Range, USA. *Geomorphology*, **129**, 309–319.

Hergarten, S., Robl, J. and Stüwe, K. (2014). Extracting topographic swath profiles across curved geomorphic features. *Earth Surface Dynamics*, **2**, 97–104.

Heritage, G. and Hetherington, D. (2007). Towards a protocol for laser scanning in fluvial geomorphology. *Earth Surface Processes and Landforms*, **32**, 66–74.

Hilley, G.E. and Arrowsmith, J.R. (2008). Geomorphic response to uplift along the Dragon's Back pressure ridge, Carrizo Plain, California. *Geology*, **36**, 367–370.

Hix, D.M. and Pearcy, J.N. (1997). Forest ecosystems of the Marietta Unit, Wayne National Forest, southeastern Ohio: multifactor classification and analysis. *Canadian Journal of Forest Research*, **27**, 1117–1131.

Hodge, R., Brasington, J. and Richards, K. (2009). In situ characterization of grain-scale fluvial morphology using Terrestrial Laser Scanning. *Earth Surface Processes and Landforms*, **34**, 954–968.

Hooshyar, M., Wang, D., Kim, S., Medeiros, S.C. and Hagen, S.C. (2016). Valley and channel networks extraction based on local topographic curvature and k-means clustering of contours. *Water Resources Research*, **52**, 8081–8102.

Hooshyar, M., Singh, A. and Wang, D. (2017). Hydrologic controls on junction angle of river networks. *Water Resources Research*, **53**, 4073–4083.

Hopkins, A.J. and Snyder, N.P. (2016). Performance evaluation of three DEM-based fluvial terrace mapping methods. *Earth Surface Processes and Landforms*, **41**, 1144–1152.

Horritt, M.S. and Bates, P.D. (2002). Evaluation of 1d and 2d numerical models for predicting river flood inundation. *Journal of Hydrology*, **268**, 87–99.

Horton, R.E. (1932). Drainage-basin characteristics. *Eos, Transactions American Geophysical Union*, **13**, 350–361.

Horton, R.E. (1945). Erosional Development of Streams and Their Drainage Basins; Hydrophysical Approach to Quantitative Morphology. *Geological Society of America Bulletin*, **56**, 275–370.

Howard, A.D. (1971a). Optimal Angles of Stream Junction: Geometric, Stability to Capture, and Minimum Power Criteria. *Water Resources Research*, **7**, 863–873.

Howard, A.D. (1971b). Simulation of Stream Networks by Headword Growth and Branching. *Geographical Analysis*, **3**, 29–50.

Howard, A.D. (1980). Thresholds in river regimes. 227–258, Allen and Unwin, London.

Howard, A.D. (1987). Modelling fluvial systems: rock-, gravel- and sand-bed channels. In K.S. Richards, ed., *River channels: environment and process*, 69–94, Blackwell, Oxford.

Howard, A.D. (1990). Theoretical model of optimal drainage networks. *Water Resources Research*, **26**, 2107–2117.

Howard, A.D. (1994). A detachment-limited model of drainage basin evolution. *Water Resources Research*, **30**, 2261–2285.

Howard, A.D. (1997). Badland Morphology and Evolution: Interpretation Using a Simulation Model. *Earth Surface Processes and Landforms*, **22**, 211–227.

Howard, A.D. (1998). Long Profile Development of Bedrock Channels: Interaction of Weathering, Mass Wasting, Bed Erosion, and Sediment Transport. In K.J. Tinkler and E.E. Wohl, eds., *Rivers Over Rock: Fluvial Processes in Bedrock Channels*, 297–319, American Geophysical Union.

Howard, A.D. and Kerby, G. (1983). Channel changes in badlands. *Geological Society of America Bulletin*, **94**, 739–752.

Howard, A.D., Dietrich, W.E. and Seidl, M.A. (1994). Modeling fluvial erosion on regional to continental scales. *Journal of Geophysical Research: Solid Earth*, **99**, 13971–13986.

Hunter, N.M., Bates, P.D., Horritt, M.S. and Wilson, M.D. (2007). Simple spatially-distributed models for predicting flood inundation: A review. *Geomorphology*, **90**, 208–225.

Hurst, M.D., Mudd, S.M., Walcott, R., Attal, M. and Yoo, K. (2012). Using hilltop curvature to derive the spatial distribution of erosion rates. *Journal of Geophysical Research: Earth Surface*, **117**.

Hurst, M.D., Mudd, S.M., Attal, M. and Hilley, G. (2013a). Hillslopes Record the Growth and Decay of Landscapes. *Science*, **341**, 868–871.

Hurst, M.D., Mudd, S.M., Yoo, K., Attal, M. and Walcott, R. (2013b). Influence of lithology on hillslope morphology and response to tectonic forcing in the northern Sierra Nevada of California. *Journal of Geophysical Research: Earth Surface*, **118**, 832–851.

Ijjasz-Vasquez, E.J. and Bras, R.L. (1995). Scaling regimes of local slope versus contributing area in digital elevation models. *Geomorphology*, **12**, 299–311.

Ioannidis, J.P.A., Allison, D.B., Ball, C.A., Coulibaly, I., Cui, X., Culhane, A.C., Falchi, M., Furlanello, C., Game, L., Jurman, G., Mangion, J., Mehta, T., Nitzberg, M., Page, G.P., Petretto, E. and van Noort, V. (2009). Repeatability of published microarray gene expression analyses. *Nature Genetics*, **41**, 149–155.

Istanbulluoglu, E. and Bras, R.L. (2005). Vegetation-modulated landscape evolution: Effects of vegetation on landscape processes, drainage density, and topography. *Journal of Geophysical Research: Earth Surface*, **110**.

Istanbulluoglu, E., Tarboton, D.G., Pack, R.T. and Luce, C. (2002). A probabilistic approach for channel initiation. *Water Resources Research*, **38**, 61.1–61.14.

Istanbulluoglu, E., Tarboton, D.G., Pack, R.T. and Luce, C. (2003). A sediment transport model for incision of gullies on steep topography. *Water Resources Research*, **39**, 1103.

Jain, V., Fryirs, K. and Brierley, G. (2008). Where do floodplains begin? The role of total stream power and longitudinal profile form on floodplain initiation processes. *Geological Society of America Bulletin*, **120**, 127–141.

Jefferson, A.J. and McGee, R.W. (2013). Channel network extent in the context of historical land use, flow generation processes, and landscape evolution in the North Carolina Piedmont. *Earth Surface Processes and Landforms*, **38**, 601–613.

Julian, J.P., Elmore, A.J. and Guinn, S.M. (2012). Channel head locations in forested watersheds across the mid-Atlantic United States: A physiographic analysis. *Geomorphology*, **177–178**, 194–203.

Jung, M., Burt, T.P. and Bates, P.D. (2004). Toward a conceptual model of floodplain water table response. *Water Resources Research*, **40**, W12409.

Katsuyama, M., Ohte, N. and Kabeya, N. (2005). Effects of bedrock permeability on hillslope and riparian groundwater dynamics in a weathered granite catchment. *Water Resources Research*, **41**, W01010.

Kim, H., Arrowsmith, J., Crosby, C.J., Jaeger-Frank, E., Nandigam, V., Memon, A., Conner, J., Baden, S.B. and Baru, C. (2006). An Efficient Implementation of a Local Binning Algorithm for Digital Elevation Model Generation of LiDAR/ALSM Dataset. *AGU Fall Meeting Abstracts*, **53**.

Kim, J., Warnock, A., Ivanov, V.Y. and Katopodes, N.D. (2012). Coupled modeling of hydrologic and hydrodynamic processes including overland and channel flow. *Advances in Water Resources*, **37**, 104–126.

Kirby, E. and Whipple, K. (2001). Quantifying differential rock-uplift rates via stream profile analysis. *Geology*, **29**, 415–418.

Kirby, E. and Whipple, K.X. (2012). Expression of active tectonics in erosional landscapes. *Journal of Structural Geology*, **44**, 54–75.

Kirchner, J.W. (1993). Statistical inevitability of Horton's laws and the apparent randomness of stream channel networks. *Geology*, **21**, 591–594.

Kirkby, M.J. (1975). Hydrograph modelling strategies. In R. Peel, M. Chisholm and P. Haggett, eds., *Process in Physical and Human Geography*, 69–90, Heinemann, London.

Kirkby, M.J. (1976). Tests of the random network model, and its application to basin hydrology. *Earth Surface Processes*, **1**, 197–212.

Kirkby, M.J. (1980). The stream head as a significant geomorphic threshold. In D.R. Coates and J.D. Vitek, eds., *Thresholds in Geomorphology*, 53–73, Allen and Unwin, Winchester, Massachusetts.

Kirkby, M.J. (1993). Long term interactions between networks and hillslopes. In K. Beven and M.J. Kirkby, eds., *Channel Network Hydrology*, 255–293, J. Wiley and Sons.

Kirkby, M.J. and Chorley, R.J. (1967). Throughflow, Overland Flow and Erosion. *International Association of Scientific Hydrology. Bulletin*, **12**, 5–21.

Kraus, K. and Pfeifer, N. (1998). Determination of terrain models in wooded areas with airborne laser scanner data. *ISPRS Journal of Photogrammetry and Remote Sensing*, **53**, 193–203.

Krishnan, S., Crosby, C., Nandigam, V., Phan, M., Cowart, C., Baru, C. and Arrowsmith, R. (2011). OpenTopography: A Services Oriented Architecture for Community Access to LIDAR Topography. In *Proceedings of the 2Nd International Conference on Computing for Geospatial Research & Applications*, COM.Geo '11, 7:1–7:8, ACM, New York, NY, USA.

Kwang, J.S. and Parker, G. (2017). Landscape evolution models using the stream power incision model show unrealistic behavior when m/n equals 0.5. *Earth Surface Dynamics Discussions*, 1–16.

Lague, D. (2014). The stream power river incision model: evidence, theory and beyond. *Earth Surface Processes and Landforms*, **39**, 38–61.

Lague, D., Hovius, N. and Davy, P. (2005). Discharge, discharge variability, and the bedrock channel profile. *Journal of Geophysical Research: Earth Surface*, **110**, F04006.

Lashermes, B., Foufoula-Georgiou, E. and Dietrich, W.E. (2007). Channel network extraction from high resolution topography using wavelets. *Geophysical Research Letters*, **34**, L23S04.

Lavé, J. and Avouac, J.P. (2000). Active folding of fluvial terraces across the Siwaliks Hills, Himalayas of central Nepal. *Journal of Geophysical Research: Solid Earth*, **105**, 5735–5770.

Lavé, J. and Avouac, J.P. (2001). Fluvial incision and tectonic uplift across the Himalayas of central Nepal. *Journal of Geophysical Research: Solid Earth*, **106**, 26561–26591.

Leopold, L. and Maddock, T. (1953). The hydraulic geometry of stream channels and some physiographic implications. USGS Numbered Series 252, United States Geological Survey.

Leopold, L.B. and Miller, J.P. (1956). Ephemeral streams - Hydraulic factors and their relation to the drainage net. USGS Numbered Series 282-A, U.S. Government Printing Office, Washington D.C.

Limaye, A.B.S. and Lamb, M.P. (2016). Numerical model predictions of autogenic fluvial terraces and comparison to climate change expectations. *Journal of Geophysical Research: Earth Surface*, **121**, 2014JF003392.

Lin, Y.C. and Mills, J.P. (2010). Factors Influencing Pulse Width of Small Footprint, Full Waveform Airborne Laser Scanning Data. *Photogrammetric Engineering & Remote Sensing*, **76**, 49–59.

Liu, X. (2008). Airborne LiDAR for DEM generation: some critical issues. *Progress in Physical Geography*, **32**, 31–49.

Liu, Y. and Gupta, H.V. (2007). Uncertainty in hydrologic modeling: Toward an integrated data assimilation framework. *Water Resources Research*, **43**, W07401.

Liu, Y., Zhou, M., Zhao, S., Zhan, W., Yang, K. and Li, M. (2015). Automated extraction of tidal creeks from airborne laser altimetry data. *Journal of Hydrology*, **527**, 1006–1020.

Lubowe, J.K. (1964). Stream junction angles in the dendritic drainage pattern. *American Journal of Science*, **262**, 325–339.

Mackey, B.H. and Roering, J.J. (2011). Sediment yield, spatial characteristics, and the long-term evolution of active earthflows determined from airborne LiDAR and historical aerial photographs, Eel River, California. *GSA Bulletin*, **123**, 1560–1576.

Mackin, J.H. (1937). Erosional history of the Big Horn Basin, Wyoming. *GSA Bulletin*, **48**, 813–894.

Mallet, C. and Bretar, F. (2009). Full-waveform topographic lidar: State-of-the-art. *ISPRS Journal of Photogrammetry and Remote Sensing*, **64**, 1–16.

Manfreda, S., Di Leo, M. and Sole, A. (2011). Detection of Flood-Prone Areas Using Digital Elevation Models. *Journal of Hydrologic Engineering*, **16**, 781–790.

Manfreda, S., Nardi, F., Samela, C., Grimaldi, S., Taramasso, A.C., Roth, G. and Sole, A. (2014). Investigation on the use of geomorphic approaches for the delineation of flood prone areas. *Journal of Hydrology*, **517**, 863–876.

Maritan, A., Rinaldo, A., Rigon, R., Giacometti, A. and Rodríguez-Iturbe, I. (1996). Scaling laws for river networks. *Physical Review E*, **53**, 1510–1515.

Marshall, J.A. and Roering, J.J. (2014). Diagenetic variation in the Oregon Coast Range: Implications for rock strength, soil production, hillslope form, and landscape evolution. *Journal of Geophysical Research: Earth Surface*, **119**, 2013JF003004.

Martel, S.J. (2011). Mechanics of curved surfaces, with application to surface-parallel cracks. *Geophysical Research Letters*, **38**, L20303.

Martin, K.L., Hix, D.M. and Goebel, P.C. (2011). Coupling of vegetation layers and environmental influences in a mature, second-growth Central Hardwood forest landscape. *Forest Ecology and Management*, **261**, 720–729.

McKean, J. and Roering, J. (2004). Objective landslide detection and surface morphology mapping using high-resolution airborne laser altimetry. *Geomorphology*, **57**, 331–351.

Melton, M.A. (1957). An analysis of the relations among elements of climate, surface properties, and geomorphology. Tech. Rep. 11.

Meng, X., Wang, L. and Currit, N. (2009). Morphology-based Building Detection from Airborne Lidar Data. *Photogrammetric Engineering & Remote Sensing*, **75**, 437–442.

Meng, X., Currit, N. and Zhao, K. (2010). Ground Filtering Algorithms for Airborne LiDAR Data: A Review of Critical Issues. *Remote Sensing*, **2**, 833–860.

Merritts, D. and Bull, W.B. (1989). Interpreting Quaternary uplift rates at the Mendocino triple junction, northern California, from uplifted marine terraces. *Geology*, **17**, 1020–1024.

Merritts, D.J., Vincent, K.R. and Wohl, E.E. (1994). Long river profiles, tectonism, and eustasy: A guide to interpreting fluvial terraces. *Journal of Geophysical Research: Solid Earth*, **99**, 14031–14050.

Milan, D.J., Heritage, G.L. and Hetherington, D. (2007). Application of a 3d laser scanner in the assessment of erosion and deposition volumes and channel change in a proglacial river. *Earth Surface Processes and Landforms*, **32**, 1657–1674.

Milodowski, D.T., Mudd, S.M. and Mitchard, E.T.A. (2015a). Erosion rates as a potential bottom-up control of forest structural characteristics in the Sierra Nevada Mountains. *Ecology*, **96**, 31–38.

Milodowski, D.T., Mudd, S.M. and Mitchard, E.T.A. (2015b). Topographic roughness as a signature of the emergence of bedrock in eroding landscapes. *Earth Surface Dynamics*, **3**, 483–499.

Mitáš, L. and Mitášová, H. (1999). Spatial interpolation. In P. Longley, M. Goodchild, D. Maguire and D. Rhind, eds., *Geographical Information Systems: Principles, Techniques, Management and Applications*, 481–492, Wiley.

Mitášová, H. and Hofierka, J. (1993). Interpolation by regularized spline with tension: II. Application to terrain modeling and surface geometry analysis. *Mathematical Geology*, **25**, 657–669.

Mitášová, H. and Mitáš, L. (1993). Interpolation by regularized spline with tension: I. Theory and implementation. *Mathematical Geology*, **25**, 641–655.

Moglen, G.E., Eltahir, E.A.B. and Bras, R.L. (1998). On the sensitivity of drainage density to climate change. *Water Resources Research*, **34**, 855–862.

Molloy, I. and Stepinski, T.F. (2007). Automatic mapping of valley networks on Mars. *Computers & Geosciences*, **33**, 728–738.

Montgomery, D.R. and Brandon, M.T. (2002). Topographic controls on erosion rates in tectonically active mountain ranges. *Earth and Planetary Science Letters*, **201**, 481–489.

Montgomery, D.R. and Buffington, J.M. (1997). Channel-reach morphology in mountain drainage basins. *Geological Society of America Bulletin*, **109**, 596–611.

Montgomery, D.R. and Dietrich, W.E. (1988). Where do channels begin? *Nature*, **336**, 232–234.

Montgomery, D.R. and Dietrich, W.E. (1989). Source areas, drainage density, and channel initiation. *Water Resources Research*, **25**, 1907–1918.

Montgomery, D.R. and Dietrich, W.E. (1992). Channel initiation and the problem of landscape scale. *Science*, **255**, 826–830.

Montgomery, D.R. and Foufoula-Georgiou, E. (1993). Channel network source representation using digital elevation models. *Water Resources Research*, **29**, 3925–3934.

Montgomery, D.R., Abbe, T.B., Buffington, J.M., Peterson, N.P., Schmidt, K.M. and Stock, J.D. (1996). Distribution of bedrock and alluvial channels in forested mountain drainage basins. *Nature*, **381**, 587–589.

Moore, I.D. and Grayson, R.B. (1991). Terrain-based catchment partitioning and runoff prediction using vector elevation data. *Water Resources Research*, **27**, 1177–1191.

Moore, I.D., O'Loughlin, E.M. and Burch, G.J. (1988). A contour-based topographic model for hydrological and ecological applications. *Earth Surface Processes and Landforms*, **13**, 305–320.

Moore, I.D., Grayson, R.B. and Ladson, A.R. (1991). Digital terrain modelling: A review of hydrological, geomorphological, and biological applications. *Hydrological Processes*, **5**, 3–30.

Morisawa, M. (1957). Accuracy of determination of stream lengths from topographic maps. *Eos, Transactions American Geophysical Union*, **38**, 86–88.

Morrison, M.L., Tennant, T. and Scott, T.A. (1994). Laying the foundation for a comprehensive program of restoration for wildlife habitat in a riparian floodplain. *Environmental Management*, **18**, 939–955.

Morsdorf, F., Nichol, C., Malthus, T. and Woodhouse, I.H. (2009). Assessing forest structural and physiological information content of multi-spectral LiDAR waveforms by radiative transfer modelling. *Remote Sensing of Environment*, **113**, 2152–2163.

Mudd, S.M. (2016). Detection of transience in eroding landscapes. *Earth Surface Processes and Landforms*, **42**, 24–41.

Mudd, S.M. (2017). cat_on_rollerskates_opendata: Cat on rollerskates version 1.0. DOI: 10.5281/zenodo.841790.

Mudd, S.M. and Furbish, D.J. (2004). Influence of chemical denudation on hillslope morphology. *Journal of Geophysical Research: Earth Surface*, **109**.

Mudd, S.M. and Furbish, D.J. (2007). Responses of soil-mantled hillslopes to transient channel incision rates. *Journal of Geophysical Research: Earth Surface*, **112**, F03S18.

Mudd, S.M., Attal, M., Milodowski, D.T., Grieve, S.W. and Valters, D.A. (2014). A statistical framework to quantify spatial variation in channel gradients using the integral method of channel profile analysis. *Journal of Geophysical Research: Earth Surface*, **119**, 138–152.

Nardi, F., Vivoni, E.R. and Grimaldi, S. (2006). Investigating a floodplain scaling relation using a hydrogeomorphic delineation method. *Water Resources Research*, **42**, W09409.

Noman, N.S., Nelson, E.J. and Zundel, A.K. (2001). Review of Automated Floodplain Delineation from Digital Terrain Models. *Journal of Water Resources Planning and Management*, **127**, 394–402.

Novotny, V. (2002). *Water Quality: Diffuse Pollution and Watershed Management*. Wiley.

O'Callaghan, J.F. and Mark, D.M. (1984). The extraction of drainage networks from digital elevation data. *Computer Vision, Graphics, and Image Processing*, **28**, 323–344.

Oguchi, T. (1997). Drainage Density and Relative Relief in Humid Steep Mountains with Frequent Slope Failure. *Earth Surface Processes and Landforms*, **22**, 107–120.

O'Loughlin, E.M. (1986). Prediction of Surface Saturation Zones in Natural Catchments by Topographic Analysis. *Water Resources Research*, **22**, 794–804.

Open Science Collaboration (2015). Estimating the reproducibility of psychological science. *Science*, **349**, aac4716.

Orlandini, S., Tarolli, P., Moretti, G. and Dalla Fontana, G. (2011). On the prediction of channel heads in a complex alpine terrain using gridded elevation data. *Water Resources Research*, **47**.

Ouimet, W.B., Whipple, K.X. and Granger, D.E. (2009). Beyond threshold hillslopes: Channel adjustment to base-level fall in tectonically active mountain ranges. *Geology*, **37**, 579–582.

Passalacqua, P., Do Trung, T., Foufoula-Georgiou, E., Sapiro, G. and Dietrich, W.E. (2010a). A geometric framework for channel network extraction from lidar: Nonlinear diffusion and geodesic paths. *Journal of Geophysical Research: Earth Surface*, **115**, F01002.

Passalacqua, P., Tarolli, P. and Foufoula-Georgiou, E. (2010b). Testing space-scale methodologies for automatic geomorphic feature extraction from lidar in a complex mountainous landscape. *Water Resources Research*, **46**, W11535.

Passalacqua, P., Belmont, P. and Foufoula-Georgiou, E. (2012). Automatic geomorphic feature extraction from lidar in flat and engineered landscapes. *Water Resources Research*, **48**, W03528.

Pavlis, T.L. and Bruhn, R.L. (2011). Application of LIDAR to resolving bedrock structure in areas of poor exposure: An example from the STEEP study area, southern Alaska. *GSA Bulletin*, **123**, 206–217.

Pazzaglia, F.J. (2013). 9.22 Fluvial Terraces. In J.F. Shroder, ed., *Treatise on Geomorphology*, 379–412, Academic Press, San Diego.

Pazzaglia, F.J. and Brandon, M.T. (2001). A Fluvial Record of Long-term Steady-state Uplift and Erosion Across the Cascadia Forearc High, Western Washington State. *American Journal of Science*, **301**, 385–431.

Pazzaglia, F.J., Gardner, T.W. and Merritts, D.J. (1998). Bedrock Fluvial Incision and Longitudinal Profile Development Over Geologic Time Scales Determined by Fluvial Terraces. In K.J. Tinkler and E.E. Wohl, eds., *Rivers Over Rock: Fluvial Processes in Bedrock Channels*, 207–235, American Geophysical Union.

Pelletier, J.D. (2004). Persistent drainage migration in a numerical landscape evolution model. *Geophysical Research Letters*, **31**, L20501.

Pelletier, J.D. (2010). Minimizing the grid-resolution dependence of flow-routing algorithms for geomorphic applications. *Geomorphology*, **122**, 91–98.

Pelletier, J.D. (2012). Fluvial and slope-wash erosion of soil-mantled landscapes: detachment- or transport-limited? *Earth Surface Processes and Landforms*, **37**, 37–51.

Pelletier, J.D. (2013). A robust, two-parameter method for the extraction of drainage networks from high-resolution digital elevation models (DEMs): Evaluation using synthetic and real-world DEMs. *Water Resources Research*, **49**, 75–89.

Pelletier, J.D. and Rasmussen, C. (2009). Geomorphically based predictive mapping of soil thickness in upland watersheds. *Water Resources Research*, **45**, W09417.

Pelletier, J.D., McGuire, L.A., Ash, J.L., Engelder, T.M., Hill, L.E., Leroy, K.W., Orem, C.A., Rosenthal, W.S., Trees, M.A., Rasmussen, C. and Chorover, J. (2011). Calibration and testing of upland hillslope evolution models in a dated landscape: Banco Bonito, New Mexico. *Journal of Geophysical Research: Earth Surface*, **116**, F04004.

Pelletier, J.D., Nichols, M.H. and Nearing, M.A. (2016). The influence of Holocene vegetation changes on topography and erosion rates: A case study at Walnut Gulch Experimental Watershed, Arizona. *Earth Surface Dynamics Discussions*, 1–45.

Peltier, W. (2004). Global glacial isostasy and the surface of the ice-age Earth: The ICE-5g (VM2) model and GRACE. *Annual Review of Earth and Planetary Sciences*, **32**, 111–149.

Perona, P. and Malik, J. (1990). Scale-space and edge detection using anisotropic diffusion. *IEEE Transactions on Pattern Analysis and Machine Intelligence*, **12**, 629–639.

Perron, J.T. and Royden, L. (2013). An integral approach to bedrock river profile analysis. *Earth Surface Processes and Landforms*, **38**, 570–576.

Perron, J.T., Dietrich, W.E. and Kirchner, J.W. (2008a). Controls on the spacing of first-order valleys. *Journal of Geophysical Research: Earth Surface*, **113**, F04016.

Perron, J.T., Kirchner, J.W. and Dietrich, W.E. (2008b). Spectral signatures of characteristic spatial scales and nonfractal structure in landscapes. *Journal of Geophysical Research: Earth Surface*, **113**, F04003.

Perron, J.T., Kirchner, J.W. and Dietrich, W.E. (2009). Formation of evenly spaced ridges and valleys. *Nature*, **460**, 502–505.

Perron, J.T., Richardson, P.W., Ferrier, K.L. and Lapôtre, M. (2012). The root of branching river networks. *Nature*, **492**, 100–103.

Personius, S.F., Kelsey, H.M. and Grabau, P.C. (1993). Evidence for Regional Stream Aggradation in the Central Oregon Coast Range during the Pleistocene-Holocene Transition. *Quaternary Research*, **40**, 297–308.

Peucker, T.K. and Douglas, D.H. (1975). Detection of Surface-Specific Points by Local Parallel Processing of Discrete Terrain Elevation Data. *Computer Graphics and Image Processing*, **4**, 375–387.

Pionke, H.B., Hoover, J.R., Schnabel, R.R., Gburek, W.J., Urban, J.B. and Rogowski, A.S. (1988). Chemical-hydrologic interactions in the near-stream zone. *Water Resources Research*, **24**, 1101–1110.

Playfair, J. (1802). *Illustrations of the Huttonian Theory of the Earth*. Edinburgh.

Press, W.H. (2007). *Numerical recipes : the art of scientific computing*. Cambridge : Cambridge University Press, 2007.

Pritchard, D., Roberts, G.G., White, N.J. and Richardson, C.N. (2009). Uplift histories from river profiles. *Geophysical Research Letters*, **36**, L24301.

Purinton, B. and Bookhagen, B. (2017). Validation of digital elevation models (DEMs) and comparison of geomorphic metrics on the southern Central Andean Plateau. *Earth Surface Dynamics*, **5**, 211–237.

Qin, C.Z. and Zhan, L. (2012). Parallelizing flow-accumulation calculations on graphics processing units—From iterative DEM preprocessing algorithm to recursive multiple-flow-direction algorithm. *Computers & Geosciences*, **43**, 7–16.

Quinn, P.F., Beven, K.J. and Lamb, R. (1995). The ln(a/tan/β) index: How to calculate it and how to use it within the topmodel framework. *Hydrological Processes*, **9**, 161–182.

Raber, G.T., Jensen, J.R., Schill, S.R. and Schuckman, K. (2002). Creation of digital terrain models using an adaptive lidar vegetation point removal process. *Photogrammetric Engineering and Remote Sensing*, **68**, 1307–1315.

Rabus, B., Eineder, M., Roth, A. and Bamler, R. (2003). The shuttle radar topography mission—a new class of digital elevation models acquired by spaceborne radar. *ISPRS Journal of Photogrammetry and Remote Sensing*, **57**, 241–262.

Reinhardt, L., Jerolmack, D., Cardinale, B.J., Vanacker, V. and Wright, J. (2010). Dynamic interactions of life and its landscape: feedbacks at the interface of geomorphology and ecology. *Earth Surface Processes and Landforms*, **35**, 78–101.

Reinhardt, L.J., Bishop, P., Hoey, T.B., Dempster, T.J. and Sanderson, D.C.W. (2007). Quantification of the transient response to base-level fall in a small mountain catchment: Sierra Nevada, southern Spain. *Journal of Geophysical Research: Earth Surface*, **112**, F03S05.

Riebe, C.S., Kirchner, J.W., Granger, D.E. and Finkel, R.C. (2000). Erosional equilibrium and disequilibrium in the Sierra Nevada, inferred from cosmogenic 26al and 10be in alluvial sediment. *Geology*, **28**, 803–806.

Riebe, C.S., Sklar, L.S., Lukens, C.E. and Shuster, D.L. (2015). Climate and topography control the size and flux of sediment produced on steep mountain slopes. *Proceedings of the National Academy of Sciences*, **112**, 15574–15579.

Rigon, R., Rinaldo, A., Rodriguez-Iturbe, I., Bras, R.L. and Ijjasz-Vasquez, E. (1993). Optimal channel networks: A framework for the study of river basin morphology. *Water Resources Research*, **29**, 1635–1646.

Rinaldo, A., Dietrich, W.E., Rigon, R., Vogel, G.K. and Rodrlguez-lturbe, I. (1995). Geomorphological signatures of varying climate. *Nature*, **374**, 632–635.

Roberts, G.G. and White, N. (2010). Estimating uplift rate histories from river profiles using African examples. *Journal of Geophysical Research: Solid Earth*, **115**, B02406.

Rodriguez-Iturbe, I. and Rinaldo, A. (1997). *Fractal river basins: chance and self-organization*. Cambridge University Press.

Rodriguez-Iturbe, I., Rinaldo, A., Rigon, R., Bras, R.L., Ijjasz-Vasquez, E. and Marani, A. (1992). Fractal structures as least energy patterns: The case of river networks. *Geophysical Research Letters*, **19**, 889–892.

Roering, J.J. (2008). How well can hillslope evolution models "explain" topography? Simulating soil transport and production with high-resolution topographic data. *Geological Society of America Bulletin*, **120**, 1248–1262.

Roering, J.J., Kirchner, J.W. and Dietrich, W.E. (1999). Evidence for nonlinear, diffusive sediment transport on hillslopes and implications for landscape morphology. *Water Resources Research*, **35**, 853–870.

Roering, J.J., Kirchner, J.W., Sklar, L.S. and Dietrich, W.E. (2001). Hillslope evolution by nonlinear creep and landsliding: An experimental study. *Geology*, **29**, 143–146.

Roering, J.J., Kirchner, J.W. and Dietrich, W.E. (2005). Characterizing structural and lithologic controls on deep-seated landsliding: Implications for topographic relief and landscape evolution in the Oregon Coast Range, USA. *Geological Society of America Bulletin*, **117**, 654–668.

Roering, J.J., Perron, J.T. and Kirchner, J.W. (2007). Functional relationships between denudation and hillslope form and relief. *Earth and Planetary Science Letters*, **264**, 245–258.

Roering, J.J., Marshall, J., Booth, A.M., Mort, M. and Jin, Q. (2010). Evidence for biotic controls on topography and soil production. *Earth and Planetary Science Letters*, **298**, 183–190.

Roering, J.J., Mackey, B.H., Marshall, J.A., Sweeney, K.E., Deligne, N.I., Booth, A.M., Handwerger, A.L. and Cerovski-Darriau, C. (2013). 'You are HERE': Connecting the dots with airborne lidar for geomorphic fieldwork. *Geomorphology*, **200**, 172–183.

Roth, G., Siccardi, F. and Rosso, R. (1989). Hydrodynamic description of the erosional development of drainage patterns. *Water Resources Research*, **25**, 319–332.

Roy, A.G. (1983). Optimal Angular Geometry Models of River Branching. *Geographical Analysis*, **15**, 87–96.

Royden, L. and Perron, J.T. (2013). Solutions of the stream power equation and application to the evolution of river longitudinal profiles. *Journal of Geophysical Research: Earth Surface*, **118**, 497–518.

Royden, L., Clark, M. and Whipple, K.X. (2000). Evolution of river elevation profiles by bedrock incision: analystical solutions for transient river profiles related to changing uplift and precipitation rates. In *EOS, Transactions of the American Geophysical Union*, vol. 81, Fall Meeting Supplement.

San, B.T. and Suzen, M.L. (2005). Digital elevation model (DEM) generation and accuracy assessment from ASTER stereo data. *International Journal of Remote Sensing*, **26**, 5013–5027.

Sangireddy, H., Carothers, R.A., Stark, C.P. and Passalacqua, P. (2016a). Controls of climate, topography, vegetation, and lithology on drainage density extracted from high resolution topography data. *Journal of Hydrology*, **537**, 271–282.

Sangireddy, H., Stark, C.P., Kladzyk, A. and Passalacqua, P. (2016b). GeoNet: An open source software for the automatic and objective extraction of channel heads, channel network, and channel morphology from high resolution topography data. *Environmental Modelling & Software*, **83**, 58–73.

Schreider, S.Y., Smith, D.I. and Jakeman, A.J. (2000). Climate Change Impacts on Urban Flooding. *Climatic Change*, **47**, 91–115.

Schulz, W.H. (2007). Landslide susceptibility revealed by LIDAR imagery and historical records, Seattle, Washington. *Engineering Geology*, **89**, 67–87.

Schumm, S.A. (1956). Evolution of Drainage Systems and Slopes in Badlands at Perth Amboy, New Jersey. *Geological Society of America Bulletin*, **67**, 597–646.

Seidl, M.A. and Dietrich, W.E. (1992). The problem of channel erosion into bedrock. *Catena Supplement*, 101–124.

Seybold, H., Rothman, D.H. and Kirchner, J.W. (2017). Climate's watermark in the geometry of stream networks. *Geophysical Research Letters*, **44**, 2016GL072089.

Shan, J. and Aparajithan, S. (2005). Urban DEM Generation from Raw Lidar Data. *Photogrammetric Engineering & Remote Sensing*, **71**, 217–226.

Shreve, R.L. (1966). Statistical Law of Stream Numbers. *The Journal of Geology*, **74**, 17–37.

Shreve, R.L. (1967). Infinite Topologically Random Channel Networks. *The Journal of Geology*, **75**, 178–186.

Shreve, R.L. (1969). Stream Lengths and Basin Areas in Topologically Random Channel Networks. *The Journal of Geology*, **77**, 397–414.

Simpson, G. and Schlunegger, F. (2003). Topographic evolution and morphology of surfaces evolving in response to coupled fluvial and hillslope sediment transport. *Journal of Geophysical Research: Solid Earth*, **108**, 2300.

Sklar, L. and Dietrich, W.E. (1998). River Longitudinal Profiles and Bedrock Incision Models: Stream Power and the Influence of Sediment Supply. In K.J. Tinkler and E.E. Wohl, eds., *Rivers Over Rock: Fluvial Processes in Bedrock Channels*, 237–260, American Geophysical Union.

Sklar, L.S. and Dietrich, W.E. (2001). Sediment and rock strength controls on river incision into bedrock. *Geology*, **29**, 1087–1090.

Slatton, K.C., Carter, W.E., Shrestha, R.L. and Dietrich, W. (2007). Airborne Laser Swath Mapping: Achieving the resolution and accuracy required for geosurficial research. *Geophysical Research Letters*, **34**, L23S10.

Small, C.J. and McCarthy, B.C. (2001). Vascular Flora of the Waterloo Wildlife Research Station, Athens County, Ohio. *Castanea*, **66**, 363–382.

Smart, J.S. (1978). The analysis of drainage network composition. *Earth Surface Processes*, **3**, 129–170.

Snyder, N.P., Whipple, K.X., Tucker, G.E. and Merritts, D.J. (2000). Landscape response to tectonic forcing: Digital elevation model analysis of stream profiles in the Mendocino triple junction region, northern California. *Geological Society of America Bulletin*, **112**, 1250–1263.

Snyder, N.P., Whipple, K.X., Tucker, G.E. and Merritts, D.J. (2003). Importance of a stochastic distribution of floods and erosion thresholds in the bedrock river incision problem. *Journal of Geophysical Research: Solid Earth*, **108**, 2117.

Sofia, G., Tarolli, P., Cazorzi, F. and Dalla Fontana, G. (2011). An objective approach for feature extraction: distribution analysis and statistical descriptors for scale choice and channel network identification. *Hydrol. Earth Syst. Sci.*, **15**, 1387–1402.

Sofia, G., Fontana, G.D. and Tarolli, P. (2014a). High-resolution topography and anthropogenic feature extraction: testing geomorphometric parameters in floodplains. *Hydrological Processes*, **28**, 2046–2061.

Sofia, G., Marinello, F. and Tarolli, P. (2014b). A new landscape metric for the identification of terraced sites: The Slope Local Length of Auto-Correlation (SLLAC). *ISPRS Journal of Photogrammetry and Remote Sensing*, **96**, 123–133.

Stock, J. and Dietrich, W.E. (2003). Valley incision by debris flows: Evidence of a topographic signature. *Water Resources Research*, **39**.

Stock, J.D. and Dietrich, W.E. (2006). Erosion of steepland valleys by debris flows. *Geological Society of America Bulletin*, **118**, 1125–1148.

Stock, J.D. and Montgomery, D.R. (1999). Geologic constraints on bedrock river incision using the stream power law. *Journal of Geophysical Research: Solid Earth*, **104**, 4983–4993.

Stoker, J.M., Greenlee, S.K., Gesch, D.B. and Menig, J.C. (2006). CLICK: The new USGS center for LIDAR information coordination and knowledge. *Photogrammetric Engineering and Remote Sensing*, **72**, 613616.

Stout, J.C. and Belmont, P. (2014). TerEx Toolbox for semi-automated selection of fluvial terrace and floodplain features from lidar. *Earth Surface Processes and Landforms*, **39**, 569–580.

Strahler, A.N. (1952). Hypsometric (area-altitude) analysis of erosional topography. *Geological Society of America Bulletin*, **63**, 1117–1142.

Strahler, A.N. (1957). Quantitative analysis of watershed geomorphology. *Transactions, American Geophysical Union*, **38**, 913–920.

Sweeney, K.E., Roering, J.J. and Ellis, C. (2015). Experimental evidence for hillslope control of landscape scale. *Science*, **349**, 51–53.

Talling, P.J. and Sowter, M.J. (1999). Drainage density on progressively tilted surfaces with different gradients, Wheeler Ridge, California. *Earth Surface Processes and Landforms*, **24**, 809–824.

Tarboton, D.G. (1996). Fractal river networks, Horton's laws and Tokunaga cyclicity. *Journal of Hydrology*, **187**, 105–117.

Tarboton, D.G. (1997). A new method for the determination of flow directions and upslope areas in grid digital elevation models. *Water Resources Research*, **33**, 309–319.

Tarboton, D.G., Bras, R.L. and Rodriguez-Iturbe, I. (1989). Scaling and elevation in river networks. *Water Resources Research*, **25**, 2037–2051.

Tarboton, D.G., Bras, R.L. and Rodriguez-Iturbe, I. (1991). On the extraction of channel networks from digital elevation data. *Hydrological Processes*, **5**, 81–100.

Tarboton, D.G., Bras, R.L. and Rodriguez-Iturbe, I. (1992). A physical basis for drainage density. *Geomorphology*, **5**, 59–76.

Tarolli, P. (2014). High-resolution topography for understanding Earth surface processes: Opportunities and challenges. *Geomorphology*, **216**, 295–312.

Tarolli, P. and Dalla Fontana, G. (2009). Hillslope-to-valley transition morphology: New opportunities from high resolution DTMs. *Geomorphology*, **113**, 47–56.

Tarolli, P., Sofia, G. and Fontana, G.D. (2012). Geomorphic features extraction from high-resolution topography: landslide crowns and bank erosion. *Natural Hazards*, **61**, 65–83.

Tesfa, T.K., Tarboton, D.G., Watson, D.W., Schreuders, K.A.T., Baker, M.E. and Wallace, R.M. (2011). Extraction of hydrological proximity measures from DEMs using parallel processing. *Environmental Modelling & Software*, **26**, 1696–1709.

Thommeret, N., Bailly, J.S. and Puech, C. (2010). Extraction of thalweg networks from DTMs: application to badlands. *Hydrol. Earth Syst. Sci.*, **14**, 1527–1536.

Thornthwaite, C.W. (1931). The Climates of North America: According to a New Classification. *Geographical Review*, **21**, 633–655.

Townsend, P.A. (2001). Relationships between vegetation patterns and hydroperiod on the Roanoke River floodplain, North Carolina. *Plant Ecology*, **156**, 43–58.

Trimble, S.W. (1999). Decreased Rates of Alluvial Sediment Storage in the Coon Creek Basin, Wisconsin, 1975-93. *Science*, **285**, 1244–1246.

Tucker, G., Lancaster, S., Gasparini, N. and Bras, R. (2001a). The Channel-Hillslope Integrated Landscape Development Model (CHILD). In R.S. Harmon and W.W.D. III, eds., *Landscape Erosion and Evolution Modeling*, 349–388, Springer US.

Tucker, G.E. (2004). Drainage basin sensitivity to tectonic and climatic forcing: implications of a stochastic model for the role of entrainment and erosion thresholds. *Earth Surface Processes and Landforms*, **29**, 185–205.

Tucker, G.E. and Bras, R.L. (1998). Hillslope processes, drainage density, and landscape morphology. *Water Resources Research*, **34**, 2751–2764.

Tucker, G.E. and Slingerland, R. (1997). Drainage basin responses to climate change. *Water Resources Research*, **33**, 2031–2047.

Tucker, G.E., Catani, F., Rinaldo, A. and Bras, R.L. (2001b). Statistical analysis of drainage density from digital terrain data. *Geomorphology*, **36**, 187–202.

Turowski, J.M. (2012). Semi-Alluvial Channels and Sediment-Flux-Driven Bedrock Erosion. In M. Church, P.M. Biron and A.G. Roy, eds., *Gravel-Bed Rivers*, 399–418, John Wiley & Sons, Ltd.

Turowski, J.M., Hovius, N., Meng-Long, H., Lague, D. and Men-Chiang, C. (2008). Distribution of erosion across bedrock channels. *Earth Surface Processes and Landforms*, **33**, 353–363.

Unruh, J.R. (1991). The uplift of the Sierra Nevada and implications for late Cenozoic epeirogeny in the western Cordillera. *Geological Society of America Bulletin*, **103**, 1395–1404.

Van Den Eeckhaut, M., Verstraeten, G. and Poesen, J. (2007). Morphology and internal structure of a dormant landslide in a hilly area: The Collinabos landslide (Belgium). *Geomorphology*, **89**, 258–273.

Van Den Eeckhaut, M., Kerle, N., Poesen, J. and Hervás, J. (2012). Object-oriented identification of forested landslides with derivatives of single pulse LiDAR data. *Geomorphology*, **173**, 30–42.

Viveen, W., Schoorl, J.M., Veldkamp, A. and van Balen, R.T. (2014). Modelling the impact of regional uplift and local tectonics on fluvial terrace preservation. *Geomorphology*, **210**, 119–135.

Vivoni, E.R., Bowman, R.S., Wyckoff, R.L., Jakubowski, R.T. and Richards, K.E. (2006). Analysis of a monsoon flood event in an ephemeral tributary and its downstream hydrologic effects. *Water Resources Research*, **42**, W03404.

Vosselman, G. (2000). Slope based filtering of Laser altimetry data. *International Archives of Photogrammetry and Remote Sensing*, **XXXIII**, 935–942.

Wallace, A., Nichol, C. and Woodhouse, I. (2012). Recovery of Forest Canopy Parameters by Inversion of Multispectral LiDAR Data. *Remote Sensing*, **4**, 509–531.

Walter, R., Merritts, D.J. and Rahnis, M. (2007). Estimating volume, nutrient conent, and rates of stream bank erosion of legacy sediment in the Piedmont and Valley and Ridge physiographic provinces, Southeastern and Central PA. Tech. rep., Pennsylvania Department of Environmental Protection, Harrisburg, PA.

Wang, L. and Liu, H. (2006). An efficient method for identifying and filling surface depressions in digital elevation models for hydrologic analysis and modelling. *International Journal of Geographical Information Science*, **20**, 193–213.

Wang, Y., Zhang, H., Zheng, D., Yu, J., Pang, J. and Ma, Y. (2017). Coupling slope–area analysis, integral approach and statistic tests to steady-state bedrock river profile analysis. *Earth Surface Dynamics*, **5**, 145–160.

Wasklewicz, T., Staley, D.M., Reavis, K. and Oguchi, T. (2013). 3.6 Digital Terrain Modeling. In J.F. Shroder, ed., *Treatise on Geomorphology*, 130–161, Academic Press, San Diego.

Wegmann, K.W. and Pazzaglia, F.J. (2002). Holocene strath terraces, climate change, and active tectonics: The Clearwater River basin, Olympic Peninsula, Washington State. *Geological Society of America Bulletin*, **114**, 731–744.

Whipple, K.X. (2001). Fluvial Landscape Response Time: How Plausible Is Steady-State Denudation? *American Journal of Science*, **301**, 313–325.

Whipple, K.X. and Tucker, G.E. (1999). Dynamics of the stream-power river incision model: Implications for height limits of mountain ranges, landscape response timescales, and research needs. *Journal of Geophysical Research: Solid Earth*, **104**, 17661–17674.

Whipple, K.X. and Tucker, G.E. (2002). Implications of sediment-flux-dependent river incision models for landscape evolution. *Journal of Geophysical Research: Solid Earth*, **107**, ETG 3–1.

Whipple, K.X., Hancock, G.S. and Anderson, R.S. (2000). River incision into bedrock: Mechanics and relative efficacy of plucking, abrasion, and cavitation. *Geological Society of America Bulletin*, **112**, 490–503.

Whipple, K.X., DiBiase, R.A. and Crosby, B.T. (2013). 9.28 Bedrock Rivers. In J.F. Shroder, ed., *Treatise on Geomorphology*, 550–573, Academic Press, San Diego.

Whittaker, A.C. and Boulton, S.J. (2012). Tectonic and climatic controls on knickpoint retreat rates and landscape response times. *Journal of Geophysical Research: Earth Surface*, **117**, F02024.

Whittaker, A.C., Cowie, P.A., Attal, M., Tucker, G.E. and Roberts, G.P. (2007). Contrasting transient and steady-state rivers crossing active normal faults: new field observations from the Central Apennines, Italy. *Basin Research*, **19**, 529–556.

Whittaker, A.C., Attal, M., Cowie, P.A., Tucker, G.E. and Roberts, G. (2008). Decoding temporal and spatial patterns of fault uplift using transient river long profiles. *Geomorphology*, **100**, 506–526.

Wiener, N. (1949). *Extrapolation, interpolation, and smoothing of stationary time series: with engineering applications*. Technology Press of the Massachusetts Institute of Technology.

Willemin, J.H. (2000). Hack's Law: Sinuosity, convexity, elongation. *Water Resources Research*, **36**, 3365–3374.

Willett, S.D., McCoy, S.W., Perron, J.T., Goren, L. and Chen, C.Y. (2014). Dynamic Reorganization of River Basins. *Science*, **343**, 1248765.

Willgoose, G., Bras, R.L. and Rodriguez-Iturbe, I. (1991). A coupled channel network growth and hillslope evolution model: 1. Theory. *Water Resources Research*, **27**, 1671–1684.

Williams, W.A., Jensen, M.E., Winne, J.C. and Redmond, R.L. (2000). An Automated Technique for Delineating and Characterizing Valley-Bottom Settings. *Environmental Monitoring and Assessment*, **64**, 105–114.

Wobus, C., Whipple, K.X., Kirby, E., Snyder, N., Johnson, J., Spyropolou, K., Crosby, B. and Sheehan, D. (2006). Tectonics from topography: Procedures, promise, and pitfalls. *Geological Society of America Special Papers*, **398**, 55–74.

Wohl, E.E. and Merritt, D.M. (2001). Bedrock channel morphology. *Geological Society of America Bulletin*, **113**, 1205–1212.

Wolman, M.G. and Leopold, L.B. (1957). River flood plains: Some observations on their formation. USGS Numbered Series 282-C, U.S. Government Printing Office, Washington, D.C.

Wood, J. (1996). *The geomorphological characterisation of Digital Elevation Models.*. PhD thesis, University of Leicester.

Woodhouse, I.H., Nichol, C., Sinclair, P., Jack, J., Morsdorf, F., Malthus, T.J. and Patenaude, G. (2011). A Multispectral Canopy LiDAR Demonstrator Project. *IEEE Geoscience and Remote Sensing Letters*, **8**, 839–843.

Wu, H., Guan, X. and Gong, J. (2011). ParaStream: A parallel streaming Delaunay triangulation algorithm for LiDAR points on multicore architectures. *Computers & Geosciences*, **37**, 1355–1363.

Yamaguchi, Y., Kahle, A.B., Tsu, H., Kawakami, T. and Pniel, M. (1998). Overview of Advanced Spaceborne Thermal Emission and Reflection Radiometer (ASTER). *IEEE Transactions on Geoscience and Remote Sensing*, **36**, 1062–1071.

Yang, J., Townsend, R.D. and Daneshfar, B. (2006). Applying the HEC-RAS model and GIS techniques in river network floodplain delineation. *Canadian Journal of Civil Engineering*, **33**, 19–28.

Yoo, K., Amundson, R., Heimsath, A.M. and Dietrich, W.E. (2005). Process-based model linking pocket gopher (Thomomys bottae) activity to sediment transport and soil thickness. *Geology*, **33**, 917–920.

Zhang, K. and Whitman, D. (2005). Comparison of Three Algorithms for Filtering Airborne Lidar Data. *Photogrammetric Engineering & Remote Sensing*, **71**, 313–324.

Zhang, K., Chen, S.C., Whitman, D., Shyu, M.L., Yan, J. and Zhang, C. (2003). A progressive morphological filter for removing nonground measurements from airborne LIDAR data. *IEEE Transactions on Geoscience and Remote Sensing*, **41**, 872–882.

Zhang, T.Y. and Suen, C.Y. (1984). A Fast Parallel Algorithm for Thinning Digital Patterns. *Commun. ACM*, **27**, 236–239.

Zhang, W. and Montgomery, D.R. (1994). Digital elevation model grid size, landscape representation, and hydrologic simulations. *Water Resources Research*, **30**, 1019–1028.